Preparation of large cold atomic ensembles and applications in efficient light-matter interfacing

Pierre Vernaz-Gris

THÈSE DE DOCTORAT
DE L'UNIVERSITÉ PIERRE ET MARIE CURIE

Spécialité : Physique

École doctorale : « Physique en Île-de-France »

réalisée

au Laboratoire Kastler Brossel
et à l'Australian National University

présentée par

Pierre VERNAZ-GRIS

pour obtenir le grade de :

DOCTEUR DE L'UNIVERSITÉ PIERRE ET MARIE CURIE

Sujet de la thèse :

Preparation of large cold atomic ensembles and applications in efficient light-matter interfacing

soutenue le 12 janvier 2018

devant le jury composé de :

M.	Thierry CHANELIÈRE	Rapporteur
M.	Joshua NUNN	Rapporteur
Mme	Valia VOLIOTIS	Examinatrice
M.	Gabriel HÉTET	Invité
M.	Ben BUCHLER	Encadrant de thèse
M.	Ping Koy LAM	Co-directeur de thèse
M.	Julien LAURAT	Co-directeur de thèse

Acknowledgements

First of all, I would like to thank the jury of my PhD defence, you all did great honour to this thesis and to my work: Valia Voliotis for presiding the jury and your investment in discovering my research topic, Joshua Nunn and Thierry Chanelière for examining my whole work, reading every single of the lines of this thesis and being great *rapporteurs* at my defence, and Gabriel Hétet for accepting my invitation to assess the progress on the Australian experiment you started and which I had the pleasure to take over.

All my gratitude goes to Julien Laurat, Ping Koy Lam and Ben Buchler for mentoring me during this doctorate, I could not have wished for better PhD advisers.

Julien, you had an instrumental role in setting up this *cotutelle* PhD and accompanying me from a preliminary bibliographic project on quantum memories all the way to the thesis submission and PhD defence. Both the latter involved many careful proof-readings and attentive rehearsals, I am thankful for your scientific guidance and your ongoing support throughout this PhD.

Ping Koy, it was a pleasure joining your group from the first day of my internship, and I was delighted to join the team a second time for this longer adventure. I am thankful for everything you arranged to make my moves across the globe a bit easier, for the expertise you were sharing with me and your advice on my PhD and beyond.

Ben, you do a great job bringing together the GEM team and orchestrating our projects, thank you for your help and I wish you the best of luck for the future endeavours with the experiment.

Thank you, Geoff Campbell, you were infinitely helpful as an informal additional PhD supervisor. It goes without saying how much I have learned from your experience in the lab, your intuition, and your overall insight.

Hanna Le Jeannic and Neil Corzo-Trejo, thanks for your untiring support in the struggles of the PhD life, I am glad to have been through these years with you.

Thanks to the GEM team: Daniel Higginbottom, Jesse Everett, Aaron Tranter, Anthony Leung and Karun Paul. Also thanks to Nick Robins, of the neighbouring Atomlaser group, and the other postdocs and PhD students who built and tamed the experiments before I got involved: Mahdi Hosseini, Ben Sparkes, Julien Bernu, Young-Wook Cho, Mingtao Cao and Jiao Geng.

Thanks to Valentina Parigi for helping me settle in at LKB, after being handed the reins of the experiment by Lucile Veissier and Lambert Giner. Thank you, Kun Huang, for joining Julien's group again but to work on the cold atoms, you did an amazing job improving and running our setup which led to great achievements. Thank you, Alexandra "Sasha" Sheremet for also rejoining the team and your contributions to everything theoretical.

I would like to thank Christophe Lambert for designing the coils for the 2D-MOT at LKB, and the mechanical workshop for this fabrication among many others: Jean-Michel

Isac, Arnaud Leclercq, Thierry Bastien, Gaël Coupin, Dore Carounagarane, Sébastien Colinot.

Brigitte Delamour, Jean-Pierre Okpisz and Loïc Garcia of the electronics workshop at the LKB, thank you for your support, your kindness and availability.

Thanks to the mechanical and electronics workshops at the ANU.

Johnny Debs, thank you for the great experience teaching "Foundations of Physics" and best of luck with the newly-founded Makerspace.

Thanks Amanda Haynes, Lynne Christians, Thierry Tardieu, Laetitia Morel, and Romain Rybka for managing all the administrative aspects of this *cotutelle*.

Last but not least, Shirin, thank you for your invaluable help across the hemispheres and the time zones, your perpetual kindness and your love.

All figures therein are my own production for this thesis, except where they are taken from coauthored articles (namely [Tranter2018] for figure 2.15; [Vernaz-Gris2018] for figures 3.5, 3.6, 3.7, 3.10, 3.11, 3.12, 3.13, 3.14, 3.15, 3.16; [Vernaz-Gris2018a] for figures 4.11, 4.12, 4.13; [Everett2017] for figure 5.5, 5.6, 5.8, 5.9; [Everett2018] for figures 5.11, 5.12, 5.13)

Some figures comprised in this thesis use ComponentLibrary, a vector graphics library for illustrations of optics experiments by Alexander Franzen, which is licensed under a Creative Commons Attribution-NonCommercial 3.0 Unported License, available at `http://www.gwoptics.org/ComponentLibrary/`.

An early version of the machine-learning algorithm presented in section 2.4 was based on M-LOOP [Hush2016]. A subsequent version is presented in the published article [Tranter2018]. I would like to thank Aaron Tranter and Harry Slatyer who led the investigation on machine-optimised atom preparations, which provided us with repeatable top-notch optical depth even when we were breaking and tweaking the experimental setup.

Contents

Introduction

Light-matter interaction leads to an extremely broad range of applications, ranging from the preparation of large atomic ensembles to the realisation of quantum memories and the generation of single photons. The PhD work presented here was undertaken as a *cotutelle* between the Laboratoire Kastler Brossel (LKB) and the Australian National University (ANU).

The LKB has a long history with light-matter interaction, stemming from the very founding of the laboratory under the name "Laboratoire de Spectroscopie hertzienne de l'ENS" (ENS laboratory of hertzian spectroscopy) in 1951, and actually a few years before that with the works of Jean Brossel and Alfred Kastler on the phenomenon of double – optical and magnetic – resonance. Optical pumping is often said to have been invented by these two founding fathers of LKB, as early as 1950, and is now a preeminent technique in any atomic experiment, either in solids, warm and cold vapours. I joined there the Quantum Networks team led by Julien Laurat, aiming at the development of quantum network resources.

The interaction of light and atoms is just as central to the Centre for Quantum Computation and Communication Technology (CQC^2T), which explains the many collaborations between the Parisian laboratory and this centre of excellence of the Australian Research Council. In particular, at its node at the ANU, the Photonics group led by Ping Koy Lam, focuses on the realisations of quantum memories, with Ben Buchler at the helm of those, and continuous-variable quantum information protocols. Holding the optical memory efficiency record since 2011 with the gradient echo memory, the memory scheme developed in the group and implemented in various forms and platforms, the group has a renowned expertise which complements perfectly the one at LKB.

When I started my PhD, the experiments in Paris and in Canberra has both gone through a very fruitful phase performing well-known protocols and it was time to explore their capabilities from there. One of the challenges at LKB was to improve the performance of the Duan-Lukin-Cirac-Zoller scheme that had been implemented over the work of previous PhD students. We hoped increasing the optical depth of the atomic ensemble with a 2D geometry would suffice, but instead the geometry first enabled us to perform the storage of polarisation qubits based on electromagnetically-induced transparency, which benefited greatly from this improvement on optical depth. At ANU, our aim was to come up with new protocols to investigate. Stationary light had been previously considered as a candidate and so fellow students and I became the pioneers of its study at ANU. We not only characterised its evolution and self-stabilisation in a cold atomic ensemble, we also extend the scope of its applications with a novel memory scheme inspired from its properties of symmetry.

The philosophy with which this thesis has been written is to share my insight on the preparation of large atomic ensembles and the experiments which use this platform for

efficient atom-light interfacing. I have become acquainted with both topics during my PhD and I present them in this thesis with a focus on all the aspects relevant to an experimental quantum optician.

Thesis layout This dissertation is organised in the following chapters:

1. I start by presenting classical and quantum interaction of light with matter, and its numerous applications, and I expose the mathematical formalism which I will use throughout this thesis. Among the applications, I focus on quantum memory schemes and I review in detail their performance achieved so far.

2. Secondly, I present the role of large atomic ensembles in experimental realisations and the state of the art of their production. I describe in detail the warm atomic vapour and the two cold-atom apparatuses that I have been using during the course of my PhD.

3. Among quantum memory schemes, the one based on electromagnetically-induced transparency is arguably the most popular and is central to the experiment at LKB which I have led. I present this phenomenon, followed by the theory of additional excited levels we have developed and the experiment of the storage of a qubit in spatially-multiplexed configuration.

4. A second experimental highlight of my PhD, this time at ANU, was the realisation of a Raman memory, where the signal and control pair are brought off resonance from the excited state transition. The uniqueness of our configuration was to recall the stored light in the backward direction, which is known to be fundamentally preferable and yet is rarely performed.

5. Stationary light, although it is generated in similar setups, differs from the "stopped"-light experiments presented in the two previous chapters. The last chapter is devoted to its theoretical description and the series of experiments involving this other form of light, followed by a new memory protocol, conceptually close to stationary light.

Publications The work presented in this thesis has led to the following articles, which have been published or are pending publication by peer-review journals:

[1] J. L. Everett, G. T. Campbell, Y.-W. Cho, P. Vernaz-Gris, D. Higginbottom, O. Pinel, N. P. Robins, P. K. Lam, and B. C. Buchler. *Dynamical observations of self-stabilizing stationary light.* Nature Physics, **13**, 68–73 (January 2016). doi:10.1038/nphys3901.

[2] J. L. Everett, P. Vernaz-Gris, G. T. Campbell, A. D. Tranter, K. V. Paul, A. C. Leung, P. K. Lam, and B. C. Buchler. *Time-reversed and coherently enhanced memory: A single-mode quantum atom-optic memory without a cavity.* Phys. Rev. A, **98**, 063846 (Dec 2018). doi:10.1103/PhysRevA.98.063846.

[3] A. D. Tranter, H. J. Slatyer, M. R. Hush, A. C. Leung, J. L. Everett, K. V. Paul, P. Vernaz-Gris, P. K. Lam, B. C. Buchler, and G. T. Campbell. *Multi-parameter optimisation of a magneto-optical trap using deep learning.* Nature Communications, **9**, 4360 (October 2018). doi:10.1038/s41467-018-06847-1.

[4] P. Vernaz-Gris, K. Huang, M. Cao, A. S. Sheremet, and J. Laurat. *Highly-efficient quantum memory for polarization qubits in a spatially-multiplexed cold atomic ensemble.* Nature Communications, **9**, 363 (January 2018). doi:10.1038/s41467-017-02775-8.

[5] P. Vernaz-Gris, A. D. Tranter, J. L. Everett, A. C. Leung, K. V. Paul, G. T. Campbell, P. K. Lam, and B. C. Buchler. *High-performance Raman memory with spatio-temporal reversal.* Opt. Express, **26**, 12424–12431 (May 2018). doi:10.1364/OE.26.012424.

Chapter 1

Description of light-matter interaction in quantum memories

To cover the broad topic of light-matter interaction, I first describe some fundamental quantum properties relevant to this whole study.

1.1 Quantum fundamentals

It is not an understatement to state the twentieth century has experienced a quantum revolution, with the emergence of the theory describing quantum phenomena in its early years. A handful of new concepts were developed, like probability amplitudes, superposition, entanglement, decoherence, to cite only a few. Stemming from these principles applied to the radiation of light, the invention of the laser in 1960 brought about what we can call a new experimental and even industrial era.

I briefly introduce here some main concepts of quantum physics. The formalism in this thesis is based on "Fundamentals of Quantum Optics and Quantum Information" by Lambropoulos and Petrosyan [Lambropoulos], where the reader can find a more complete framework and further references on the topics covered hereafter.

1.1.1 Superposition

Let us consider a classical object which can be in a number of possible states, noted state 1, state 2, etc. We can affect a number $i = 1, 2, \ldots$ to each state and we additionally assume that the physical processes are completely deterministic, *i.e.* a given operation on state i always gives the same result. If the exact state of the object is unknown but we can attribute a probability p_i to the state i, we say the object is a statistical mixture of the states i. A measurement made on the statistical mixture has a probability p_i to yield the result of the same measurement made on state i. The particle has to be in one of its possible states, so the probabilities $\{p_i\}$ verify $\sum_i p_i = 1$.

A coherent superposition of states $\{i\}$ with amplitudes $\sqrt{p_i}$ corresponds to the state which can be written in Dirac notation:

$$|\psi\rangle = \sqrt{p_1}\,|1\rangle + \sqrt{p_2}\,|2\rangle + \ldots$$

A measurement made on state $|\psi\rangle$ also has a probability $|\langle i|\psi\rangle|^2 = p_i$ to give the result as if made on state $|i\rangle$, but a coherent superposition is quite different from a statistical mixture, as we will see now. Indeed, let us consider a which-path experiment: a particle

is sent through a plate pierced with two slits or pin-holes, and then detected on a screen. If the particle goes along one of the two paths, without any observer knowing, quantum physics state that it is in a coherent superposition of state 1, which corresponds to the first path, and state 2, the second path. If the two paths are subsequently recombined, it can lead to *quantum interference*. If somehow the path taken by the particle is known by some other observer, but we do not have access to this information, the interference is blurred and what we observe simply corresponds to a statistical mixture of states 1 and 2. The superposition state conveys the idea that the particle has simultaneously taken both paths, an especially bewildering quantum peculiarity.

In addition to the absolute value of the coefficient for state $|i\rangle$, which corresponds to the square root of the probability to detect the object in this state, each coefficient also has a phase φ_i, which manifests only in interference effects. As an example, let us consider the spin of a particle. Simply put, the spin is a unit vector in three dimensions but a measurement along a given axis of a spin can only take discrete – quantised – values which are equally spaced and by definition separated by integer values. A spin ½ is the spin of smallest non-zero value, whose measurements can take two values: $+1/2$ and $-1/2$. A spin ½ can therefore *a priori* be considered in a superposed state $|\psi\rangle$ defined as:

$$|\psi\rangle = \alpha \left|+\frac{1}{2}\right\rangle + \beta \left|-\frac{1}{2}\right\rangle .$$

with α and β two complex numbers which verify $|\alpha|^2 + |\beta|^2 = 1$. This relation is reminiscent of the cartesian equation of a circle of a radius 1, $x^2 + y^2 = 1$, which is also a trigonometric circle if we define $\cos^2(\theta/2) = |\alpha|^2$ and $\sin^2(\theta/2) = |\beta|^2$. We notice, however, that the single variable θ cannot fully describe the two complex numbers α and β on its own, and indeed no information on their phase is included. If we consider α to be real and positive (which is equivalent to aligning the x-axis onto its value, or also equivalent to choosing the argument origin at α), we can define a phase φ so that:

$$\alpha = \cos\left(\frac{\theta}{2}\right) \quad \beta = \sin\left(\frac{\theta}{2}\right) e^{\mathrm{i}\varphi}.$$

We now have a bijection between (α, β) and (θ, φ) and because $\theta \in [0, \pi]$ and $\varphi \in [0, 2\pi]$, we can place any state $|\psi\rangle$ on a unit-radius sphere, called the Bloch sphere, pictured in figure 1.1. The north and south poles of this sphere correspond to state $|+1/2\rangle$ and $|-1/2\rangle$, respectively, and any point elsewhere on the sphere corresponds to a state $|\psi\rangle$ fully characterised by θ its latitude and φ its longitude. Statistical mixtures are represented inside the sphere.

1.1.2 Entanglement

The second property is arguably the most compelling of quantum systems: entanglement. In a Hilbert space $\mathcal{H}$ which is a tensorial product of subspaces A and B, each with a corresponding Hilbert space $\mathcal{H}_\mathrm{A}$ and $\mathcal{H}_\mathrm{B}$, *i.e.* $\mathcal{H} = \mathcal{H}_\mathrm{A} \otimes \mathcal{H}_\mathrm{B}$, a quantum state is said to be *entangled* if it cannot be written in the separable form of a tensor product of states $|\psi\rangle_\mathrm{A} \otimes |\phi\rangle_\mathrm{B}$, with states $|\psi\rangle$ and $|\phi\rangle$ lying in subspaces A and B, respectively, denoted by the indices. Not being separable means that measurements on one state

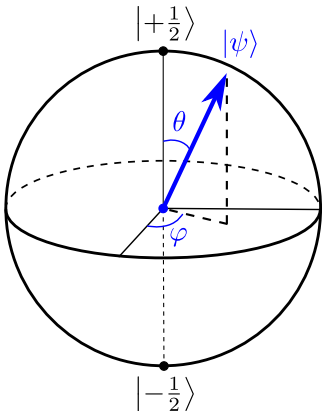

Figure 1.1: Representation of the state $|\psi\rangle = \cos(\theta/2)\,|+1/2\rangle + \sin(\theta/2)\exp(\mathrm{i}\varphi)\,|-1/2\rangle$ on the Bloch sphere. The latitude θ defines the projection of state $|\psi\rangle$ on the zenith direction, which gives the probability to measure the state in state $|+1/2\rangle$ or $|-1/2\rangle$. The longitude φ defines the phase between the two components, which only plays a role for example when interfering with another state. Pure states belong to the surface of the sphere, statistical mixtures are inside it.

affect the outcome of the measurements on the other one, in whatever arrangement of the measurement in space-time, seemingly in violation of the principle of local realist causality when it would require super-luminal signalling to be explained.

It remains an open question, given the density matrix of any multipartite state, to determine whether the state is entangled. In a given system, it is possible to build an entanglement witness, which is an observable which only exhibits values in a specific range for (some) entangled states. To quote a famous example, the Clauser-Horne-Shimony-Holt (CHSH) inequality constrains the correlation of the measurements outcomes on two particles A and B [Clauser1969]. The measurement on A (B) can take the value a or a' (b or b'), and we note $E(a,b)$ the expectation value of the event when a and b are coincidentally measured. We can define the operator S:

$$S = E(a,b) - E(a,b') + E(a',b) + E(a',b').$$

The CHSH inequality states that local realism implies $|S| \leq 2$, whereas a class of entangled states of A and B satisfies $2 < S \leq 2\sqrt{2}$. The quantity S is therefore an entanglement witness for the system of particles A and B: if it takes any value greater than 2, it implies the system state is necessarily entangled. However, there are usually many entangled states which are not witnessed as being so by this observable. In general, entanglement witnesses give a sufficient yet not necessary condition for being entangled.

The Peres-Horodecki criterion [Horodecki1996, Peres1996], which is based on the partial transposition of density matrices, is one of the rare entanglement conditions which are necessary and sufficient. This only occurs in systems of dimension 2×2 and 2×3, *i.e.* a system of two *qubits* or one *qubit* and one *qutrit*, terms which will be introduced just next, in 1.1.3.

		bit Q	
		0	1
bit P	0	0	1
	1	1	0

Table 1.1: Truth table for the *xor* operation on boolean variables P and Q.

1.1.3 Quantum information

Quantum bits, dubbed *qubits*, are the most fundamental unit of quantum information. Their classical counterpart, the binary digit, bit, carries the information of having one of two values, called logical values, usually represented as 0 and 1, or *true* and *false*. In the context of quantum information one does not use binary values but quantum states $|0\rangle$ and $|1\rangle$, called the logical states. The Bloch sphere, previously shown in figure 1.1, can be used to represent a qubit with the poles corresponding to these logical states.

The most exemplary operation between two bits in classical information processing is the *exclusive or*, also known as *xor*, noted by the symbol $\oplus$, and whose truth table is shown in table 1.1. Its counterpart in quantum information processing is the *controlled-NOT*, also known as *CNOT*, gate, where the control qubit, $|P\rangle$, flips the target qubit, $|Q\rangle$, when the former is in state $|1\rangle$. Let us consider the qubits in their general form, $|P\rangle = \alpha\,|0\rangle + \beta\,|1\rangle$ and $|Q\rangle = \alpha'\,|0\rangle + \beta'\,|1\rangle$. The qubit flip corresponds to the transformation of the target state $|Q\rangle$ into:

$$\left|\overline{Q}\right\rangle = \alpha'\,|1\rangle + \beta'\,|0\rangle\,.$$

This flip is performed by the CNOT gate for the $|1\rangle$ component of the control qubit. The output of the gate can be written as:

$$|P\rangle \otimes |Q\rangle \rightarrow \alpha\alpha'\,|00\rangle + \alpha\beta\,|01\rangle + \beta\alpha'\,|10\rangle + \beta\beta'\,|11\rangle$$

This gate is often referred to as an *entangling* gate because the resulting target state is no longer separable. It represents a fundamental resource in quantum information processing as, in addition to the easily obtainable one-qubit gates, it suffices to have this two-qubit gate to perform universal quantum computing, *i.e.* the implementation of any quantum algorithm.

It is insightful to visualise this in the Bloch sphere picture. The qubit flip corresponds to inverting the poles, or equivalently to rewriting the transformed target state as [1]:

$$\left|\overline{Q}\right\rangle = \sin\left(\frac{\theta}{2}\right) e^{\mathrm{i}\varphi}\,|0\rangle + \cos\left(\frac{\theta}{2}\right)|1\rangle$$

$$\left|\overline{Q}\right\rangle \propto \left[\cos\left(\frac{\theta}{2}+\frac{\pi}{2}\right)|0\rangle + \sin\left(\frac{\theta}{2}+\frac{\pi}{2}\right) e^{\mathrm{i}\varphi'}\,|1\rangle\right].$$

[1] Quantum states are defined up to a global phase, which explains the mathematical shortcut with $\left|\overline{Q}\right\rangle$ proportional to this second expression, and the cryptic φ'. There is not much interesting physics in there, only a redefinition of the phase origin.

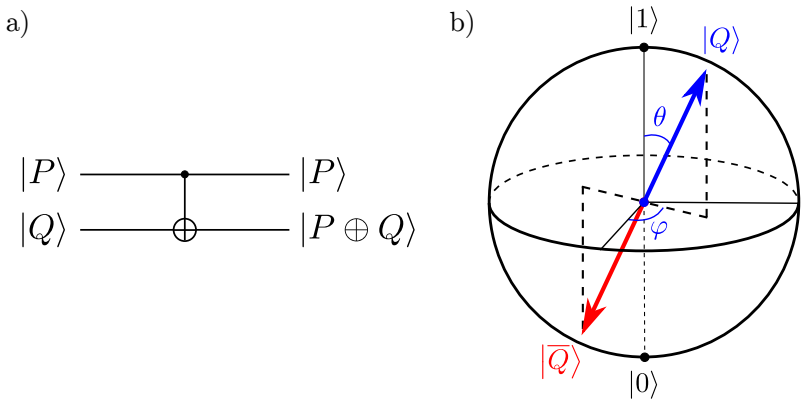

Figure 1.2: a) Representation of the controlled-NOT gate with qubits $|P\rangle$ and $|Q\rangle$ in a quantum circuit. b) Representation of $\left|\overline{Q}\right\rangle$, the qubit flipped by a NOT operation, on the Bloch sphere.

which is mainly the transformation $\theta \rightarrow \theta + \pi$. Therefore, this flip corresponds to a π rotation around an equatorial axis on the Bloch sphere, and a CNOT gate is a *controlled-phase* gate of phase shift $\Delta\phi = \pi$. The experimental realisation of phase gates of large phase shift is a major endeavour in quantum information processing, which we will review in 1.3.1.

The concept of units of information can be extended to states with three logical values, named *qutrits*, and even generalised to d-dimensional units as *qudits*. Quantum information can also take the form of continuous variables, a subject I won't detail here. I instead refer the curious reader to the review [Braunstein2005]. Whichever form quantum information is taking, its efficient transmission between different parties and how it can be stored and processed are core topics, reviewed in 1.3.1.

1.1.4 Properties of light and matter

Having formalised these few concepts, we can now move to the main frame of this thesis, the physics governing light-matter interaction.

Using radiation, especially light, to probe the properties of matter, is a technique known as spectroscopy, which has been an abundant source of knowledge on the material world around us. A whole field of spectroscopy in the microwave and mid- and far-infrared frequency ranges is dedicated to the study of vibrational and rotational states of molecules, degrees of freedom that atoms do not possess. Spectroscopy for crystals additionally involves x-rays, and, for nuclei, gamma rays, and other types of spectroscopy use particles or acoustic waves: they are completely different realms to the one covered here, which involve the interaction of light with atoms on transitions at visible, near-infrared or near-ultraviolet frequencies.

Light, from intense beams down to single photons

Light is an electromagnetic field which can be described by the Maxwell equations. These equations describe the evolution of the electric and magnetic fields in the presence

or absence of charges and currents, in particular those of an atomic medium: the propagation of light is derived from the Maxwell equations, as well as the polarisation of a collection of dipoles in the presence of light. The formalism of these phenomena is described in 1.2.

The most easily available form of laser light typically is at intensity levels in the range $10\,\mu W\,cm^{-2}$ – $100\,mW\,cm^{-2}$, with a transverse diameter between $10\,\mu m$ and a few centimetres. This light is well described in terms of coherent light. This is usually the case for light used as a classical control parameter changing the properties of the system, as will be described in the following chapters.

At very low intensities, the quantised nature of light favours its description in terms of photons, the quantum of the electromagnetic field. For experimental quantum optics, the previous semi-classical approach holds in most cases, even when "weak" probes and signals are used, as those are weak enough not to saturate the atoms but are usually made out of $10^3 - 10^6$ photons, numbers much greater than a few units. The quantum picture is required when specifically single-photon-level light, or actual single or few photons, are used. In this thesis, this is especially looked into in section 3.3 which describes the storage of an optical qubit encoded in light at the single-photon level.

Photons are ideal candidates as carriers of quantum information, as they are elementary quantum objects, intrinsically possess many modes to encode this information [Heshami2016] and can be quickly distributed in a quantum information network. Photon-photon interaction in vacuum is however intrinsically low [Roy2017]. As a result, in order to perform anything else than sending light from one place to another, it calls for the addition of a second ingredient to mediate the interaction: atoms.

The Playground: Atoms

Whereas two photons cannot directly interact between themselves, they can both be coupled to an atomic medium which effectively mediates this interaction. Moreover, in contrast to photons which usually propagate at the speed of light, atoms represent stationary quantum resources.

Atoms as single quantum objects can now be obtained. Single ions and neutral atoms can be trapped and individually addressed by light. Artificial atoms such as quantum dots can be integrated in nanophotonics circuits. However, strong coupling between light and single ions or atoms is experimentally challenging, with avenues consisting of placing them at the focus of high-aperture optics, or in structured arrays.

Another widespread solution to compensate the weak coupling with individual atoms consists in preparing large atomic ensembles to enhance this coupling. This preparation can be made in warm vapours or laser-cooled ensembles, two methods which are extensively described in chapter 2. With an ensemble which can potentially couple efficiently to light, the interaction still needs to be engineered to provide the form of interaction of interest.

Engineering the light-matter interaction

The most natural non-engineered interaction with an atomic ensemble is the absorption of light around a set of optical frequencies, which forms the basis of the spectroscopy introduced earlier.

When we look into more detail, the atoms can either coherently or incoherently absorb this light, resulting in two very different regimes. In the first case, the absorbed light is reversibly mapped to a collective atomic excitation – the system keeps some information on the impinging light –whereas in the second one all information is lost. This coherent mapping has been studied extensively in the last decades, in particular for the conversion of "flying" photonic qubits to "stationary" atomic qubits, which is the essential operation of optical quantum memories reviewed in 1.4.

Slow light is another scheme of light manipulation enabled by atoms, one of the first collective effects to be engineered for applications in quantum information processing. More recently, the stationary light effect has enabled "formally-zero" group velocities and also keeping all light under its photonic form. This new regime of light-matter interaction is compelling by itself and also promises great enhancement for a range of applications.

Before going into more details of the mechanism of the interaction between atoms and light, I will now present the range of applications in quantum information enabled by this interaction.

1.2 Light-matter interfacing formalism

I describe in this section the formalism used to describe the atomic and photonic states, and especially their interplay through the interaction processes that will be used throughout this thesis.

1.2.1 Classical matter and light

Let us start with the "semi-classical" behaviour of light and atoms.

Polarisability

A basic model for the atom is a single electron bound to the nucleus by a harmonic force, with ω_0 the atomic resonance frequency, and a damping of coefficient γ. The response of the electron to an external electric field $\vec{E} = \vec{E}_0 \exp(-\mathrm{i}\omega t)$ is given by the equation:

$$\frac{d^2\vec{r}}{dt^2} + \gamma\frac{d\vec{r}}{dt} + \omega_0^2\vec{r} = -\frac{e\vec{E}_0}{m}\exp(-\mathrm{i}\omega t),$$

with m the mass of the electron, of charge $q_e = -e$. The steady state solution to this equation is the dipole $\vec{d}(t) = -e\vec{r}_0 \exp(-\mathrm{i}\omega t)$ where:

$$\vec{d_0} = -e\vec{r_0} = \varepsilon_0\alpha_\mathrm{c}\vec{E}_0$$

with ε_0 the electric permittivity of vacuum, and α_c the classical polarisability given by:

$$\alpha_\mathrm{c}(\omega) = \frac{e^2}{m\varepsilon_0}\frac{1}{\omega_0^2 - \omega^2 - \mathrm{i}\gamma\omega}.$$

The motion of the electron is accompanied by its dipole radiation. The average power radiated by the atom is given by the Larmor formula:

$$\mathcal{P} = \frac{\varepsilon_0}{12\pi c^3}|\alpha_c|^2\omega^4\left\|\vec{E}_0\right\|^2,$$

with c the speed of light in vacuum. For a plane wave, the incident power per unit surface is $\mathcal{P}_{\text{pw}} = \varepsilon_0 c\left\|\vec{E}_0\right\|^2/2$, hence a diffusion cross section:

$$\sigma_c(\omega) = \frac{\mathcal{P}}{\mathcal{P}_{\text{pw}}} = \frac{8\pi}{3}r_e^2\frac{\omega^4}{(\omega_0^2-\omega^2)^2+\gamma^2\omega^2}. \tag{1.1}$$

Close to resonance, this cross section becomes:

$$\sigma_c(\omega \approx \omega_0) = \frac{8\pi}{3}r_e^2\frac{\omega_0^2}{4(\omega_0-\omega)^2+\gamma^2},$$

which is proportional to a Lorentzian of width γ, the damping coefficient of the motion of the electron.

Light propagation

The propagation of an electric field at frequency ω satisfies:

$$\Delta\vec{E} + \frac{\omega^2}{c^2}\varepsilon_{\text{r}}\vec{E} = \vec{0},$$

with ε_{r} the relative permittivity also known as the dielectric constant. The medium refraction index n satisfies $n^2 = \varepsilon_r$. To identify the dispersion and attenuation of the electric field, the real and imaginary parts of the index, hence of the polarisability α_{c}, need to be made explicit. The imaginary part of the classical polarisability, which describes the attenuation, hence its absorption by the medium, is given by:

$$\text{Im}\left[\alpha_{\text{c}}(\omega)\right] = \frac{e^2}{m\omega_0}\frac{\gamma\omega}{(\omega_0^2-\omega^2)^2+\gamma^2\omega^2}. \tag{1.2}$$

Optical depth

The most universal figure of merit for atomic ensembles is their optical depth (OD), which measures the coupling of light with the atoms on its path through the ensemble.

We commonly refer to the attenuation of resonant light through a medium from an intensity I_0 to an intensity I to be caused by the OD of the medium, noted d, which equals $-\ln(I/I_0)$. OD can be defined in terms of an *effective* cross-section σ:

$$d = \frac{\sigma}{A}N,$$

where N is the total number of atoms and A the cross-section between the light and the atomic medium it is going through. The cross-sections are proportional to λ_0^2, with $\lambda_0 = 2\pi c/\omega_0$ the wavelength associated with the resonance frequency, as seen in equation 1.1. The adjective "effective" now hides the atom-light coupling. We know this coupling to depend on the dipole strength at a given frequency for the considered atoms. The expression of the OD for light resonant with an excited level of linewidth Γ is derived in [Gorshkov2007b] as:

$$d = \frac{4g^2 NL}{\Gamma c}, \tag{1.3}$$

with g the coupling of the light field to one atom, and L the length of the sample.

Our definition of OD is that the intensity of resonant light is attenuated by a factor $\exp(-d)$[2].

The absorption from the atoms can be obtained from the polarisability expressed in equation 1.2: it has the shape of a Lorentzian, which means that light detuned by a frequency difference $\delta = \omega - \omega_0$ from the excited state is attenuated down to:

$$I(\delta) = I_0 \exp\left[-\frac{d}{1 + 4(\delta/\Gamma)^2}\right].$$

This equivalently gives, knowing the attenuation of light detuned by δ from resonance, the OD:

$$d = \left[1 + 4\left(\frac{\delta}{\Gamma}\right)^2\right] \ln\left(\frac{I_0}{I}\right).$$

1.2.2 Description of quantum atom-light systems

To go into more details than the absorption in terms of a heuristic OD introduced previously, a quantum description of the atoms is now required.

Single atom

The simplest system is made of only one atom, which is additionally assumed to have only a few levels.

Two-level atom Let us consider the simplest case of a two-level atom. The two levels are taken non-degenerate *i.e.* have different energies. The lowest-energy state is by convention called the ground state, and very often noted $|g\rangle$, and the higher-energy one is called the excited state, $|e\rangle$. Their energy difference in the context of atom-light coupling is best expressed as $\hbar\omega_{eg}$, which is the energy of a photon at frequency ω_{eg}. Before going into the details of how such a photon can change the quantum state of the atom, we can define a raising operator that transfer the atom from state $|g\rangle$ to state $|e\rangle$:

$$\hat{\sigma}_+ = |e\rangle\langle g|.$$

And conversely, a lowering operator:

$$\hat{\sigma}_- = |g\rangle\langle e|.$$

The Pauli matrices span the Bloch sphere, which was introduced in figure 1.1, with poles $|g\rangle$ and $|e\rangle$. They make explicit the correspondence between any unitary vector

[2] An *amplitude* attenuation of $\exp(-d)$, which means an *intensity* attenuation of $\exp(-2d)$, is sometimes found in the literature.

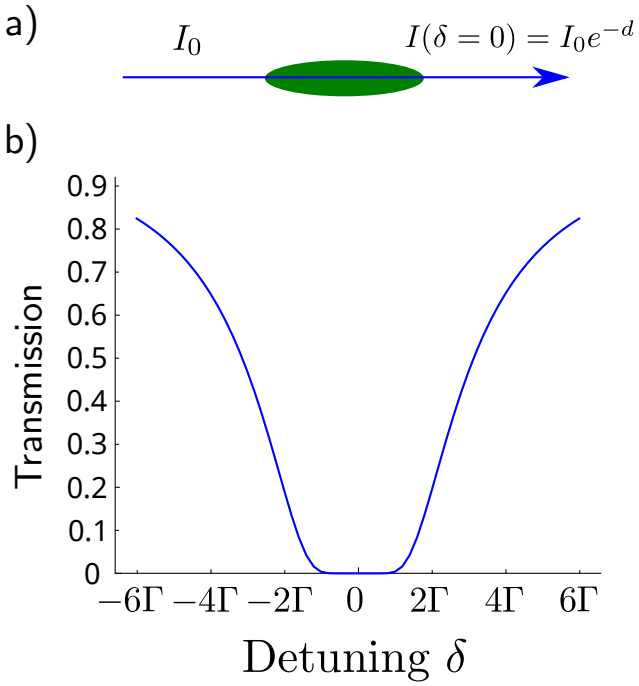

Figure 1.3: a) Incident light of intensity I_0 and detuning δ from resonance with an excited state is attenuated down to intensity $I(\delta)$ after crossing an atomic cloud of optical density d. On resonance ($\delta = 0$), the light is attenuated down to $I_0 \exp(-d)$. b) Transmission profile $I(\delta)/I_0$ in function of the detuning δ. Γ corresponds to the linewidth of the excited state.

on the sphere and the projection of this vector. These operators can be expressed in the basis of Pauli matrices, which are expressed in the $\{|g\rangle, |e\rangle\}$ basis as:

$$\begin{cases} \hat{\sigma}_x = \begin{pmatrix} 0 & 1 \\ 1 & 0 \end{pmatrix} \\ \hat{\sigma}_y = \begin{pmatrix} 0 & -\mathrm{i} \\ \mathrm{i} & 0 \end{pmatrix} \\ \hat{\sigma}_z = \begin{pmatrix} 1 & 0 \\ 0 & -1 \end{pmatrix} \end{cases}$$

In terms of the Pauli matrices, the raising and lowering operators correspond to:

$$\begin{cases} \hat{\sigma}_+ = \dfrac{\hat{\sigma}_x + \mathrm{i}\hat{\sigma}_y}{2} = \begin{pmatrix} 0 & 1 \\ 0 & 0 \end{pmatrix} \\ \hat{\sigma}_- = \dfrac{\hat{\sigma}_x - \mathrm{i}\hat{\sigma}_y}{2} = \begin{pmatrix} 0 & 0 \\ 1 & 0 \end{pmatrix} \end{cases}$$

Taking as a reference of zero energy the midpoint between the ground and excited levels, the energy of the atom is given by an operator proportional to $\hat{\sigma}_z$:

$$\frac{\hbar\omega_{eg}}{2}\hat{\sigma}_z = \frac{\hbar\omega_{eg}}{2}\left(|e\rangle\langle e| - |g\rangle\langle g|\right),$$

hence an atomic Hamiltonian:

$$H_0 = \frac{\hbar\omega_{eg}}{2}\hat{\sigma}_z.$$

The interaction of the atomic dipole with an external electric field leads to the raising to the excited state or lowering to its ground state. For an external electric field $\vec{E} = \vec{E}_0\cos(\omega t + \varphi)$, it is found that the Hamiltonian describing the atom-light interaction in the dipole approximation reads:

$$H_{\text{int}} = -\vec{\mu}.\vec{E}_0\cos(\omega t + \varphi)\hat{\sigma}_x = -\hbar\Omega\cos(\omega t + \varphi)\hat{\sigma}_x.$$

with $\vec{\mu}$ the dipole moment of the atom. $\Omega = \vec{\mu}\cdot\vec{E}_0/\hbar$ is called the Rabi frequency associated with the electric field $\vec{E}_0$ and it is very common to directly bypass the whole electric field description to keep only the Rabi frequency of the field, which, we will see, is fundamental in the context of atom-light coupling.

In the interaction representation, the full Hamiltonian is:

$$\tilde{H} = \frac{\hbar}{2}\left(\omega_{eg} - \omega\right)\hat{\sigma}_z - \frac{\hbar}{2}\Omega\left(e^{\mathrm{i}(\omega t+\varphi)} + e^{-\mathrm{i}(\omega t+\varphi)}\right)\left(e^{\mathrm{i}\omega t}\hat{\sigma}_+ + e^{-\mathrm{i}\omega t}\hat{\sigma}_-\right).$$

where we can define the detuning $\Delta = \omega_{eg} - \omega$.

The rotating wave approximation consists in neglecting the terms varying at frequencies $\pm 2\omega$ and keeping only the constant terms:

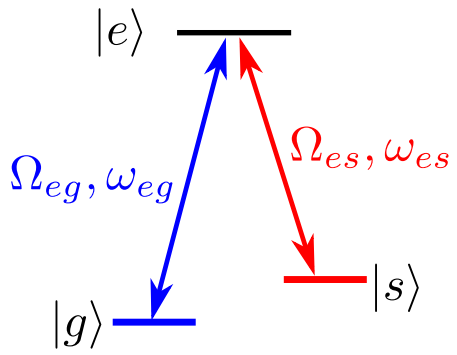

Figure 1.4: Λ-type three level atom. A light field of Rabi frequency Ω_{eg} (Ω_{es}) and frequency $\omega_{eg}(\omega_{es})$ couples to the $|g\rangle$ ($|s\rangle$) $\rightarrow |e\rangle$ transition.

$$\begin{aligned}\tilde{H} &= \frac{\hbar}{2}\Delta\hat{\sigma}_z - \frac{\hbar}{2}\Omega\left(\hat{\sigma}_+ e^{-\mathrm{i}\varphi} + \hat{\sigma}_- e^{\mathrm{i}\varphi}\right) \\ &= \frac{\hbar}{2}\Omega'\hat{\sigma}_{\vec{n}}.\end{aligned}$$

with $\hat{\sigma}_{\vec{n}}$ the spin operator in the direction $\vec{n}$:

$$\vec{n} = \frac{-\Omega\cos\varphi\vec{e}_x - \Omega\sin\varphi\vec{e}_y + \Delta\vec{e}_z}{\Omega'}.$$

In the interaction picture, the evolution on the Bloch sphere of the state of the atom coupled to light is the rotation around the $\vec{n}$-axis at angular frequency Ω':

$$\Omega' = \sqrt{\Omega^2 + \Delta^2}.$$

Three-level atom Without losing generality, I am choosing to describe Λ-type atomic structures as this is the configuration chosen in most realisations of EIT, including ours, and all the experiments described in this thesis. [3] This configuration is also sometimes referred to as the Raman configuration, as it allows Raman scattering processes, which I describe in chapter 4.

The interaction Hamiltonian of an atom with a Λ-shaped structure, with ground state $|g\rangle$, excited state $|e\rangle$, and a second ground state, also called *metastable* state $|s\rangle$, shown in figure 1.4, has the general form:

$$H_{\text{int}} = -\frac{\hbar}{2}\left(\Omega_{eg}e^{-\mathrm{i}\omega_{eg}t}\left|e\right\rangle\left\langle g\right| + \Omega_{es}e^{-\mathrm{i}\omega_{es}t}\left|e\right\rangle\left\langle s\right|\right) + h.c.$$

where Ω_{ji} is the Rabi frequency of the field addressing the $|i\rangle \rightarrow |j\rangle$ transition. We call light which addresses the $|g\rangle \rightarrow |e\rangle$ transition *probe* light, and $|g\rangle \rightarrow |s\rangle$ *control* light, denoted with indices p and c, respectively.

[3] Ladder (Ξ) and *"vee"* (V) are the two other possible structures with three atomic levels.

Atomic ensembles

In the case of N identical atoms, the interaction Hamiltonian is:

$$H_{\text{int}} = -\frac{\hbar}{2}\left(g\sqrt{N}\,\hat{\mathcal{E}}e^{-\mathrm{i}\omega_{\text{p}}t}\left|e\right\rangle\left\langle g\right| + \Omega_{\text{c}}e^{-\mathrm{i}\omega_{\text{c}}t}\left|e\right\rangle\left\langle s\right|\right) + h.c.$$

As large atomic ensemble are considered, the continuous limit approximation can reasonably be made: the atomic quantities are a function of a continuous position variable, in lieu of discrete atoms, each at a given location (or each with an individual position wave function).

Spin wave The Raman scattering with the emission of an anti-Stokes photon, defined in chapter 4, leaves the atomic ensemble with a collective excitation: one of all the atoms from the ensemble has been transferred to state $|s\rangle$. This is reminiscent, in a collection of spins[4], of the superposition of all the possible states where one given spin is raised (or lowered): this state is called a *spin wave*. This collective state, where the total spin of the system has been increased, is an eigenstate of the system. In our case, the state resulting from anti-Stokes Raman scattering is also commonly referred to as a spin wave in the literature, a name I also adopt in the following.

The spin wave can be seen as a Dicke state of the form:

$$\left|\psi\right\rangle = \frac{1}{\sqrt{N}}\sum_{j=1}^{N} e^{\mathrm{i}\varphi_j}\left|g\right\rangle_1 \ldots \left|s\right\rangle_j \ldots \left|g\right\rangle_N,$$

where φ_i is the phase acquired by the j-th atom in the Raman process. In the case of plane waves for the pump and anti-Stokes light fields, this phase equals $\varphi_j = \Delta\vec{k}.\vec{z}_j$, with $\Delta\vec{k}$ the wave-vector mismatch between these light fields and $\vec{z}_j$ the position of the j-th atom. The creation of a spin wave is reversed by the off-resonant absorption of a photon at frequency ω_{es} producing a photon at frequency ω_{eg}. [5].

So far, for simplicity, I have only referred to single absorption and emission, this picture, however, holds with more than one photon being absorbed, which results in multiple collective excitations.

1.2.3 Optical Bloch equations

We adopt the notations shown in figure 1.5 to describe probe and control fields coupling to a Λ-type atom. The probe is denoted by the light field $\hat{\mathcal{E}}$, the control field by its Rabi frequency Ω_{c}. The set of optical Bloch equations for this system is:

$$\begin{cases} \left(\partial_t + c\partial_z\right)\hat{\mathcal{E}}(z,t) = \mathrm{i}gN\hat{\sigma}_{ge}(z,t) \\ \qquad \partial_t\hat{\sigma}_{ge}(z,t) = -\left(\Gamma + \mathrm{i}\Delta\right)\hat{\sigma}_{ge}(z,t) + \mathrm{i}g\hat{\mathcal{E}}(z,t) + \mathrm{i}\Omega_{\text{c}}\hat{\sigma}_{gs}(z,t) \\ \qquad \partial_t\hat{\sigma}_{gs}(z,t) = -\left(\gamma_{gs} + \mathrm{i}\delta\right)\hat{\sigma}_{gs}(z,t) + \mathrm{i}\Omega_{\text{c}}^{*}\hat{\sigma}_{ge}(z,t). \end{cases}$$

[4] For example, a ferromagnet.

[5] Note that this does not exactly correspond to the standard case of the generation of a Stokes photon because the atomic ensemble is considered to be in state $|\psi\rangle$, not with all the atoms initially in $|s\rangle$.

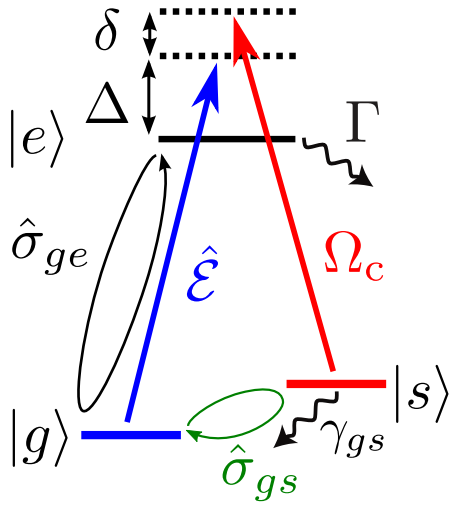

Figure 1.5: Notations on a three-level atom: a probe $\mathcal{E}$ is detuned by Δ from the $|g\rangle \rightarrow |e\rangle$ transition, coupling to $\hat{\sigma}_{ge}$ atomic coherence. A control field of Rabi frequency Ω_c is detuned by $\Delta + \delta$ from the $|s\rangle \rightarrow |e\rangle$ transition. It couples $\hat{\sigma}_{ge}$ to $\hat{\sigma}_{gs}$, the atomic coherence between the ground states. The excited state $|e\rangle$ has a linewidth Γ, and $\hat{\sigma}_{gs}$ a decoherence rate γ_{gs}.

with $\hat{\sigma}_{ij}$ the atomic coherence between states $|i\rangle$ and $|j\rangle$, Γ the linewidth of state $|e\rangle$, and γ_{gs} the decoherence rate of coherence $\hat{\sigma}_{gs}$. The collective observables which can be defined from the atomic populations are the polarisation operator $\hat{P}$ and the spin-wave operator $\hat{S}$, defined as:

$$\begin{cases} \hat{P}(z,t) = \sqrt{N}\,\hat{\sigma}_{ge}(z,t) \\ \hat{S}(z,t) = \sqrt{N}\,\hat{\sigma}_{gs}(z,t). \end{cases}$$

Using these notations, we obtain the following set of canonical Maxwell-Bloch equations:

$$\begin{cases} (\partial_t + c\partial_z)\,\hat{\mathcal{E}} = \mathrm{i}g\sqrt{N}\,\hat{P} \\ \qquad \partial_t \hat{P} = -(\Gamma + \mathrm{i}\Delta)\hat{P} + \mathrm{i}g\sqrt{N}\,\Gamma\hat{\mathcal{E}} + \mathrm{i}\Omega_c\hat{S} \\ \qquad \partial_t \hat{S} = -\left(\gamma_{gs} + \mathrm{i}\delta\right)\hat{S} + \mathrm{i}\Omega_c^*\hat{P}. \end{cases} \tag{1.4}$$

In these equations, we can identify the coupling factor in terms of the OD: $d = g^2 N$. An approximation which is almost always true in the realisations described in this thesis is that the excited state population remains small, and does not vary significantly, which gives $\partial_t \hat{P} = 0$ and:

$$\hat{P} = \frac{\mathrm{i}\sqrt{d}\,\Gamma\hat{\mathcal{E}} + \mathrm{i}\Omega_c\hat{S}}{\Gamma + \mathrm{i}\Delta}.$$

In this approximation, the remaining Maxwell-Bloch equations simplify to:

$$\begin{cases} \left(\partial_t + c\partial_z\right)\hat{\mathcal{E}} = \mathrm{i}\left(d\dfrac{\Gamma}{\tilde{\Delta}}\hat{\mathcal{E}} + \sqrt{d}\dfrac{\Omega_c}{\tilde{\Delta}}\hat{S}\right) \\ \partial_t\hat{S} = -\left(\gamma' + \mathrm{i}\delta'\right)\hat{S} + \mathrm{i}\sqrt{d}\dfrac{\Gamma\Omega_c^*}{\tilde{\Delta}}\hat{\mathcal{E}}. \end{cases} \tag{1.5}$$

with the effective one-photon detuning δ' – which includes the Stark shift from the control Rabi frequency – and effective spin-wave decay rate γ'_{gs} and complex detuning $\tilde{\Delta}$:

$$\begin{cases} \delta' = \delta - \dfrac{|\Omega_\mathrm{c}|^2\Delta}{\Gamma^2+\Delta^2} \\ \gamma'_{gs} = \gamma_{gs} + \Gamma\dfrac{|\Omega_\mathrm{c}|^2}{\Gamma^2+\Delta^2} \\ \tilde{\Delta} = \dfrac{\Delta^2+\Gamma^2}{\Delta+\mathrm{i}\Gamma}. \end{cases}$$

These equations are sufficient to describe most of the dynamics of the optical memories investigated in this thesis when the three-level approximation stands. This is not the case of the EIT-based qubit storage described in chapter 3, where additional excited states on the D_2 line have a significant effect. Chapters 4 and 5 only require the addition of the role of forward and backward signal-and-control pairs.

1.3 Quantum information networks and applications

The development of a global quantum network, dubbed the quantum internet, is an exciting prospect of the development of quantum information science [Kimble2008]. This research endeavour has seen numerous achievements in the last three decades, which I describe now.

1.3.1 Implementations of quantum information

The quantum properties of light and matter as carriers of information grant them a number of properties which are at the core of their applications in the context of quantum information, which are presented in this section.

Quantum communication

Quantum networks require the transmission of quantum information over thousands of kilometres to reach the global scale. Similarly, in classical communication because of the losses on transmission over optical fibres, the channel features repeaters that re-amplify the signal. A quantum version of these repeaters, however, is not trivial to build: precisely the quantum nature of the transmitted information prevents signal amplification or "measure-and-prepare" scheme. In a measurement, the quantum state is projected onto the measurement basis, and all its information is not recovered,

making those solutions unsuitable. Fundamentally, any of these schemes cannot be acceptable as it otherwise would violate the "no-cloning" theorem stating that it is fundamentally forbidden by quantum mechanics to deterministically create copies of an unknown quantum state. Quantum repeaters based on entanglement swapping of memory-synchronised photon pairs allow scalable quantum information transmission at long range [Briegel1998]. The architecture involving quantum repeaters enables the error probability to scale only polynomially instead of exponentially with the distance, along with logarithmic scaling for the number of particles whose control is required.

As a fibre would experience at best attenuation of the order of 15 dB over a distance of 100 km, a recently demonstrated alternative is the space-borne quantum communication scheme that was first envisioned in [Aspelmeyer2003]. A series of landmark articles showed the feasibility of free-space quantum key distribution [Hughes2002, Kurtsiefer2002], distribution of entangled photons pairs over kilometre distances [Peng2005] and quantum teleportation schemes [Aspelmeyer2003, Yin2012]. Quantum key distribution with low-orbiting ($\sim$ 100 km) satellites has recently been demonstrated [Yin2017].

Information processing

Transferring quantum information from one location to another is one of the major aspects studied in the literature, the other aspects concern the processing of this information.

The solving of linear systems of equations is an example of a general computation problem. It can be performed with quantum resources [Harrow2009], and even specifically with only photons and linear optics, a technique known as linear optical quantum computation (LOQC) [Knill2001]. Although this computational system would show a quantum advantage, a computer like the classical version we are familiar with is easily re-programmable: a promising alternative to LOQC which would be adaptable involves the generation of cluster states, where a large collection of qubits are intricately entangled and the performed computation is chosen by classical measurements and operations on nodes of this cluster state [Walther2005].

Quantum cryptography

The "no-cloning" theorem mentioned above and the perturbation of a quantum state by its measurement are actually aspects of quantum information which can be exploited not as a limitation but as a feature. Indeed, the perturbation of a quantum state means that two parties can communicate on a quantum information channel and realise if an eavesdropper is listening to the channel. Moreover, they are guaranteed that the information they exchange is secure, as it is impossible to duplicate it [Gisin2002].

These ideas can also be used to produce unforgeable quantum money, an idea dating to the premises of quantum cryptography [Wiesner1983, Bennett1983]. This topic has been increasingly popular in the last years, arguably due to the emergence of cryptocurrencies like Bitcoin or Ethereum, the former unexpectedly skyrocketing to values above 16k$US at the close of 2017, starting from below a thousand early that year.

1.3.2 Realisation of quantum network elements with light and atoms

Light and atoms are central to the implementations of quantum information protocols, both as carriers of this information and as sources of quantum states through their interaction.

Encoding of information in photonic and atomic qubits

Photonic qubits are central to quantum networks as they can easily be distributed between distant nodes, a reason for which they are often dubbed *flying qubits*, in contrast with qubits defined on atoms, ions, superconducting circuits, etc. which are usually *stationary*, although they can in some cases be moved around over small distances by optical tweezers, for example in proposals of scalable quantum computers with the transport of ions qubits [Cirac2000, Kielpinski2002]. They both have their own advantage, flying qubits connecting different nodes, exchanging information, while stationary qubits in each node are addressable and can be coupled to other qubits, in order to process that information.

Just like in classical information, where the logical values 0 and 1 correspond to two different values of voltage in a circuit, or the presence or absence of light through an optical fibre, the quantum logical states $|0\rangle$ and $|1\rangle$ are two states of a given mode in the considered system. In our case, with light and atoms, many options are available, which we can group into two main categories, corresponding to either internal states or external degrees of freedom. The external degrees of freedom can be the location within the system or the path taken by the carrier of information. A popular encoding is the time-binning: the time at which the carrier can trigger a detector is divided into *bins*, two or many more, which each corresponds to a mode to encode information. Alternatively, among internal states, qubits can be defined on the polarisation, frequency, phase, value of the orbital-angular-momentum, etc.[6].

Quantum state generation

The interaction between light and matter can be used to generate the non-classical states required in quantum information protocols. In 2001, a major practical implementation was proposed for the generation of single photons [Duan2001], defining the so-called Duan-Lukin-Cirac-Zoller (DLCZ) protocol. The process relies on the preparation of an on-demand single photon from the heralded writing of a collective atomic excitation.

Its principle consists in preparing a spin wave from a spontaneous Raman process, the non-classical resource of this protocol emerges from the single-photon photodetector used to herald the success of loading the atomic ensemble. Once the atomic ensemble is loaded with a single excitation, a classical read pulse deterministically triggers the emission of a single photon in a well-determined mode.

The DLCZ protocol was first realised a few years after its proposal [Kuzmich2003], then the heralded photon was isolated [Chou2004] and stored in a remote quantum memory [Chaneliere2005]. The protocol was made more elaborate with frequency

[6] The number of excitations can also define the logical state, with however the limitation that if there are losses anywhere in the network operation, the fidelity of the qubit quickly degrades.

conversion of the photon to telecommunication wavelengths [Radnaev2010]. A recent demonstration involved, after conversion to telecom wavelength, the transmission in a fibre and storage in a solid-state memory, therefore performing a full transfer between two heterogeneous nodes of an elementary quantum network [Maring2017].

In a broader context, the brightness of single-photon sources can greatly benefit from quantum memories to synchronise the probabilistic generation of single photons, as well as making the sources deterministic [Nunn2013]. These quantum memories are described in the following.

1.3.3 Quantum memories

In the description of the above quantum network elements, a recurrent theme has been the storage, synchronisation and conversion of quantum information. Essentially, quantum memories do not only perform the storage of quantum information but more broadly the transfer to and from the different forms of this information [Matsukevich2004]. In this section, I describe optical quantum memories and their characterisation in the most general case. The different memory schemes and their specificity are extensively reviewed in the following section 1.4.

Historical introduction

The last decade has seen the experimental realisation of the envisioned optical memory schemes proposed in the early 2000's, such as dynamically-controlled electromagnetically-induced transparency applied to light storage [Fleischhauer2000], and controlled-reversible inhomogeneous broadening (CRIB) proposed the following year in [Moiseev2001]. Since then, quantum memories are and remain one of the most sought-after applications of the interaction of light and matter, with a handful of dedicated reviews [Bussieres2013, Heshami2016, Ma2017].

Figures of merit

With many different memory platforms and schemes, the comparison between experimental realisations relies on a set of universal figures of merit, listed in table 1.2 and described in the following.

Figure of merit	Definition	Comments and thresholds
Efficiency η	$\eta = E_{\text{out}}/E_{\text{in}}$	No-cloning requires >50%
Fidelity $\mathcal{F}$	$\mathcal{F}(\rho_{\text{in}}) = \text{Tr}\left(\sqrt{\rho_{\text{in}}}\rho_{\text{out}}\sqrt{\rho_{\text{in}}}\right)$	Classical limit: 2/3
Memory lifetime T_{S}	Time at which $\eta(t = T_{\text{S}}) = \eta_0/2$	Delay-bandwidth product $T\Delta\omega$
Bandwidth $\Delta\omega$	Frequencies at which $\eta > \eta_0/2$	
Multimode capacity	Nb of simultaneously stored modes	> 2 for qubit storage

Table 1.2: The table lists the most commonly-cited figures of merit for quantum memories. The second column gives the usual definition of these figures of merit. The third column indicates the usual thresholds to compare to. E_{out} and ρ_{out} (E_{in} and ρ_{in}) are the energy and density matrix the output (input) of the memory, η_0 represents the efficiency at immediate retrieval and at the centre frequency.

Efficiency (storage, retrieval) The operation of a quantum memory proceeds in two steps: the storage of information within it, and the subsequent retrieval from it. Each step is performed with some efficiency, limited by the imperfect nature of the transfer, by the loss of energy to other channels than the one used for retrieval, etc. The universal definition of the memory efficiency is the ratio between the output and input energies, E_{out} and E_{in}:

$$\eta = \frac{E_{\text{out}}}{E_{\text{in}}}.$$

Sometimes, especially when the stored quantum state is prepared *in situ* instead of being externally produced and transferred in the memory, the memory efficiency is broken down in storage and retrieval efficiencies, η_{s} and η_{r}, obviously with $\eta = \eta_{\text{s}}\eta_{\text{r}}$. This distinction between the two steps is especially meaningful when we distinguish between schemes with forward and backward retrieval, *a priori* with the same dynamics of storage. Contrasting these schemes for a Raman memory is the purpose of section 4.1.3.

The storage-and-retrieval efficiency of quantum memories is a stringent parameter for their envisioned applications [Bussieres2013, Heshami2016], especially for the scalability of optical quantum networks [Sangouard2011]. A main threshold for memory efficiencies is 50%: above, more information is retrieved than lost after being stored in the memory. It is necessary to perform above this limit to be in the no-cloning regime. Indeed, if more information is lost to the environment than retrieved, it is possible that the state read-out from the memory is a copy of the input state, which is itself kept somewhere else. We can never prevent this scenario if the efficiency is below 50%. On the other hand, performing above this limit enables error correction on qubit losses in linear optics quantum computation [Varnava2006] and unconditional security in quantum communication protocols [Grosshans2001].

To reach high efficiencies, optical quantum memories require a strong coupling between photons and atoms [Gorshkov2007]. Two main approaches are considered to enhance this coupling: placing individual quantum systems in high finesse cavities [Specht2011], or mapping the photonic states onto collective atomic excitations

[Duan2001, Fleischhauer2000]. In both case, the main limitation to the efficiency of memories is ultimately the available OD of the system [Gorshkov2007a, Gorshkov2007b]. As a result, the increase of OD in atomic ensembles is a key to efficient light-matter interfacing: it has been a central element of my research and chapter 2 is dedicated to this topic.

Fidelity The involved fidelity is implied as being between the output and input quantum states handled by the memory. If we can define a density matrix for each of these states, ρ_{out} and ρ_{in} respectively, then the fidelity is defined as the following trace:

$$\mathcal{F}\left(\rho_{\text{in}}\right) = \text{Tr}\left(\sqrt{\rho_{\text{in}}}\rho_{\text{out}}\sqrt{\rho_{\text{in}}}\right).$$

The memory fidelity is defined as the lowest fidelity over the set of possible inputs ρ_{in}.

The fidelity lies in the $[0, 1]$ interval, reaching 1 when $\rho_{\text{out}} = \rho_{\text{in}}$. In the case of pure states $|\psi\rangle$ and $|\varphi\rangle$, the fidelity is given by the square of their overlap $|\langle\psi|\varphi\rangle|^2$.

An important bound here complements the no-cloning limit introduced for the efficiency. The bound known as the classical limit is the maximum fidelity achievable by a classical memory. It is shown that for a state with N photons, this bound is equal to $(N+1)/(N+2)$ [Massar1995]. In particular, for single photons, this equals $2/3$, *i.e.* approximately 67%.

In the case of qubits, on average, a random output has a $1/2$ overlap with the input. The performance should be considered with this lower bound in mind, rather than zero.

Memory lifetime The typical memory time is defined as the storage duration at which half[7] of the information initially stored remains. This duration has to be compared to the relevant time scales of the system. For example, in a two-level structure where the excited state has a bandwidth of the order of the megahertz, the typical decay time is at the microsecond scale, which means that memory times appreciable at a human scale, of the order of the second or the minute, represent quite a challenge, however tackled in [Dudin2013, Heinze2013].

Bandwidth Bandwidth is the converse aspect of storage duration. Many endeavours aim at providing a quantum memory with the largest achievable bandwidth, as it not only enables a full storage of the fast-varying features in the temporal profile of the signal, but also the simultaneous storage of several signals defined in different frequency bands or a train of pulses, for example. For a memory relying on the absorption of signal light, one could think this figure is limited by the width of the atomic absorption lines, which is of the order of a few MHz for the excited state of the alkali D lines. On the other hand, single photons generated by spontaneous down-conversion typically have natural bandwidths of a few nanometres, which can be reduced by the use of cavities. Many memory schemes do circumvent this limitation and obtain increased memory bandwidths by a clever use of broadening. These schemes are detailed in the following review in section 1.4.

[7] Decay times can be defined at $1/e$, or $1/e^2$.

Delay-bandwidth product A figure of merit unifying the two previous ones is the delay-bandwidth product, the product of the typical delay enabled by the memory and its bandwidth, *i.e.* the ratio of memory lifetime and the pulse duration. The delay-bandwidth product indicates how many pulses would fit in the typical decay time of the memory efficiency.

Specifically quantum memories can assist with the synchronisation of probabilistic operations of success probability p only if the quantum memories display a delay-bandwidth product greater than $1/p$.

It is a useful metric to compare memories operating at very different time scales.

Multimode capacity Some memories are able to simultaneously store more than one mode supporting information, in which case they are said to be *multimode*. The multimode capacity denotes the number of modes stored simultaneously and independently. It is required that simultaneous storage is completely independent *i.e.* that each memory mode can be written and read-out independently and without alteration of any stored mode from another stored one. A large bandwidth can be divided up in order to store multiple signals in the frequency domain; multimode storage can rely on other degrees of freedom, reviewed in the upcoming section 1.4.

For example, for qubits, a suitable quantum memory needs to be able to uniformly store the two modes on which the qubit is encoded. This ability to store multiple modes requires multiplexing, which can either be either temporal [Nunn2008], spatial [Higginbottom2012, Nicolas2014, Zhou2015] or spectral [Sinclair2014, Higginbottom2015].

Extended figures of merit A few additional figures of merit are sometimes quoted in the literature, which I am listing here, although the memories I have worked on during my thesis perform quite poorly on these.

Operating wavelength suitability Atomic quantum memories can only store signals at a set of wavelengths corresponding to atomic transitions and those are not necessarily compatible with other elements of a prospective quantum network. In particular, optical fibres have been optimised to transmit the light at telecommunication wavelength bands, defined in the range $1260\,\mathrm{nm} - 1675\,\mathrm{nm}$. Rare-earth ion doped solids (REIDS) have been put forward for their compatibility at those wavelength. In contrast, the D spectral lines of the commonly-used alkali species are in the visible and near-infrared range. However frequency conversion of the light stored in alkali ensembles is an available solution to integrate this category of memories in a future global quantum network [Maring2017].

Implementation practicality A typical cold atom vacuum system is human-sized and would not be easily duplicated. For this reason, a push is made to reduce the size of the memories, as well as simplifying the alignments, required optical powers, etc. in order to be able to easily scale up and multiply the number of memories within a network.

Another concern linked to the scaling of quantum technologies is the integrability of all the devices. An ideal quantum device will not be a patchwork of juxtaposed devices

with many losses on the interconnections, but rather a single platform integrating all the functional elements. Considering the progress of the silicon industry to that regard, quantum devices which can directly be integrated on a silicon wafer are actively sought after.

Difference between optical and quantum memories Before going into the details of the quantum memory platforms, we should define the vocabulary which is used in the literature. A major distinction to be made here is the difference between quantum memories and memories which are only said to be *optical* for example. The adjective quantum does imply non-classical properties which need to be demonstrated: the storage of laser light mediated by the quantum states of a collection of atoms is not sufficient to prove the quantum character of the memory. Conversely, "true" quantum resources such as single photons or entanglement are not needed to demonstrate it, an often misconceived aspect. Noise is another critical factor challenging the operation in the quantum regime, and benchmarking the noise level is crucial for both proof-of-principle demonstrations as well as actual applications in quantum information processing.

The relevant figure of merit is the fidelity of the memory which was previously defined. The quantum performance of these memories can be demonstrated by achieving a fidelity outperforming the best performance attainable by a classical device [Hammerer2010], which was defined as the classical limit. In the case of qubits, *i.e.* one quantum of information, the classical limit equals 2/3, like for a single photon.

Checking that property does not necessarily involve storing actual single photons or entanglement but can instead be done using weak coherent light, in particular at the single-photon level [Riedmatten2008, Hedges2010]. One could naively think that the coherent state $|\alpha = 1\rangle$ is weak enough and a good approximation of the single photon. In fact, such a coherent state is defined as:

$$|\alpha = 1\rangle = \sum_n \frac{1}{\sqrt{n!}} |n\rangle = e^{-1/2} \left(|0\rangle + |1\rangle + \frac{1}{\sqrt{2}} |2\rangle + \frac{1}{\sqrt{6}} |3\rangle + \dots \right)$$

The overlap of $|\alpha = 1\rangle$ with a single photon is $\langle 1|\alpha = 1\rangle = 1/\sqrt{e}$, which means the probability of measuring exactly one photon from a coherent state with $\alpha = 1$ is $|\langle 1|\alpha = 1\rangle|^2 = 1/e \approx 37\%$. It is also just as likely to obtain a vacuum state in this case. More importantly, though, the two-photon component is rather large ($|\langle 2|\alpha = 1\rangle|^2 = 1/(2e) \approx 18\%$). This component and those of even more photons contaminate the quantum state, which has a direct effect on using coherent states with values of α around 1 when trying to benchmark the quantum operation of a memory. The one-photon to two-photon component ratio is $\sqrt{2}/\alpha$, therefore a solution to decrease the relative contribution from two and more photons is to choose a lower value for α. This choice is at the expense of an even larger vacuum component, however. For example, with $\alpha = 0.1$, the coherent is made up of roughly 90% vacuum, 9% single photon and less than 0.5% two photons and more. The consequence is that the success rate of the preparation of one photon is low, but this is not necessarily an issue, for example if the interaction of the single photon with the memory can be heralded. Using weak coherent states is nonetheless rather common as they are a widely-available resource, and low values of α can be obtained simply by attenuating the intensity of a laser on a

beam-splitter or with neutral density filters.

The terms "classical" or "optical" memory can state explicitly that the quantum nature of the memory has not been demonstrated. For example when the information is redundant in the stored signal, one could rely on a "measure-and-prepare" strategy – a classical solution – to outperform the performance of the memory, storing information for a arbitrarily long duration as this would simply be determined by the time at which a copy of the measured signal is prepared. On another hand, as for most memory schemes, there has already been demonstrations in the quantum regime which prove the process is indeed quantum, it is usually more convenient to operate well above the single-photon level, which explains why many realisations operate in this regime.

More than just memories

As interaction platforms between light and matter, optical quantum memories find applications even beyond the general quantum state transfer [Bussieres2013]. Indeed, they can encode nonlinear operations between qubits "within" the memory, during their storage or by altering the retrieval stage. For example, a configurable LOQC network can be built only relying on quantum memories [Campbell2014].

Among nonlinear operations between qubits, cross-phase modulation (XPM) is one of the applications we have had in mind since the beginning of our investigations of stationary light, as it essentially is a controlled-phase gate, which would lead to the realisation of a controlled-NOT gate for universal quantum computation. Indeed, the topic has attracted a lot of attention in the past decade, with counterarguments [Gea-Banacloche2010] formulated against a proposed scheme based on EIT-based "giant Kerr effect" to provide XPM [Schmidt1996]. Indeed, as is explained in chapter 3, it can be interpreted that the increase of the interaction time with a decrease in group velocity is accompanied by a shift of the polariton coefficients to a large atomic component and a low photonic one. As a result, it cannot lead to enhanced nonlinear interaction such as XPM. Stationary light, on the other hand, can precisely decrease the group velocity while keeping the signal in its light field mode. The nature and generation of stationary light is the topic of chapter 5.

1.4 Review of optical quantum memory schemes

As I intend in this section to provide an overall vision of the vast field of quantum memories, let us classify them in a few categories, choose common notations and focus on their similarities and differences.

While all quantum memories are handling similar inputs of a quantum nature (be it single photon, squeezed light, entanglement, etc.), a central aspect to each quantum memory which differentiates the different schemes is the way there are classically controlled. Two main approaches are chosen here, as pointed out in the review paper [Ma2017]: memories that are optically-controlled and those based on engineered absorption. In the first category, classical auxiliary fields are used to control the memory operation, for example to dynamically change the susceptibility of the atomic medium to store and retrieve light. In the second, the absorption spectrum of the atoms is initially prepared thereby storing light for a pre-programmed duration.

1.4.1 Pre-programmed delay

A pre-programmed memory does not require any intervention when an incident signal arrives, its properties have been prepared to perform light storage for a given duration.

Fibre loop

Sending light through a fibre is a basic way of delaying it, which does present many drawbacks: first of all, although the loss of light in optical fibres is minimised at telecommunication wavelengths around 1550 nm, light propagates in a physical material and bounces off the core-cladding interface, leading to inevitable losses. The state of the art of fibres have losses of $0.15\,\mathrm{dB\,km^{-1}}$, which is equivalent to $0.03\,\mathrm{dB\,\mu s^{-1}}$. This constitutes nonetheless a benchmark for quantum memories: can they outperform the most straightforward solution of delaying the light in a fibre loop? High efficiency and long storage time need to be simultaneously obtained in order to outperform a fibre. For example, the 50% efficiency limit, above which operation in the no-cloning regime is possible, corresponds to a propagation in a fibre for 100 µs. So far only the ANU experiment reported in [Cho2016] performed in this region.

Atomic Frequency Comb

The Atomic Frequency Comb (AFC) scheme relies on the preparation of a collection of atoms starting with a large inhomogeneously-broadened absorption profile which is then shaped as a periodic comb with optical pumping techniques. The atoms start in ground state $|g\rangle$, have an excited level $|e\rangle$ and can be shelved to a long-lived auxiliary state $|\mathrm{aux}\rangle$ which is decoupled from all the optical transitions of interest. Only the atoms j which have a frequency detuning which is a multiple integer of Δ are kept in state $|g\rangle$: $\delta_j = m_j\Delta$, $m_j \in \mathbb{Z}$. The others atoms are transferred to $|\mathrm{aux}\rangle$. This results in an absorption spectrum for the atomic ensemble which is a series of absorption at a regular interval Δ. After an AFC medium absorbs a photon, the atoms quickly dephase, but they all rephase at a pre-programmed time $2\pi/\Delta$, which leads to a coherent photon echo.

If we can approximate each absorption peak to be a narrow Gaussian of full-width half maximum γ, the memory has a finesse $F = \Delta/\gamma$ and an effective OD close to d/F, with a memory efficiency crucially depending on the latter. The memory requires therefore a compromise between finesse and memory efficiency.

This scheme was proposed in [Afzelius2009] and subsequently demonstrated the following year in [Afzelius2010]. It has since established itself as a remarkable memory on many figures of merit, especially bandwidth [Saglamyurek2011] and multimode capacity [Gundogan2013, Jobez2016]. An AFC memory in an impedance-matched cavity has been used to demonstrate an efficiency of 56% [Afzelius2010a].

AFC can also be extended to an on-demand memory with delay by involving a metastable state, forming a Λ configuration, the so-called Λ-AFC configuration [Jobez2014].

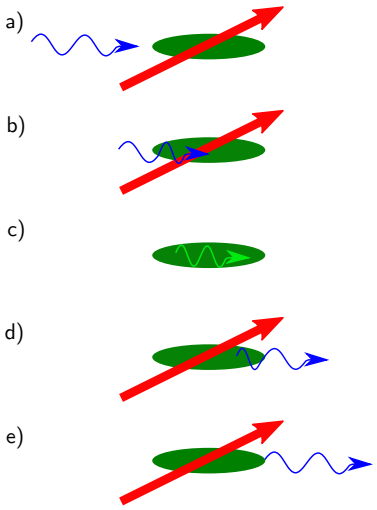

Figure 1.6: Principle of dynamic EIT a) A signal (blue) is sent to an atomic ensemble (green) in which a transparency window is opened by a control field (red). b) The signal experiences a slowdown effect as it enters the atomic ensemble. c) When the whole signal pulse fits inside the atomic ensemble, turning off the control field causes the signal to be converted to stopped light (light green). d) Turning the control field back on restores the propagation of the signal. e) As the signal exits the atomic ensemble, it recovers its original shape.

1.4.2 Dynamic Electromagnetically-Induced Transparency

Electromagnetically-induced transparency (EIT) is accompanied by a decrease of the group velocity, which enables the dynamic control of the propagation of the light. The slowdown can be controlled by the intensity of a auxiliary control field, and the light can even be brought to a halt by decreasing this control to zero.

EIT originates from coherent population trapping (CPT) which manifested through a decrease in the fluorescence of sodium atoms in a vapour cell, in the seminal paper [Alzetta1976]. The name of the phenomenon conveys the idea that the evolution of atoms starting from any state eventually brings them to a so-called dark state, from which they are decoupled to the rest of the system and therefore remain trapped there. The application of CPT is mainly the preparation of atomic states for clocks [Scully1992], magnetometry [Vanier2005] and laser cooling [Aspect1988]. It is not directly applicable as a input-output quantum memory for light in our case. CPT also allows the preparation of single nuclear spins at room temperature, with possible information storage applications [Jamonneau2016].

The EIT phenomenon itself, where atoms are made transparent to light they would normally be opaque to, was first observed in 1991 [Boller1991] before being formally described in the context of dark-state polaritons and applied to light storage [Fleischhauer2000, Fleischhauer2002]. The first demonstrated EIT memory was performed in [Andre2005]. Of particular interest for us, in comparison with our qubit storage experiment reported in chapter 3, is the storage of polarisation

qubits. It has been performed with vacuum-stimulated Raman adiabatic passage in trapped single atoms [Specht2011, Kalb2015], atomic frequency combs in rare-earth doped solids [Clausen2011, Zhou2012, Gundogan2012, Clausen2012, Jin2015, Laplane2015], as well as EIT in warm [Cho2010, Kupchak2015] and cold atomic ensembles [Matsukevich2006, Choi2008, Lettner2011, Zhang2011, Xu2013]. Some quantum memories have also simultaneously stored multiple photonic degrees of freedom [Tiranov2015, Parigi2015, Zhang2016].

1.4.3 Raman Memory

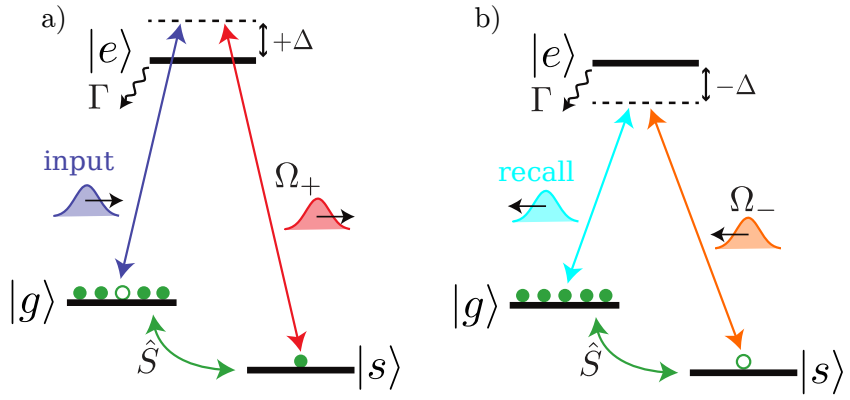

Figure 1.7: Raman memory with backward retrieval. a) A signal $\mathcal{E}_+$ traverses an elongated atomic cloud where a two-photon resonant control beam Ω_+ converts it to a collective atomic excitation. b) A backward-propagating control beam Ω_- subsequently retrieves the signal in the backward direction, as $\mathcal{E}_-$.

Simply put, Raman memory is the far-detuned variant of EIT. There are, however, some significant differences between the two schemes. A Raman memory relies on the absorption of signal light and its conversion to a spin-wave coherence, mediated by the control field. It is not a slowdown effect like EIT. Both memory scheme nonetheless share the aspect that when the control field is turned off, the signal becomes entirely atomic, it corresponds to stopped light.

Figure 1.7 shows the configuration for a Raman memory with backward retrieval, accordingly to the experiment reported in chapter 4. Although the backward configuration exhibits a mirror symmetry that enhances retrieval, it is not usually chosen in realisations of Raman memories, even the most performing to date [Reim2010, Reim2011, Reim2012, Michelberger2015, Saunders2016]. A few experiments do employ elements of a backward geometry in Raman systems to immediate advantages [Chen2013a]. Beyond the replacement of the control beam at the retrieval stage by its mirror image, configurations with the simultaneous application of a pair of counter-propagating control beams has led to the recent development of stationary light, which brings a range of novel effects [Moiseev2006, Nikoghosyan2009, Wu2010, Iakoupov2016, Blatt2016, Iakoupov2016a, Everett2017].

Symmetry can be introduced between the storage and read-out processes with an angle between the control with the signal, which cancels the longitudinal component spin wave k-vector. Moreover, the read-out can be made conveniently collinear with the signal axis in the configuration where the long-lived storage state lies below energetically and the control angle compensates the wave vector mismatch from this energy difference [Surmacz2008].

As pointed out in [Gorshkov2007a], the condition of large detuning in the case of large atomic ensembles is $\Delta \gg d\Gamma$ and not the usual condition $\Delta \gg \Gamma$ which is valid for a single atom. Our configuration at ANU uses a detuning which is only around 200 MHz, which under this condition would not exactly be referred to as Raman memory. The condition is however perfectly verified in the realisation of the group of Ian Walmsley in Oxford, where detunings — as well as bandwidths — of the order of the gigahertz [Nunn2007, Michelberger2015], or even terahertz [Bustard2013] are used.

1.4.4 On-demand photon-echo techniques

Another type of quantum memories rely on photon echoes, which correspond to the time reversal of the absorption of light: it usually corresponds to the reversal of the broadening of the medium [Tittel2010]. The first photon-echo memories originate from a proposal in 2001 [Moiseev2001] to use counter-propagating pulses to generate photon echoes with high efficiency in spite of the inhomogeneous Doppler broadening present in an atomic gas. The technique was extended to solids in [Moiseev2003] and very soon after led to the controlled-reversed inhomogeneous broadening protocol.

Controlled-Reversed Inhomogeneous Broadening

Controlled-Reversed Inhomogeneous Broadening (CRIB) is experimentally very close to the photon-echo concept described above but it really was in 2005 with [Nilsson2005] where controllable external fields are used to create this inhomogeneous broadening, which can therefore be reversed, that the name was given to the technique as a whole and adopted in the first subsequent realisations, for example [Alexander2006, Hetet2008]. CRIB is still a popular scheme in rare-earth-doped solids [Chaneliere2015] and has also led to the emergence of other memory protocols based on photon echo: revival of silenced echo and gradient echo memory.

Revival of silenced echo

Revival of silenced echo (ROSE) is a two-pulse photon echo which circumvents the need to prepare the atomic population as in the CRIB, AFC and Gradient Echo Memory protocols. This technique was developed at the Laboratoire Aimé Cotton [Damon2011] and it subsequently demonstrated a 42% retrieval efficiency, at telecom wavelength [Dajczgewand2014].

Gradient Echo Memory

Fundamentally, the Gradient Echo Memory (GEM) scheme is very close to the Raman memory previously described, but it incorporates elements of CRIB and is

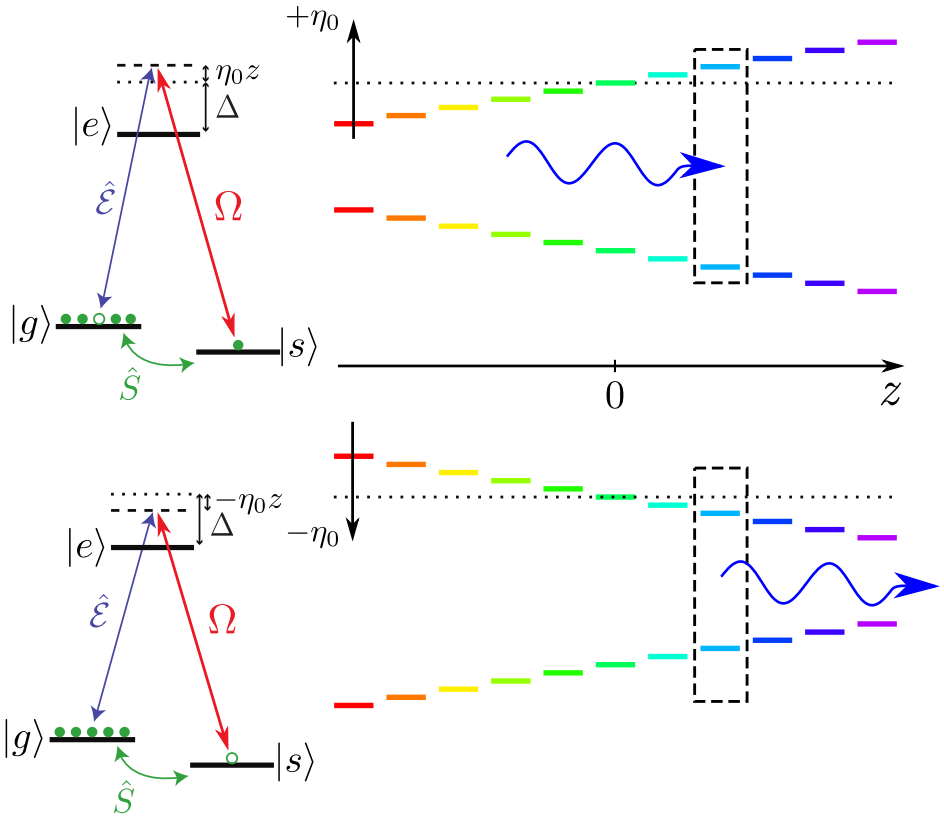

Figure 1.8: Principle of the gradient echo memory. Top: a signal $\hat{\mathcal{E}}$ is coupled to a spin wave $\hat{S}$ by the control field of Rabi frequency Ω. The atomic medium is inhomogeneously broadened by a longitudinal frequency gradient in the z direction $+\eta_0$ is applied on the atomic transitions. Each frequency component of the signal is stored at the location in the cloud which corresponds to the two-photon resonance with the control field. Bottom: The gradient is reversed to $-\eta_0$. At the time symmetric from the storage time relative to the gradient reversal time, the frequency components of the signal — stored in spin waves along the z axis — all simultaneously rephase, producing a photon echo.

now usually treated separately from Raman in the literature. In common with all the GEM realisations, a longitudinal atomic frequency gradient is applied on the ensemble during storage, and subsequently reversed in order to generate a photon echo. The main advantages of this technique are that it is applicable to two-level atoms, instead of the original CRIB proposal that required atoms with three levels. It also did not require the optical π pulse to reverse the atomic dynamics. The electro-optical control instead of optical-optical (optical control and π pulse) was considered an advantage at that time.

The initial proposal and realisation were at ANU and date from 2006 and were published in 2008 [Hetet2008]: a linearly-varying electric field generates a position-dependent Stark shift of the optical transition of two-level atoms. The following proposal was to use a magnetic gradient with a vapour of warm atoms, as such atoms do not have a linear Stark shift [Hetet2008b]. The realisation in warm atoms saw many protocol implementations, such as a coherent pulse sequencer [Hosseini2009], the highest optical memory efficiency [Hosseini2011], and spatial-mode storage [Higginbottom2012]. Since then, still at ANU, the realisation in cold atomic ensembles at high OD also met the highest reported memory efficiencies [Sparkes2013], dual-rail storage [Higginbottom2015] and the previously-mentioned performance above 50% which also beat the loss on a fibre for the same delay [Cho2016].

1.4.5 Heralded preparation

Although they do not operate as memories with an input and and output, it can be argued that the heralded preparation of an on-demand quantum resource constitutes a quantum memory. All these memories are related to the original DLCZ protocol proposal.

The Duan-Lukin-Cirac-Zoller protocol

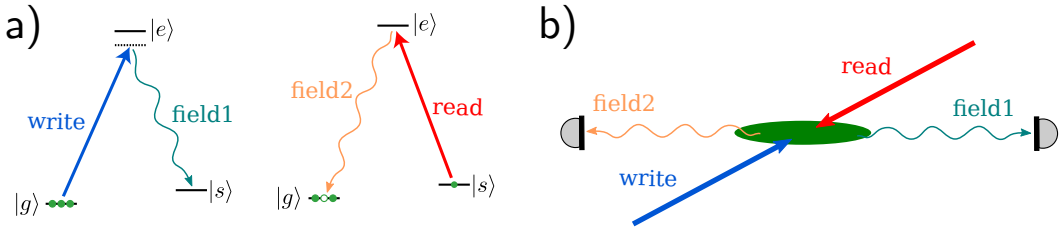

Figure 1.9: Principle of the DLCZ protocol. a) A write pulse, detuned from the excited state probabilistically generates a single photon in mode field 1, whose detection heralds a single collective excitation in $|s\rangle$. Subsequently applying a strong resonant read pulse deterministically produces a single photon in field 2. b) The geometry of the write and read beams to generate counter-propagating field 1 and field 2.

The DLCZ protocol was described in the previous section concerning the generation of quantum resources. Its principle is represented in figure 1.9: it relies on the detection

of a field 1 photon generated probabilistically from a write pulse, which heralds the preparation of the atomic ensemble with a single quantum of collective excitation, which can deterministically be converted into a single field 2 photon by a strong resonant read pulse.

The conditional retrieval efficiency can be compared to the efficiency of the retrieval-only process in a standard quantum memory. Efficiencies of retrieval in free space of 50% [Laurat2006] and 84% with cavity enhancement [Simon2007] have been obtained.

1.4.6 Performance comparison

The highest reported performance of optical memories was recently compiled in [Ma2017]. Table 1.3 lists the relevant figures of merit for our discussion of quantum memories. Note that each figure of merit is independent of the others for the same platform, *i.e.* high efficiency and high bandwidth can be listed for a memory scheme, this does not necessarily mean that both have or can be obtained simultaneously.

Memory scheme	Efficiency η	Storage time T_S	$\Delta\omega_{max}$	Multimode capacity
EIT	78%	1 s	100 MHz	Low
Raman	30%†	1.5 µs	1 THz	Low
CRIB/GEM	80%	0.2 ms	1 GHz	Moderate
AFC	56%	5 µs	1 GHz	High
Raman-GEM	87%	1 ms	1 GHz	Moderate
Λ-AFC	12%	1 ms	1 GHz	High

Table 1.3: Record reported memory performance. $\Delta\omega_{max}$ stands for maximum memory bandwidth. References to the articles reporting the figures for efficiency and storage time are given in table 1.4.

The references are listed in table 1.4.[8]

Category	Memory scheme	Efficiency η	Storage time T_S
Optically-controlled (on-demand)	EIT	[Chen2013]	[Heinze2013]
	Raman	[Reim2011]	[England2012]
Engineered absorption (pre-programmed)	CRIB/GEM	[Sparkes2013]	[Sparkes2013]
	AFC	[Sabooni2013a]	[Maring2014]
Hybrid (on-demand with delay)	Raman-GEM	[Hosseini2011]	[Cho2016]
	Λ-AFC	[Jobez2014]	[Jobez2015]

Table 1.4: References to the values of memory efficiency and storage time shown in table 1.3.

Looking at this collection of results indicates that different strategies, platforms and specific memory schemes give heterogeneous performance on the different figures of merit. In the context of the work presented in this thesis, we notice in particular how the record efficiency for Raman memories seems comparatively low to either EIT or Raman-GEM, although one could think realisation with high memory efficiency in either of these schemes should also perform well with a Raman memory. This, however, can be contrasted with the high bandwidth obtained in the reported Raman memories, which could hint that the groups working on those have mainly focused on this figure of merit instead of the storage-and-retrieval efficiency. A second point is the multimode capacity of EIT which is stated as low, and although there were some challenging aspects of performing qubit, *i.e.* two-mode, storage at LKB, our prospects for the future

[8] †Our result of backward-retrieval Raman memory presented in chapter 4, which is pending peer review, would set the record efficiency of Raman memories up to 68%.

of the experiment may question a supposedly-low multimode capacity of EIT-based memories.

Chapter Conclusion

In this introductory chapter:

- The context of atom-light interaction has been introduced, especially its applications in quantum information encoding, transfer and processing.
- A formalism for light-matter interaction in large atomic ensembles has been presented, including a general set of optical Bloch equations for Λ-type atoms, which are referred to throughout this thesis.
- The state of the art of photonic implementations was presented, especially optical quantum memories schemes whose performance were reviewed, in order to appreciate the results presented in this thesis.

Chapter 2

Key elements for the preparation of large atomic ensembles

The central piece to all the experiments reported in this thesis is a large atomic ensemble. They all relied on the preliminary preparation of a collection of atoms, either via the heating-up of a vapour cell or cycles of trapping, cooling and release of an atomic cloud in vacuum. As seen in section 1.3, the achievable optical depth (OD) in these ensembles is a crucial parameter to enable efficient light-matter interfacing. Therefore, significant efforts are devoted to enhance the experimental apparatus and tune the atom preparation sequence in order to reach denser atomic ensembles and consequently higher OD. As the techniques for atomic ensemble preparation evolved over the years, the ensembles indeed got denser by several orders of magnitude and their atomic coherence longer-lived. My arrival at LKB coincided with the cold atomic ensemble running into the limitation of its moderate OD and ongoing efforts aiming at improving this number. On the other hand, new highs in OD were being obtained at ANU with the help of the neighbouring atom-laser group led by Nick Robins. There was a significant overlap between the challenges in both institutions and some expertise which could be shared both ways. Contrasting the realisations, through my personal experience with them, has let me see the broader picture as well as the perks of each atom preparation.

This chapter is a review of the modern techniques used for warm and cold atom preparation that I have become familiar with during my PhD. Hopefully this list provides all the useful guidelines for the preparation of large atomic ensembles and highlights the relevant aspects for the protocols I describe in the following chapters.

2.1 Considerations for atomic ensemble preparation

Our objective is to achieve efficient light-matter interfacing, for example in order to store an optical signal as an atomic excitation. There are a handful of avenues to this end which involve a variety of atomic media, two of which I have been acquainted with and which are described in this chapter: warm atomic vapours, more briefly, and, in more detail, cold atomic clouds prepared by magneto-optical trapping. Alternative preparations include crystals with atom-like impurities, such as ions dopants or vacancies like nitrogen in diamond, to cite only a few of the other platforms. Review articles such as [Hammerer2010] compare and contrast the various atomic media investigated for light-matter interfacing.

One of the attributes required of this ensemble preparation is that it should be well controlled, repeatable and stable, so that it does not change significantly between its characterisation and its use as a platform for quantum protocols. This is usually easily obtained with magnetically-shielded warm vapours, which simply need to be heated up at a constant rate, and which stabilise within tens of minutes. This is not so much the case with laser-cooled ensembles which are exposed to variations of the ambient magnetic field – from electronics anywhere in the vicinity being turned on or off, or a screwdriver forgotten close to magnetic coils – variations in power or polarisation of the cooling laser, or variations of the frequency of any laser used to prepare the ensemble, caused by a change in the ambient temperature, by mechanical vibrations or by the drop of an electro-optical lock. These environmental issues aside, and provided a few daily realignements, both methods ideally yield a ensemble in a deterministic fashion.

The preparation of cold atomic ensembles was initiated by previous group members in the recent years, in both labs, and many details can be found in their PhD theses [Sparkes2013PhD, Veissier2013PhD, Giner2013PhD, Nicolas2014PhD].

2.2 Warm atomic ensembles

Warm atomic ensembles are relatively easy and cheap to obtain, especially when we compare them to cold atoms in vacuum which require an apparatus of many elements, vacuum chamber parts, pumps, laser light dedicated to the preparation, etc. I describe them in the next section. Instead for warm atoms, it is sufficient to buy a vapour cell, *i.e.* a glass cell containing the atoms, usually in a solidified form on the walls at room temperature. Obtaining an appreciable vapour only requires to heat it up above this temperature, usually with a resistance wire coiled around the windows and the cold point where the vapour condenses when cooling down. In our case, rubidium has a melting point of 39°C and caesium 28.5°C, with a vapour pressure of 10^{-6} Torr – 10^{-7} Torr at 25°C. In practice, at ANU, the temperature reached for the cell in which the quantum protocols are performed is of the order of 60°C and the ones used for filtering is closer to 120°C to obtain very high densities at the expense of more atomic collisions, which is acceptable as light just goes through those cells. The ambient magnetic field can be cancelled by using shielding, for example with mu-metal. A photo of the main vapour cell for the GEM experiments at ANU, along with a filter cell, is shown in figure 2.1.

The main drawback of warm vapours is obviously their temperature. The atoms have a root mean squared velocity of a few hundreds of metres per second, which leads to detrimental effects on different aspects relevant to the prospective quantum applications.

2.2.1 Doppler shift

The distribution of velocities in a warm atomic vapour at temperature T is well described by a Boltzmann distribution. The probability $p(v)$ to find an atom with velocity v on along an axis is given by:

$$p(v) = \frac{1}{\sqrt{2\pi}} \left(\frac{m}{k_\mathrm{B}T}\right)^{3/2} \exp\left(-\frac{mv^2}{2k_\mathrm{B}T}\right).$$

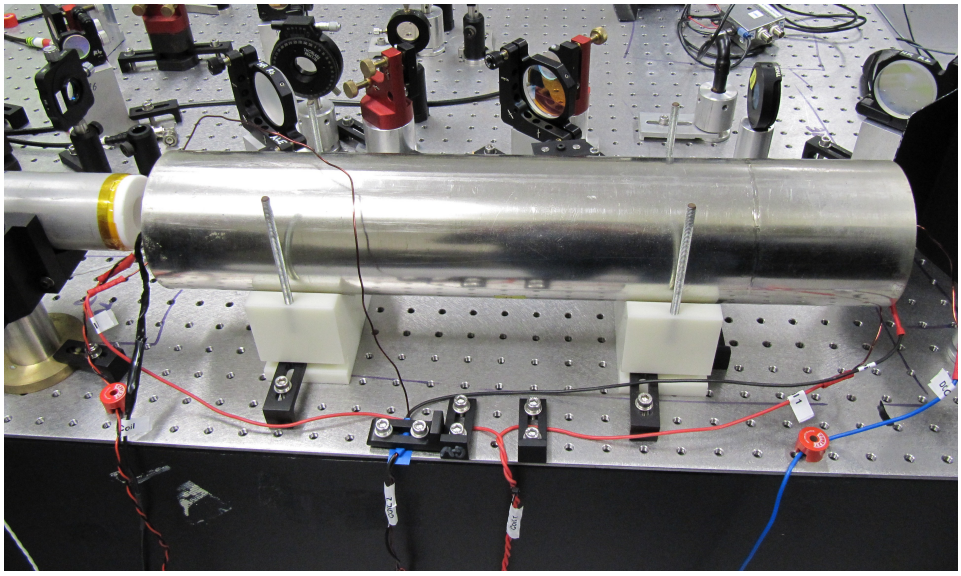

Figure 2.1: A rubidium-87 vapour cell inside a mu-metal shielding can be seen in the centre. On the left, inside a mu-metal cylinder of smaller diameter, a rubidium-85 filter cell is held by teflon caps on each end. In front, the cables of the gradient coils and heating wires.

With this distribution, the root mean squared velocity is $v_{\mathrm{rms}} = \sqrt{3k_{\mathrm{B}}T/m}$, which, for rubidium, equals $320\,\mathrm{m\,s^{-1}}$ at 80°C. The first consequence of this atomic motion is frequency shifts due to the Doppler effect. Light at frequency ω_0 and wave-vector $\vec{k}_0$ is seen by an atom moving at velocity $\vec{v}$ is shifted to:

$$\omega(\vec{v}) = \omega_0 - \vec{k}_0 \cdot \vec{v}.$$

For the D_1 line transitions at $\lambda_0 = 795\,\mathrm{nm}$, this corresponds to a typical frequency shift $\Delta_{\mathrm{D}} = 2\pi v_{\mathrm{rms}}/\lambda_0 = 2\pi \times 400\,\mathrm{MHz}$, which is a significant shift, relatively to the linewidth of the excited level around 5 MHz. The main issue is that the Doppler shift is not uniform, the width of the atomic velocity distribution translates into an inhomogeneous broadening of the atomic transitions, of the order of Δ_{D}.

For two-photon processes, with co-propagating light fields of wave vectors $\vec{k}_1$ and $\vec{k}_2$, the effect partially cancels out as both light fields experience the same Doppler shift. There is a residual shift δ_{12} when the frequency of the light fields does not match, as the wave vectors also do not; the residual shift is equal to $\delta_{12} = (\vec{k}_1 - \vec{k}_2) \cdot \vec{v}$. For example, for a Raman process between the hyperfine states of alkali species, which differ in energy by the splitting $\Delta\omega_{\mathrm{hf}} \sim$ GHz, we have $\delta_{12} = 2\pi v_{\mathrm{rms}} \Delta\omega_{\mathrm{hf}}/c \sim 10\,\mathrm{kHz}$.

Introducing a small angle $\beta \ll 1$ between the wave vectors accounts for a quickly increasing shift: $\delta'_{12}(\beta) \approx k_1 v_{\mathrm{rms}}\,(1 - \cos\beta) = k_1 v_{\mathrm{rms}} \beta^2/2 + \mathcal{O}(\beta^4)$. For an angle of 1°, that is already a shift of the order of the megahertz. Of course the worst case scenario corresponds to counter-propagating light fields, which are shifted in opposite directions by the atoms in a given velocity class.

2.2.2 Sources of decoherence

We see here that the Doppler effect does not make the frequency shifts that dramatic when the wave vectors are strictly co-propagating. The other type of limitation due to the temperature of the atoms is their decoherence.

As we have seen in 1.3, the aim of many quantum protocols relies on the atomic coherence created in an ensemble. In a warm vapour, however, the atoms diffuse and collide inelastically with each other, which leads to decoherence. The diffusion effects in memory experiments are reviewed in [Chrapkiewicz2014], and collisional decoherence in [Horsley2013]. Both these effects can be mitigated by using buffer gases, which consists in adding an inert gas in the cell, usually at pressures of the order $\sim 1\,\mathrm{Torr} - 10\,\mathrm{Torr}$ [Arimondo1996a]. In the presence of this buffer gas, the atoms of interest are more likely to elastically collide with them than with each other inelastically. These collisions effectively reduce both the diffusion and collision decoherence rates. The drawback comes from collisional broadening, resulting from the additional decay channel for the excited state of the atoms. The kinetic collision rate with the buffer gas is given by [Erhard2001]:

$$R_\mathrm{k} = \frac{p}{k_\mathrm{B}T}\sigma_\mathrm{k} v_\mathrm{rms},$$

with p the pressure of the buffer gas and σ_k the kinetic cross section for the considered mix of gases.

The atoms not only collide with other gases in the cell, but also with the walls of the cell itself. A now widespread solution to prevent these collisions to be inelastic is to coat the inside walls of the cell with an anti-relaxation coating, which makes the wall collisions preserve the atomic spin state. This technique using paraffin has been known for some time [Bouchiat1966] and has specifically been used since the first few memory experiments in warm vapour in Polzik's group [Julsgaard2001, Schori2002, Julsgaard2004], or at LKB during the PhD of Jean Cviklinski [Cviklinski2008PhD]. Alternatively to paraffin, coatings can be made of alkanes, alkenes and other hydrocarbons [Balabas2013]. In spite of these limitations, atomic memories at room temperature were recently reported with a storage time as long as 150 ms [Katz2017].

2.3 Large cold atomic ensembles

Atomic ensembles can be prepared at temperatures in the nanokelvin-microkelvin range from laser cooling of a low-pressure background vapour in vacuum. This prevents many decoherence processes due to atomic motion or collisions, between atoms or between atoms and their environment. A standard magneto-optical trap (MOT), however, only reaches ODs of a few tens or hundreds, which is below the thousands easily attainable in warm vapours [Hosseini2012]. Nonetheless there are techniques to prepare atomic ensembles reaching such high ODs, an achievement which was only met recently [Sparkes2013, Hsiao2014]. This section first reminds the important aspects of a MOT, in order to introduce the more advanced methods to reach large cold atomic ensembles with ODs in the same range as the warm vapours.

2.3.1 Atom cooling and trapping

A MOT relies on a velocity- and position-dependent atom-light interaction, which enables the cooling and trapping of an atomic ensemble. The principle behind the optical and magnetic components of a MOT are reminded here.

Optical cooling

In a usual MOT, six beams – three pairs of counter-propagating beams – are used to cool down the atoms. They are usually referred as *trapping* or *cooling* beams. The principle of this cooling, and what makes it velocity dependent is the following.

Radiation pressure When an atom is promoted to the excited state $|e\rangle$ by the absorption of a photon of momentum $\hbar\vec{k}$, this momentum is fully transferred to the atom. When the atom decays back to the ground state, it also emits a photon of momentum $\hbar\vec{k}$, although this emission is isotropic and therefore does not contribute to a net force. Overall, a single absorption-reemission sequence results in a radiation pressure force from the net momentum exchange $\Delta\vec{p} = \hbar\vec{k}$.

The rate of decay for an atom in the excited state is equal to the excited state linewidth Γ, the rate at which these absorptions occur is simply Γ multiplied by the average population of the excited state. In the presence of a laser light which couples the ground and excited states, we found this population to be:

$$\sigma_{ee} = \frac{1}{2}\frac{s}{1+s},$$

with s the saturation parameter, which is given on resonance as $s = I/I_s$, with I the intensity of the laser and I_s the saturation intensity characteristic of the atoms and typically of the order of a few $\mathrm{mW\,cm^{-2}}$. The average radiation pressure force therefore is:

$$\vec{F}_{\mathrm{rp}} = \frac{\Gamma}{2}\frac{s}{1+s}\hbar\vec{k}.$$

Doppler cooling The radiation pressure force depends on the detuning of the cooling light, which is itself affected by the Doppler effect. Red-detuned light can actually be resonantly absorbed by an atom moving towards it. To explain this quantitatively, let us have a look at the saturation parameter with the detuning taking into account the Doppler shift:

$$s(\vec{v}) = \frac{\Omega^2/2}{\delta(\vec{v})^2 + \Gamma^2/4} = \frac{I}{I_s}\frac{1}{1 + 4\delta(\vec{v})^2/\Gamma^2},$$

$$\text{with } \delta(\vec{v}) = \underbrace{\omega - \omega_0}_{\delta_0} - \vec{k}\cdot\vec{v}.$$

The radiation pressure force as a function of the detuning δ is represented in figure 2.2 for different I/I_s ratios.

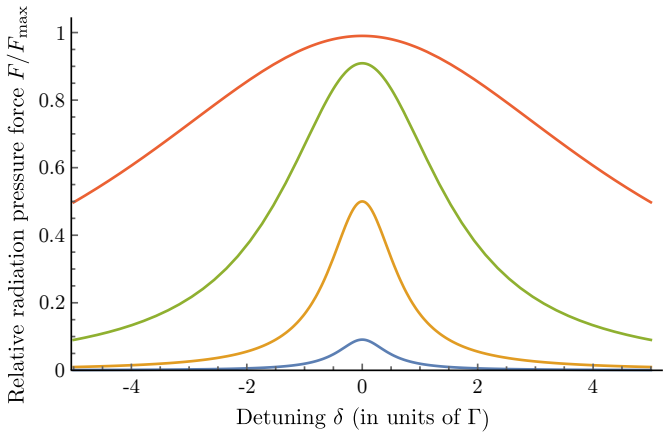

Figure 2.2: Dependence of the radiation pressure pressure force with the laser detuning, δ. The force is scaled to the maximum one, which is obtained with $I \gg I_s$ and at resonance. The detuning is given in units of Γ, the excited state linewidth. The radiation pressure is given for I/I_s ratios equal to 0.1 (blue), 1 (yellow), 10 (green) and 100 (red).

δ_0 is the detuning for the class of atoms whose velocity is orthogonal to the cooling light wave vector. The saturation parameter for those can be noted s_0. Hence a velocity-dependent radiation pressure force:

$$\vec{F}_{\text{rp}}(\vec{v}) = \frac{\Gamma}{2}\hbar\vec{k}\frac{\Omega^2/2}{\Omega^2/2 + \Gamma^2/4 + (\delta_0 - \vec{k}\cdot\vec{v})^2}.$$

For small enough velocities, *i.e.* $\left|2\delta_0\vec{k}.\vec{v}\right| \ll \Omega^2/2 + \Gamma^2/4 + \delta_0^2$, this expression can be linearised as:

$$\vec{F}_{\text{rp}}(\vec{v}) = \frac{\Gamma}{2}\hbar\vec{k}\frac{\Omega^2/2}{\Omega^2/2 + \Gamma^2/4 + \delta_0^2}\left(1 + \frac{2\delta_0}{\Omega^2/2 + \Gamma^2/4 + \delta_0^2}\vec{k}\cdot\vec{v}\right) + \mathcal{O}\left(\vec{k}\cdot\vec{v}^2\right). \qquad (2.1)$$

In practice, the condition comes down to $\left|\vec{k}\cdot\vec{v}\right| \ll \Gamma/2$.

For simplicity, I now assume that both the velocity and the cooling light are on the z-axis, *i.e.* $\vec{v} = v\vec{e}_z$ and $\vec{k} = k\vec{e}_z$, with $\vec{e}_z$ the unit vector in the $+z$ direction. For red-detuned cooling light, $\delta_0 < 0$, the velocity dependent term radiation pressure force is of the form $\vec{F} = -\alpha v\vec{e}_z$, which is a friction force. The force is maximal when $|\delta_0|\Gamma\Omega^2/\left(\Omega^2/2 + \Gamma^2/4 + \delta_0^2\right)^2$ is. This factor is actually:

$$\frac{2\delta_0\Gamma}{\delta_0^2 + \Gamma^2/4} \times \frac{s_0}{(1+s_0)^2},$$

which is found to be maximal with:

$$\delta_0 = -\frac{\Gamma}{2} \quad \text{and} \quad s_0 = 1.$$

The force in this case equals:

$$\vec{F}_{\mathrm{rp}}(v) = \vec{F}_{\mathrm{rp}}(\vec{v} = \vec{0}) - \frac{\hbar k^2}{4} v\vec{e}_z + \mathcal{O}\Big(k^2 v^2\Big).$$

The force can be interpreted in terms of the recoil energy from one cooling photon, $\hbar^2 k^2/2m$. At low saturation values $s_0 \ll 1$, the radiation pressure force is:

$$\vec{F}_{\mathrm{rp}}(v) = \vec{F}_{\mathrm{rp}}(\vec{v} = \vec{0}) - \frac{\alpha}{2} v\vec{e}_z + \mathcal{O}\Big(v^2\Big),$$

with the friction coefficient:

$$\alpha = 2 s_0 \hbar k^2 \frac{|\delta|\Gamma}{\delta^2 + \Gamma^2/4}. \tag{2.2}$$

The stochastic scattering of cooling photons causes the atoms to diffuse. Their spread Δz is given by:

$$\Delta z^2 = 2Dt,$$

with the diffusion coefficient $D = \Gamma/k^2$ for $\delta_0 = -\Gamma/2$. D is of the order of $1\,\mathrm{mm}^2\,\mathrm{s}^{-1}$, to be compared to the typical cross-section of the cooling beams, a few centimetres. In a MOT, such cooling beams cross from all six directions of space, reducing the overall kinetic energy of atoms close to the crossing point.

With real atoms, however, there are always other states to which the atoms can decay from the excited state. In particular, alkali species have two hyperfine ground states, separated by much more than the linewidth of a typical cooling beam, hence only the atoms in one of these states are effectively trapped and cooled down. Atoms which decay to the other state are not addressed by the cooling beam, and if their temperature is still high, they escape from the trapping volume. In order to restore these atoms to a trapped state, repump beams are used, usually resonant to the transition between the other ground states and the excited level.

Zeeman trapping

Starting from a low background pressure, however, there are few atoms in the capture region of the cooling beams, which demands the addition of a position-dependent force to prepare dense clouds, which is what the second half of magneto-optical trapping provides, through its magnetic component.

For a linear magnetic gradient along the z-axis, $\vec{B} = bz\vec{e}_z$, the magnetic sub-levels $|F, m_F\rangle$ are shifted by the energy [SteckCesium]:

$$E_{|F,m_F\rangle}(z) = \hbar\omega_{|F,m_F\rangle}(z) = \mu_{\mathrm{B}} g_F m_F b z,$$

with μ_{B} the Bohr magneton and g_F the Landé factor in state F. The detuning δ_0 in the radiation pressure force 2.1 is replaced by the m_F-dependent detuning:

$$\delta_{m_F}(z) = \delta_0 - \frac{\mu_B g_F m_F b}{\hbar} z.$$

The idea of magneto-optical trapping is to use this detuning for a position and state-dependent radiation pressure force. To this end, circularly-polarised cooling light is used, with a $\sigma^{\pm}$-polarised beam along the $\pm z$-direction. This cooling light exerts a force:

$$\vec{F}^{\pm}_{\mathrm{rp},m_F}(\vec{v}=\vec{0},z) = \pm\frac{\Gamma}{2}\hbar\vec{k}\frac{\Omega^2/2}{\Omega^2/2+\Gamma^2/4+(\delta_0 \mp \mu_B g_F m_F b z/\hbar)^2}.$$

In the simplest case of a unique ground state $|g\rangle = |F=0, m_F=0\rangle$ and a $|F=1\rangle$ excited state, the atomic level structure is made of three Zeeman sub-levels $m_F \in -1, 0, +1$. $\sigma^{\pm}$-polarised light only addresses the $|g\rangle \to |F=1, m_F=\pm 1\rangle$ transition.

The same derivation as the velocity-dependent force gives a position-dependent force:

$$\vec{F}(z) = -\kappa z \vec{e}_z \quad \text{with} \quad \kappa = \frac{\mu_B g_F b}{\hbar k}\alpha, \tag{2.3}$$

with α defined in equation 2.2.

This expression stands near the centre $z < z_c = \hbar\Gamma/(\mu_B g_F b)$, which defines a capture range of the order of z_c. With the typical numbers of a rubidium MOT, we have $z_c \sim$ cm, which is the desired order of magnitude to trap atoms within cooling beams whose diameter is a few tens of millimeters. In practice, the magnetic gradient in three directions is provided by a set of quadrupole coils, with the direction of the axis of the coils experiencing twice the magnetic gradient in order to satisfy $\mathrm{div}\vec{B} = 0$. This detail, however, does not change the principle of Zeeman trapping in three dimensions.

Two-dimensional magneto-optical-trap geometry

An elongated ensemble geometry consists in shaping the atomic cloud along the optical axis, which enables a much larger proportion of the atoms to be addressed by the signal. This idea was demonstrated in [Lin2008a] and now a widespread configuration.

This geometry is obtained by giving the atoms a position-dependent recoil only in two directions, and leaving them free to expand in the third one, giving it the name of *2D-MOT*. In practice, a pair of coils on the third direction, usually called cap coils, implements a small gradient (about 10 times smaller than the axial one) in order to keep the atoms in the overlapping region of the trapping beams.

> This configuration easily enables ODs above 100. To refer to my own experience, the LKB MOT typically yielded OD around 50 in the conventional 3D-confinement geometry. When we changed its configuration to a 2D-MOT one, along with 50-mm-diameter trapping beams but comparable optical trapping power, with no other changes to the loading scheme, ODs up to 150 were obtained. This corresponds to a three-fold improvement, comparable with the increase reported in the original 2D-MOT proposal.

Dynamical compression

A technique used to further increase the OD, at least transiently, is to radially compress the atomic cloud by increasing the magnetic gradient at the end of the loading

sequence, possibly accompanied by a further detuning of the optical trapping beams [Petrich1994]. From equation 2.3, we notice that both result in a stronger radiation pressure force towards the centre of the MOT, effectively compressing the atomic cloud. A large magnetic gradient or a far-detuned optical trapping beam decrease the capture efficiency from the low-pressure atomic background. Instead, MOT loading sequences preferably start with a loading phase during which a low magnetic gradient and trapping beams closer to resonance collect a large number of atoms. It is at the end of the preparation sequence that the atomic cloud is dynamically compressed to increase its density.

There is limit on the achievable OD by the usual techniques to load a 2D-MOT, without compression. For example, at the ANU, the atomic cloud reached at best an OD of 300. The use of a dynamical compression phase at the end of the loading typically yields a 50% increase of the OD.
However this process where atoms are being pushed to the centre of the MOT can intuitively be associated to an increase in the overall temperature. The effect is mitigated or maybe even cancelled by simultaneously performing a temperature reduction sequence, such as polarisation-gradient cooling, introduced in the following section.

2.3.2 Temperature reduction

Atomic motion results in a velocity-dependent Doppler shift of the atomic transitions. Within atomic ensembles, a non-zero temperature results in the so-called Doppler broadening of the transitions, and this broadening causes a decrease in the coherence time of the atoms. Despite the techniques to mitigate this effect, for example with two-photon transitions from co-propagating beams, the performance of warm vapours is limited by the atomic motion at temperatures close to the room one. While MOTs provide atomic ensembles with a temperature orders of magnitude below this, the residual motion of the atoms has a detrimental effect, for example on their ability to store information [Tikhonov2015]. Therefore, the temperature of the atoms captured in the MOT is another crucial parameter to reduce, and the methods to do so are described in this section.

Polarisation-Gradient Cooling

Also known as Sysiphus cooling, polarisation-gradient cooling (PGC) is a technique to decrease the temperature of the atomic cloud obtained initially. Indeed the cooling beam intensity and frequency profiles are first optimised to collect as many atoms as possible in the centre of the MOT. The second step consists in decreasing the heating rate from the intense cooling beams by gradually increasing their detuning from resonance. With a decrease in the pumping rate to the other ground state, the repump intensity can concurrently be decreased without losing atoms to states not addressed by the MOT. This also contributes to decreasing the unnecessary atom-light interaction for the atoms accumulated in the MOT. In practice, for rubidium and caesium, that gives temperatures of the order of $10\,\mu K - 100\,\mu K$.

Dark spontaneous-force optical trap

Temporal dark spontaneous optical trapping (dark SPOT) is similar to the PGC sequence described previously. Another implementation is the spatial dark SPOT, with a region within the atomic cloud where the cooling or repump beams are masked. When entering this region, the atoms are not addressed by light anymore, and the higher their temperature is, the faster the rate at which they exit it. This effectively selects atoms at lower temperatures in this *dark* region.

2.3.3 Typical experimental setup

Now that all the relevant concepts have been introduced, I present the components of a typical experimental setup and the values of the different parameters involved.

Vacuum

The aim of atom cooling and trapping is to replace ensembles in warm vapour cell, where their collisions – with the walls or other atoms – fundamentally limit their coherence time to $\sim 10\,\mu s - 100\,\mu s$ [Horsley2013]. To prevent such collisions with a warm background, the preparation of cold atoms is performed in vacuum, at residual ambient pressures of the order of 10^{-10} Torr. For the detail procedure to reach this pressure level, I refer the reader to the previous theses at LKB [Giner2013PhD, Gouraud2016PhD].

Dispensers

The atoms used to form the MOT are provided by dispensers, also known as getters[1]. Their principle relies on the heating up of a alkali-metal wire to dispense a vapour of a given element in a vacuum background.

Dispensers from SAES (SAES CS/N F/3.9/12F T 10) are used at LKB. They contain 5 mg of caesium and should last 6 months each, if used on average 10h per day. In practice during the course of my PhD, we have switched dispensers twice in 4 years.

At ANU, where the experiment uses rubidium, we are also using dispensers, from Alfavakuo, formerly known as Alvatec, with similar specifications. Rubidium having two stable isotopes, the dispensers provide a mixture of these, with their natural abundance. However as their atomic transitions differ, only one isotope is captured in the MOT, the other one only contributing to background pressure.

Magnetic trapping

A typical magneto-optical trap uses a 10-G cm^{-1} magnetic gradient over 10 cm, most commonly achieved with a pair of coils in an anti-Helmholtz configuration, in two or all three directions of space, whether it is a 2D or 3D MOT. The anti-Helmholtz configuration ensures the cancellation of the magnetic field in the centre and a uniform gradient over the overlap region of the cooling beams, with minimal next-order contribution off the anti-symmetry axis.

[1] The term *getter* usually refers to the use of the component to react and condense, *i.e.* "get", residual gas inside a sealed vacuum system.

Wire radius The radius of the coil wire limits the maximum current they can sustain with no other heat dissipation than standard air flow, possibly helped by placing radiators on the coils thermally-conductive structure. Although some realisations involve the use of water cooling, a standard MOT setup usually simply relies on using wires with a large-enough radius to decrease their resistance. The compromise is made on the volume taken by a coils with the tens if not hundreds of turns required to achieve the desired gradient. Secondarily, a thicker wire is less pliable, which makes the winding more challenging: often the practicality of tightly winding the coil calls for using the thinnest wire capable of supporting the required current. In practice, typical wires have a $1\,\mathrm{mm} - 2\,\mathrm{mm}$ radius.

Current source The typical current used during a MOT loading sequence ranges between $5\,\mathrm{A} - 10\,\mathrm{A}$, with coils which have a resistance of a $1\,\Omega - 10\,\Omega$. The simplest way to provide this current is with a power supply, of about 1 kW and capable of delivering the relatively high current. A commercial solution adopted on both experiments I worked on is the Delta Elektronika SM 52-30. Usually such a source cannot sink the current injected in the high inductance circuit. This task needs to rely on another component, which can in this case be a solid-state relay like the Power-IO HDD-1V50. The original setup at ANU consisted of having the relay in series with the coils, and relying on its internal resistance when switched off to dissipate the current, effectively giving a 1 ms current decay time, on the same order as the decay of the eddy currents induced in nearby conductors by the varying magnetic field. The relays, especially newer units, can wear off quickly with this operation, however, as it does not correspond to their intended use. Shorter decay times and a more sustainable solution would be to use a capacitor and resistor in parallel to the coils, in order to form a critically damped RLC circuit when switching off the relay. This solution is currently being investigated.

Previously at LKB, a current source was developed by our electronic engineers Jean-Pierre Okpisz and Brigitte Delamour to commute the coils to a discharge circuit when we want the magnetic gradient turned off. The discharge circuit was made of a few 1 mF capacitors capable of withstanding the potential difference and speeding up the decrease of the current by effectively applying an opposite voltage to the loading one, yielding decay times around $50\,\mu\mathrm{s} - 100\,\mu\mathrm{s}$.

Sources of light for optical trapping

A general rule with optical trapping is that the more available power, the better. Indeed it is always desirable to increase the trapping detuning to reduce the scattering on the atoms, and this can be done without compromising on the number of captured atoms by increasing the intensity of the trapping beams.

A typical experiment uses trapping beams with total power around $100\,\mathrm{mW} - 500\,\mathrm{mW}$, and diameters of 25 or 50 millimetres. Laser diode light amplified by a tapered amplifier typically provides around 1 W of continuous light power. Frequency control and gating with AOMs and coupling in single-mode fibres reduces this figure to the required power range. This light is then divided in several beams to provide the six-directional optical trapping. A widespread method to roughly divide by two the amount of power needed is to retro reflect each of three beams. This however limits the flexibility of independently

fine tuning the power in each direction, and the retro-reflected beams always experience some losses due to the optics reflecting them.

2.3.4 Preparation sequences

I describe here the typical atom preparation sequences used in both experiments, at LKB and ANU.

LKB experiment

The atomic transitions involved in the elongated MOT for caesium-133 atoms at LKB are shown in figure 2.3. The preparation features dynamic compression, a polarisation-gradient-cooling phase and depumping to the lower ground state $F = 3$, as shown in the preparation sequence presented in figure 2.4.

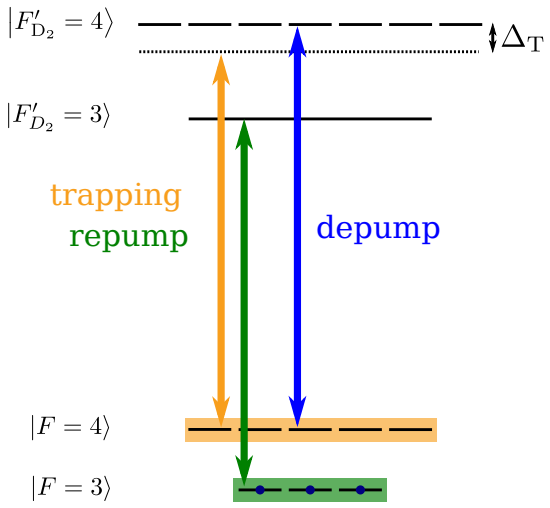

Figure 2.3: The atomic level scheme for the MOT preparation at LKB. During loading, the three retro-reflected 50-mm-diameter cooling beams have a total power around 300 mW and the repump beams have 10 mW. At the end of the preparation sequence, the atoms are "depumped" to the lower ground state, in $|g\rangle = \left|6S_{1/2}, F = 3\right\rangle$, in a superposition of all the Zeeman sub-levels. This is performed by a depump beam resonant with the $|s\rangle \rightarrow \left|6P_{3/2}, F' = 4\right\rangle$ transition, accompanied by a the trapping beams relatively close to resonance and the repump off. The repetition rate of the complete sequence is 16 Hz.

The two-dimensional magneto-optical trapping consists of a set of rectangular coils for radial confinement, completed by a pair of cap coils to generate a shallow gradient along the optical axis. Three retro-reflected 50-mm-diameter cooling beams have a total power around 300 mW, corresponding to a density of 17 mW cm^{-2}, and the repump beams 10 mW, which corresponds to 0.5 mW cm^{-2}. At the end of the preparation sequence, the atoms are "depumped" to the lower ground state, in $|g\rangle = \left|6S_{1/2}, F = 3\right\rangle$, in a superposition of all the Zeeman sub-levels. This is performed by a depump

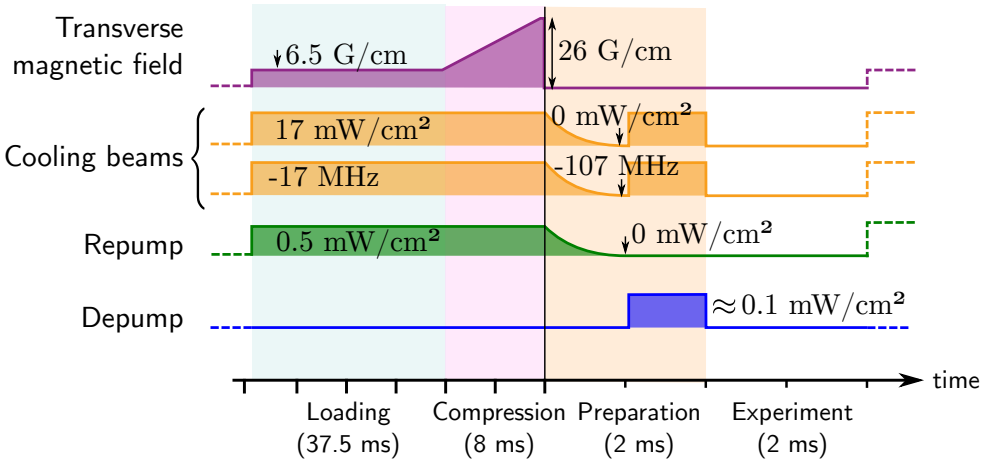

Figure 2.4: The typical atomic ensemble preparation sequence at LKB. An elongated ensemble of caesium atoms is prepared by loading a two-dimensional magneto-optical trap with a magnetic gradient of $6.5\,\mathrm{G\,cm^{-1}}$.

beam resonant with the $|s\rangle \rightarrow \left|6\mathrm{P}_{3/2}, F' = 4\right\rangle$ transition, with an intensity around $0.1\,\mathrm{mW\,cm^{-2}}$, accompanied by the trapping beams relatively close to resonance and the repump off.

The ambient magnetic field is compensated by a set of three orthogonal coils and measured by the Raman spectroscopy technique presented in section 2.3.5. The compensation is performed down to 20 mG, corresponding to an inhomogeneous broadening because of the equally-populated Zeeman sub-levels around 50 kHz. It is equivalent to a $8\,\mathrm{mG\,cm^{-1}}$ gradient over the 2.5-cm length of the atomic cloud.

ANU experiment

The atomic transitions involved in the elongated MOT for rubidium-87 atoms at ANU are shown in figure 2.5. The preparation features dynamic compression, a cooling phase and optical pumping to the edge Zeeman sub-level, as shown in the preparation sequence presented in figure 2.6.

The two-dimensional magneto-optical trapping consists of a set of rectangular coils for radial confinement, completed by a pair of coils for longitudinal capping, and three retro-reflected 50-mm-diameter cooling beams that intersect at the zero-magnetic-field location. The cooling beams have a total power around 400 mW, which corresponds to a intensity $\sim 20\,\mathrm{mW\,cm^{-2}}$. During loading, repump has a total power of and 40 mW, which provide 50-mm-diameter beams of intensity $2\,\mathrm{mW\,cm^{-2}}$ on the $\left|5S_{1/2}, F = 1\right\rangle \rightarrow \left|5P_{3/2}, F' = 2\right\rangle$ transition combined with the cooling beams. Follows a 20-ms sequence where the atomic ensemble is radially compressed and further cooled down by a "temporal" dark spontaneous-force optical trapping technique. Last, a uniform bias magnetic field of 0.5 G is applied along the optical axis direction to lift the degeneracy between the Zeeman sub-levels and the atoms are transferred to the $|g\rangle = \left|5S_{1/2}, F = 2, m_F = +2\right\rangle$ state by employing a $\sim 0.7\,\mathrm{mW\,cm^{-2}}$ σ_+-polarised optical pumping beam resonant with the

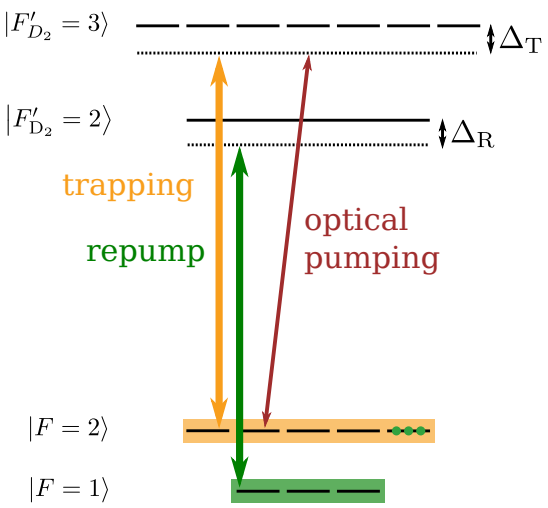

Figure 2.5: The atomic level scheme for the MOT preparation at ANU. During loading, the three retro-reflected 50-mm-diameter cooling beams have a total power around 400 mW and 40 mW for repump light. At the end of the preparation sequence, the atoms are optically-pumped to the edge Zeeman state by a σ_+-polarised beam, at the same frequency as the cooling beams. The optical pumping is accompanied by a resonant repump to leave the atoms in the ground state $|g\rangle = \left|5S_{1/2}, F = 2, m_F = +2\right\rangle$.

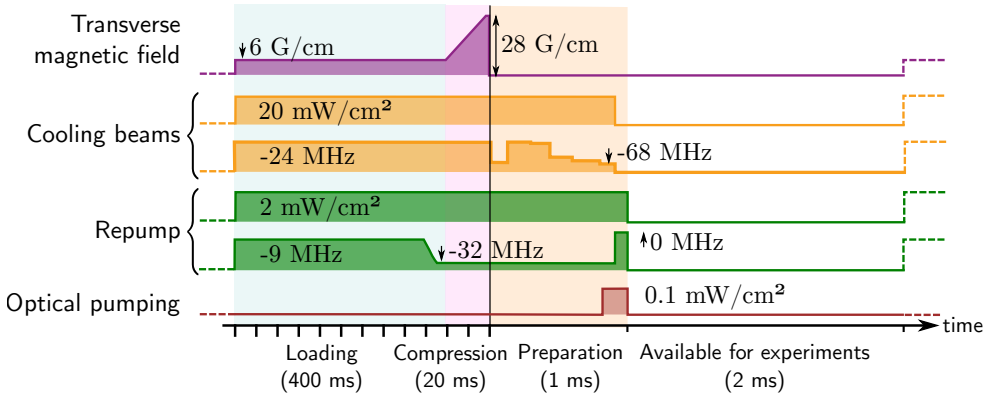

Figure 2.6: The typical atomic ensemble preparation sequence at ANU. The sequence is divided in a MOT loading phase, a compression and a final preparation phase. The magnetic gradient, intensity and detuning profile is as represented here. The repetition rate is around 2 Hz The atoms are optically-pumped to the edge Zeeman state by a σ_+-polarised beam, sent along a resonant repump to leave the atoms in the ground state $|g\rangle = \left|5S_{1/2}, F = 2, m_F = +2\right\rangle$.

$|g\rangle \rightarrow \left|5P_{3/2}, F' = 2\right\rangle$ transition. The Earth magnetic field is cancelled by a set of three orthogonal 1-meter-diameter coils.

2.3.5 Atomic ensemble characterisation

Now that preparation sequences for cold atomic ensembles have been presented, this section describes the tools to characterise the ensemble which is obtained, in particular its OD.

Measurement of optical depth

The OD being the limiting factor for the efficiency of the light-matter interfacing, it is crucial to be able to measure it in our atomic ensemble. There are several methods to this end, depending on the precision needed and the available probe frequencies.

Off-resonance absorption In order to measure the OD, the simplest method would be to send a resonant probe beam and measure the transmitted intensity. However, this would only work at very low ODs as the transmission on resonance goes as $\exp(-d)$. The second simplest technique is to detune the probe from resonance by δ and determine the on-resonance OD with the formula:

$$d = \left[1 + 4\left(\frac{\delta}{\Gamma}\right)^2\right] \ln\left(\frac{I_0}{I}\right), \tag{2.4}$$

with I_0 the incident intensity, and I the transmitted one. In practice, because this consists in extrapolating the OD from a single measurement, it is rather imprecise, yielding ODs that typically vary by 10% from run to run.

A more elaborate measurement requires a probe beam whose frequency can be varied around the resonance frequency with the transition of interest, and consists in sending it through the atoms and to a high-sensitivity photo-detector. The measured transmission can be fitted with the model of equation 2.4 and a value of the OD be determined. Figure 2.7 shows a typical experimental absorption profile and its fit. Signal-to-noise ratio is enhanced with polarisation and spatial filtering by coupling the probe beam to an optical fibre. This allows the operation at low intensity levels, which ensure the probe light does not saturate the atoms. However, because the near-resonant probe beam is not only attenuated by the atomic transition but also deflected with the "atomic lensing effect" occurring in the spatially inhomogeneous atomic cloud, we collect the probe using a large-core multi-mode fibre. We scan the frequency of the probe beam around resonance using a acousto-optical modulator (AOM) in double-pass configuration. The transmission at each frequency is measured by alternating sequences with the atomic cloud fully loaded and without atoms to update the intensity of the incident beam which can fluctuate over time.

The application of this method is illustrated in figure 2.8. It corresponds to a series of OD measurements which were performed on the LKB experiment with different values of the current through gradient cap coils along the axis of the 2D-MOT. These measurements were taken in order to determine the optimal gradient in this direction

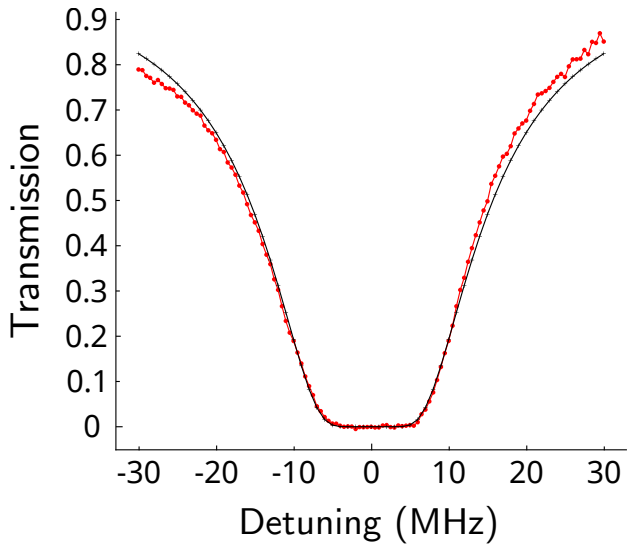

Figure 2.7: Typical transmission profile for a moderate OD around 20. The frequency of the probe is varied on an AOM and the transmission at each frequency (red) is measured by a sensitive photodiode. The best fit to the experimental transmission profile provides an estimate of the OD.

to increase the density of the MOT in the interaction volume, without decreasing this volume by reducing the length of the atomic cloud with a too steep gradient.

Raman line In the far off-resonance Raman configuration, a single probe does not experience any significant absorption. A control field is required to observe the so-called Raman lines, sharp absorption peaks where the frequency difference between the probe and control matches the hyperfine splitting with an atomic level. The addition of the control field comes with another parameter: its intensity. Measuring the OD of the ensemble adds the complexity of also calibrating this intensity.

In order to perform this calibration as well as determining the OD, the Zeeman sub-levels are split by a bias field, typically of $0.5\,\mathrm{G} - 1\,\mathrm{G}$, and the optical pumping and polarisation of the probe and control are chosen so that they can address more than one Raman transition. The frequency of the probe pulse is swept over a couple of megahertz, which covers the splitting of the Zeeman sub-levels at this value of the bias field. A control beam at fixed frequency is sent simultaneously, with its intensity, and thereby its Rabi frequency, being varied across acquisitions. This results in absorption lines corresponding to the different Zeeman sub-levels, as shown in figure 2.9. The depth of each absorption peak depends on the OD, the Rabi frequency of the control, as well as the Clebsch–Gordan coefficient corresponding to this transition. Additionally, the relative Stark frequency shift of each line depends on the square of the Rabi frequency. This method enables an independent calibration of the OD and of the Rabi frequency for each control field intensity, as performed on the presented set of experimental Raman lines. The absorption lines are explained by the atomic susceptiblity for each atomic

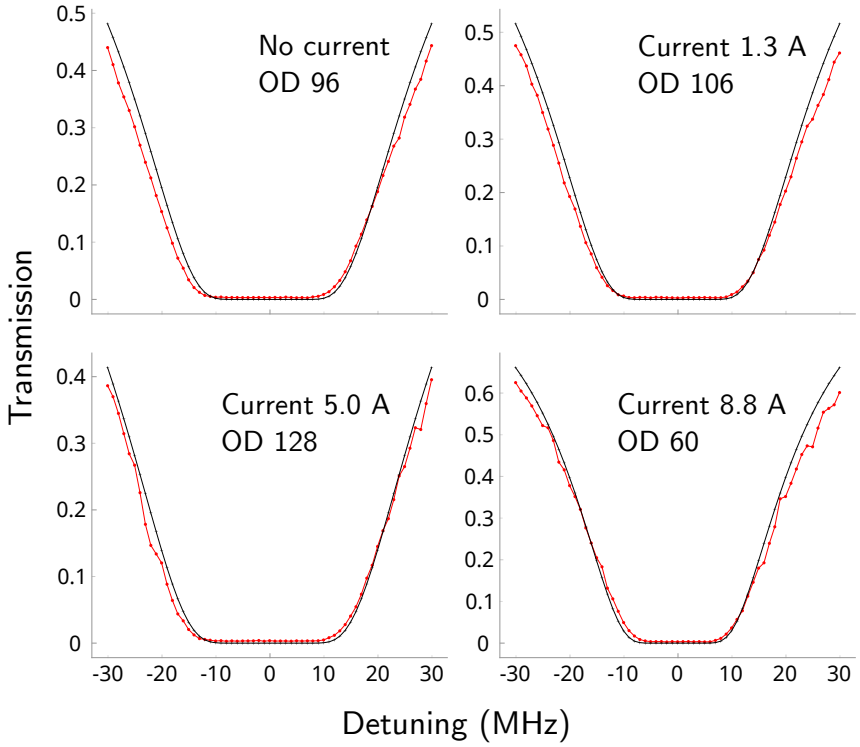

Figure 2.8: Transmission profiles for increasing current in the cap coils of the MOT. The OD of best fit is indicated as an inset of each plot. The top-left plot corresponds to no current through the coils. Increasing it slightly (top-right) provides some MOT Zeeman trapping along the optical axis, but increasing it further shortens the atomic ensemble, and in the limit of a longitudinal gradient of the same order of magnitude than the axial one, corresponds to a 3D-MOT configuration, of lower OD. The optimal current is found to correspond to an intermediate current of 5.0 A, realising an OD of 128, a 30% increase on the initial OD without cap coils.

transition, given by the following expression ([Lambropoulos], equation (6.50) adapted with the notations of this thesis):

$$\chi = \frac{\mathrm{i}d\Gamma}{\Gamma + \mathrm{i}\left(\Delta - \delta\right) + \Omega^2 / \left(\gamma - \mathrm{i}\delta\right)},$$

with d the optical depth, δ the probe detuning to the considered atomic transition,Γ the excited level of linewidth, Ω the control field Rabi frequency and γ the decoherence rate of the ground states.

Magnetic cancellation

Unlike warm atoms which could be shielded from any environmental magnetic field, cold atoms not only require a lot of optical access which prevents a shielding in all directions, their preparation with a MOT actually involves magnetic gradients to trap them. Even if these gradients are turned off, eddy currents are generated in surrounding electrical conductors and the magnetic field at the location of the atomic ensemble changes and is rarely truly zero. Compensation coils aim at minimising this magnetic field by creating an opposite field in a volume around the atoms to cancel the total magnetic field there.

An atom-light interaction which is sensitive to the inhomogeneous magnetic broadening of the atoms, such as a Raman two-photon process, or electromagnetically-induced transparency, can be used to evaluate the residual magnetic field. Another method is to perform the Raman spectroscopy of the atoms [Ringot2001]. The principle is illustrated in figure 2.10, in the case of caesium atoms initially prepared in state $|g\rangle = \left|6S_{1/2}, F = 4\right\rangle$. The residual magnetic field defines a quantisation axis, along which its amplitude is B_z. This causes a lift in the degeneracy of the energy of the Zeeman sub-levels. A microwave pulse of frequency ν_{MF} is sent by an antenna placed close the atoms. Its frequency is sweeped around the hyperfine splitting of the ground states. When this frequency corresponds to the energy difference with Zeeman sub-level of state $|s\rangle$ with $\Delta m_F \in \{-1, 0, +1\}$, the pulse populates this sub-level. Ideally in the case of a pulse of area π, all the population in the sub-level of $|g\rangle$ is transferred to $|s\rangle$. Subsequently, a probe beam $\mathcal{E}_{\mathrm{p}}$ is sent through the atoms to measure the population in $|s\rangle$. The probe needs to have a large enough spectrum — which usually implies it is short — to address the whole $|s\rangle$-state manifold to an excited state only coupled to $|s\rangle$ and uncoupled to $|g\rangle$, for example the state $|F' = 2\rangle$ on the D_2 line of caesium. After the probe interrogation of the atoms, a reference level is obtained by repumping the atoms to $|g\rangle$ and sending the probe again. The OD on the $|s\rangle \rightarrow |F' = 2\rangle$ transition is measured by the absorption during the interrogation, relative to this reference level. The profile of the OD shows frequency peaks which correspond to Zeeman sub-levels with different m_F. The range over which these peaks are observed indicates the residual magnetic field seen by the atoms. Moreover, the initial population distribution in the different m_F sub-levels can be inferred from the relative heights of the absorption peaks. For example, an atomic ensemble integrally pumped to the edge state $m_F = +4$ will display only one absorption peak, corresponding to the $|g, m_F = +4\rangle \rightarrow |s, m_F = +3\rangle$ transition. If pumped to the magnetically-insensitive state $m_F = 0$, the spectroscopy graph displays absorption peaks corresponding to the transition to the Zeeman sub-

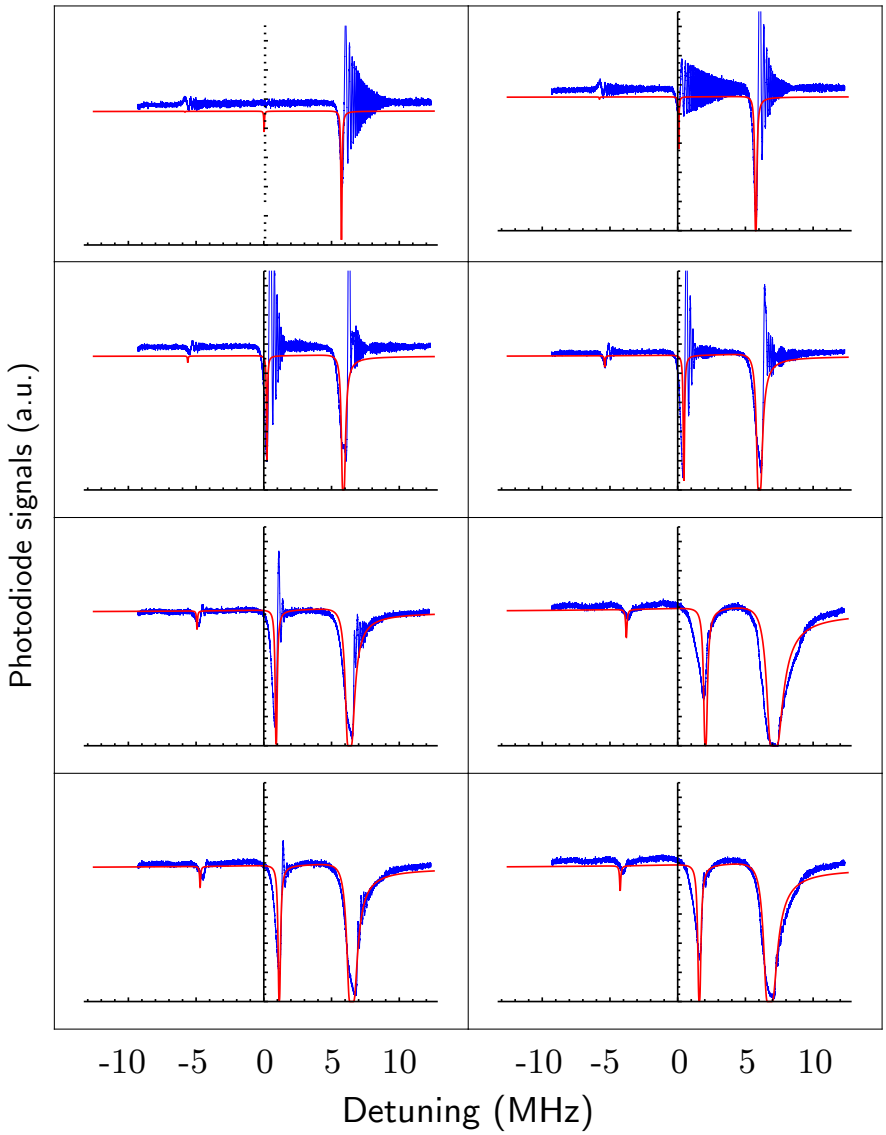

Figure 2.9: Raman line profiles in the ANU cold atomic ensemble, for a control-field detuning $\Delta = 200\,\text{MHz}$, for increasing control field power (for left to right, and top to bottom: $\mathcal{P}_\text{c} \in \{1; 3; 10; 20; 30; 40; 50; 70; 90\}\,\text{mW}$). The zero of the vertical axis is on the horizontal axis and dropped for clarity. The blue curve corresponds to the experimental photodiode signal when the probe frequency is sweeped over the detuning shown in the x-axis. The theoretical absorption profile, in red, is manually tuned to match all the experimental curves, which provides a measurement of the OD, as well as the correspondence between the control field power and its Rabi frequency as seen by the atoms. In this case, the OD is found to be equal 250, along with the following set of parameters: $\Gamma = 6.066\,\text{MHz}$, $\gamma_{gs} = 8\,\text{kHz}$ and the correspondence between Rabi frequency and control field power as $\Omega/\Delta \approx 1.7 \times \mathcal{P}_\text{c}$, with $\mathcal{P}_\text{c}$ in mW, *i.e.* Rabi frequencies from $8.5 \times 10^{-3}\Delta$ up to $8.1 \times 10^{-2}\Delta$.

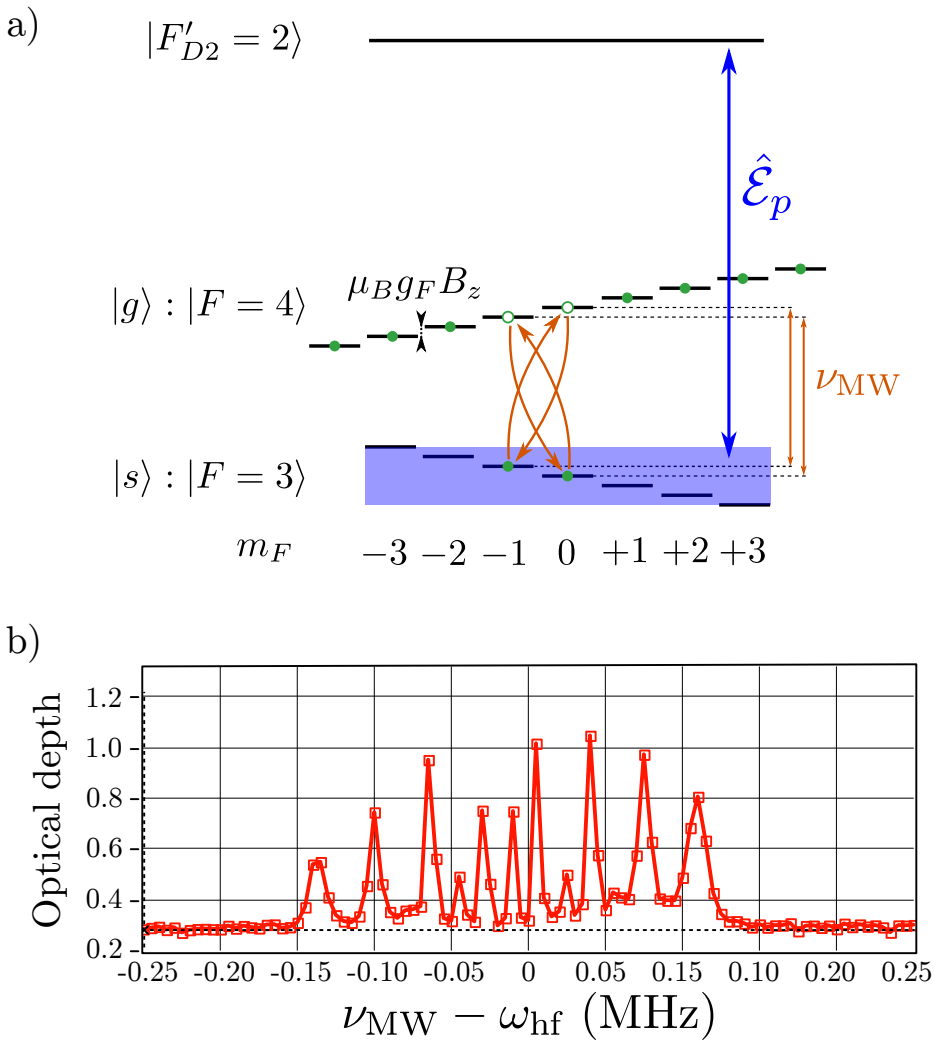

Figure 2.10: a) Raman spectroscopy scheme for caesium atoms initially prepared in $|g\rangle = \left|6S_{1/2}, F=4\right\rangle$, in the presence of a magnetic field B_z. The energy difference between adjacent Zeeman sub-levels is $\mu_{\mathrm{B}} g_F B_z$. The frequency of a microwave π-pulse, ω_{MF}, is sweeped around the hyperfine splitting of the ground states, ω_{hf}. When this frequency corresponds to the energy difference with Zeeman sub-level of state $|s\rangle$ with $\Delta m_F \in \{-1, 0, +1\}$, the π-pulse populates this sub-level. A short probe beam $\mathcal{E}_p$ addresses a transition to the state $|F'=2\rangle$ on the D_2 line. b) The optical depth on the $|s\rangle \rightarrow |F'=2\rangle$ transition is measured by monitoring the transmission of the probe right after the application of the microwave pulse, and after a repump phase to restore the atoms the ground state $|g\rangle$. The profile of the optical depth shows frequency peaks which correspond to Zeeman sub-levels of different m_F. The range over which these peaks are observed indicates the residual magnetic field seen by the atoms.

levels $m_F = -1$ and $m_F = -1$, with no peak in the centre as the $m_F = 0 \to m_F = 0$ transition is forbidden.

Using this spectroscopic method to evaluate the residual magnetic field at LKB, we can then adjust the magnetic compensation to reduce this residual field. In practice, we can then achieve cancellation of the magnetic field down to a few tens of milligauss, which corresponds to a broadening in the 10-kHz range.

Temperature measurement

Temperature is usually thought of as a macroscopic quantity that is not necessarily relevant for cold atomic ensembles. Thermal velocity is probably the concept that best captures their non-zero temperature.

Doppler broadening The direct effect of temperature is to broaden the absorption lines via the Doppler effect. We could argue that temperature can be measured this way. There are, however, many sources of broadening and it is only when we can distinguish the thermal contribution from magnetic and collision broadening, or ignore the latter, that this technique gives access to the temperature.

Time-of-flight technique When free from any external force, an atomic cloud will fall due to gravity and the distribution of the velocity within it becomes apparent over time. The spatial extent of an atomic cloud having fallen over a given height can be linked to their initial temperature distribution, governed by Boltzmann statistics.

Dropping the atomic cloud and imaging them after a given time is referred to as the time-of-flight technique. Sample images are shown in figure 2.11. Because the velocities in the atomic cloud are initially distributed according to a Boltzmann statistic, the width r of the atomic cloud after a time t is given by:

$$r^2(t) = r_0^2 + \frac{k_\mathrm{B} T}{m} t^2$$

where the temperature of the atoms T appears explicitly.

However, it is not obvious how to measure the width of the atomic cloud from the images taken, if the imaging system is not perfectly known, which may depend on the exact focal length of a zoom lens, for example. However, the release of the atoms from the MOT also coincidentally causes its free fall, as it is subjected to gravity. While this means even atoms at extremely low temperatures would eventually escape the interaction area, it provides us with a easily-accessible calibration of the imaging system: the position of the centre of mass of the atoms is known to fall with gravity being the only force acting on it, therefore following the equation $z = z_0 - gt^2/2$, when the initial vertical velocity distribution can be assumed to be symmetric. This enables us to calibrate the pixel scale in the imaging plane, and subsequently to determine the cloud temperature, as shown in figure 2.12.

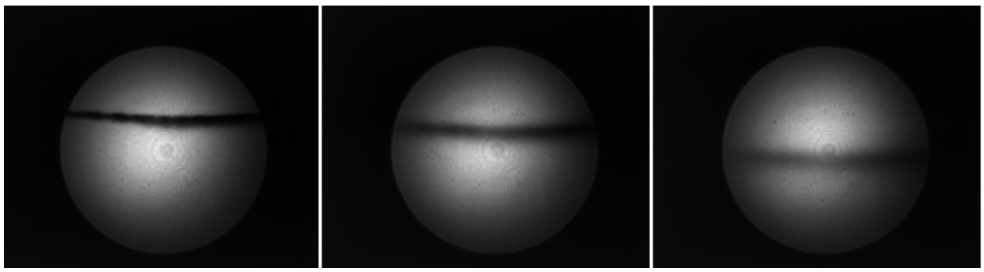

Figure 2.11: Time-of-flight measurement: the atomic cloud is imaged at different time intervals after its release from the magneto-optical trap. The position and spatial extent of the atoms is obtained by shining an imaging beam covering the whole cloud and monitoring its absorption on a CCD. The vertical position of the centre of mass of the ensemble follows the accelerating down-fall due to gravity. The expansion of the cloud transverse size indicates the initial velocity distribution, which gives access to the cloud temperature. This series of images are taken 2, 19 and 33 ms after releasing the cloud of caesium 133 atoms. The expansion of the cloud is found to correspond to a temperature around 20 µK.

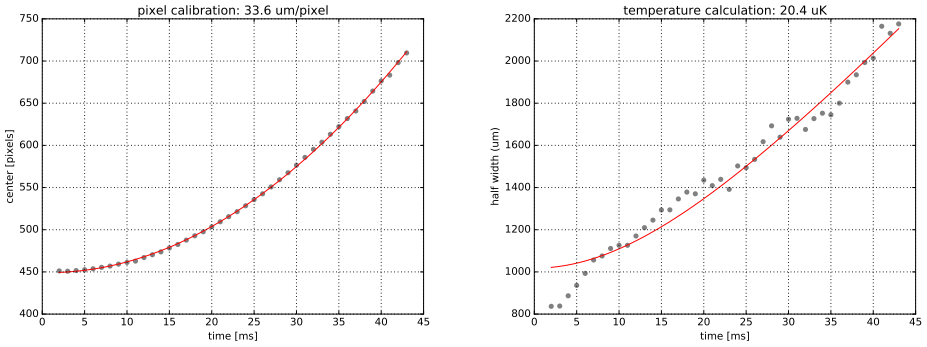

Figure 2.12: a) Position of the atomic centre of mass with time of flight. Knowing the mass of the atoms, a free-fall model gives access to the pixel scale for the imaging system. b) The width of the atomic cloud with the time of flight indicates the cloud temperature from a Boltzmann statistics.

2.4 Machine-learning optimisation

We have mentioned the relevant parameters for MOT compression and PGC, and the LKB preparation sequence shows a ramp profile for the parameters during these phases. Ramp profiles are commonly used in experiments because they are the simplest profile that "makes sense". A closer look to the ANU preparation sequence shows a ragged profile. This results from a current approach using a machine-learning algorithm, a method that has already proved to be successful in the optimisation of these phases.

The idea is that the atomic ensemble preparation can be optimised using an online machine-learning optimisation process which can find sets of parameters a human

experimentator would not. The machine-optimised solutions enable to reach higher OD and lower temperatures. In order to set up this process, the OD is probed close to resonance in order to give the machine-learning algorithm a cost function to work with. The algorithm is given control over a set of parameters and it is first trained by letting it try values for these parameters over their whole range, and measure the cost function for each set of values. A second step after this training, when the algorithm has conceived a model for these measurements, is to let it explore the region where it predicts a minimum of the cost function associated with a maximum of OD, according to this model. After some exploration, the algorithm is looped back to training itself to refine its model, then come back with a better prediction, and so on, until hopefully it converges to a minimum of the cost function.

A similar method has been used to optimise the evaporation cooling of a Bose-Einstein condensate [Wigley2016], but also dynamical decoupling [Mavadia2017] and the feedback control of a qubit [August2017].

This optimisation, especially the inner workings of the machine-learning algorithm, was mainly investigated by my colleague Aaron Tranter. My contribution focused more on the interfacing with the experiment. We have reported the MOT preparation sequence enhanced by machine-learning in the co-authored article [Tranter2018].

2.4.1 Teaching the machine-learner

The machine-learning optimisation algorithm is first trained to infer a statistical model over a multidimensional parameter set. A probe pulse close to resonance on the $|g\rangle \rightarrow |e\rangle$ transition is sent through the atoms and its absorption, which is linked to the OD, is monitored. The photodiode signal is used as feedback for the algorithm, which translates it into a cost function and actively minimises that cost in the machine-learning process.

Our first implementation used a Gaussian process to infer the statistical model, available at [Hush2016]. With the available computing power, the learner was limited to about 20 parameters, and at that limit it actually spent more time computing the model than learning from probing the experiment. It was however sufficient to perform optimisation over fewer parameters, and the preparation sequence presented in 2.6 was optimised by a Gaussian process.

Nonetheless, we quickly moved to another process to infer the model: artificial neural networks (ANN), and more precisely in our case, three independent ANN that together form a stochastic artificial neural network (SANN). The structure of a neural network, presented in figure 2.13, consists of a series of layers of neurons, the first one being a set of inputs, and the last one the output. Neurons are linked with different weights and have an activation function, typically a logistic function. A large range of functions can already be approximated with a handful of layers of a few neurons each. With the same computing power, the algorithm could sustain the 63 independent parameters we used, corresponds to 21 time-bin values on three different quantities: the magnetic gradient from the trapping coils through their current, the trapping and repump frequencies which are varied during the compression-and-cooling sequence after the loading of the MOT and directly before using the ensemble to perform the memory experiments.

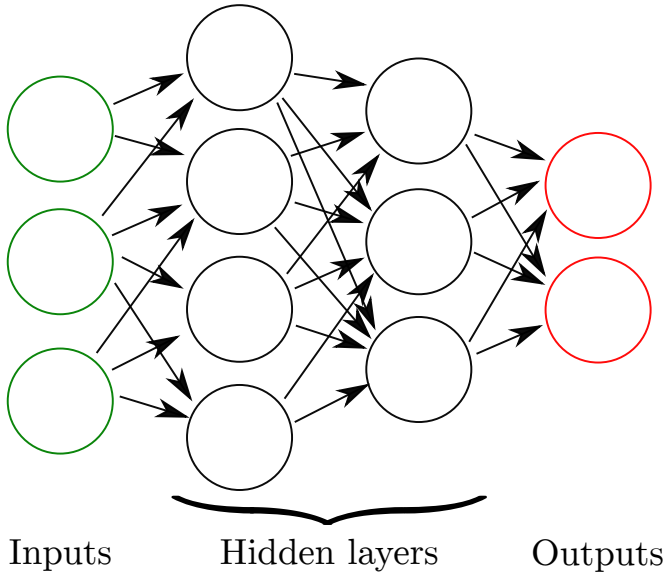

Figure 2.13: In analogy with the vocabulary of biological neural networks, a neural network structure is made of neurons (circles) and synapses (one-way connections between neurons, indicated as arrows). At the input layer (leftmost column), each neuron is attributed a value, which it transmits as a signal to one or more neurons in the following layer. In the middle, hidden, layers, each neuron computes the signals it received, and output the results to the next layer, and so on until the last layer, whose values are the outputs of the network.

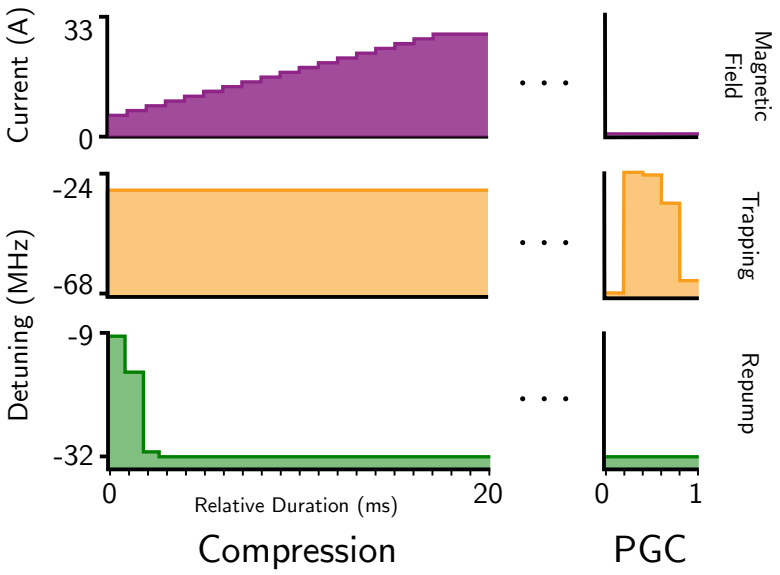

Figure 2.14: The compression and polarisation-gradient cooling sequences are divided into 20 and 5 time bins, respectively, and are passed onto a machine-learning algorithm with a model inferred by a Gaussian process. This algorithm determines the optimal values of repump and cooling beam frequencies, and current through the transverse coils for magnetic trapping. A typical optimised set of parameters is presented here.

2.4.2 Machine-learned compression-and-cooling sequence

The task of the machine-learning algorithm was to enhance the compression-and-cooling sequence. For the Gaussian process, it was granted control over the time profile of the magnetic trapping current, the trapping frequency, and the repump frequency, divided into 21 time bins of 1 ms duration during the compression phase, and parameterised to linear ramps. During the cooling phase, where the magnetic gradient is off, the repump frequency was fixed to be red-detuned from resonance by 32 MHz, the trapping frequency was divided into 5 time bins over a period of 1 ms. These points were not restricted to a ramp and could be moved independently. The experimental conditions were varying noticeably over days. The optimal parameters for cooling and compression were investigated once a day, before each memory run. A typical profile of the resulting compression and preparation sequence is presented in figure 2.14.

It was shown that our neural-network process can handle three sets of 21 parameters in real time. The principle of the neural-network optimisation is shown in figure 2.15.

The solution provided by the neural network yielded an OD of 970 ± 20, to be compared to the best "human-optimised" solution with an OD equal to 530 ± 8, an almost twofold increase in OD which is promising for the use of a neural network to assist with the optimisation of the preparation of the atomic ensemble on a daily basis.

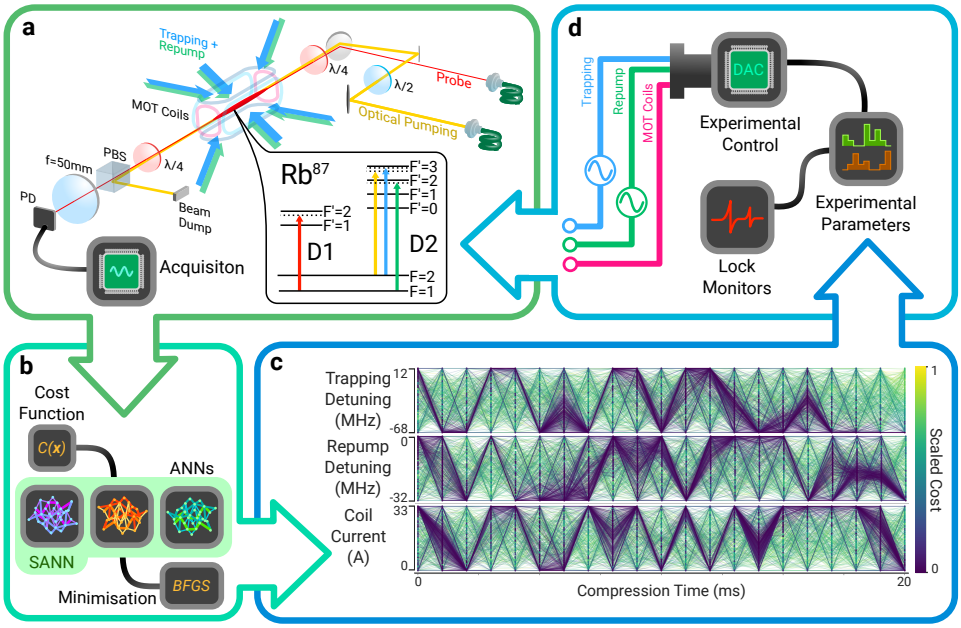

Figure 2.15: Figure from [Tranter2018]. Online optimisation of optical depth. **(a)** Initially a MOT captures rubidium atoms via laser cooling. The ensemble is then transiently compressed using a set of 21 time bins for trapping frequency, repump frequency and current for the trapping coil. The off-resonant OD is measured from the transmission of a probe field incident on a photo detector. This value is passed to the SANN **(b)** where a cost function is calculated for the current set of parameters. Each ANN that comprises the SANN is trained using this and the previous training data. Each ANN generates a parameter set by minimising the predicted cost landscape using the Broyden-Fletcher-Goldfarb-Shanno (BFGS) algorithm. An example of parameter sets that were tested during an experimental run is shown in **(c)**. Each line represents one set of parameters that was tried and is coloured by the corresponding measured cost. Each predicted parameter set is sequentially passed to **(d)**, the experimental control systems which monitor the lock state of the experiment and convert the parameter set to physical values. This loop continues until either a minimisation condition or maximum run number is reached.

	Cooling	No cooling
Compression	730	430
No compression	250	270

Table 2.1: Comparison between the optimal OD obtained by the machine-learning algorithm depending whether the algorithm was given control of the parameters to perform compression and cooling of the atomic ensemble. The lower value when the algorithm was allowed to perform cooling than when it was not is an artefact that could be due to the uncertainty of the OD measurement.

2.4.3 Comparison of preparation sequences

Another application of the machine-learning optimisation is to investigate the importance of different parameters during the preparation of the atomic ensemble. It should be possible to extract this information from the inferred model of algorithm, and it is hinted on figure 2.15 where for some parameters at given time bins, such as the last ones of the trapping, most of the possible values at a given time bin have been explored a similar number of times.

A second approach which was undertaken is to restrict the parameters that the algorithm has access to and see how good is the optimal OD it yields after optimisation on this subset. We performed this by preventing or letting the algorithm perform compression and/or cooling. When the algorithm was not allowed to perform those preparation sequences, it was nonetheless given one parameter: it could choose a constant value for the duration of the sub-sequence, similarly to how a human usually optimises a MOT preparation. To estimate the contributions of the compression and cooling sequences, one-off trials with and without these sequences were performed in a row, and the results are presented in table 2.1. These results correspond to trials performed before the implementation of the final neural-network optimisation, which explains why the values of OD shown here are lower compared to the typical OD obtained in the previous section.

2.4.4 Going beyond the optimisation of optical depth

The machine-learning algorithm optimises a cost function and there is of course no reason that OD should be the only figure of merit the algorithm optimises. Actually, an easy extension is to optimise OD after a given duration during which the atoms released from the MOT diffuse: the lower the temperature of the atomic cloud, the slower is its diffusion. In that case, both the OD and the temperature are simultaneously optimised. Our next step, however, is to directly optimise another figure of merit: memory efficiency and its decay. Until now, the setup to measure the cost function has simply been the transmission of a probe close to resonance, which had to be minimised. Optimising a memory performance directly implies performing the full memory scheme, and providing an adequate cost function to the algorithm. It should especially be remembered that such unsupervised machine-learning algorithm have a tendency to "cheat" in the following sense. Let us assume that we ask the algorithm to optimise storage-and-retrieval in an atomic ensemble, with a cost function corresponding to light

received on a photodiode in a given time window. If it is given control over auxiliary laser beams, it won't sound unreasonable to the algorithm to try blasting these lasers in every direction: if somehow, by saturation of filtering optics, diffraction or reflection from odd places, light can reach the detector when the read-out from the memory is expected, it can accept it as a solution. Definitely, careful planning will have to be considered before extending the parameter range of the machine-learning algorithm for more complex optimisation goals.

Chapter Conclusion

In this chapter:

- We have characterised the experimental methods to prepare large ensembles of cold atoms and fully characterise them, in particular their optical depth (OD), which is a crucial figure of merit in the applications presented in the following of this thesis.
- The state-of-the-art preparation techniques and typical sequences were presented here, along with the OD they achieve on a reproducible basis.
- As much as possible, the OD improvement of individual preparation techniques were given, such as the use of a 2D-MOT, the compression and the polarisation-gradient-cooling sequences.
- An extensive toolbox for the optimisation of the OD with any relevant parameter of the MOT was introduced with our first trials with a machine-learning algorithm. This algorithm can also be used to characterise the role of different elements of the preparation sequence.

Chapter 3

Efficient qubit storage based on electromagnetically-induced transparency

The storage-and-retrieval efficiency of quantum memories is a stringent parameter for their envisioned applications. Boosting this key figure of merit has been a long-standing effort for a large community, using different physical platforms and a variety of protocols. While efficient storage of light pulses has been obtained, the storage of optical qubits is still limited to an efficiency below 30% whatever the platform or the qubit encoding. This is attributed to the very challenging features of the storage of the two modes that define the qubit, which requires some form of multiplexing. The limitation of the memory efficiency constitutes a current hurdle for further tests of quantum network functionalities or synchronised photonic circuits.

In the work realised in this thesis and presented in this chapter, we more than double this key figure of merit. More importantly, our device enabled us to perform an optical qubit mapping for the first time in the no-cloning regime without post-selection, with a storage-and-recall efficiency at 68%. Relative to previous works, this advance has been possible by combining a high-OD medium — whose preparation was the topic of the previous chapter —, an efficient spatial multiplexing, and a low-noise operation.

The research article reporting this work has been published in Nature Communications [Vernaz-Gris2018].

3.1 Background

The memory we have demonstrated relies on EIT. Since the building of a magneto-optical trap at LKB during the course of Sidney Burks and Lambert Giner's thesis [Burks2010PhD, Giner2013PhD], EIT has been at the core of the research done there. The first published work was the study of the transition between the Autler-Townes splitting and EIT models [Giner2013], which was followed by memory experiments: storage and retrieval of light with conservation of its orbital angular momentum (OAM) [Veissier2013] and subsequently a memory for OAM qubits [Nicolas2014], as well as a memory for rotationally-invariant vector beams at the single-photon level [Parigi2015]. During my thesis, with the substantial increase in OD, we could perform the quantum storage of polarisation-encoded qubits, for the first time with large efficiency. At ANU, EIT has also been a benchmark for the highest OD obtained in our cold atomic ensembles at that time, especially for investigating four-wave mixing effects [Geng2014].

3.2 Formalism with three-level atoms

I first come back to the dynamics of ideal three-level atoms described in 1.2 in order to introduce the EIT phenomenon and how it is applied to light storage. The content of this section forms prior knowledge which is presented in the referenced articles – and summarised in chapter 3.6 of [Lambropoulos] – except for the theory of the subsection 3.2.5 which is an addition developed in the scope of this thesis. The theoretical work was mainly done by my colleague Alexandra S. Sheremet, and is more thoroughly derived in the supplementary material of the corresponding coauthored article [Vernaz-Gris2018].

3.2.1 Coherent Population Trapping

For Λ-type atoms, we have defined the interaction Hamiltonian:

$$H_{\text{int}} = -\frac{\hbar}{2}\left(\Omega_{\text{p}} e^{-\text{i}\omega_{\text{p}}t}\left|e\right\rangle\left\langle g\right| + \Omega_{\text{c}} e^{-\text{i}\omega_{\text{c}}t}\left|e\right\rangle\left\langle s\right|\right) + h.c.$$

This Hamiltonian has two eigenstates, bright $|B\rangle$ and dark $|D\rangle$:

$$\begin{cases} |B\rangle = \sin\theta\,|g\rangle + \cos\theta\,|s\rangle \\ |D\rangle = \cos\theta\,|g\rangle - \sin\theta\,|s\rangle \end{cases}$$

$$\text{with} \quad \cos\theta = \frac{\Omega_{\text{c}}}{\sqrt{\Omega_{\text{p}}^2 + \Omega_{\text{c}}^2}} \quad \text{and} \quad \sin\theta = \frac{\Omega_{\text{p}}}{\sqrt{\Omega_{\text{p}}^2 + \Omega_{\text{c}}^2}}.$$

The eigenstate $|D\rangle$ satisfies $H_i\,|D\rangle = 0$ which means that $|D\rangle$ is indeed a *dark* state as it couples to neither the probe or control fields. This property is the essence of *coherent population trapping* (CPT). We notice that in the absence of control field ($\Omega_{\text{c}} = 0$), the state $|s\rangle$ is decoupled from the system, and therefore corresponds to the dark state, $|s\rangle \equiv |D(\Omega_{\text{c}} = 0)\rangle$, while the ground state $|g\rangle$ is the dark state with no probe field $|g\rangle \equiv |D(\Omega_{\text{p}} = 0)\rangle$. As a result, for atoms starting in state $|g\rangle$, if we assume the evolution of the probe and control Rabi frequencies to be slow enough to be adiabatically followed by the atoms, then ramping the probe field up, and the control field down transfers the atoms to state $|s\rangle$, without populating the excited state $|e\rangle$. This technique is named *stimulated Raman adiabatic passage* (STIRAP) [Oreg1984, Gaubatz1988].

3.2.2 The Electromagnetically-Induced Transparency phenomenon

We have seen what superposition of ground states $|g\rangle$ and $|s\rangle$ are dark states, in the presence of a coupling to the excited state $|e\rangle$ by a control field. I am now going to add a few subtleties to the basic model used so far.

Single atom, two-photon-resonant probe and control First, let us assume the probe and control fields are not necessarily on resonance, with a detuning Δ_{p} from $|g\rangle \to |e\rangle$ and Δ_{c} from $|s\rangle \to |e\rangle$, although for now we assume they still are two-photon resonant, *i.e.* $\delta = 0$ or $\Delta_{\text{p}} = \Delta_{\text{c}} = \Delta$.

To describe the following dynamics, it is helpful to consider the EIT phenomenon in a different picture, involving the dressed states of the atoms [Eberly1994]. A strong

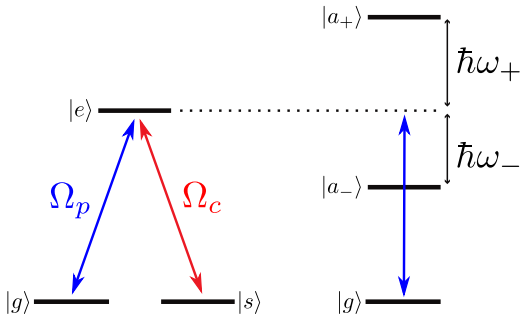

Figure 3.1: Equivalent configurations assuming a weak probe $\Omega_\mathrm{p} \ll \Omega_\mathrm{c}$. (Left) three-level atom with transition $|s\rangle \to |e\rangle$ addressed by a control field of Rabi frequency Ω_c. (Right) Autler-Townes doublet $|a_\pm\rangle$ of energies shifted by $\hbar\omega_\pm$ from the bare excited state.

control field splits the excited level into the Autler-Townes doublet $|a_\pm\rangle$ [Autler1955]:

$$\begin{cases} |a_+\rangle = \sin\phi\,(\sin\theta\,|g\rangle + \cos\theta\,|s\rangle) + \cos\phi\,|e\rangle \\ |a_-\rangle = \cos\phi\,(\sin\theta\,|g\rangle + \cos\theta\,|s\rangle) - \sin\phi\,|e\rangle \end{cases}$$

with $\tan 2\phi = \sqrt{\Omega_\mathrm{p}^2 + \Omega_\mathrm{c}^2}/\Delta$. We recognise here the bright eigenstate $|B\rangle = \sin\theta\,|g\rangle + \cos\theta\,|s\rangle$. These states are separated from $|e\rangle$ by energy $\hbar\omega_\pm = \hbar/2\left(\Delta \pm \sqrt{\Delta^2 + \Omega_\mathrm{p}^2 + \Omega_\mathrm{c}^2}\right)$, as shown in figure 3.1 [Fleischhauer2005]. In the approximation of a weak probe ($\Omega_\mathrm{p} \ll \Omega_\mathrm{c}$), the dark state $|D\rangle$ is $|g\rangle$ and the bright one $|B\rangle$ is $|s\rangle$, as previously noted. Indeed we have $\cos\theta \to 1$ and $\sin\theta \to 0$. Additionally, on resonance ($\Delta = 0$), ϕ approaches $\pi/4$, hence the Autler-Townes doublet states become:

$$\begin{cases} |a_+\rangle = \dfrac{|s\rangle + |e\rangle}{\sqrt{2}} \\ |a_-\rangle = \dfrac{|s\rangle - |e\rangle}{\sqrt{2}} \end{cases}$$

These two states are orthogonal, and their energies are equidistant to the excited level: $\hbar\omega_\pm = \pm\hbar\Omega_\mathrm{c}/2$. Their contributions to the linear susceptibility destructively interfere and the medium is made transparent, which is the EIT effect.

Dependence on the frequency of the probe and control Moreover, this transparency depends on the relative frequency of the probe and control, which we now introduce as being non-zero. Let us assume the probe is detuned by δ relative to the control, *i.e.* $\Delta_p = \Delta_c + \delta$. Up to the pre-factor notably including the OD, the susceptibility is found to be proportional to:

$$\chi(\delta) \propto \frac{\delta + \mathrm{i}\gamma_{gs}}{\delta^2 - \Omega_c^2/4 - \Gamma\gamma_{gs}/2 + \mathrm{i}\delta(\Gamma/2 + \gamma_{gs})}. \tag{3.1}$$

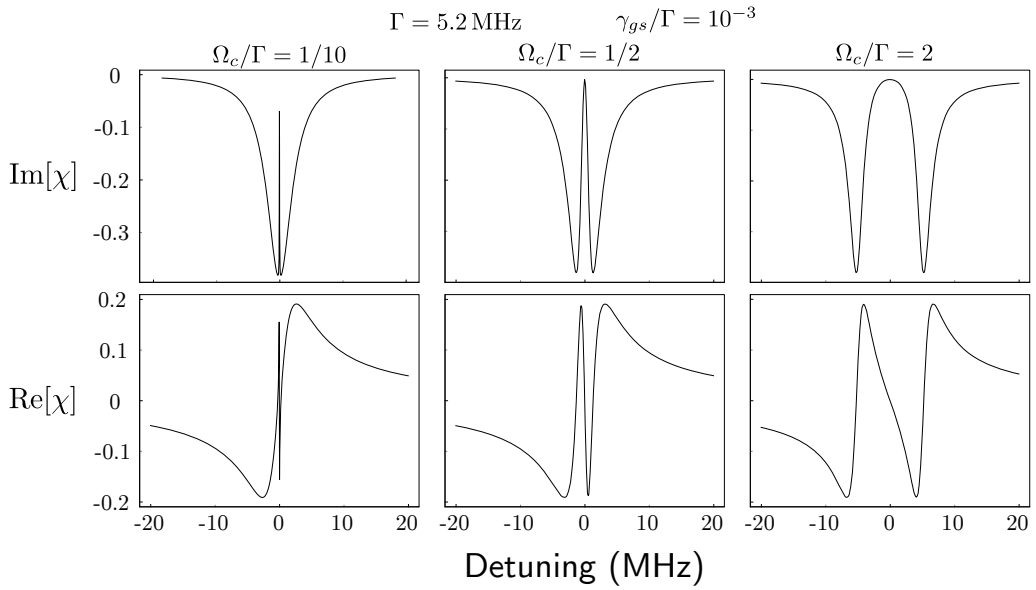

Figure 3.2: Electromagnetically-induced transparency as a function of the probe detuning from two-photon resonance with the control. The top row represents the imaginary part of the medium susceptibility, the bottom row its real part. Each column corresponds to different value of the control Rabi frequency. In all graphs, Γ corresponds to the reference value for the D_2 line of caesium 133, 5.2 MHz, the ground state decoherence rate γ_{gs} equals $10^{-3}\Gamma$. The imaginary part displays a transparency window within the absorption profile in the first two columns, which is wider and comes closer to zero absorption for a larger control Rabi frequency. In the rightmost column, the susceptibility is better described as two Lorentzians of similar widths on each side of the two-photon resonance. The real part displays a sharper variation for lower control Rabi frequencies, denoting a stronger decrease of a stored pulse group velocity.

This is represented in figure 3.2, with different values of the Rabi frequency. The value used for Γ is the reference value for the D_2 line of caesium 133 [SteckCesium] and γ_{gs} is typical of the LKB experiment as $10^{-3}\Gamma$. Depending whether Ω_c is larger than the factor $\Gamma/2 + \gamma_{gs}$, the poles of the susceptibility are real or imaginary. In the case $\Omega_c < \Gamma/2 + \gamma_{gs}$, the absorption profile is a Lorentzian of width close to Γ with a narrow transparency window centred around the two-photon resonance. If $\Omega_c > \Gamma/2 + \gamma_{gs}$, the absorption profile is best approximated with two Lorentzians of similar widths on each side of the two-photon resonance. The transition between these two behaviours has been studied experimentally in the group at LKB [Giner2013].

Collection of atoms Now, let us consider a homogeneous collection of N identical atoms forming a uniform ensemble, with the same energy levels and other characteristics. For brevity, the collective state of atom 1 in state $|\varphi_1\rangle$, atom 2 in state $|\varphi_2\rangle$, and so on, is noted $|\varphi_1 \dots \varphi_i \dots \varphi_N\rangle$. With all atoms initially prepared in state $|g\rangle$, the only states

coupled by the interaction Hamiltonian are under the form [Fleischhauer2002]:

$$\begin{cases} |\boldsymbol{g}\rangle = |g_1 \dots g_N\rangle \\ |\boldsymbol{s}\rangle = \dfrac{1}{\sqrt{N}} \displaystyle\sum_{j=1}^{N} |g_1 \dots s_j \dots g_N\rangle \\ |\boldsymbol{ss}\rangle = \dfrac{1}{\sqrt{2N(N-1)}} \displaystyle\sum_{i\neq j=1}^{N} |g_1 \dots s_i \dots s_j \dots g_N\rangle \\ \dots \end{cases}$$

We define the tensor product of the atoms and light field $|\varphi\rangle \otimes |n\rangle$ – shortened to $|\varphi, n\rangle$ – with $\varphi \in \{\boldsymbol{g}, \boldsymbol{s}, \boldsymbol{gg}, \dots\}$ and $|n\rangle$ the Fock state with n photons in the probe light field. The collective dark state, $|\boldsymbol{D}\rangle$, along with a single photon in the probe is:

$$|\boldsymbol{D}, 1\rangle = \cos\theta\, |\boldsymbol{g}, 1\rangle - \sin\theta\, |\boldsymbol{s}, 0\rangle\,,$$

$$\text{with} \quad \cos\theta = \frac{g\sqrt{N}}{\sqrt{g^2 N + \Omega_\mathrm{c}^2}} \quad \text{and} \quad \sin\theta = \frac{g\sqrt{N}}{\sqrt{g^2 N + \Omega_\mathrm{c}^2}}.$$

The case of probes with more than one photon but much fewer photons than the number of atoms are governed by similar dynamics to the single-photon case. In practice, we ensure this is always the case by choosing probes of low-enough intensities.

3.2.3 Dynamic control over slow light

In the context of optical memory schemes, the light field previously used to *probe* the atoms can now be seen as a *signal* to store and retrieve. This time-varying signal, as will be explained, experiences a slowdown effect within the narrow transparency window of the atoms, and can even be brought to a halt by dynamically controlling the control field.

Group velocity

The real and imaginary parts of the susceptibility are linked by the Kramers-Kronig relations[1]. These relations mean that a narrow transparency window is associated by a fast variation of the dispersion index, which in turn leads to a decrease of the group velocity of a probe pulse around the resonant frequency: this is the *slow light* phenomenon associated with EIT.

To quantitatively describe slow light, we need to introduce a time dimension, which has been absent from our equations so far. The Maxwell-Bloch equations 1.4 for a one- and two-photon resonant probe and control are:

[1] For a complex function $\chi(\omega) = \chi_\mathrm{r}(\omega) + \mathrm{i}\chi_\mathrm{i}(\omega)$, with χ_r and χ_i real functions, then $\chi_\mathrm{r}(\omega) = (1/\pi)\mathcal{P}\int_{-\infty}^{\infty} \mathrm{d}\omega'\, \chi_\mathrm{i}(\omega')/(\omega' - \omega)$. $\mathcal{P}$ denotes Cauchy principal value.

$$\begin{cases} (\partial_t + c\partial_z)\,\hat{\mathcal{E}}(z,t) = \mathrm{i}g\sqrt{N}\,\hat{P}(z,t) \\ \qquad \partial_t \hat{P}(z,t) = -\Gamma\hat{P}(z,t) + \mathrm{i}g\sqrt{N}\,\hat{\mathcal{E}}(z,t) + \mathrm{i}\Omega_\mathrm{c}\hat{S}(z,t) \\ \qquad \partial_t \hat{S}(z,t) = \mathrm{i}\Omega_\mathrm{c}^*\hat{P}(z,t) \end{cases} \tag{3.2}$$

Performing a Fourier transform on these equations yields the linear susceptibility for the weak probe component at frequency ω, detuned from resonance by δ[2]:

$$\chi(\delta) = -d\frac{\Gamma}{2}\frac{\delta + \mathrm{i}\gamma_{gs}}{\delta^2 - \Omega_\mathrm{c}^2/4 - \Gamma\gamma_{gs}/2 + \mathrm{i}\delta(\Gamma/2 + \gamma_{gs})}.$$

The effective optical index of the medium is given by $n = 1 + \mathrm{Re}\,[\chi]$. The group velocity of the probe is by definition $v_\mathrm{g} = \partial\omega/\partial k$, which can also be obtained from the susceptibility. Evaluated around resonance[3], the group velocity equals:

$$v_\mathrm{g} = \frac{2\Omega_\mathrm{c}^2 L}{\Gamma d}.$$

This expression encompasses all the relevant factors for slow light:

- A large control Rabi frequency enables transparency but also increases the group velocity, which indicates it is preferable to keep it below a certain threshold. This threshold corresponds to a sufficient diminution of the group velocity so that the whole pulse fits inside the atomic medium. On the other hand, so that its spectrum is contained in a narrow transparency window, the probe should preferably be long, which makes it harder to fit inside the length of the atoms.

- The independent parameter here is the OD: it enhances every aspect of the storage of light with EIT by making the coupling with the atoms stronger and reducing the group velocity. This stresses on the importance of achieving large OD in the preparation of the atomic ensemble. However, as will be explained next, either fundamental or experimental limitations usually lead to residual absorption, which imposes a compromise on the optimal OD.

Adiabatic transfer to a halted pulse

A decrease of the control Rabi frequency down to zero while the signal is contained within the atoms closes down the transparency window. This causes the group velocity to also decrease to zero: the signal is *stopped*. To describe this mechanism, the polariton picture introduced in [Fleischhauer2002] is probably the most insightful. The dark state polariton is defined as:

$$\hat{\Psi}(z,t) = \cos\theta(t)\hat{\mathcal{E}}(z,t) - \sin\theta(t)\sqrt{N}\,\hat{\sigma}_{12}(z,t),$$

[2] The susceptibility $\chi(\omega)$ is defined by the expression of the probe light field exiting the ensemble $\hat{\mathcal{E}}(L,\omega) = \exp\mathrm{i}\,(1+\chi(\omega))\,kL\hat{\mathcal{E}}(0,\omega)$.

[3] This expression is valid only for a control field resonant with the $|s\rangle \to |e\rangle$ transition. Otherwise, for a one-photon detuning of the control Δ, we need to add $-\mathrm{i}\Delta\Gamma/2 - \Delta\delta$ to the denominator of $\chi(\delta)$, with our notations [Anisimov2008].

$$\text{with} \quad \cos\theta(t) = \frac{g\sqrt{N}}{\sqrt{g^2N + \Omega_c^2(t)}} \quad \text{and} \quad \sin\theta(t) = \frac{g\sqrt{N}}{\sqrt{g^2N + \Omega_c^2(t)}}.$$

which are now explicitly time-dependent. In the approximation of slowly-varying envelope for the control field, the time evolution of the dark state polariton is given by:

$$\left(\partial_t + c\cos^2\theta(t)\partial_z\right)\hat{\Psi}(z,t) = 0.$$

This indicates that the polariton propagates at a velocity $c\cos^2\theta(t)$ through the medium, which can be controlled with the mixing angle $\theta(t)$ via the control field intensity. A decrease of the control field down to zero brings the polariton to become fully atomic ($\hat{\Psi}(z,t) \to -\sqrt{N}\hat{\sigma}_{12}(z,t)$); the light is *stopped*. Furthermore, in the assumption that the ground state decoherence is negligible, the polariton does not decay.

Subsequently, increasing the coupling field intensity back to its previous value results in the conversion of the polariton back to a superposition of slow-propagating light and atomic coherence. This light exits the atomic medium as an optical pulse in the same mode as the input one. That recall is obtained on-demand thanks to the classical control over the coupling intensity.

3.2.4 Residual absorption

In more practical terms, performing EIT in a real, non-ideal system does not exactly follow the behaviour I have described until now. The transparency of the atomic medium is usually imperfect. I now list the factors which can result in residual absorption and what is performed experimentally to find the set of optimal parameters.

Control intensity

The intensity of the control beam not only determines the width of the transparency window, it also defines how much transparency is obtained with a finite ground-state decoherence. The transparency window should be wide enough for the spectral width of the signal while providing enough slowdown so that the pulse fits in a medium of finite length. These two effects are seen in figure 3.2: a large control intensity increases the amount of transparency and the width of the window while it reduces the sharpness of the optical index variation and reduces the slowdown effect.

A non-ideal configuration results in incoherent absorption of the frequency components of the signal outside a window which is too narrow, and leakage of parts of the pulse when the slowdown is not sufficient. Additionally, a strong control field intensity causes inhomogeneous power broadening, which in turn increases incoherent absorption and therefore should be avoided. The compromise which needs to be made on control intensity is always favoured by large ODs as it increases the group velocity reduction and does not affect the transparency window in ideal three-level atoms.

Absorption from Zeeman sub-levels

In a system with more levels than in the ideal three-level case considered so far, the signal can simultaneously address several transitions. Taking into account the Zeeman

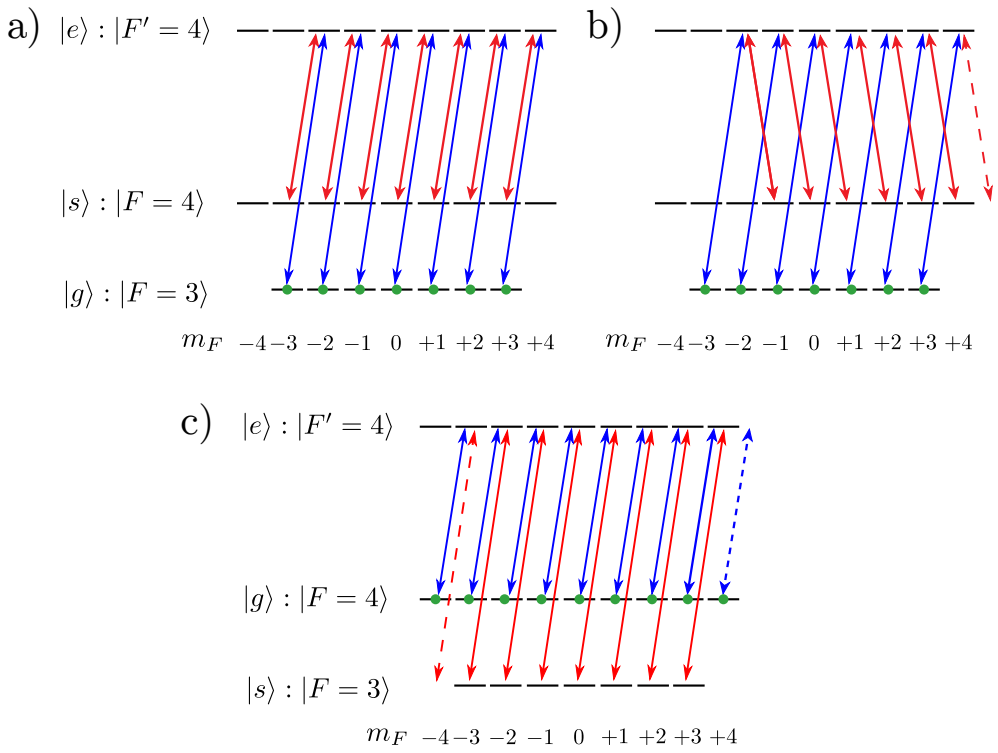

Figure 3.3: Different atomic level configurations for EIT on the caesium D_1 or D_2 lines. Probe and control have circular polarisations. The probe transition is represented in blue, the control in red. a) The probe and control field have the same circular polarisation. There are Zeeman sub-levels in $|s\rangle$ to form an EIT system with all sub-levels in $|g\rangle$: perfect transparency is theoretically achievable. b) Probe and control of opposite circular polarisation form EIT systems with ground states of $|\Delta m_F| = 2$: there is absorption from the atoms populating the edge Zeeman sub-level, $m_F = +3$ in the example represented here. c) Starting with the atoms in the ground state of higher energy ($|g\rangle = |F = 4\rangle$) results in residual absorption from one edge of the Zeeman states, here $m_F = -4$. Note also that atoms in state $m_F = +4$ do not contribute to any absorption, which effectively decreases the OD of the ensemble.

structure of the atoms, even in the degenerate case, the absorption on some transitions may not be made transparent by EIT when there is no ground state the control can address. The different configurations with caesium atoms, of hyperfine ground states $|F = 3\rangle$ and $|F = 4\rangle$, are illustrated with circular polarisations in figure 3.3.

With atoms whose Zeeman sub-levels are equally populated, a higher OD means more residual absorption from the uncoupled transitions. This can be prevented using an adequate optical pumping removing the sub-levels involved in these transitions. In a configuration where the uncoupled transitions cannot be fully suppressed, OD is a parameter which has to be mitigated, unlike for the previous source of residual absorption.

3.2.5 Additional excited levels

In real atoms, there are also other excited states at different transition frequencies and they can generate incoherent absorption which cannot be prevented with any choice of polarisation or ground state. Similarly to the absorption from some Zeeman sub-levels, large ODs give a prominence to this detrimental effect. At the ODs required for near-unity storage efficiencies, our investigation showed that incoherent absorption from additional excited states was significant. We have developed the formalism presented in the following to quantify this absorption in the qubit storage experiment we performed, in particular because it determines the maximum achievable storage efficiency. The study of EIT in more complex atomic structures than three levels had been the subject of previous theoretical work in our group at LKB [Mishina2011, Sheremet2010], but this new model is the fullest to date and provides good agreement with the experimental data presented later in 3.3.

Theoretical model for all excited levels

We have developed a model to take into account all the excited levels in the interaction Hamiltonian. I describe this model specifically in the case of the D_2 line of caesium atoms initially prepared in $\left|6S_{1/2}, F = 3\right\rangle$, but it can easily be adapted to other alkali species by changing the value of the total atomic angular momentum F and of the detunings involved.

Atomic level structure We suppose the atoms initially occupy all the Zeeman sub-levels $|g_m\rangle$ defined as $|6S_{1/2}, F = 3, m_F = m\rangle$. The excited levels that a σ_+-polarised probe can address on the D_2 line are the $|e_{F',n}\rangle = \left|6P_{3/2}, F' \in \{2, 3, 4\}, m_{F'} = n = m + 1\right\rangle$ states. On this line, the excited levels are relatively close to each other — $\Delta\omega(F', F' + 1) \sim 100\,\text{MHz}$ — compared to the D_1 line — $\Delta\omega(F' = 3, F' = 4) \sim 1\,\text{GHz}$ — with the latter also advantageously having only two excited levels [SteckCesium]. The D_2-line configuration is shown in figure 3.4.

The ensemble is addressed by a probe at frequency ω_p. We can define a detuning from the probe to each Zeeman sub-level n of each excited level, $|e_{F',n}\rangle$: $\Delta_p(F', n) = \omega_p - [E_e(F', n = m + 1) - E_g(m)]$. Similarly, the control field at frequency ω_c is detuned by $\Delta_c(F', n) = \omega_c - [E_e(F', n = m + 1) - E_s(m)]$. Additionally, in the presence of a

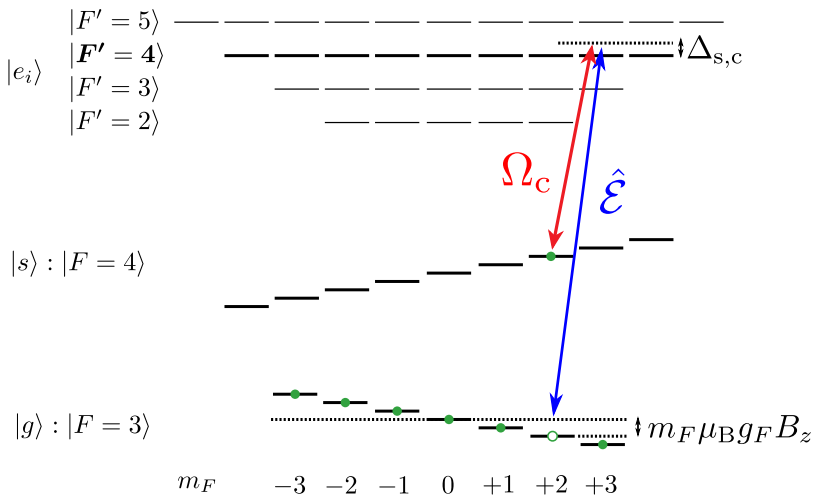

Figure 3.4: Full atomic level structure for EIT on the D_2 line of caesium. The probe $\hat{\mathcal{E}}$ and control Ω_{c} are detuned by Δ_{p} and Δ_{c} from the $|F'=4\rangle$ excited state. Moreover, a residual magnetic field along the quantisation axis, B_z, splits the Zeeman sub-levels by $m_F\mu_{\mathrm{B}}g_F B_z$.

magnetic field $B(z)$ at position z, the degeneracy of the Zeeman sub-levels is lifted and the detunings are shifted by:

$$\begin{cases} \delta_m^{(\mathrm{p})}(z) = \dfrac{\mu_{\mathrm{B}}B(z)}{\hbar}\left\{mg_g - (m+1)g_{e,F'}\right\} \\ \delta_m^{(\mathrm{c})}(z) = \dfrac{\mu_{\mathrm{B}}B(z)}{\hbar}\left\{mg_s - (m+1)g_{e,F'}\right\} \end{cases}$$

with g_g,g_s and $g_{e,F'}$ the hyperfine Landé factors of $|g\rangle$,$|s\rangle$ and $|e_{F'}\rangle$, respectively.

Optical Bloch equations There is a dipole transition associated to all possible excited levels from $|g\rangle$ and $|s\rangle$, which all contribute to the dynamics. The dipole interaction Hamiltonian is written as:

$$\begin{cases} \hat{V}_{\mathrm{p}} = -\displaystyle\sum_{m=-3}^{3}\sum_{F'\in\{2,3,4\}} d_{eg,F',m}\,|e_{F',m+1}\rangle\langle g_m|\,E_{\mathrm{p}}^{(+)} + h.c. \\ \hat{V}_{\mathrm{c}} = -\displaystyle\sum_{m=-3}^{3}\sum_{F'\in\{3,4,5\}} d_{es,F',m}\,|e_{F',m+1}\rangle\langle s_m|\,E_{\mathrm{c}}^{(+)} + h.c. \end{cases}$$

with $d_{eg,F',m}$ the dipole moment $\langle e_{F',m+1}|\,\hat{d}\,|g_m\rangle$, and similarly for $d_{es,F',m}$.

With this more complex dipole interaction, we obtain a set of optical Bloch equations for the optical coherences between $|g_m\rangle$, $|s_m\rangle$ and $|e_{F',m+1}\rangle$. The slowly-varying amplitude of the optical coherence between $|g_m\rangle$ and $|e_{F',m+1}\rangle$ is noted $\sigma_{eg,F',m}(t,z) = \rho_{eg,F',m}(t,z)\exp(-\mathrm{i}\omega_{\mathrm{p}}t)$ and satisfies the equation:

$$\frac{\mathrm{d}\sigma_{eg,F',m}}{\mathrm{d}t} = \mathrm{i}\left(\Delta_\mathrm{p} + \delta_m^{(\mathrm{p})}(z) - \omega_{ee,F',m+1}(z) + \mathrm{i}\frac{\Gamma}{2}\right)\sigma_{eg,F',m}(t,z) + \mathrm{i}\left(\frac{\Omega_{eg,F',m}^{(\mathrm{p})}}{2}\rho_{gg,m} + \frac{\Omega_{es,F',m}^{(\mathrm{c})}}{2}\sigma_{sg,m}(t,z)\right), \quad (3.3)$$

where $\hbar\omega_{ee,F',m+1}(z)$ is the energy difference between the hyperfine level $|e_{F',m+1}\rangle$ and $|e_{F'=4,m+1}\rangle$ at position z, and $\Omega_{eg,F',m}^{(\mathrm{p})}$ ($\Omega_{es,F',m}^{(\mathrm{c})}$) the Rabi frequency of the probe (control) for the dipole transition between $|g_m\rangle$ ($|s_m\rangle$) and $|e_{F',m+1}\rangle$.

Likewise, the slowly-varying amplitude of the optical coherence between $|g_m\rangle$ and $|s_m\rangle$ is given by:

$$\frac{\mathrm{d}\sigma_{sg,m}}{\mathrm{d}t} = \mathrm{i}\left[\left(\Delta_\mathrm{p} + \delta_m^{(\mathrm{p})}(z)\right) - \left(\Delta_\mathrm{c} + \delta_m^{(\mathrm{c})}(z)\right) + \mathrm{i}\gamma_{gs}\right]\sigma_{sg,m}(t,z) + \mathrm{i}\sum_{F'\in\{3,4,5\}}\frac{\Omega_{se,F',m}^{(\mathrm{c})}}{2}\sigma_{eg,F',m}(t,z). \quad (3.4)$$

Equations 3.3 and 3.4 are solved by taking the Fourier transform of the atomic coherences, $\tilde{\sigma}_{ij,F',m}(\omega,z) = \int_{-\infty}^{\infty}\mathrm{d}t\,\sigma_{ij,F',m}(t,z)\exp(\mathrm{i}\omega t)$. From the solutions, we can define the linear response of the atomic system to a weak probe field, which can then be described by the susceptibility $\chi(\omega,z,\Delta_\mathrm{p},\Delta_\mathrm{c})$ with contributions from all atomic states of the D_2 line:

$$\chi(\omega,z,\Delta_\mathrm{p},\Delta_\mathrm{c}) = -\sum_{m=-3}^{3}\sum_{F'\in\{2,3,4\}} n_0(z) d_{eg,F',m}\tilde{\sigma}_{eg,F',m}(\omega,z),$$

with $n_0(z)$ the atomic density at position z.

Results

Effective Stark shift and ground state decoherence The coupling to the excited states $F'=3$ and $F'=5$ give rise to an additional Stark shift and increase the ground state decoherence rate relatively to a Λ-type three-level system. The effective probe detuning including this Stark shift and the effective decoherence rate can be written as:

$$\begin{cases} \Delta_\mathrm{p}^{(\mathrm{eff})} = \Delta_\mathrm{p} + \displaystyle\sum_{m=-3}^{3}\sum_{F'\in\{3,5\}}\frac{\left|\Omega_{es,F',m}^{(\mathrm{c})}\right|^2/4}{\omega_{ee,F',m+1}} \\ \gamma_{gs}^{(\mathrm{eff})} = \gamma_{gs} + \displaystyle\sum_{m=-3}^{3}\sum_{F'\in\{3,5\}}\frac{\left|\Omega_{es,F',m}^{(\mathrm{c})}\right|^2/4}{\omega_{ee,F',m+1}}\frac{\Gamma}{2} \end{cases}$$

Importantly, these additional terms depend on the power of the control. Recently these contributions were also described in [Hsiao2016] for N-type four-level configuration

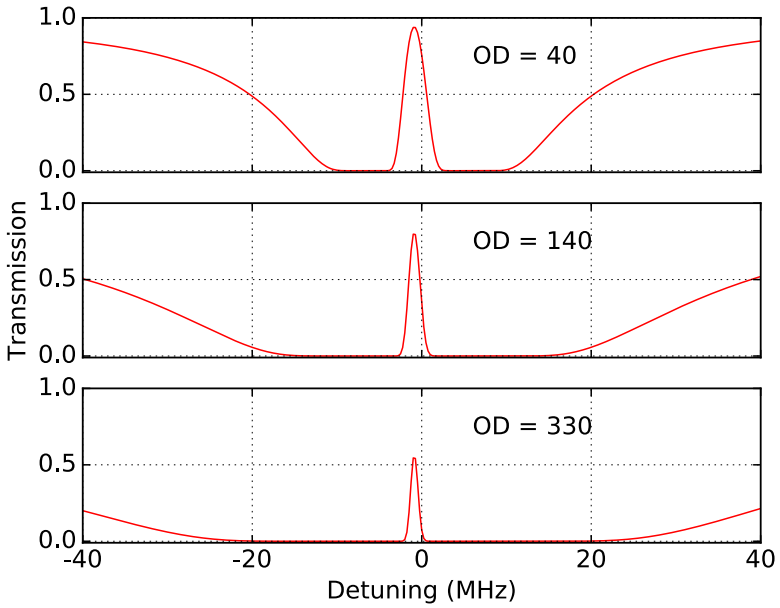

Figure 3.5: Theoretical transmission spectra with increasing OD and constant control power. The simulation parameters are: hyperfine ground state decoherence $\gamma_{gs} = 10^{-3}\Gamma$, residual magnetic field modelled as a gradient $b_0 = 8\,\mathrm{mG\,cm^{-1}}$ over a cloud length $L = 2.5\,\mathrm{cm}$, control power $P = 1\,\mathrm{mW}$.

in the context of optical memories with atoms optically-pumped to one Zeeman sub-level. In contrast, the present model includes not only the several excited levels but also all the Zeeman sub-levels.

Propagation losses through the medium The propagation of the signal through the medium can be modelled by a macroscopic Maxwell equation for the light field of amplitude ϵ:

$$\left[\frac{1}{c}\frac{\partial}{\partial t} + \frac{\partial}{\partial z}\right]\epsilon(z,t) = 2\pi\mathrm{i}\frac{\omega}{c}\int_{-\infty}^{t}\mathrm{d}t'\,\chi\left(z,t,t'\right)\epsilon(z,t').$$

The light field from the memory medium, written as $\epsilon_{\mathrm{out}}(t) = \epsilon(z = L, t)$, is given by:

$$\epsilon_{\mathrm{out}}(L,t) = \int_{-\infty}^{\infty}\frac{\mathrm{d}\omega}{2\pi}e^{-\mathrm{i}\omega t}\epsilon_{\mathrm{in}}(0,\omega)\exp\left[-2\pi\mathrm{i}\frac{\omega}{c}\int_{0}^{L}\mathrm{d}z\,\chi\left(\omega,z,\Delta_{\mathrm{p}},\Delta_{\mathrm{c}}\right)\right],$$

where $\epsilon_{\mathrm{in}}(\omega) = \epsilon(z = 0, \omega)$ is the component at frequency ω of the input probe pulse and L the length of the atomic cloud.

The transmission spectrum of the atomic ensemble is obtained from the imaginary part of the susceptibility:

$$T(\omega) = \exp\left[-4\pi\frac{\omega}{c}\,\mathrm{Im}\left[\int_{0}^{L}\mathrm{d}z\,\chi\left(\omega,z,\Delta_{\mathrm{p}},\Delta_{\mathrm{c}}\right)\right]\right].$$

This EIT transmission spectrum is shown in figure 3.5 for increasing ODs, showing a decrease of the maximal transmission with OD as well as the frequency shift on where this maximum occurs.

The overall loss during the propagation is obtained by integrating over all the frequency components of the input and output pulses or, equivalently, over all times. The upper bound for the storage-and-recall efficiency of the EIT memory is thereby given by the transmission :

$$\eta_{\max} = \frac{\int_{-\infty}^{\infty} \mathrm{d}t \, |\epsilon_{\mathrm{out}}(t)|^2}{\int_{-\infty}^{\infty} \mathrm{d}t \, |\epsilon_{\mathrm{in}}(t)|^2}. \tag{3.5}$$

Pulse storage and recall The value given by equation 3.5 only sets a maximum storage-and-recall efficiency of the EIT memory due to the absorption during the necessary propagation through the length of the cloud, whatever the dynamics of the storage and recall. In practice, the achieved efficiency may be lower due to leakage of the input pulse and decoherence during storage.

The signal pulse is given a Gaussian profile of full-width half-maximum (FWHM) τ, centred around $t = 0$:

$$\epsilon_{\mathrm{in}}(t) = \epsilon_0 \exp\left(-2 \ln 2 \frac{t^2}{\tau^2}\right).$$

The control is assumed to be turned off at a time T_c. The leakage is discarded by considering the output pulse only after T_c. The atomic density $n_0(z)$ is assumed to be a Gaussian distribution of the form $n_0(z) = \overline{n}_0 \exp\left(-4z^2/L^2\right)$. The optical depth is defined as $d_0 = \overline{n}_0 L \lambda^2/(2\pi)^2$. At each OD, the control power is chosen so that the pulse experiences a delay $T_d = 2\tau$. The stopped pulse is then stored over 4τ.

Figure 3.6 illustrates the effect of the additional excited states on the maximum memory efficiency in two configurations. In the first one, the atoms populate all the Zeeman sub-levels, in the second, they are regrouped in a single sub-level, corresponding for example to the case when the atomic ensemble is optically pumped to this sub-level. The hyperfine ground state decoherence is taken to be $\gamma_{gs} = 10^{-3}\Gamma$, the residual magnetic field is modelled as a gradient $b_0 = 8\,\mathrm{mG\,cm^{-1}}$ over a cloud length of $L = 2.5\,\mathrm{cm}$. The FWHM of the input pulse, τ, is taken to be $0.5\,\mu\mathrm{s}$, for which the storage time, 4τ, is $2\,\mu\mathrm{s}$.

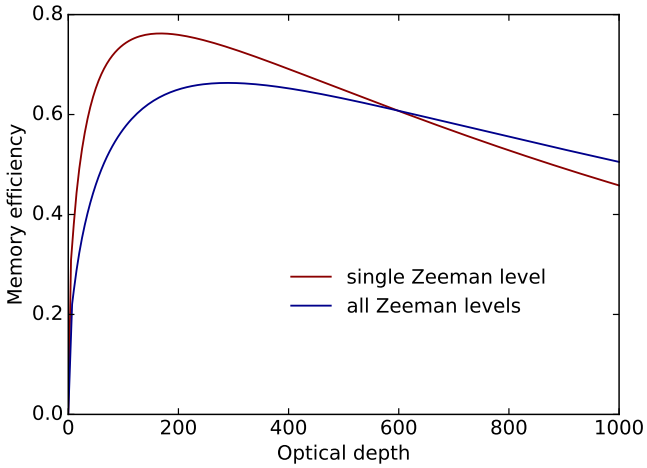

Figure 3.6: Numerical simulation of the maximum achievable storage-and-recall efficiency with EIT on the D_2 line of caesium versus optical depth when the excited states $|e_{F'}\rangle = \left|6_{3/2}, F' \in \{2,3,4\}\right\rangle$ are considered. The blue line corresponds to the case where all the ground state Zeeman sub-levels are equally populated, the red line when only Zeeman sub-level $\left|6S_{1/2}, F=3, m_F=3\right\rangle$ is populated. The simulation parameters are: hyperfine ground state decoherence $\gamma_{gs} = 10^{-3}\Gamma$, residual magnetic field modelled as a gradient $b_0 = 8\,\mathrm{mG\,cm^{-1}}$ over a cloud length $L = 2.5\,\mathrm{cm}$, signal pulse is a Gaussian of FWHM $\tau = 0.5\,\mu\mathrm{s}$ and storage time is $2\,\mu\mathrm{s}$.

The storage process has an efficiency close to unity for moderately-large OD (> 50), which corresponds to a negligible leakage but at low OD, the signal pulse cannot be entirely contained in the atomic medium and a significant part of the pulse leaks from the medium. The effective ground state decoherence increases with the control field Rabi frequency. This decoherence becomes more significant in the region of large ODs due to the large control power needed. This dependency leads to a reduction of the EIT transparency and, as a result, of the memory efficiency. In our configuration, without optical pumping, the efficiency is expected to be limited to about 70%. With all the atoms in a single Zeeman sub-level, the maximum achievable memory efficiency increases by about 10%, and the maximum is obtained at a slightly lower OD.

3.3 Multiplexed polarisation qubit storage

Now that an extended formalism has been presented to fully describe EIT storage on the D_2 line at large ODs, the experiment central to this chapter can be introduced. The atomic ensemble is prepared for multiplexed storage, using a dual-rail geometry. In the logic of the experiments in the group, this extension was somehow a natural step

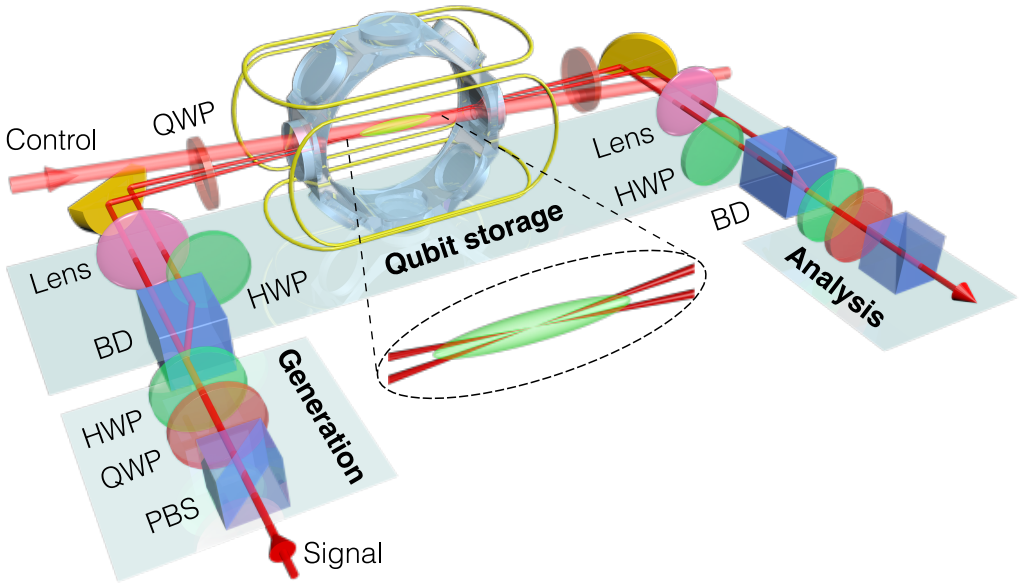

Figure 3.7: A polarisation qubit is encoded via a quarter- (QWP) and a half-wave plate (HWP) and converted into a dual-rail qubit with a beam-displacer (BD). The orthogonally-polarised beams, separated by 4 mm, are then mapped into an elongated ensemble of laser-cooled caesium atoms prepared in a 2D magneto-optical trap in a glass chamber. The spatial multiplexing is realised by focusing the two parallel paths into the 2.5-cm-long ensemble with a small crossing angle of 0.5° in order to preserve a large OD for each mode, an essential but challenging feature. A large OD of 300 is obtained. A single control beam propagates with an angle of 1° relative to the signal modes in the plane of symmetry.

after having greatly enhanced the OD with the elongated-MOT geometry, using the methods described in the previous chapter. We wanted to prove in this new setup that we had not lost the spatial multimode capacity we used for the storage of OAM-encoded qubits [Nicolas2014]. It was now time to prove this improved platform could surpass the previous realisations and this experiment was the perfect benchmark for that.

3.3.1 Polarisation encoding: preparation, manipulation and detection

In our implementation, depicted in figure 3.7, we have chosen to encode the qubits on polarisation. The preparation of different qubit states only requires a well-defined polarisation for the input, easily obtained with polarisation optics, namely retardation wave plates in our case. Simply the rotation of these optics gives us access to the whole parameter space to prepare input qubits for storage. This resource requirement is much less stringent than the previous experiment we performed in the group with the preparation and analysis of OAM-encoded qubits, which required Spatial Light Modulation (SLM) and holographic plates, respectively.

3.3.2 Storage of orthogonal polarisations

Polarisation qubits require the storage of two orthogonal polarisations on which the quantum information is written. Our configuration with all the ground-state Zeeman sub-levels initially populated, however, prevents us from simply extending the basic storage protocol for light we studied previously in this chapter to the storage of polarisation qubits. Instead, we choose to convert the orthogonal polarisation components of the qubit into two spatially-separated beams which can be stored in the atomic ensemble. This ends up using not a multimode capacity in the polarisation modes of light, but rather different spatial modes.

In the context of spatially-multiplexed optical memories, the signal is usually in a single spatial mode and its multimode character is in another degree of freedom. The signal components are divided into several rails, the details of the division depending on the scheme, and all the rails can be stored in different locations of the memory. Upon their retrieval, the rails are recombined into a common spatial mode, restoring the initial signal.

3.3.3 Atom preparation for dual-rail storage

We use the MOT loading sequence described in 2.3.4, which produces an atomic cloud of cold caesium atoms prepared in state $|g\rangle = \left|6S_{1/2}, F = 3\right\rangle$. We do not perform Zeeman optical pumping, and actually do not properly define a quantisation axis, which *a fortiori* leaves the atoms in an equal superposition of all Zeeman sub-levels. We have seen that this atomic level configuration with circularly-polarised signal and control allows unity-transparency EIT, with the only residual absorption being accountable to the additional excited levels on the D_2 line.

The increase in OD comes at the expense of spatial multimode capacity as the atomic cloud is elongated along a direction and radially compressed, resulting in a smaller transverse size. Spatial multiplexing can only be performed in atomic ensembles whose transverse size is kept sufficient to support spatially-separated modes. Indeed, a spatial separation of at least a few waists is required to ensure the modes do not overlap and induce cross-talk. The new geometry and the MOT compression had greatly reduced the transverse size of the atom cloud and preliminary tests showed that the signal beam was not overlapping the whole ensemble, so it was unlikely that a second signal beam could be added in the system and "fit" equally well in the cloud.

Dual-rail storage can be performed in different fashions in an atomic ensemble. Here are the possibilities we have considered, shown in figure 3.8:

- Parallel rails: The first one consists of two parallel signal beams with a separation larger than their transverse size over the cloud depth. In the end, with a $1/e^2$-waist of 250 µm and a required separation by a few waist diameters, the compromise to be made on the MOT compression was too detrimental to the OD and this solution was abandoned.

- Rails separated and crossing in the middle of the atomic ensemble. This is an acceptable solution because the EIT process would not induce cross-talk between the stored polaritons generated from signals crossing at an angle, because of the

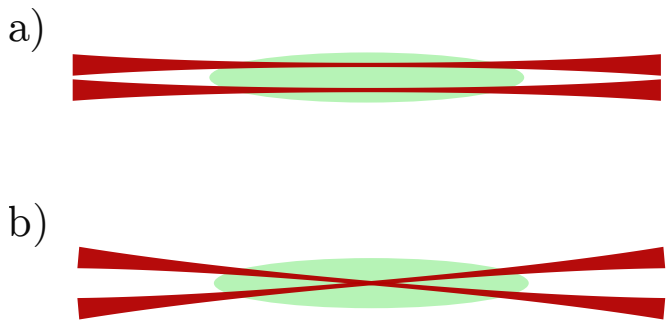

Figure 3.8: Diagrams for two different rail configurations envisioned for the spatially-multiplexed EIT storage. a) The two rails are parallel, with a separation larger than their transverse size over the cloud depth. b) The two rails are crossing in the middle of the cloud. Their angular separation ensures that they do not contaminate each other.

phase-matching requirement between the polariton and each output signal. The angle was made to be 1° to ensure sufficient selectivity. The control beam could make the same angle with both signal paths by making a vertical angle with the plane where the signals belong. This is the solution that was eventually adopted.

Moreover, in this second configuration, the alignment was considered in two variants, shown in figure 3.9:

- The two rails can be independently aligned with a set of beam-splitters and mirrors. This configuration was expected to allow an optimisation of the overlap of each rail with the atomic ensemble, resulting in larger ODs. Its main limitation, however, was the interferometric stability of two very differentiated optical paths: the length of each rail was likely to change significantly relatively to the wavelength and the relative phase between the signals on the two rails was altered.

- The crossing angle between two parallel rails is introduced by a lens placed at its focal distance from the centre of the atomic cloud. The angle is determined by the initial beam separation and the focal length, both fixed by the chosen optics, which therefore limits its versatility. On the other hand, this configuration provides interferometric stability of the two rails, which was crucial to provide uniform storage of both rails.

In the chosen configuration of figure 3.9(b), the separation of the orthogonal polarisation components of light into two parallel beams can be obtained by polarisation-selective beam-displacing optics, a calcite displacer in our case (Thorlabs BD40). The sufficient separation between the two rails, 4 mm, allows us to control the polarisation of one rail only, with a wave plate, so that the signal going through the atomic ensemble effectively has the same polarisation on both rails, and therefore can be addressed by the same control beam. The signal on the rail whose polarisation was changed is restored to its original one by a second wave plate. The geometry involving only one pair of wave plates on one rail and no other optics makes it a passively-stabilised interferometer.

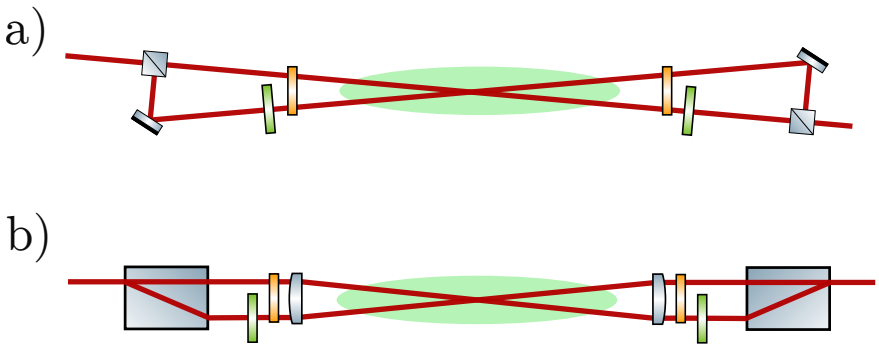

Figure 3.9: Configurations for crossing rails: a) The two rails are independently aligned with a set of adjustable beam-splitters and mirrors. This configuration is expected to be more flexible: the angle can be easily tuned and the overlap of each rail with the atomic ensemble can be maximised, resulting in larger ODs. b) The two rails correspond to the two parallel output ports of a beam-displacer, which are then focused at the middle of the atomic ensemble by a lens. This configuration advantageously provides interferometric stability of the two rails. In both configurations, half-wave plates (in green) are placed on a single rail to have both incoming beams with the same polarisation. Additionally, quarter-wave plates (in yellow) make the beams circularly-polarised.

3.3.4 Transparency measurement

The control beam is chosen with a 2-mm waist, so it can overlap with both rails which intersect at the centre of the MOT. The control is making a small angle of 1°, vertically from the plane of the signals. The transparency of the atomic ensemble on each rail was measured for different ODs, with the results presented in figure 3.10. The experimental data is shown against the theoretical model from the previous section, with independently-measured parameters. In particular, we remind that the hyperfine ground state decoherence is taken as $\gamma_{gs} = 10^{-3}\Gamma$, corresponding to a residual magnetic field independently measured by Raman spectroscopy and modelled as a gradient $b_0 = 8\,\mathrm{mG\,cm^{-1}}$ over a cloud length $L = 2.5\,\mathrm{cm}$. The control power was measured as $P = 1\,\mathrm{mW}$ and kept constant across the measurements.

Higher OD enable narrower transparency windows at moderate control field intensities — which prevents inhomogeneous broadening — and the reduction of the group velocity, enabling the storage of long pulses. The decrease in transparency which is observed at larger ODs, in spite of the increase the coupling efficiency with the ensemble, confirms the prediction made in our theoretical model. Precisely in the case of non-negligible incoherent scattering from the other excited states, we want to limit the interaction strength to those, which can only be achieved by a compromise on the OD. We eventually found that relatively high ODs around 200 correspond to the optimum for the performance of the EIT memory protocol explained in the following.

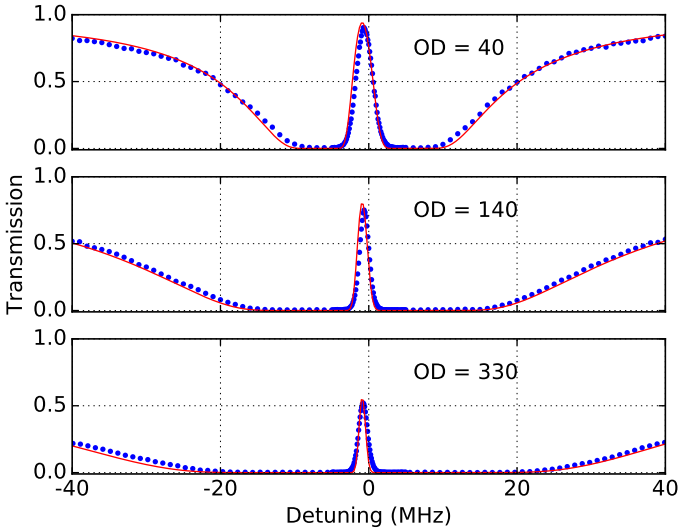

Figure 3.10: Transmission spectra with increasing OD. The experimental data (red) is shown against the theoretical model including additional excited states (blue). The model parameters are taken as: hyperfine ground state decoherence $\gamma_{gs} = 10^{-3}\Gamma$, residual magnetic field modelled as a gradient $b_0 = 8\,\mathrm{mG\,cm^{-1}}$ over a cloud length $L = 2.5\,\mathrm{cm}$, control power $P = 1\,\mathrm{mW}$.

3.3.5 Memory efficiency

Having prepared a large-OD ensemble, we now turn to the memory protocol. EIT enables the conversion of a signal photon into a long-lived collective excitation by dynamically changing the power of an auxiliary control field. The laser source for the control is an external-cavity diode (Toptica Photonics, DL Pro) which provides the 10-mW repump and is also used for the signal. The signal and control beams are tightly phase locked at the caesium hyperfine splitting frequency (Vescent Photonics, D2-135). Special care is taken with alignment of the light polarisation, as only a slightly-wrong matching of the polarisation would lead to a significant absorption of the signal in a high-OD medium like the one prepared here.

To ensure negligible leakage during the storage process, the power of the control beam is chosen to provide a slow-light delay equal to twice the signal pulse duration of 1 µs when the control is continuously on. Figure 3.11 gives a single-photon level measurement of the slowed pulse and an example of a dynamic memory operation with a few microseconds of storage. Before detection, the signal passes through a homemade atomic filter and a commercial lens-based cavity for spectral filtering (Quantaser FPE001A), with an overall rejection of 70 dB for the control field.

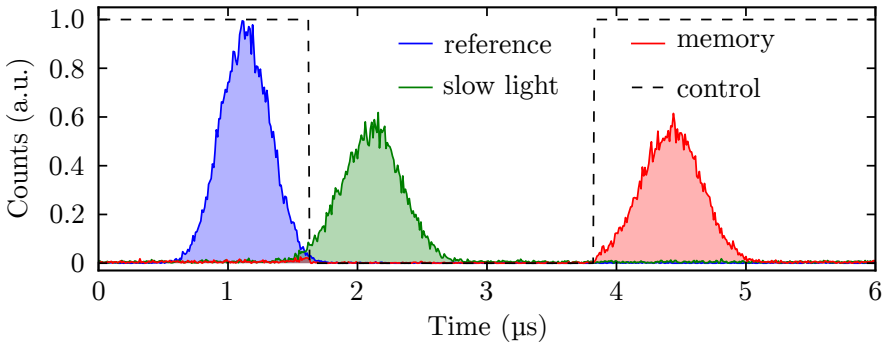

Figure 3.11: Histogram of the photodetection counts. The blue-filled region gives the reference pulse without atoms while the green and red regions correspond to the slow and the stored-and-retrieved pulses, respectively. The black dashed line indicates the control intensity for the storage experiment. The memory efficiency reaches (69 ± 1)%.

Thanks to the range of ODs achievable in this atomic ensemble, we could investigate the scaling behaviour of the storage-and-retrieval efficiency with OD, to compare with the model shown in figure 3.6. Figure 3.12 shows the efficiency as a function of the OD, which is varied by adjusting the power of the trapping beams during loading. At each value, the time delay is maintained constant and equal to twice the signal duration by adapting the intensity of the control beam. As can be seen, the memory efficiency saturates at an OD of around 200 before decreasing. The maximal efficiency achieved here reaches $(69 \pm 1)\,\%$. This represents a record on the caesium D_2 line and, more importantly, the highest achievable value in this configuration. We also obtain strong agreement between the measurements from the experiment and the model where all the Zeeman sub-levels are equally populated. The model also confirms that the intrinsic ground state decoherence $\gamma_{gs} = (1.0 \pm 0.5) \times 10^{-3}\Gamma$ estimated in our experiment is not the limiting factor for the memory performance.

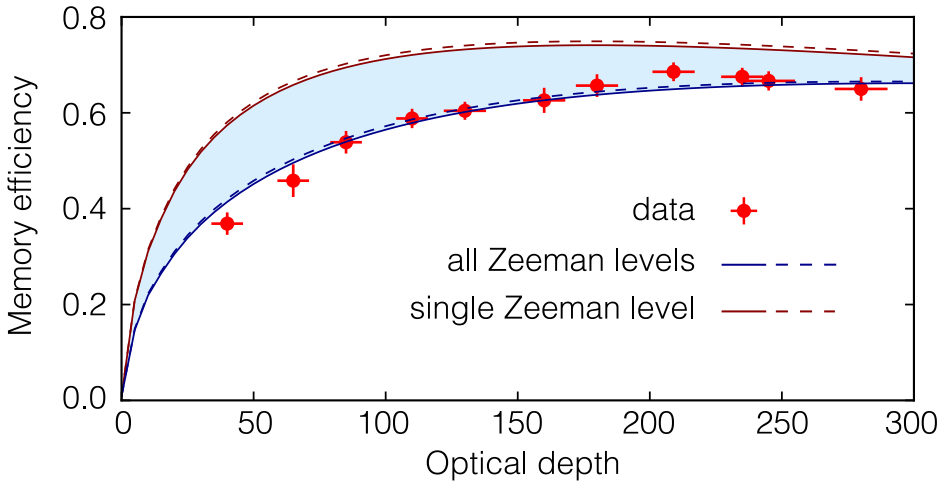

Figure 3.12: Storage-and-retrieval efficiency as a function of the OD. Red dots correspond to the experimental measurements of the memory efficiency, with error bars from the uncertainty on the determination of OD and the statistical uncertainty on photon counts across acquisitions. The theoretical lines correspond to the two limiting cases with a single Zeeman sub-level (in red) and all Zeeman sub-levels (in blue), respectively. For each case, the solid lines correspond to an intrinsic ground state decoherence estimated to $\gamma_{gs} = 10^{-3}\Gamma$ while the dashed lines correspond to the limiting case with $\gamma_{gs} = 0$.

3.4 Qubit storage and retrieval

We now proceed to the qubit storage in this dual-rail setting. At the memory output, the two paths are recombined into a single spatial mode with a second beam displacer. The position of the second lens is optimised to obtain a visibility over 99% between these two paths, which is a critical step to achieve high fidelity. The two displacers form a passively-stable Mach-Zehnder interferometer, where the relative phase is set to zero by adjusting the tilt of the second beam displacer. The recombined state should be as faithful as possible to the prepared one, which is evaluated quantitatively by the fidelity of the memory process.

3.4.1 Quantum state tomography

The retrieved states are then characterised by usual quantum state tomography. Figure 3.13 gives the reconstructed density matrices in the $\{H, V\}$ logical basis. From the measured matrices, one can estimate the conditional fidelity of the output states with the initially-encoded state. The values for the complete set of inputs are listed in table 3.1. The average fidelity is $(97.7 \pm 0.8)\%$ and raises up to $(99.5 \pm 0.5)\%$ after correction for background noise that mainly comes from residual control leakage and detector dark counts.

In the absence of an input signal, the background floor corresponds to 5.10^{-4} events per detection window. The storage-and-retrieval efficiencies for each prepared state

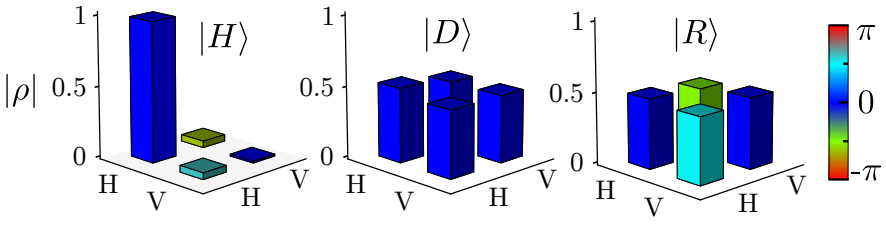

Figure 3.13: Reconstructed density matrices in the $\{H, V\}$ basis from preparing, storing and retrieving input states $|H\rangle$, $|D\rangle$ and $|R\rangle$, after a 1.2-µs storage time. The height of the bar represents the absolute value while the colour denotes the phase. No background has been subtracted.

Input state	Fidelity $\mathcal{F}$ (%)	Efficiency η (%)
$\|H\rangle$	98.7 ± 0.1	68.9 ± 1.5
$\|V\rangle$	98.5 ± 0.1	69.7 ± 2.6
$\|D\rangle$	97.5 ± 0.1	68.1 ± 2.3
$\|A\rangle$	96.8 ± 0.1	67.5 ± 2.8
$\|R\rangle$	97.3 ± 0.1	68.8 ± 1.3
$\|L\rangle$	97.2 ± 0.1	67.4 ± 1.2
Average	97.7 ± 0.8	68 ± 2

Table 3.1: Conditional fidelity and memory efficiency for the three standard polarisation bases, and their average. The error bars for the fidelity are estimated by taking into account the statistical uncertainty of photon counts. The error for the efficiency is obtained from multiple measurements. The mean number of photons per input pulse is $\bar{n} = 0.5$, storage time is $\tau_s = 1.2\,\mu s$.

are also given in the table, with an average efficiency that reaches $(68.5 \pm 2)\%$. The performance of the memory is uniform over these six canonical states, within two percent of efficiency.

Figure 3.14 presents the achieved fidelities as a function of the mean photon number per pulse $\bar{n}$.

3.4.2 Quantum storage benchmarking

In order to conclude about the quantum performance of the storage, we need to compare our fidelity with the maximum achievable using a classical memory device, based for instance on the so-called measure-and-prepare strategy. It can be shown that the classical benchmark is given by a fidelity equal to $(N + 1)/(N + 2)$ for a state containing N photons [Massar1995], which is equal to $2/3$ for the particular case of a single photon. In the limit $N \gg 1$, the fidelity becomes close to unity: the quantum character of the memory cannot be demonstrated with such bright states.

Polarisation qubits are implemented with weak coherent states with a mean photon number per pulse $\bar{n} = 0.5$ and subsequently stored into the memory. In this case, using coherent states, the bound has to be modified to take into account the Poissonian statistics of the signal and the finite memory efficiency, as done in [Specht2011, Gundogan2012].

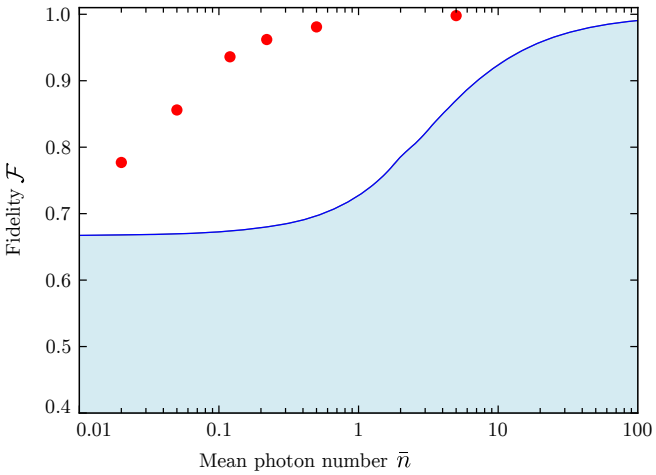

Figure 3.14: Storage and retrieval beyond classical benchmark. The fidelity is given as a function of the mean photon number per pulse $\bar{n}$, for a 1-µs storage time. No background correction has been applied. The blue solid line indicates the classical limit for the finite storage-and-retrieval efficiency and takes into account the Poissonian statistics of the weak coherent states. The error bars are smaller than the data points and are given by the standard deviations of fidelities for the set of stored states.

The coherent mapping of arbitrary polarisation states of light into and out of the memory was performed with fidelities of $97 \pm 1\%$, well above the classical benchmark, which unambiguously indicates that the optical memory is operating in the quantum regime. Moreover, this quantum feature is still verified when storing coherent light with an average photon number as low as 0.02, below which the control leakage and detector dark counts become predominant.

3.4.3 Storage time

To evaluate the decay time of the memory, we measure the probability to measure the retrieved light after a variable storage time. Figure 3.15 shows the decay of the memory efficiency, as measured experimentally. The efficiency is corrected for the losses from the atoms to the APD, and the efficiency of the detector. Moreover, we compare these measurements to the following model, with three decoherence mechanisms which can be evaluated independently:

- First, the atomic motion related to the finite temperature results is a possible loss of the atoms from the interaction area. With a temperature estimated at 20 µK by time-of-flight measurement and a 250-µm signal beam diameter, the corresponding transit time is evaluated to $\tau_1 = 7$ ms. This is not a limiting factor in our experiment.

- The two other decoherence contributions come from dephasing of the collective

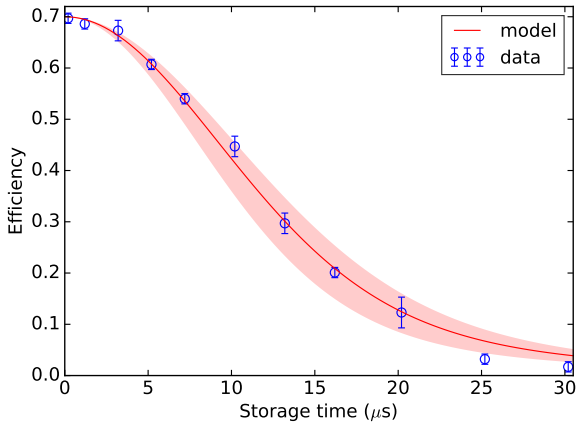

Figure 3.15: Retrieval efficiency as a function of the storage time. The blue points give the experimental measurements and the red solid line corresponds to our model including additional excited levels. with a measured OD equal to 200 and a 50-kHz inhomogeneous broadening. The shaded area corresponds to an uncertainty on the residual magnetic field equal to $\pm 1\,\mathrm{mG\,cm^{-1}}$.

excitation. The first source of possible dephasing is the so-called motional dephasing due to the strong angular dependence of EIT. In the experiment, we used indeed an off-axis configuration and the control and signal beams are overlapped with an angle $\theta = 1°$. The resulting lifetime is then given by:

$$\tau_2 = \frac{\lambda}{2\pi \sin\theta}\sqrt{\frac{m}{k_B T}}\,.$$

In our case, this expression leads to a decay time $\tau_2 = 220\,\mu\mathrm{s}$.

- The second dephasing process is caused by residual magnetic fields which result in an atom-dependent Larmor precession. The magnetic field is compensated via three pairs of coils and the inhomogeneous broadening in the ground state is therefore limited to around 50 kHz, as measured via microwave spectroscopy. By assuming a gradient of magnetic field equal to $b_0 = 8\,\mathrm{mG\,cm^{-1}}$ over a cloud length $L = 2.5\,\mathrm{cm}$ and a quadratic atomic distribution, the expected time constant is $\tau_3 = 15\,\mu\mathrm{s}$. This dephasing is the main decoherence source in our experiment.

The model is represented with an independently-measured OD equal to 200 and a 50-kHz inhomogeneous broadening. The shaded area corresponds to an uncertainty on the residual magnetic field of $\pm 1\,\mathrm{mG\,cm^{-1}}$.

Figure 3.16 shows the decay of the fidelity with storage time, and the fidelity benchmark, which increases because the memory efficiency decreases with storage time. The quantum nature of the memory is maintained for a storage time of more than 20 µs.

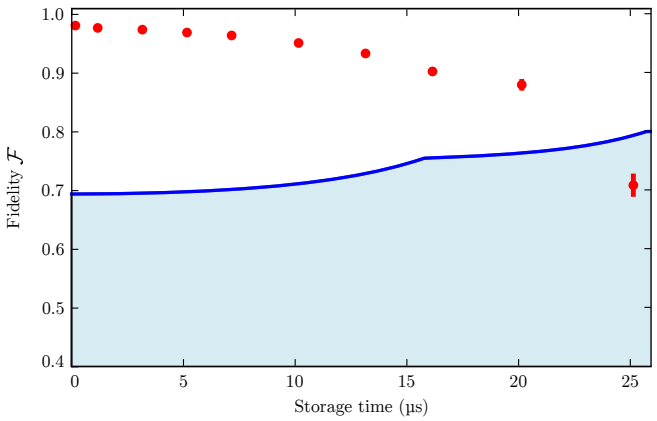

Figure 3.16: Fidelity as a function of the storage time, for a mean photon number $\bar{n} = 0.5$. No background correction has been applied. The blue solid line indicates the classical limit for the finite storage-and-retrieval efficiency and takes into account the Poissonian statistics of the weak coherent states. The error bars are smaller than the data points and are given by the standard deviations of fidelities for the set of stored states.

3.4.4 Discussion

This value is the highest efficiency reported so far for a reversible memory that demonstrates the quantum storage of photonic qubits. Moreover, we have shown that, because of the multiple level structure of the caesium D_2 line, the achieved efficiency is close to the highest one which can be obtained in this configuration. Direct extension of our setup to the D_1 line where excited levels are much more separated should enable us to reach an efficiency above 90% [Hsiao2016], although this has yet to be demonstrated in the quantum regime.

In our realisation, the pulse duration of the qubits has been chosen around 400 ns to obtain the highest efficiency after one pulse-width delay. It corresponds to a memory bandwidth of a few MHz, as expected from EIT storage. Single-photon sources with sub-MHz bandwidths have been demonstrated [Du2008, Fekete2013, Rambach2016] and can be adapted to our reported quantum memory.

3.5 Future of the experiment

The most immediate improvement foreseen for the experiment is the use of D_1-line transitions for the memory scheme, with the incoherent absorption on the D_2 line identified as the main limitation in the performed experiment. New diode lasers are being bought as I write these lines and EIT without this limitation will soon be studied.

The realisation of qubit storage follows a series of multimode experiments with the free-space setup, and this one explores once again the spatial multimode capacity of the ensemble. Bases of orthogonal polarisation states, however, are limited to spanning only two modes. Laguerre-Gauss (LG) modes, which carry orbital-angular momentum (OAM), which were previously investigated in the group, or alternatively

linear-polarisation (LP) modes, do not suffer from this limitation. Low-loss phase plates for the generation of LG modes were manufactured on the ultra precision lathe (Nanotech 250UPL) at ANU during the course of my thesis. Following this course, the next planned experiment is to demonstrate the storage in a basis of more than ten modes.

Concurrently to the progress of the free-space experiment, our neighbours working on nanofibre-guided light are greatly improving the achievable OD, which should soon enable efficient EIT storage as well.

Chapter Conclusion

We have introduced the cornerstone effect of electromagnetically-induced transparency, which is the basis for our realisation of a dual-rail memory for polarisation qubits that gathers the following achievements:

- The memory possesses the highest reported storage-and-retrieval efficiency for a qubit memory, close to 70%, along with near-unity fidelity for the preparation and memory processes, above 99% conditionally.
- This result is enabled by the high-efficiency storage on two optical paths through the same elongated cold caesium ensemble, yielding the ability to store two modes that encode a polarisation qubit without compromising on efficiency.
- A quantitative theoretical model was developed to represent realistic atomic level configurations with additional excited levels which become relevant at the high ODs obtained in current cold atomic ensembles. Maximum efficiency for the EIT scheme on the D_2 line is achieved for an optimal value of OD. This was verified experimentally, and sets our result within the best efficiencies achievable on this line.
- The model also predicts it is possible to perform better on the D_2 line with the preparation of the atoms in a single Zeeman sub-level, although the enhancement would only be of about 10%.
- Operation on the D_1 line would not suffer from such a stringent limitation, due to the interaction with off-resonant excited levels, and would allow storage efficiencies above 90%.

Chapter 4

High-performance backward-recall Raman memory

Moving on from the last chapter covering EIT and the experiment led at the LKB in Paris, I will now cover another memory scheme linked to a different experimental setup: the Raman memory scheme, which I investigated at the ANU in Canberra.

The Gradient Echo Memory (GEM) variant of a off-resonant Raman memory has experienced many improvements in its realisations in the group at the ANU over the last decade. After originating there with the first experiments in rare-earth solids [Alexander2006, Hedges2010] and a warm vapour of rubidium atoms [Hetet2008, Hetet2008a, Hosseini2011], it was later implemented in a cold atomic ensemble breaking records of ODs [Sparkes2010, Sparkes2013, Higginbottom2015]. My very first research experience at the ANU during my master's in 2012 was towards the end of the first era, when the prospect of moving to cold atoms was the best promise to extend the memory performance – especially its lifetime – to a new high. During my second visit, then starting as a PhD student, the original warm vapour experiment was an available platform for new ideas and experiments that Jesse Everett and I were in full charge of. It was at this time that we first investigated stationary light, in numerical simulations and experimental trials in the warm vapour, which I discuss in the next chapter. It was finally during the last years of my PhD that I got to work on the cold-atom setup, although we had moved on from GEM to focus on stationary light realisations.

In this chapter, I report on a high-performance optical Raman memory which uses backward retrieval. We achieved a recall efficiency of $65 \pm 6\%$ and a delay-bandwidth product of 160. It is the first reported Raman memory with an efficiency above 50%, which is an important criterion for unconditional security in quantum communication protocols.

This work has led to an article published in Optics Express [Vernaz-Gris2018a].

4.1 Theoretical basis for a Raman memory

In order to apprehend the Raman memory experiment, in particular the backward-retrieval configuration we investigated, I begin this chapter with an extension on the few theoretical aspects relevant to the experiment.

4.1.1 From scattering to a memory scheme

Light scattering is a prominent effect of atomic physics, described in section 1.2. It can indeed be applied to quantum memories if we consider this process as a reversible quantum-state transfer from light to the atoms: all the information from impinging light is converted via inelastic scattering into information encoded in the atomic state, and *vice versa*. Raman scattering is the exemplary form of inelastic scattering with photons of low energy compared to the ionisation energy[1]. Let us give a quick reminder on the Raman scattering process and then look into the details of how it can be applied to a memory scheme.

Reminder on Raman scattering In a Λ configuration, a light field at frequency ω can lead to the emission of an anti-Stokes photon at frequency ω' which matches the energy difference between states $|g\rangle$ and $|s\rangle$, and which transfers one atom to state $|s\rangle$, as shown on figure 4.1[2]. The process involves a virtual level of energy $\hbar(\omega_3 + \Delta) = \hbar(\omega_1 + \omega) = \hbar(\omega_2 + \omega')$, where Δ is the frequency difference between the excited state $|e\rangle$ and this virtual level.

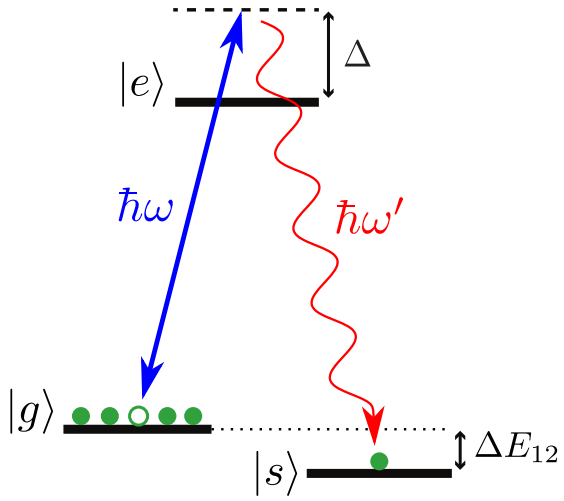

Figure 4.1: The absorption of a pump photon ω and emission of an anti-Stokes photon at frequency ω'. This operation transfers one atom from state $|g\rangle$ to $|s\rangle$.

The emission of a photon at frequency ω' can be strongly enhanced with stimulated emission: applying a strong driving field at this frequency results in *stimulated Raman scattering*.

Another form of scattering is *coherent anti-Stokes Raman scattering* (CARS), which corresponds to the simultaneous generation of a Stokes and anti-Stokes photons from two pump photons. As it involves four electromagnetic waves, the process is often dubbed *four-wave mixing* (FWM)[3].

[1] Photons with energies much larger than the ionisation energy lead to Compton scattering.

[2] In the case of state $|g\rangle$ lying energetically below $|s\rangle$, it is a less energetic Stokes photon that is emitted, verifying $\hbar\omega' = \hbar\omega - \Delta E_{12}$.

[3] The acronym for the process is sometimes written as *4WM*

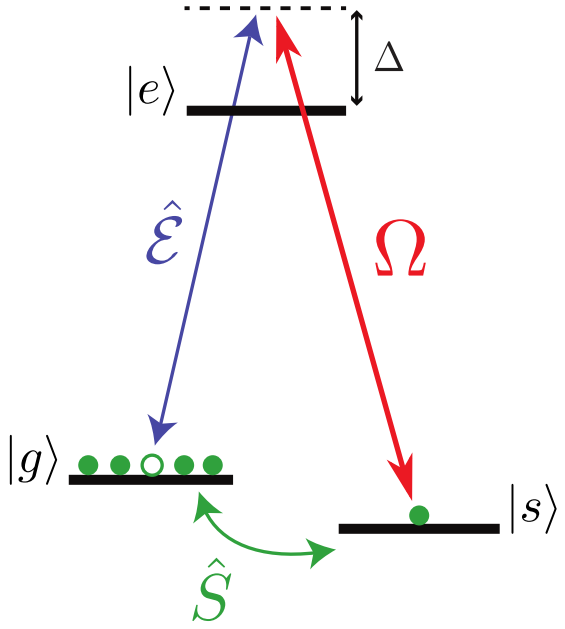

Figure 4.2: The signal $\hat{\mathcal{E}}$ detuned by Δ from the $|g\rangle \rightarrow |e\rangle$ transition is mapped to the spin-wave $\hat{S}$ between $|g\rangle$ and $|s\rangle$ by the two-photon resonant control Ω.

Spin wave The Raman scattering with the emission of an anti-Stokes photon leaves the atomic ensemble with a collective excitation: one of all the atoms from the ensemble has been transferred to state $|s\rangle$.

Raman memory scheme In the context of optical quantum memories, it is customary to define the light field to be stored as the *signal* and the auxiliary field stimulating the scattering as a *control* or *coupling* beam. The Raman memory scheme in Λ-type atoms consists of the absorption and subsequent retrieval of a signal detuned by Δ from the transition between ground state $|g\rangle$ and excited state $|e\rangle$, stored in a spin wave between states $|g\rangle$ and $|s\rangle$ (see figure 4.2).

Although the applicable theory of stimulated Raman scattering has been known for much longer [Raymer1985, Raymer1981], and similar equations were laid out during the first demonstration of a quantum memory [Kozhekin2000], I use as a reference the 2007 article series by Alexey Gorshkov, which is the most comprehensive in the analytical treatment of Λ-type atomic ensembles [Gorshkov2007a, Gorshkov2007b, Gorshkov2007c]. The thorough description of this type of system is aimed at the storage of light, which is especially relevant to our approach.

As a reminder of chapter 1.2, Λ-type three-level atoms are governed by the set of Maxwell-Bloch equations 1.5. On resonance, and additionally ignoring the Stark shift and dispersion terms, these equations simplify to:

$$\begin{cases} (\partial_t + c\partial_z)\,\hat{\mathcal{E}} = \mathrm{i}\sqrt{d}\,\dfrac{\Omega(t)}{\Delta}\,\hat{S}(z,t) \\ \partial_t \hat{S} = \mathrm{i}\sqrt{d}\,\Gamma\,\dfrac{\Omega(t)}{\Delta}\,\hat{\mathcal{E}}(z,t). \end{cases} \tag{4.1}$$

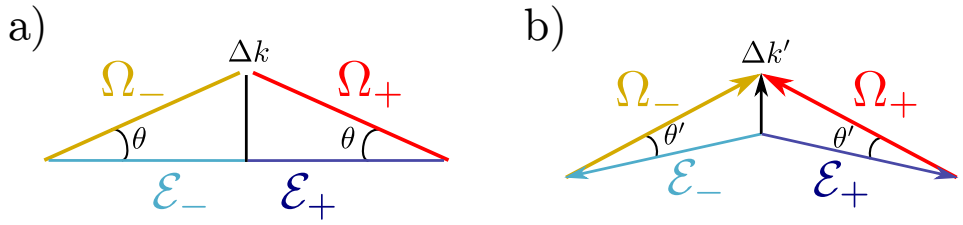

Figure 4.3: Symmetric configuration for backward-retrieval Raman memories: a) The spin-wave is orthogonal to the signal axis, as the angle θ between the signal and control matches their energy mismatch. The spin-wave displays a k-vector mismatch Δk. b) The spin-wave is not orthogonal to the signal axis. Consequently, the retrieved signal is not collinear with the input. Notice that the k-vector mismatch $\Delta k'$ is smaller than Δk in the previous configuration.

Efficient retrieval Upon retrieval, the choice can be made to retrieve the signal in the backward direction and indeed time-reversal of the absorption process in the memory medium implies re-emission in this direction [Moiseev2011]. To this end, the mirror image of the control beam needs to be applied. This backward-retrieval configuration enables fundamentally-higher conversion efficiencies to and from any memory based on three-level atoms than in the forward direction [Gorshkov2007b, Nunn2007, LeGouet2009], an argument I will now explain.

First, a necessary extension to the theoretical model is the introduction of the backward versions of the signal and control, noted with a minus subscript, and for clarity a plus subscript is added to the forward-propagating quantities. The propagation in the backward direction modifies the set of equations as follows:

$$\begin{cases} (\partial_t + c\partial_z)\,\hat{\mathcal{E}}_+ = +\mathrm{i}\sqrt{d}\,\dfrac{\Omega_+}{\Delta_-}\hat{S} \\ (\partial_t - c\partial_z)\,\hat{\mathcal{E}}_- = -\mathrm{i}\sqrt{d}\,\dfrac{\Omega_-}{\Delta_+}\hat{S} \\ \partial_t \hat{S} = \mathrm{i}\sqrt{d}\,\Gamma\left(\dfrac{\Omega_+}{\Delta_+}\hat{\mathcal{E}}_+ + \dfrac{\Omega_-}{\Delta_-}\hat{\mathcal{E}}_-\right). \end{cases} \tag{4.2}$$

The z and t dependence have been dropped for clarity. Note the minus sign of the left-hand side of the second equation, describing the propagation in the $-z$ direction. Most notably, the spin-wave, which can now be converted into either forward or backward light through the controls Ω_+ and Ω_-, is governed by the third equation.

As we want to perform backward retrieval, special care has to be taken of the phase matching of the storage-and-retrieval process, as previously shown in [Surmacz2008]. Choosing the storage state energetically below the initial state, enables the configuration depicted in figure 4.3(a), with an angle θ between each signal-and-control pair, in which the spin wave is orthogonal to the signal axis, which conveniently makes the input signal

and its read-out collinear. Figure 4.3(b) shows an alternative symmetric configuration where the signal and control make an angle $\theta' < \theta$ instead, which makes the effective k-vector mismatch smaller[4]. Only the control beams, not the signals, can be made collinear if the storage state lies energetically above the initial state.

Moreover, as pointed out in [Moiseev2011], the time-reversal of the storage process requires the detuning of the control beam to be inverted for read-out, *i.e.* $\Delta_+ = -\Delta_-$. As will be explained in the description of the experiment, with available light resonant on $|s\rangle \rightarrow |e\rangle$ transition, the forward and backward control can have opposite detuning by respectively picking the positive and negative orders of the AOM on each beam path.

4.1.2 Optimal shaping

With the main elements of a Raman memory having been introduced, we can further study the question of the retrieval direction. More specifically, we will see in the light of the optimal shaping (of the signal to be stored, or equivalently the spin wave which is subsequently recalled) and what considerations are raised by the configuration involving forward or backward retrieval.

The spatial and temporal profile of light emitted from an atomic ensemble has very specific properties which carry information of the ensemble. Conversely, signal light with various spatio-temporal shapes will couple differently to the atomic ensemble, and some will more efficiently map to collective excitations. The study of optimal shaping aims at determining the light field profiles which couple the most efficiently, and the corresponding spin wave shapes [Nunn2007].

Degrees of excitation of light and spin wave

Let us first describe formally the relevant efficiencies which correspond to the quantities the shaping process should optimise.

Considering a time-varying input field $\hat{\mathcal{E}}_{\text{in}}(t)$, it comprises a number of photons given by:

$$N_{\text{in}} = \int_{-\infty}^{\infty} \mathrm{d}t \left\langle \hat{\mathcal{E}}_{\text{in}}^{\dagger}(t)\hat{\mathcal{E}}_{\text{in}}(t) \right\rangle .$$

If the quantum properties of the signal are not relevant for the storage efficiency, we can consider the number of photons simply as the integrated squared norm of the field amplitude:

$$N_{\text{in}} = \int_{-\infty}^{\infty} \mathrm{d}t |\mathcal{E}_{\text{in}}(t)|^2.$$

In the case where no extra excitation can be produced by the process, the number of excitations in the spin wave N_S (in the atomic ensemble which ranges from 0 to L on the z-axis) and photons in the retrieved field N_r are the respective results of the storage and retrieval processes. These numbers are defined as:

[4] Note that equations 4.2 are only valid for collinear signal fields, *i.e.* the configuration shown in figure 4.3(b).

$$N_{\mathrm{s}} = \int_0^L \mathrm{d}z|S(z)|^2 \quad \text{and} \quad N_{\mathrm{r}} = \int_{-\infty}^{\infty} \mathrm{d}t|\mathcal{E}_{\mathrm{r}}(t)|^2.$$

The aim of an optical memory is to convert the excitation in the light in field $\hat{\mathcal{E}}_i$ into excitations of the spin wave $\hat{S}$, hence the storage and retrieval efficiencies are given as:

$$\eta_{\mathrm{s}} = \frac{\int_0^L \mathrm{d}z|S(z)|^2}{\int_{-\infty}^{\infty} \mathrm{d}t|\mathcal{E}_{\mathrm{in}}(t)|^2} \quad \text{and} \quad \eta_{\mathrm{r}} = \frac{\int_{-\infty}^{\infty} \mathrm{d}t|\mathcal{E}_{\mathrm{r}}(t)|^2}{\int_0^L \mathrm{d}z|S(z)|^2}.$$

and an overall storage-and-retrieval efficiency simply as the product $\eta = \eta_{\mathrm{s}}\eta_{\mathrm{r}}$.

As a quantum memory needs to be a linear operation of its inputs, it implies that the mapping to and from a spin-wave are linear maps. Therefore, the spin-wave can be written:

$$S(z) = \int_{-\infty}^{\infty} \mathrm{d}tK(z,t)\hat{\mathcal{E}}_{\mathrm{in}}(t),$$

where K is the Green's function of the mapping from the input signal to the spin wave. The properties of K depend on the interaction process between the light and the atoms. The optimisation to maximise the storage efficiency η_s can therefore be made with a focus on the Green's function.

Linear algebra provides us powerful tools to delve into the inner workings of mappings, which is especially useful in the context of finding the best-case-scenario performance of a quantum memory as versatile as a large-bandwidth Raman memory. Not only can an algebraic analysis of the spin-wave conversion tell us its highest achievable efficiency, it can also indicate the pulse shape enabling this optimum, and is therefore of considerable experimental usefulness. Let us first define the Singular Value Decomposition which is the relevant mathematical tool at our disposal in this case.

Singular Value Decomposition

The Singular Value Decomposition consists of the decomposition of any matrix M as the following:

$$M = UDV^{\dagger},$$

where U and V are unitary matrices, and D is a diagonal matrix with non-negative real numbers on the diagonal. The 2D case can be visualised as shown in figure 4.4.

The spectral decomposition and SVD are the same for a Hermitian matrix, but the second technique is more general: M and D can be rectangular, in which case U and V have the appropriate dimension. Let us assume in the following that M describes a map from $\mathbb{C}^n$ to $\mathbb{C}^m$, with $n \leq m$.

Conventionally, the numbers on the diagonal of D, are not called eigenvalues but singular values, noted s_i and they are ordered: $s_1 \geq s_2 \geq \ldots \geq s_n \geq 0$. The other terms of D,$\{s_{ij}\}_{i\neq j}$ are zero. In particular when D is rectangular, the additional rows or columns are empty.

In the decomposition basis, obtained by the transformation of the input by U, an

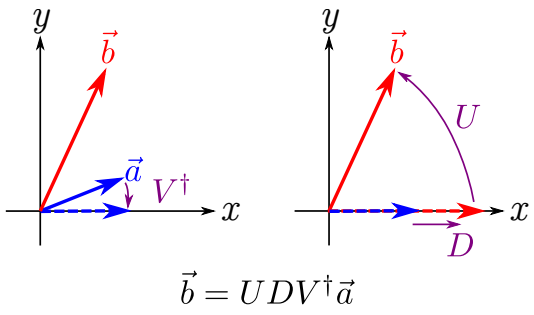

Figure 4.4: Singular Value Decomposition: a matrix M addressing the vector $\vec{a}$ to $\vec{b}$ can be visualised in 2D as a rotation $V^\dagger$ onto the x-axis, followed by a rescaling D and a rotation U onto the axis of vector $\vec{b}$. The SVD theorem states that these two rotations and the rescaling can be found for any linear mapping described by M, in any dimension.

input vector $\vec{a}$ can be decomposed as

$$\vec{a} = \begin{bmatrix} a_1 \\ a_2 \\ \vdots \\ a_n \end{bmatrix}$$

It follows that when the matrix M is applied to a unitary vector $\vec{a}$ $\left(\|\vec{a}\| = \sum_{i=1}^{n} |a_i|^2 = 1\right)$, then the norm of $\vec{b} = M\vec{a}$ satisfies:

$$\left\|\vec{b}\right\|^2 = \sum_{i=1}^{m} |b_i|^2 = \sum_{i=1}^{n} s_i^2 |a_i|^2.$$

Because s_1 is the largest singular value, we have:

$$\begin{aligned} \left\|\vec{b}\right\|^2 &\leq |s_1|^2 \sum_{i=1}^{n} |a_i|^2 \\ &\leq |s_1|^2. \end{aligned}$$

Therefore, characterising the largest singular value s_1 indicates the maximum efficiency achievable by the mapping M, which corresponds to the storage and/or retrieval process[5].

SVD is performed on matrices, i.e. in finite dimension, whereas the usual equations involved in the description of Raman memories are continuous. We need to discretise the temporal and spatial domains of the signal pulse shape and spin wave, respectively, to generate a matrix that can be decomposed using this method. A fine enough grid

[5] The interested reader can refer to [Wasilewski2006] for a detailed theoretical analysis of SVD applied to stimulated Raman scattering, leading to two-mode squeezed state generation.

correctly describes the behaviour of the system, which is usually verified numerically where some convergence of the optimum with the grid size is observed. The Green's function K that we previously described is what we decompose according to the SVD.

Note that the Schmidt decomposition many physicists are familiar with is a special type of SVD.

Numerical model

Starting from the Maxwell-Bloch equations introduced in 1.2, we can move to the co-moving frame, defining a local time $t' = t - z/c$, and introduce dimensionless parameters:

- We change the spatial variable z to the dimensionless $\tilde{z} = \int_0^z dz' n(z')/N$. In the case of a uniform linear density, we have $n(z) = N/L$, which is equivalent to $\tilde{z} = z/L$. The latter form shows more explicitly that the interaction length corresponds to $\tilde{z}$ between 0 and 1.
- We define the dimensionless time $\tilde{t} = \gamma t'$, which reduces all the quantities expressed in terms of frequency: $\tilde{\gamma}_{\mathrm{S}} = \gamma_{\mathrm{S}}/\Gamma$, $\tilde{\Delta} = \Delta/\Gamma$, $\tilde{\Omega} = \Omega/\Gamma$.

Following these notations, the Maxwell-Bloch equations are reduced to:

$$\begin{cases} \partial_{\tilde{z}}\hat{\mathcal{E}} = \mathrm{i}g\sqrt{d}\,\hat{P} \\ \partial_{\tilde{t}}\hat{P} = -\mathrm{i}(1+\mathrm{i}\tilde{\Delta})\hat{P} + \mathrm{i}\sqrt{d}\,\hat{\mathcal{E}} + \mathrm{i}\tilde{\Omega}\hat{S} \\ \partial_{\tilde{t}}\hat{S} = -\tilde{\gamma}_S\hat{S} + \mathrm{i}\tilde{\Omega}^*\hat{P}. \end{cases}$$

The above assumptions on the system simplifies the general Maxwell-Bloch equations in order to obtain a computionally-tractable numerical model or a solvable eigenvalue equation.

Finding the optimum

Largest singular value The optimal solution consists of choosing an input $A_{\mathrm{in}}(t)$ as the right singular function $\phi_1(t)$ associated with the largest singular value of K, λ_1. In the case of a Raman memory with detuning Δ, excited state width Γ and control Rabi frequency $\Omega(t)$, we can define the integrated Rabi frequency:

$$\omega(t) = \int_{-\infty}^{t} \mathrm{d}t' \left|\Omega(t')\right|^2,$$

$$\text{and } W = \omega(\infty) = \int_{-\infty}^{\infty} \mathrm{d}t' \left|\Omega(t')\right|^2,$$

and the coupling parameter C:

$$C = \frac{\sqrt{d\Gamma W}}{|\Gamma + \mathrm{i}\Delta|}.$$

The right singular function ϕ_1 is defined as [Surmacz2008]:

$$\phi_1(t) = \exp\left[\mathrm{i}\omega(t)\Delta/\left|\Gamma + \mathrm{i}\Delta\right|^2\right]\Omega(t)\Phi_1\left[C\left(1 - \frac{\omega(t)}{W}\right)\right], \tag{4.3}$$

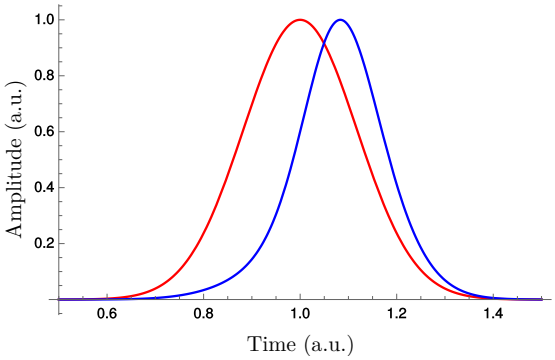

Figure 4.5: The optimal signal shape (in blue) for forward-retrieval of a given Gaussian-shaped control (red). The simulation parameters are $d = 100$, $\tilde{\Delta} = 20$, $\Delta\tau_s \approx 0.42\Gamma^{-1}$. The largest singular value is found to be 35% and the control $1/e^2$-width $\approx 0.97\Gamma^{-1}$.

where Φ_1 is the right singular function associated with the largest singular value of the kernel $\tilde{K}$, which is equivalent to K, previously defined, up to a unitary transform:

$$\tilde{K}(y, y') = \int_0^C \mathrm{d}x\, k(y, x)k(x, y),$$

$$\text{with } k(x, y) = e^{-\sin(\beta)(x/R+Ry)} J_0\left(2e^{\mathrm{i}\beta}\sqrt{xy}\right),$$

with $R = \sqrt{W/(d\Gamma)}$ and $\beta = \pi/2 - \arg(\Gamma + \mathrm{i}\Delta) = \Gamma/\Delta + \mathcal{O}\left[(\Gamma/\Delta)^3\right]$ for large detuning $\Delta \gg \Gamma$.

$\tilde{K}$ and k are defined on $[0, C]^2$. We can sample these intervals in order to find numerically the singular values associated with $\tilde{K}$. We take $N + 1$ samples of $[0, C]$, valued $\{y_j\}_{j\in\{0..N\}} = \{C.j/N)\}_{j\in\{0..N\}}$ and define the matrix $\mathcal{K}$ from elements $\mathcal{K}_{ij} = \tilde{K}(y_i, y_j)$. There are powerful tools to numerically perform the SVD of matrix $\mathcal{K}$, for example in Mathematica. They provide in particular the largest singular value λ_1 that we can link to the optimal storage-and-retrieval efficiency, as well as the right singular function Φ_1 to which it is associated. Equation 4.3 finally provides the optimal signal pulse shape ϕ_1. This has been performed numerically with the script presented in the appendix of this thesis, in order to find the optimal signal shape for a given Gaussian-shaped control (figure 4.5).

Numerical iterations To converge to the optimal spin wave shape, we can rely on the fact that the read-out process will favour the shape associated with the largest singular value associated with the mapping between the spin wave and the output field, *i.e.* the highest retrieval efficiency.

The optimal spin wave shape is the eigenvector associated with the largest eigenvalue of the problem [Gorshkov2007b]:

$$\eta_r S(z) = \int_0^L \mathrm{d}z' k_r(z, z')S(z'),$$

where $k_{\mathrm{r}}(z, z')$ is the kernel associated to the retrieval process, obtained from the experimental parameters.

By renormalising the spin-wave obtained by computing the right-hand side of this equation with a test spin-wave $S_1(z)$, we obtain a spin-wave $S_2(z)$, etc. Performing this protocol many times converges to the optimal spin wave S_d enabling maximum retrieval efficiency. The index d denotes that this optimal spin wave shape depends only on the OD.

This is especially heuristic when comparing the forward and backward retrieval schemes of a Raman memory, which possess different pairs of kernel functions for storage and retrieval.

Optimisation results

The analyses were made both in the case of a known control field profile (which can represent, for example, the constraint of limited control power) [Nunn2007] and with known signal fields, what would be the optimal control shape and power [Gorshkov2007], enabling optimisation in both situations. A variant of this optimisation with gradient ascent is described in [Gorshkov2008].

The experiment in [Novikova2007] performs the optimisation steps of storage in an EIT memory with an arbitrary control field profile. Starting with a test signal Gaussian profile, the procedure successfully minimises the leakage at the write-in stage and maximises the retrieved pulse area, matching the theoretical prediction with the numerical optimisation previously described.

Now that we have seen how to access optimal signal and spin wave shapes depending on the memory dynamics, in the next section, we focus on the role of the retrieval direction which drastically affects the optimal shape, as well as the phase-matching conditions.

4.1.3 Backward and forward retrieval configurations

It was studied in detail in [Gorshkov2007b] how large OD is always beneficial to reach higher conversion efficiency. It was also found that, even at large ODs, the asymptotic scaling of storage and retrieval efficiencies, as well as the optimal spin wave shape, greatly differ whether the forward or backward signal retrieval is performed, as shown in figure 4.6. Indeed, the spin wave optimised for backward retrieval is linear, which optimises both the storage with a signal from one direction and its recall in the opposite direction, whereas the optimal spin wave for forward retrieval compromises between the two processes. This is in contrast with the idea that one can get away with careful shaping and strong coupling provided they have a large enough OD.

Moreover, the optimal mode shapes can also be associated with very strong control powers in forward retrieval, which is non-ideal for inhomogeneous broadening and noise considerations [Nunn2007], and are also arguably less convenient and possibly harder to generate as they are spatially more complex than in the backward retrieval case. Phase matching is known to determine the direction of the re-emitted signal [Braje2004] and has also been shown to impose, more specifically for the applications of quantum memories, a limitation on the achievable forward-retrieval efficiency [Surmacz2008].

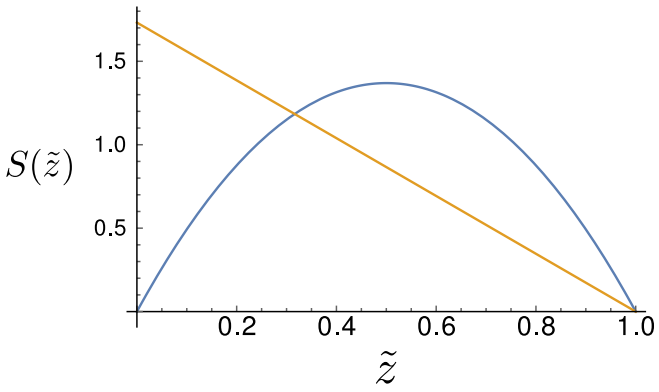

Figure 4.6: Optimal spin wave shapes $S(\tilde{z})$ for forward retrieval (blue) and backward retrieval (orange), from the solutions computed in [Gorshkov2007b], for Λ-type atoms with degenerate ground states, in the limit of infinite optical depth. $\tilde{z}$ is a dimensionless distance through the atomic medium and the signal is assumed to be stored from propagating to the positive $\tilde{z}$. The spin wave optimised for backward retrieval corresponds to linearly absorbed light during storage from left to right, which becomes a linearly amplified from right to left. On the other hand, the spin wave optimised for forward retrieval is a parabola which is a compromise between a spin wave optimised for storage (which is the backward-optimised shape) and the one for forward retrieval (the symmetric of that shape).

Another aspect is that in the case of non-degenerate ground and storage states, which is the usual case when two hyperfine states are used as the long-lived ground states, the backward-retrieval Raman memory scheme suffers from imperfect phase-matching, arising from the differentiated propagation inside the medium [Nunn2007].

From a practical point of view, the control power can be a limited resource, especially in large-detuning experiments, and it usually cannot be afforded to split it between the two beams involved in backward retrieval. A control beam forming an angle with the signal axis also needs to be wider in order to overlap with the signal along the atomic ensemble: the effective control intensity is decreased compared to a collinear configuration.

Last, the angle between the signal and control in each pair, and the counter-propagating geometry of the two pairs, both introduce Doppler broadening which can become prohibitive in warm-vapour experiments.

With these considerations and, to our knowledge so far, the absence of reported experiments demonstrating a Raman memory with backward-retrieval, we decided to conduct one in the cold atom experiment at ANU.

4.2 Experimental Raman memory

Now that we have seen the relevant theoretical background behind Raman memories, and understood the advantages of a backward-retrieval scheme, I will introduce the experiment performed at ANU of a versatile backward-Raman memory.

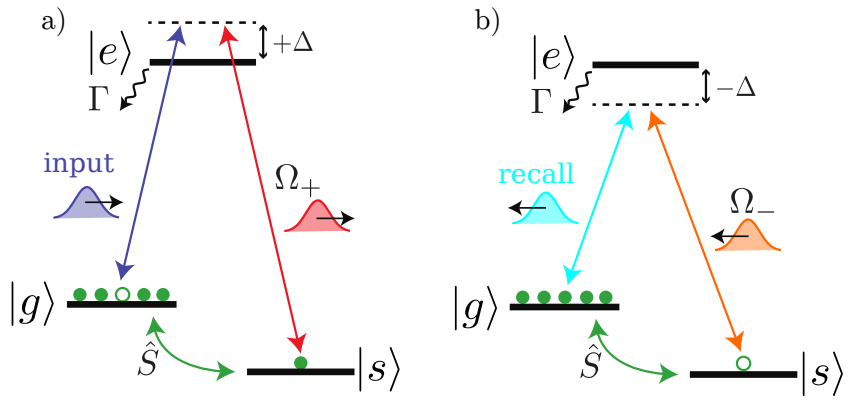

Figure 4.7: a) A signal $\mathcal{E}_+$ traverses an elongated atomic cloud where a two-photon resonant control beam Ω_+ converts it to a collective atomic excitation. b) A backward-propagating control beam Ω_- subsequently retrieves the signal in the backward direction, as $\mathcal{E}_-$.

4.2.1 Experimental setup

Atomic ensemble preparation

An elongated cloud of rubidium 87 atoms is prepared using the 2D-Magneto-Optical Trap configuration described in 2.3.4. The atomic level scheme is shown in figure 4.7. The initial state in which we pump the atoms is $|g\rangle = \left|5S_{1/2}, F = 2, m_F = +2\right\rangle$. This is conveniently the Zeeman edge state of the $F = 2$ hyperfine ground state, enabling near-perfect optical pumping with a σ_+-polarised beam. The optical pumping beam is produced by the same diode laser as the optical trapping and has the same frequency. It has an intensity of $0.7\,\mathrm{mW\,cm^{-2}}$ and is applied with a 0.5 G bias magnetic field to define a quantisation axis and slightly lift the Zeeman-sublevel degeneracy. The storage state can be chosen as $|s\rangle = \left|5S_{1/2}, F = 1, m_F = 0\right\rangle$, which is the magnetically-insensitive Zeeman sub-level of the hyperfine level $F = 1$, with $\Delta m_F = -2$ from state $|g\rangle$, therefore addressed by the two-photon Raman transition of orthogonal circularly-polarised beams, which enables polarisation filtering. The excited state is taken on the D_1-line as $|e\rangle = \left|5P_{1/2}, F' = 1\right\rangle$.

Signal and control beams

The layout of the experiment is diagrammatically shown in figure 4.8. The signal, denoted $\mathcal{E}_+$, is blue-detuned by 230 MHz from the $|g\rangle \rightarrow |e\rangle$ transition. A forward-propagating control, denoted by its Rabi frequency Ω_+ and equally detuned from $|s\rangle \rightarrow |e\rangle$, forms an angle of about 6 mrad with the signal. The forward control maps the signal onto a spin-wave between the states $|g\rangle$ and $|s\rangle$. A symmetrically(red)-detuned control of Rabi frequency Ω_- is a mirror image of Ω_+. Ω_- addresses the spin-wave and couples it to the 230-MHz-red-detuned signal, noted $\mathcal{E}_-$, which is the counter-propagating version of $\mathcal{E}_+$ in the same spatial mode.

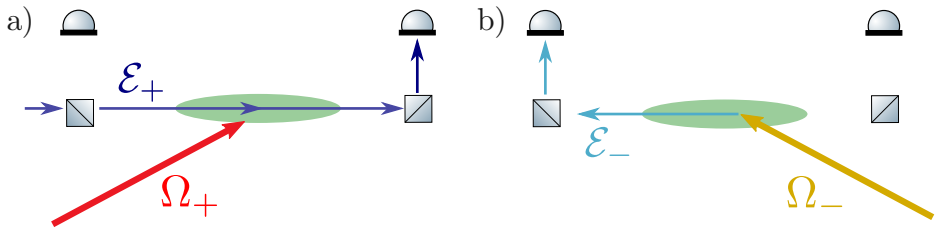

Figure 4.8: Configuration of the signal and control beams: a) The forward-propagating signal $\mathcal{E}_+$ and forward control beam Ω_+ form an angle of 6 mrad. As a result, the spin-wave wave vector is orthogonal to the signal axis. b) The backward control Ω_- and retrieved signal $\mathcal{E}_-$ are mirror images of Ω_+ and $\mathcal{E}_+$, which ensures a symmetry between the storage and retrieval processes. Detectors are placed after beam-splitters in the forward and backward directions from the atoms to monitor a $\mathcal{E}_+$ signal without the atoms, leakage and retrieval in any direction.

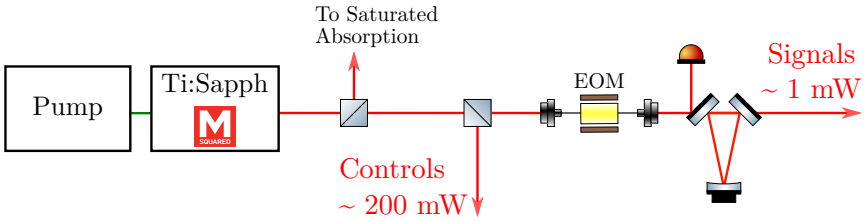

Figure 4.9: D_1-light layout: The titanium-sapphire laser is frequency-locked on a saturated absorption channel (not depicted), and divided into control and signal channels. The signal channel goes through a fibre-EOM and the +6.8 GHz side-band is separated from the carrier on a ring cavity.

Laser light source

Reference light on the rubidium-87 D_1 line (around 795 nm) is provided by a MSquared SolsTiS titanium-sapphire laser, frequency-locked to the saturated absorption on the $|s\rangle \rightarrow |e\rangle$ transition. As described in the layout 4.9, about 200 mW is injected into a fibre brought to the MOT table for the generation of the forward and backward control beams. This setup enables a relatively stable relative phase between the control beams, whereas two independent fibres would have been more prone to phase shifts due to mechanical vibrations.

Light resonant with the $|g\rangle \rightarrow |e\rangle$ transition for signals is obtained from filtering out the +6.8 GHz side-band of an EOM-phase-modulated beam on a ring cavity with finesse $F = 100$. We are limited in producing signal light by the power the fibre-EOM can handle, which on the order of a couple of milliwatts. AOMs are used to shape the forward and backward signal beams, which are fibre-coupled and injected in the experiment on the two ends of the MOT table. For this experiment, the signal sent for

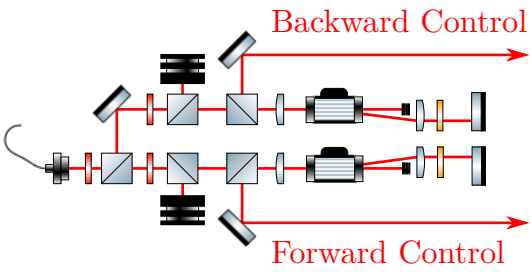

Figure 4.10: Forward and backward control beam powers are distributed on two channels and independently controlled. AOMs provide spectro-temporal shaping of the control pulses. Opposite diffraction orders are chosen and ensure symmetrical detuning relative to excited level $|e\rangle$.

storage was chosen as a coherent beam with a mean photon number $|\alpha|^2 \sim 10^6$.

More details on the signal generation from cavity filtering can be found in the theses of previous students [Hosseini2012PhD, Sparkes2013PhD].

Forward and backward pairs The configuration depicted in figure 4.10 shows how optical power was divided between the two beams, and individually controlled. This provided around 100 mW of total available control power. A similar configuration is adopted to generate forward and backward signals, which was central to the TRACE scheme developed in section 5.4 but also significantly helped the alignment procedure of the Raman memory, as we will see.

Choice of the one-photon detuning The detuning of the signal and control beams to state $|e\rangle$ was initially chosen to be 160 MHz, upon availability of AOMs with a centre frequency at 80 MHz[6], but it was found that, for example, at a typical OD of 500, incoherent absorption accounts for more than 11%. This absorption is experimentally verified by comparing the forward detector signal without control, with and without atoms. As memory efficiencies around 70% were eventually achieved, this absorption not contributing to the memory process was an unfortunate limitation. The AOMs were swapped to a model with a higher centre frequency and the detuning was increased to 230 MHz, the highest frequency at which our arbitrary waveform generator could sample sine-modulated Gaussian pulses for the signal and control AOMs. At 230 MHz and the same OD, incoherent absorption is predicted to be reduced to less than 6%. The only trade-off was the control beam intensity which needed to be increased to keep the same Raman coupling, which scales as Ω/Δ. This would have been an impediment for operation at the single-photon level, as our filtering capability is limited. However, it was not a drawback considering the available control power and the storage of bright pulses.

[6] enabling detunings equal to twice this frequency in the double-pass configuration.

Pulse shaping and filtering A Gaussian-shaped signal pulse with a full width at half-maximum (FWHM) of 2 µs is coherently mapped onto the atomic ensemble and subsequently recalled in the backward direction with a pair of forward and backward Gaussian-shaped control pulses. The width, delay and intensity of the co-propagating control pulse for storage is optimised to minimise the leakage of signal light through the atoms. The retrieval control pulse, counter-propagating, is given the same shape as the optimal storage pulse, which is found numerically and experimentally to be a Gaussian pulse with a FWHM around 3 µs. The intensity of the backward control is optimised on the amount of retrieved signal. Polarisation filtering is achieved on a Glan-Taylor prism, with an isolation of 30 dB and spatial filtering on a 150-µm pin-hole in the focal point of telescope formed by two 150-mm lenses give a 90% transmission of the signal and 15 dB of additional isolation from the control. Moreover, after crossing the atomic ensemble, each of the control beams is sent to a photodiode and their residual leakage onto the signal detectors is subtracted.

Optical depth and Rabi frequency calibration We need to find the relation between the optical power measured on each control beam path and the Rabi frequency involved in the Raman memory dynamics. This correspondence is obtained from the frequency scanning of the Raman lines. Optical pumping to $m_F = +2$ is skipped in the atomic preparation sequence, enabling the Raman line absorption from an additional m_F state, namely $\left|5S_{1/2}, F = 2, m_F = +1\right\rangle$, addressed to $\left|5S_{1/2}, F = 1, m_F = -1\right\rangle$. A probe pulse, whose frequency is swept during the 400 µs of its duration, is sent simultaneously with a control beam at fixed frequency. The intensity of the control, and thereby its Rabi frequency, is varied across acquisitions. This results in absorption lines on the $m_F = +2, +1$ states with a depth relative to the Rabi frequency of the control. Additionally, the relative Stark frequency shift of each line depends on the square of the Rabi frequency, which enables an independent calibration of the OD, on one hand, and the Rabi frequency as experienced by the atoms in $|g\rangle$ as a function of the control beam power, on the other hand.

Alignment procedure An avalanche photodiode (Thorlabs APD120A) is placed after the atomic ensembles to calibrate the energy of the input signal and the portion that leaks through. A portion of the signal is injected into a single-mode fibre and the coupling efficiency is optimised to match the spatial mode of the fibre to the one of the signal. A reference beam is subsequently sent through this fibre in the backward direction. The path to the backward detector is aligned onto this reference beam and a collection lens ensures a wide enough detection plateau. Losses through all the optics from the atomic ensemble to forward and backward detectors are carefully characterised in order to calibrate the quantum efficiencies of the detectors. The losses on the forward and backward channels are estimated to $(50 \pm 10)\,\%$ and the ratio forward/backward of the overall detection efficiencies is found to be 1.2 ± 0.1. Measured photodiode signals are scaled accordingly. I believe the difficulty of calibrating the pair of forward and backward detectors which come after different optical paths from the atomic ensemble is definitely a reason why the backward-recall scheme is not very popular in the implementations of Raman memories.

4.2.2 High-efficiency memory

The memory efficiency is defined as the ratio between the integration of the retrieved signal on the backward detector and the signal without atoms on the forward detector, corrected for the detection losses and sensitivities.

The highest reproducible memory efficiency after a storage time of one pulse width is found to be $(65 \pm 6)\%$. The large uncertainty is owed to the imperfections of measuring the optical losses on the two different detection paths. This figure more than doubles the previous recorded efficiency of 30% for an optical Raman memory and also outperforms the maximum achievable efficiency of 54% with Controlled-Reversed Inhomogeneous Broadening with forward retrieval [Sangouard2007, Longdell2008]. The amount of four-wave mixing gain is estimated to be low enough to be ignored at this detuning value.
In the conducted experiment, the signal can be incoherently absorbed by the excited level, which fundamentally limits the memory efficiency. Previous Raman memory experiments, such as the ones performed in Walmsley's group in Oxford, mitigate this incoherent absorption by operating at very large detuning.

4.2.3 Memory lifetime

The storage duration is determined by the delay of the read-out control beam, which can be controlled at will. The memory efficiency is measured after different storage duration, shown in figure 4.11. The memory efficiency over time is fitted as the product of exponential and Gaussian decay functions, found to have the characteristic times $\tau_{\text{exp}} = 190\,\mu\text{s}$ and $\tau_{\text{gaussian}} = 120\,\mu\text{s}$, respectively linked to the magnetic biasing inhomogeneities and the motional dephasing of the atoms. An alternative analysis is based on the model described in [Jenkins2012], which yields a dephasing time $\tau_D = 110\,\mu\text{s}$ and a transit time $\tau_T = 170\,\mu\text{s}$. These analyses suggest that the thermal motion of the atoms is the limiting factor to the memory lifetime.

4.2.4 Delay-bandwidth product

We have employed the same protocol for the storage of shorter pulses, demonstrating large delay-bandwidth products with little compromise on the efficiency. To maintain a comparable efficiency, the control beams intensity had to be increased for shorter signal pulse widths and the memory was eventually limited by the available laser power, as well as the optical depth of the ensemble.

The highest delay-bandwidth product of 160 was obtained with a signal of 360-ns $1/e^2$-width, for which the measured characteristic decay time was $\tau = 60\,\mu\text{s}$. A storage efficiency after one pulse-width was limited to 40%, as the memory process was much less efficient with such a short pulse, with the amount of available OD and control power.

Figure 4.12 shows the reference experimental photodiode signal for the pulse to be stored in the memory, and the signals for recalls at times $t_1 = 1.5\,\mu\text{s}$ and $t_2 = 41\,\mu\text{s}$.

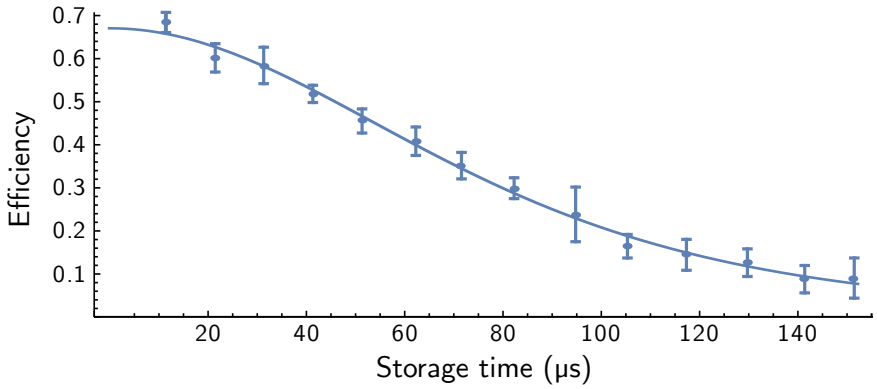

Figure 4.11: Decay of the memory efficiency with storage time. The error bars correspond to the standard deviation. The efficiency is fitted to a decoherence model, with dephasing and transit times $\tau_D = 110\,\mu s$ and $\tau_T = 170\,\mu s$. The storage-and-retrieval efficiency at the origin is $\eta_0 = (69 \pm 6)\%$.

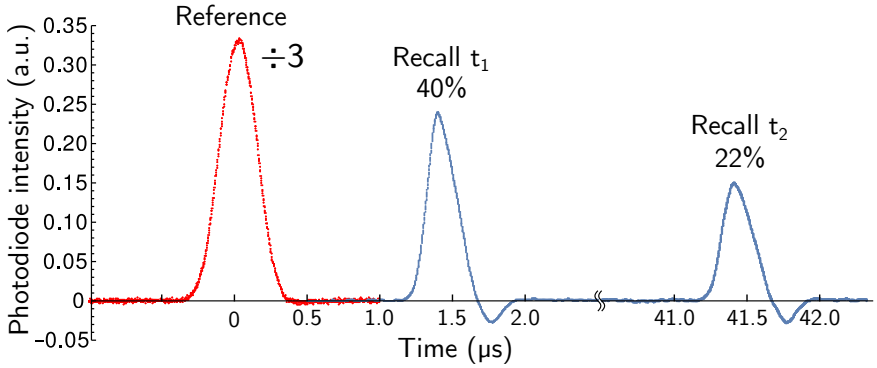

Figure 4.12: Storage and recall of a 360-ns $1/e^2$-width signal. Photodiode signals for reference (in red, scaled down) and recalls at times $t_1 = 1.5\,\mu s$ and $t_2 = 41\,\mu s$ (blue) are shown, with their storage-and-retrieval efficiency. The decay of the memory efficiency corresponds to a delay-bandwidth product of 160. The photodiode signal going negative is an artefact of the photodiode with signal durations close to its bandwidth limit.

For comparison, delay-bandwidth products of the order of 10^4 have been demonstrated in cold atomic ensembles [Bao2012] although from the creation of a spin-wave with a write pulse, not the storage of an input signal, and [Dudin2013] where the memory decay time has been extended on the minute scale, but the storage efficiency is limited around 14%. The drawbacks in these two realisations set the context for our simultaneous realisation of a modest delay-bandwidth product also at a relatively high efficiency.

4.2.5 Dynamically-reprogrammable beam-splitting

The memory can be used as dynamically-reprogrammable array of beam-splitters, an application first demonstrated in Raman memories in [Reim2012] and depicted in figure 4.13. This operation finds many uses in the context of quantum information processing. For example, a weak control beam has a low probability of reading-out the memory, however the beam-splitter operation can be repeated many times until one output photon is detected: this leads to the photon subtraction of the stored state which is available for efficient recall at a subsequent time with now a strong control beam.

This scheme has been shown to enable a doubly-exponential enhancement on the scaling of continuous-variable entanglement distillation [Datta2012]. This beam-splitting operation enables interference between the memory read-out and another input sent simultaneously [Campbell2012]. This is of course reminiscent of a cavity where “fresh” light is sent after a integer number of round-trips inside the cavity: this is the effect that has been investigated in [Pinel2015]. This study of polariton interference has led to the development of the TRACE memory, described in section 5.4.

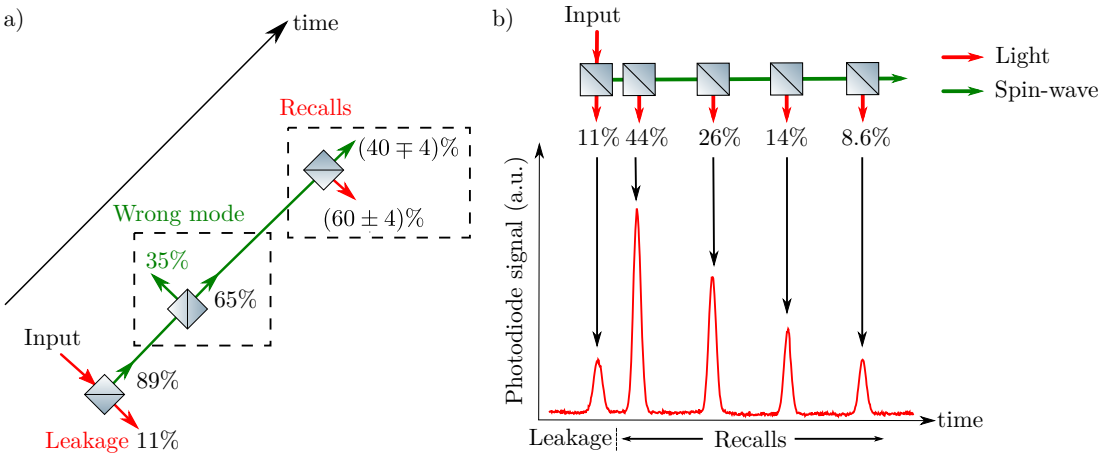

Figure 4.13: a) Schematic of an beam-splitter array equivalent to the Raman memory read with a series of weak control pulses. The percentages represent the losses and conversion efficiencies at different stages. First a fraction of the input light leaks from the atomic ensemble and is not addressed to a collective atomic excitation. Second, some of the absorbed light is not mode-matched to be efficiently recalled. It is estimated at roughly 35% in this short-pulse configuration. Then, at the given control beam intensity, each retrieval pulse extracts only about $60 \pm 4\%$ of the stored spin wave, the remainder is left for a subsequent retrieval step. The memory decay between retrievals is ignored at this time scale. b) Experimental photodiode signal for the subsequently-retrieved pulses and correspond beam-splitter array with the fractions of the total signal intensity.

4.3 Discussion of the results

4.3.1 Backward-retrieval geometry

Phase-matching between the spin-wave and the optical fields is known to determine the direction of the retrieved signal [Braje2004] and has also been shown to impose a limit on the achievable efficiency of memories in forward- and backward-retrieval configurations [Surmacz2008]. The memory efficiency benefits from the backward-retrieval geometry of our realisation, as it more than doubles the record storage-and-recall efficiency for a Raman memory [Reim2011].

Few experiments employ elements of a symmetrical geometry in Raman systems, although this symmetry is found to enhance the conversion of light to spin-waves. To our knowledge, however, our realisation is the first Raman memory with backward retrieval. This demonstration has enabled the experimental verification of the predicted contrast with its forward-retrieval variant and the improvement on the memory performance in a backward-retrieval geometry.

4.3.2 Outlook for this Raman memory realisation

We can argue that with Gaussian pulses only and the limited amount of control power we have ($\approx 100\,\mathrm{mW}$ with a waist of $250\,\mu\mathrm{m}$), there could be other limitations to the maximum achievable efficiency, not taking into account the decrease in efficiency due to incoherent absorption. We are aware that this procedure generated unavoidable noise on our detectors, which prevents us from demonstrating the quantum operation of our system. The improvement of the filtering stages could enable the operation at the single-photon level, or with heralded single photons generated from the spontaneous down-conversion source developed at the University of Queensland, developed by Markus Rambach and Till Weinhold, reported in [Rambach2016] and brought to the ANU to experiment with the storage of single photons.

The memory lifetime is limited by atomic motion, which has been predicted as a main limitation on backward-retrieval Raman experiments, blurring the spin wave [Tikhonov2015, Surmacz2008]. Further optimisation of the cooling sequence with the machine-learning algorithm is expected to decrease the temperature of the atoms. In parallel, the redesign of the biasing coils should enhance the uniformity of the magnetic field environment. I have additionally designed voltage-controlled current sources which enable the dynamical control over the current for the cancellation of the ambient magnetic field when no bias is applied. These extra steps are expected to decrease the temperature of the atoms to a few tens of µK and removing limitations caused by an imperfect magnetic environment, which should consequently extend the memory lifetime by an order of magnitude.

Chapter Conclusion

This chapter has been focused on the off-resonant Raman memory:

- We have explored — theoretically and experimentally — retrieval from a Raman memory in the forward and backward directions.
- Our realisation of a Raman memory was the first reported one with backward retrieval. This retrieval direction, symmetrical to the storage, is known to improve its efficiency.
- Our memory implementation showed a storage-and-retrieval efficiency of $65 \pm 5\%$, setting it as the first Raman memory with an efficiency above the no-cloning limit of 50%.
- We also employed the memory with shorter pulses of 360-ns-width and demonstrated a delay-bandwidth product of 160.
- With weak recall control pulses, we used the memory as a dynamically-reprogrammable array of beam-splitters.

Chapter 5

Spin-wave interference for stationary light and memory enhancement

The memory schemes that were discussed until now store signal light in a stopped form: it is converted into collective atomic excitations, it does not subsist as light *per se*. An alternative form of light is *stationary light* (SL), which is light with a vanishing group velocity. SL has been proposed in the early 2000's, followed by a few numerical simulations and only a handful of experimental realisations. We had in mind to investigate it at ANU, after the realisation of the spin wave resonator [Pinel2015] with which it shares a few concepts which are detailed in this chapter. In early 2015 after exchanging with Darrick Chang, visiting at LKB, we also started collaborating with Anders Sørensen on the theoretical study of SL. Their approach is documented in Ivan Iakoupov's PhD thesis [Iakoupov2016PhD].

A landmark achievement during this PhD was the study of the dynamics leading to the generation of SL. This work led to the publication in Nature Physics [Everett2017]. Following this first study, we then implemented the TRACE memory, a novel memory scheme closely related to SL, as well as the backward-retrieval Raman memory of the previous chapter. This new memory scheme exploits the constructive interference between spin waves stored from counter-propagating signal-and-control pairs. An article covering the theoretical aspects of the TRACE memory and its experimental proof-of-concept has been published in Physical Review A [Everett2018].

5.1 Stationary light history and formalism

The approach to SL has evolved a great deal since it was first conceived. It was first mentioned in [Andre2002], in the context of EIT with the addition of a standing wave, creating a "photonic band gap" in which light propagation is forbidden. Light within this band gap would be made stationary, and unlike traditional EIT, with non-vanishing photonic component.

Early proposals justified the phenomenon as Bragg reflections off periodically spaced absorption peaks, a representation that was later proved not to be correct. The study in [Bajcsy2003] displayed a misleading schematic illustration of the spatial variation of the signal absorption throughout the atomic ensemble, and [Andre2005] stated "the signal light cannot propagate in the medium due to Bragg reflections off the sharp absorption peaks, resulting in vanishing group velocity of the signal pulse".

The key to understanding more accurately SL dynamics stemmed from [Moiseev2006]

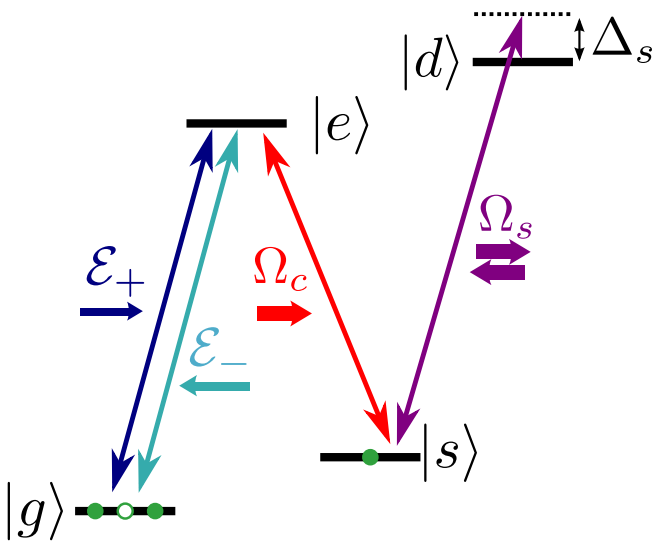

Figure 5.1: $|g\rangle$, $|s\rangle$ and $|e\rangle$ form a three-level EIT system, with signal $\mathcal{E}_+$ and control of Rabi frequency Ω_c. The standing wave of Rabi frequency Ω_s, off-resonant from state $|d\rangle$, induces a spatially-modulated refraction index, which generates Bragg scattering into the backward signal $\mathcal{E}_-$.

which extended SL to a Raman system. Moreover it introduces a two-colour variant, *i.e.* forward and backward signal-control pairs have different one-photon detuning to the excited state. In this picture, SL was relying on multi-wave mixing. The description of SL with Bragg gratings was explicitly challenged in [Lin2009], titled "Stationary Light Pulses in Cold Atomic Media and without Bragg Gratings". Indeed in this realisation, although it is based on EIT, the forward and backward controls open transparency windows on two different, non-degenerate excited states, and therefore do not establish a standing wave. The formalism was refined in [Wu2010, Wu2010a] with the inclusion of the interaction between counter-propagating signal and control, which can be two-photon resonant when the Doppler frequency shift is minimal, for example in cold atomic media.

The description of the generation of SL was specifically addressed in [Zhang2012a, Zhang2013].

5.1.1 Electromagnetically-Induced-Transparency Stationary Light

The first SL scheme involves EIT in a Λ configuration, with an additional standing wave between state $|s\rangle$ and an additional state noted $|d\rangle$, as shown in figure 5.1.

The establishment of a dark-state polariton is governed by the dynamics presented in chapter 3. The mixing angle of the polariton is noted $\theta(\tau)$, it satisfies $\tan\theta(\tau) = g\sqrt{N}/\Omega_c(\tau)$.

If initially only the forward polariton is populated, the addition of the standing wave couples the forward and backward propagating polaritons, leading to the equations [Andre2002]:

$$\begin{cases} \Psi_+(k,\tau) = \left[\cos(\zeta\tau) - \mathrm{i}\dfrac{kc}{\zeta}\sin(\zeta\tau)\right]\Psi_+(k,0) \\ \Psi_-(k,\tau) = \mathrm{i}\dfrac{\chi}{\zeta}\sin(\zeta\tau)\,\Psi_+(k,0) \end{cases}$$

with Ω_s the Rabi frequency of the standing wave light field, $\chi = \Delta_\mathrm{s}(\tau)\tan^2\theta(\tau) = (g^2N/\Delta)\,\Omega_\mathrm{c}^2/\Omega_\mathrm{s}^2$ and $\zeta = \sqrt{(kc)^2+\chi^2}$.

Owing to the opposite and equal propagation of the forward and backward polaritons, light remains trapped within the atomic ensemble, with a non-vanishing photonic component, proportional to the non-zero Ω_c Rabi frequency. There remains electromagnetic energy in the ensemble, which is stationary. This contrasts with a stopped light scheme, where the control field is turned off and the photonic component of the polariton disappears.

The experiment was conducted in [Bajcsy2003] and a central element which inspired our implementation was the side-imaging of the fluorescence of the atoms, which enables the visualisation of the polariton when SL is generated.

5.1.2 One-colour Raman stationary light

The simplest Raman configuration is the *one-colour* configuration represented in figure 5.2. All the light fields, signals and controls, in both forward and backward directions, address the same virtual state, detuned by Δ from the excited one:

$$\begin{cases} \partial_t\rho_{21} = -\gamma\rho_{21}(z,t) + \mathrm{i}\Omega^*(z,t)\rho_{31}(z,t) \\ \partial_t\rho_{31} = -(\Gamma - \mathrm{i}\Delta)\rho_{31}(z,t) + \mathrm{i}\Omega(z,t)\rho_{21}(z,t) + \mathrm{i}gN\mathcal{E}(z,t) \end{cases}$$

The signal $\mathcal{E}$ is made of its forward component, $\mathcal{E}_+$, and backward component, $\mathcal{E}_-$:

$$\mathcal{E}(z,t) = \mathcal{E}_+(z,t)\exp(+\mathrm{i}kz) + \mathcal{E}_-(z,t)\exp(-\mathrm{i}kz).$$

The controls are represented by their Rabi frequency $\Omega_\pm$:

$$\Omega(z,t) = \Omega_+(t)\exp(+\mathrm{i}kz) + \Omega_-(t)\exp(-\mathrm{i}kz).$$

In this configuration, *a priori* all the coherences can couple with each other. To make this explicit, the spin coherence and optical coherence can be decomposed as [Wu2010a]:

$$\begin{cases} \rho_{21}(z,t) = \displaystyle\sum_{n=-\infty}^{\infty} \rho_{21}^{(2n)}(z,t)\exp(+2n\mathrm{i}kz) \\ \rho_{31}(z,t) = \displaystyle\sum_{n=-\infty}^{\infty} \rho_{31}^{(2n+1)}(z,t)\exp(+(2n+1)\mathrm{i}kz) \end{cases}$$

Usually, only the quantities with the superscripts (0), (+1) and (−1) are considered, and the higher-order terms are ignored. Including these higher-order terms yields:

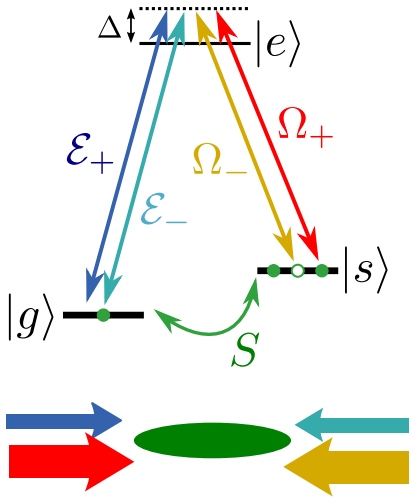

Figure 5.2: One-colour SL configuration. Forward and backward signals $\mathcal{E}_\pm$ and controls $\Omega_\pm$ are all equally-detuned from the excited state $|e\rangle$ and address the same spin wave S.

$$\begin{cases} \partial_t \rho_{21}^{(2n)} = -\gamma \rho_{21}^{(2n)} + \mathrm{i}\Omega_+^* \rho_{31}^{(2n+1)} + \mathrm{i}\Omega_-^* \rho_{31}^{(2n-1)} \\ \partial_t \rho_{31}^{(+1)} = -(\gamma_{31} - \mathrm{i}\Delta)\rho_{31}^{(+1)} + \mathrm{i}\Omega_+ \rho_{21}^{(0)} + \mathrm{i}\Omega_- \rho_{21}^{(+2)} + \mathrm{i}gN\mathcal{E}_+ \\ \partial_t \rho_{31}^{(-1)} = -(\gamma_{31} - \mathrm{i}\Delta)\rho_{31}^{(-1)} + \mathrm{i}\Omega_+ \rho_{21}^{(-2)} + \mathrm{i}\Omega_- \rho_{21}^{(0)} + \mathrm{i}gN\mathcal{E}_- \\ \partial_t \rho_{31}^{(2n+1)} = -(\gamma_{31} - \mathrm{i}\Delta)\rho_{31}^{(2n+1)} + \mathrm{i}\Omega_+ \rho_{21}^{(2n)} + \mathrm{i}\Omega_- \rho_{21}^{(2n+2)} \quad \text{for } 2n+1 \notin \{-1, +1\} \end{cases}$$

In this model, the spin ρ_{12} can generate optical coherences both forward (ρ_{31} with an increased superscript, $\rho_{12}^{(2n)}$ generates $\rho_{31}^{(2n+1)}$) and backward (decreased superscript), mediated by Ω_+ and Ω_- respectively. However, only $\rho_{31}^{(+1)}$ and $\rho_{31}^{(-1)}$ directly couple to $\mathcal{E}$ (and vice versa). The main addition is that control fields can also interact with the counter-propagating probe (the terms with opposite signs for the control and the probe coherence, $\mathrm{i}\Omega_-\rho_{21}^{(+2)}$ and $\mathrm{i}\Omega_+\rho_{21}^{(-2)}$), populating the higher-momentum component of the spin-wave.

To better understand which terms have been added compared to the usual model, let us have a look at the equations involving $\rho_{21}^{(+2)}$, for example:

$$\begin{cases} \partial_t \rho_{21}^{(+2)} = -\gamma \rho_{21}^{(+2)} + \mathrm{i}\Omega_+^* \rho_{31}^{(+3)} + \mathrm{i}\Omega_-^* \rho_{31}^{(+1)} \\ \partial_t \rho_{31}^{(+1)} = -(\gamma_{31} - \mathrm{i}\Delta)\rho_{31}^{(+1)} + \mathrm{i}\Omega_+ \rho_{21}^{(0)} + \mathrm{i}\Omega_- \rho_{21}^{(+2)} + \mathrm{i}gN\mathcal{E}_+ \end{cases}$$

If we consider that initially, all the atoms are in the ground state $|g\rangle$, $\rho_{31}^{(+1)}$ becomes non-zero when a forward signal $\mathcal{E}_+$ is sent into the atomic medium and in turn it couples to $\rho_{21}^{(+2)}$ through Ω_-. This coupling between $\mathcal{E}_+$ and Ω_-, via ρ_{31} (*i.e.* the polarisation operator $\hat{P}$) has been neglected so far, as indeed it involves the absorption and emission of photons in opposite direction, generating a spin-wave of wave vector $+2k$.

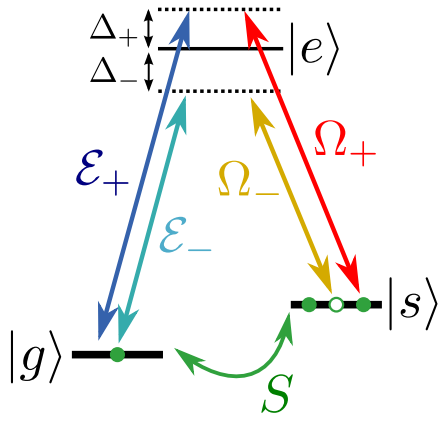

Figure 5.3: Two-colour SL configuration. Forward signal and control pairs are oppositely-detuned from the excited state $|e\rangle$.

Phenomenologically in [Lin2009], the authors have introduced a decay rate $\gamma_2 \geq \gamma_1$ for the higher-order coherences. In the case of warm atomic media, atomic motion causes decoherence and a large γ_2. The atomic motion in warm vapours blurs the higher-momentum components on a time-scale $t \approx (k_c^2 D)^{-1}$. In cold media, on the other hand, $\gamma_2 \ll \Gamma$ is possible, and these coherences get populated, which contributes to the loss and diffusion of signal light instead of its conversion to a SL form, as studied in [Lin2009, Wu2010a]. This addresses the concern expressed in [Nikoghosyan2009] that the secular approximation is not valid with atoms at a standstill.

5.1.3 Two-colour Raman stationary light

The previous model can simply be altered to contrast the forward and backward pairs by having each one at a different detuning, $\Delta_\pm$, as shown in figure 5.3.

We assume that the spectral width of all the light fields is small compared to the difference $|\Delta_+ - \Delta_-|$ so that each control is only coupled to its co-propagating probe. The configuration we impose is the one with $+\Delta_+ = -\Delta_- = \Delta$:

$$\begin{cases} \partial_t \hat{S}(z,t) = \mathrm{i}\sqrt{d}\dfrac{\Gamma}{\Delta}\left(\Omega_+\hat{\mathcal{E}}_+ + \Omega_-\hat{\mathcal{E}}_-\right) - \gamma\hat{S} \\ \partial_z \hat{\mathcal{E}}_+(z,t) = \mathrm{i}\sqrt{d}\dfrac{\Omega_+}{\Delta}\hat{S} \\ \partial_z \hat{\mathcal{E}}_-(z,t) = -\mathrm{i}\sqrt{d}\dfrac{\Omega_-}{\Delta}\hat{S} \end{cases}$$

The resulting equation for $\hat{\mathcal{E}}_-$ can either be seen as a π-phase-shifted spin-wave, or a derivative from the far end of the ensemble: $\partial_{(L-z)} = -\partial_z$. This ensures a symmetry between the forward- and backward-propagating quantities, either in the amplitude of the spin-wave, or the propagation dynamics of the probes.

In our case, the change in frequency is negligible on the scale of the absolute optical frequency: $2|\Delta| \ll \omega_{ij}$, and therefore plays no role for the wave-vector matching. We can perform a formal spatial integration on $\hat{\mathcal{E}}_\pm$ under the form:

$$\hat{\mathcal{E}}_{\pm}(z) - \hat{\mathcal{E}}_{\pm}(z_0) = \pm \mathrm{i}\sqrt{d}\frac{\Omega_{\pm}}{\Delta}\int_{z_0}^{z} \mathrm{d}z'\, S(z',t).$$

For each light field, it is more natural to integrate with the origin at the corresponding entrance into the atomic cloud, which is $z_0 = 0$ for $\hat{\mathcal{E}}_+$, and $z_0 = L$ for $\hat{\mathcal{E}}_-$. In the case $\Omega_+ = \Omega_- = \Omega$ and a negligible spin-wave decay rate $\gamma \approx 0$, the spin-wave evolves according to the simplifying equation:

$$\begin{aligned}\partial_t \hat{S}(z,t) &= -d\frac{\Gamma\Omega^2}{\Delta^2}\left(\int_0^z \mathrm{d}z'\, S(z',t) - \int_L^z \mathrm{d}z'\, S(z',t)\right)\\ &= -d\frac{\Gamma\Omega^2}{\Delta^2}\int_0^L \mathrm{d}z'\, S(z',t).\end{aligned}$$

The right-hand side does not depend upon z anymore, which conveys a uniform decay of the spin-wave at a constant rate, proportional to its integral over the atomic domain $[0, L]$, $\int_0^L \mathrm{d}z'\, S(z',t)$. It ensues that a spin-wave integrating to zero does not decay, neither does the light field: this is stationary light.

5.2 Early experimental stationary light investigations

With the Gradient Echo Memory moved to the neighbouring cold atomic ensemble, its warm vapour implementation was decommissioned and I had an available platform to experiment with SL. Our knowledge of the technique as the time was limited to the literature I have mentioned in the previous section: there had been no trials in the group before.

My initial trial was to introduce a backward control to retrieve the $\mathcal{E}_-$ signal. That backward control would match the existing (forward) one and would go through the atomic cell from its far end. This configuration required beam-splitters before and after the cell, to send in the backward control and to extract the backward signal, as shown in figure 5.4.

The measurement of forward signal required isolating the signal and filtering out the co-propagating control, which was performed by two types of filtering: polarisation filtering of about 20 dB on a polarising beam-splitter, and frequency filtering on a 20-cm long rubidium-85 cell providing about 100 dB of isolation. Moreover, the heterodyne detection provided additional mode filtering. The same detection setup was copied for the backward signal, with a rubidium-85 filter cell and heterodyne detection. However unlike the forward detection arm, this backward one did not have a readily available probe to align it to, and the backward control could not easily be fine tuned: the backward recall was not expected to produce a signal brighter than the control light background.

The alignment procedure I developed was to separate an additional, backward-propagating beam, made to overlap with the probe as far as possible. This reference beam, or backward probe, shown in figure 5.4, was bright enough to place the filter cell and the optics of the heterodyne detection, and align the local oscillator of the

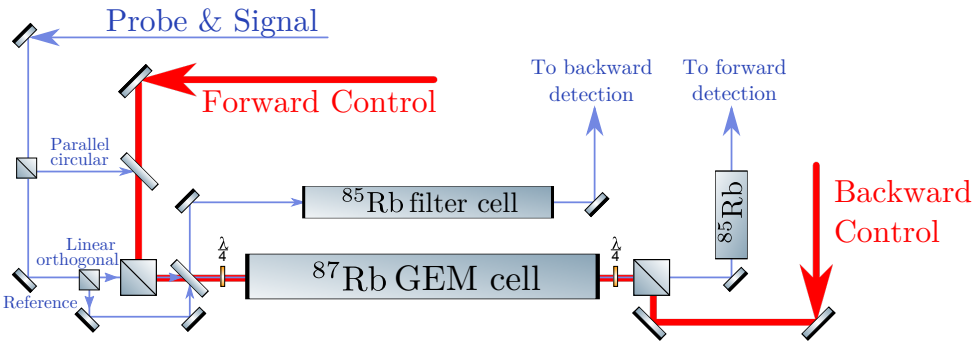

Figure 5.4: Experimental layout for trial investigation of SL in the warm vapour of rubidium-87 atoms usually used for GEM protocols. Rubidium-85 filter cells are placed on forward and backward detection arms. A reference beam is separated from the forward probe and signal and made to overlap with this beam in the backward direction, in order to align the backward detection arm. Forward and backward control beams are combined with the signal on beam-splitters.

latter. From there, after coarsely aligning it to be counter-propagating with its forward counterpart, tweaking the backward control alignment yielded a noticeable signal on the heterodyne, which was our backward recall and could be optimised with the parameters of the backward control.

Our first investigations showed that we could observe a distribution of signal light between forward and backward, depending on the ratio of the controls. It was however hard to make it quantitative. A more fundamental problem was to answer the question: "How do we prove that we have stationary light?". Indeed, we would need to show that no light is escaping from the atoms, and yet argue that this light is not lost. No optical access was possible from the side, because of the magnetic shielding, and demonstrating interaction between SL and probe light seemed like a too-long leap forward.

In parallel, more study of the available bibliography on SL showed that forward and backward signal-control pairs oppositely-detuned from the excited level was preferable as it ensures a temporal symmetry between the processes involving the spatially-symmetric pairs of signal and control. The issue was that the filtering with rubidium-85 was only possible for a few values of detuning that made the control frequency fall in the absorption of that isotope, there was not a solution to filter out the second control, symmetrically-detuned. Spatial filtering was limited because no angle could be introduced with warm atoms.

5.3 Self-stabilising stationary light in a cold atomic ensemble

With the numerous limitations in the warm atomic system, we decided to develop SL experiments in the cold atomic ensemble. The first achievement came from the study

of the self-stabilisation dynamics of an atomic spin wave to a solution that supports SL. I detail here the model for these dynamics and their experimental verification which has led to a publication in Nature Physics [Everett2017].

5.3.1 Atom-light configuration

An elongated cloud of rubidium-87 atoms is prepared by the sequence described in 2.3.4. The atoms are optically-pumped to the $m_F = +1$ Zeeman sub-level. Weak counter-propagating probe fields ($\mathcal{E}\pm$) are each addressed to the same spin wave by a Raman process with mirror-imaged control fields ($\Omega_\pm$), and the light escaping from the atoms is acquired on a forward and backward detectors. The experimental layout is shown in figure 5.5 and the wave-vector geometry in its inset. The bright control fields drive the spin wave in the atoms through a coherent scattering process. The forward and backward probe-control pairs have opposite detunings, which corresponds to a two-colour SL configuration.

5.3.2 Self-stabilisation dynamics

We first describe theoretically how an initial spin wave encoded in the atoms evolves to a spatial distribution which is stable and accompanied by SL.

Theoretical description of the stabilisation process

After adiabatically eliminating the excited state by assuming the one-photon detuning to be much larger than the excited-state linewidth $\Delta \gg \Gamma$, we obtain the following Maxwell–Bloch equations governing the system:

$$\begin{cases} \partial_t \hat{S}(z,t) = \mathrm{i}\sqrt{d}\,\dfrac{\Gamma}{\Delta}\left(\Omega_+ \hat{\mathcal{E}}_+(z,t) + \Omega_- \hat{\mathcal{E}}_-(z,t)\right) \\ \partial_z \hat{\mathcal{E}}_\pm(z,t) = \pm\mathrm{i}\sqrt{d}\,\dfrac{\Omega_\pm}{\Delta}\hat{S}(z,t) \end{cases} \tag{5.1}$$

A formal integration of the $\hat{\mathcal{E}}_\pm$ equations over space yields:

$$\begin{aligned} \partial_t \hat{S}(t) &= -d\Gamma\frac{|\Omega|^2}{\Delta^2}\left[\int_0^z \mathrm{d}z'\,\hat{S}(z',t) - \int_L^z \hat{S}(z',t)\right] \\ &= -d\Gamma\frac{|\Omega|^2}{\Delta^2}\int_0^L \mathrm{d}z'\,\hat{S}(z',t). \end{aligned}$$

The right-hand side is proportional to the integral of the spin wave over the length of the ensemble, which means that the time derivative of $\hat{S}(z)$ is equal at all points in the ensemble. Consequently, the integrated spin-wave amplitude will evolve at the rate $d\Gamma|\Omega|^2/\Delta^2$ towards a state where the average of $\hat{S}(z)$ over the ensemble is zero.

In the case where the spin wave is uniform, it will decay to zero. It evolves to a non-zero spin wave if it possesses an initial spatial structure. Moreover, when the spatial integral of $\hat{S}(z)$ is zero, in this formalism, the amplitudes of the probe fields drop to zero outside the ensemble. This means that the counter-propagating probe fields within the

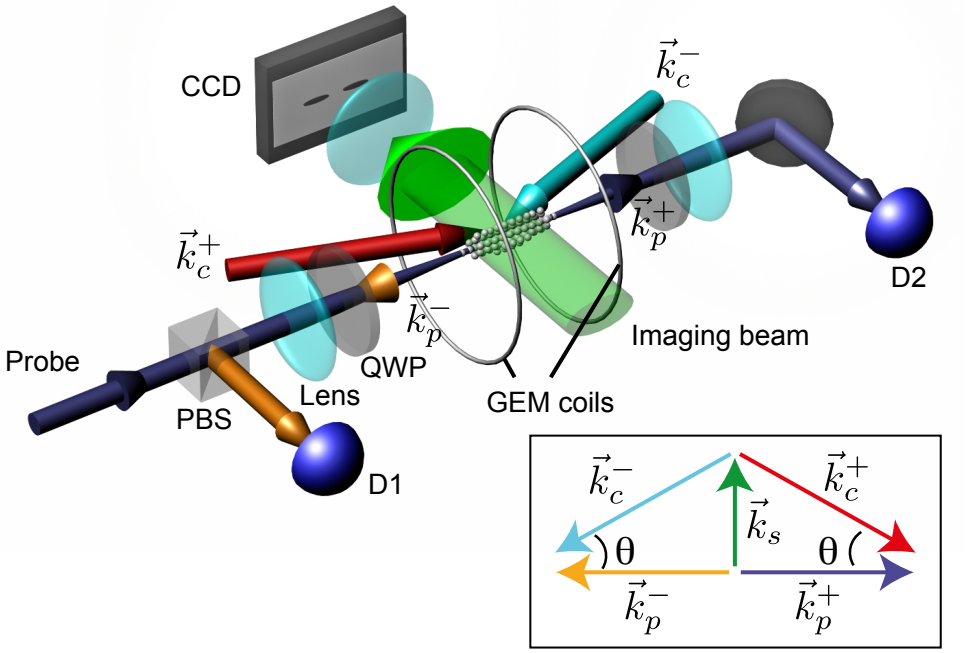

Figure 5.5: The experimental schematic for the SL pulse generation in an ensemble of cold ^{87}Rb atoms. The spin-wave is created by storing a probe pulse via the gradient echo memory technique with forward control field. The magnetic field gradient over the ensemble is controlled by a set of coils (GEM coils). A backward control field couples to a backward probe, counter-propagating with its forward counterpart. Forward and backward probe and control beams are denoted by their wave vector $\vec{k}^{\pm}_{(\mathrm{p,c})}$. An imaging beam resonant with $|s\rangle \rightarrow \left|5^2P_{3/2}(F'=2)\right\rangle$) is used for the absorption imaging of the spin-wave. Detector D1 measures the backwards probe field; D2 measures the forward probe field; QWP is a quarter-wave plate and PBS is a polarising beam-splitter. Inset: The angles between the forward (backward) probe field and the forward (backward) control field are set to be $\theta \approx 6\,\mathrm{mrad}$, where the phase matching condition $\vec{k}_\mathrm{p}^+ - \vec{k}_\mathrm{c}^+ = \vec{k}_\mathrm{p}^- - \vec{k}_\mathrm{c}^- = \vec{k}_\mathrm{s}$ is satisfied. Here, $\vec{k}_\mathrm{s}$ denotes the spin-wave wave vector. Please note that the convention for probe and control colour fields slightly differs in this figure from [Everett2017].

ensemble have equal magnitude but opposite phase, which corresponds to a destructive interference which manifests as a suppression of the emission of probe light outside of the ensemble.

These dynamics can also be translated in terms of bright and dark eigenstates, $\hat{\Psi}_{\mathrm{b}}$ and $\hat{\Psi}_{\mathrm{d}}$:

$$\begin{cases} \hat{\Psi}_{\mathrm{b}} = \dfrac{\Omega_+\hat{\mathcal{E}}_+(z,t) + \Omega_-\hat{\mathcal{E}}_-(z,t)}{\sqrt{|\Omega_+|^2 + |\Omega_-|^2}} \\ \hat{\Psi}_{\mathrm{d}} = \dfrac{\Omega_-\hat{\mathcal{E}}_+(z,t) - \Omega_+\hat{\mathcal{E}}_-(z,t)}{\sqrt{|\Omega_+|^2 + |\Omega_-|^2}} \end{cases}$$

Equation 5.1 becomes:

$$\begin{cases} \partial_t\hat{S}(z,t) = \mathrm{i}\sqrt{d}\dfrac{\Gamma}{\Delta}\sqrt{|\Omega_+|^2 + |\Omega_-|^2}\hat{\Psi}_b \\ \partial_z\hat{\mathcal{E}}_\pm(z,t) = \pm\mathrm{i}\sqrt{d}\dfrac{\Omega_\pm}{\Delta}\hat{S}(z,t). \end{cases}$$

It shows that the spin-wave decay is driven by the bright state only, which in turns leads to the emission of light out of the system. On the other hand, the dark state is decoupled from the evolution of the spin wave. It is not however decoupled from the atom-light interaction, as it gives rises to the counter-propagating probe fields with equal magnitude and opposite phase within the ensemble. This corresponds to stationary light which is stable and remains in the atomic medium.

Evolution of spin-wave pairs with a relative phase

To represent the dynamics of the stabilisation of SL, we consider two initial spin-wave configurations that both consist of equal amplitude Gaussian excitations at each end of the atomic ensemble, which differ by a relative phase φ. The first configuration corresponds to excitations at each end with an opposite phase ($\varphi = \pi$), the second one to excitations in phase ($\varphi = 0$). With equal Rabi frequency of both controls, the spin-wave with opposite-phase excitations is a dark state. Figure 5.8 shows the spatial distribution of the spin-wave and probe light amplitude in the memory, initially and after at time $5T$ with T the duration of the probe light used to write each of the Gaussian spin-wave excitations that compose the initial states. Sub-figures 5.8(a,b) illustrates that this solution is stationary and that no probe light can escape the atoms. With spin waves of equal phase, the system evolves as illustrated in figure 5.8(c,d). The initial unstable spin wave self-stabilises to a dark state where there is no further coherent emission of probe light. The initial spin wave can be interpreted as a sum of a bright state and a dark state. The former decays, resulting in the emission of light out the ensemble, while the latter remains stable.

5.3.3 Experimental spin-wave imaging

To verify the SL dynamics derived theoretically, we implement a protocol with the writing of two spin-waves with relative phase in an elongated atomic ensemble

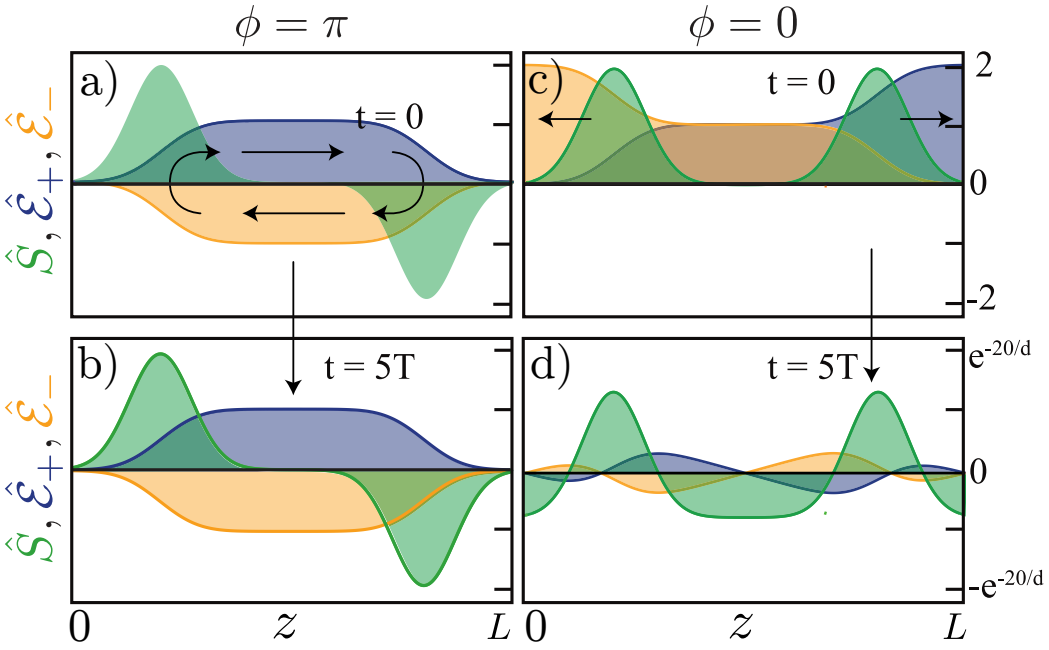

Figure 5.6: Evolution of spatially-structured spin waves along the ensemble of length L. The total initial spin wave is made of two spin waves, each written by a probe light Gaussian spin-wave of duration T. The spin waves have a relative phase φ. a) The two spin waves have an opposite phase ($\varphi = \pi$). Forward and backward controls drive the coupling of the spin waves to forward and backward probes $\mathcal{E}_+$and $\mathcal{E}_-$, which cancel out outside the atomic ensemble and cycle between the two spin waves. b) After a coupling duration of $5T$, the overall spin wave has not evolved, it corresponds to a dark eigenstate of the system. c) The spin wave are in phase ($\varphi = 0$), they couple to probe emission out of the ensemble. d) After at duration $5T$, the spin wave has significantly decreased and stabilised to a spatial distribution where it integrates to zero over the ensemble.

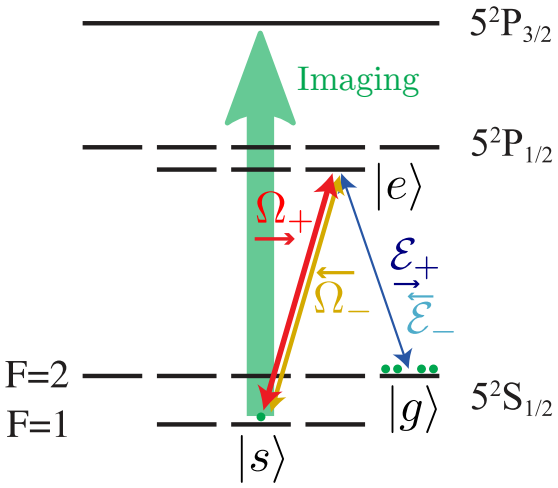

Figure 5.7: The spatial profile of the spin wave is directly imaged by probing the $|s\rangle \rightarrow \left|5^2P_{3/2}(F'=2)\right\rangle$ transition from the side of the atomic ensemble, onto a CCD camera. The atomic transitions corresponding to the probes $\mathcal{E}_\pm$, controls $\Omega_\pm$, and the imaging beam are shown.

with the GEM technique. With a magnetic gradient along the ensemble, the spatial distribution of the initial spin wave, and especially the phase at each point, can be precisely engineered with the spectral properties of an input probe light. With a probe spectrum made of two carrier frequencies, each with the same Gaussian envelope, we can write two Gaussian excitations of equal amplitude in the ensemble. Moreover, for a given magnetic gradient, they can be placed at each end of the ensemble by choosing adequately the carrier frequencies. The relative phase φ can be chosen by tuning the relative phase of the carriers.

Imaging setup

After an initial spin wave is written in the ensemble, forward and backward control fields are turned on and the spin-wave spatial profile at any time can be directly imaged by probing the $|s\rangle \rightarrow \left|5^2P_{3/2}(F'=2)\right\rangle$ transition, with the absorption imaging setup shown in figure 5.7. The evolution of the spin wave is monitored by repeating the experiment with the same initial spin-wave preparation and imaging the atomic ensemble at different times. Results are shown in figure 5.9. Sub-figures (i-iii) correspond to the spin wave after 60 µs, for (i) only the forward control field on, and spin waves have a relative phase (ii) $\varphi = \pi$ (iii) $\varphi = 0$ with forward and backward control fields on. The results of numerical simulations that solve the equations of motion with decay for the three-level system are shown directly underneath each experimental image. The simulations use the experimental parameters, apart from a small difference in the rephasing time which is introduced to match the experimental rephasing. Sub-figure (c) shows the simulated optical field envelope within the ensemble, illustrating the SL that coexists with the observed spin wave, but cannot be directly measured.

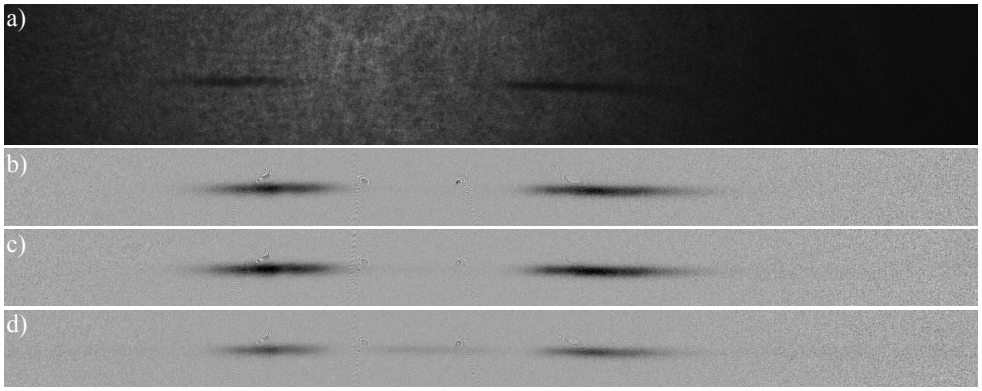

Figure 5.8: CCD images for a 4-µs imaging pulse during a 300-µs exposition time, corresponding to the duration of the whole SL experiment. Each measurement is constructed from ten images that are averaged to reduce shot-to-shot noise of the CCD camera. a) Single raw image capture showing a shadow where a spin wave has been written to the atoms. Averaged image over the ten acquisitions, hinting more precisely where spin-wave intensity $\left|\hat{S}\right|^2$ — and therefore absorption — is significant: b) after the optical pulse is initially encoded in the atoms, and after it has evolved into a steady state for spin waves c) with opposite phase, d) with the same phase.

Agreement between measurements and simulations

The relative phase of the spin waves cannot be measured directly, which prevents us from checking the two configurations effectively correspond to spin waves in phase and in phase opposition. Nonetheless, the two cases correspond to very different spin-wave dynamics. Therefore, the measured spin-wave evolution can be compared to the theoretical prediction of it.

This comparison shows that our experimental data show excellent agreement with the behaviour predicted by the simulations. The middle column of figure 5.9 shows results and simulations for a stationary spin wave, where the integrated amplitude of the initial spin wave is zero. In this case, as expected, we observe no evolution of the shape of the spin wave, similarly to the theoretical result shown in figure 5.6. When the counter-propagating control fields are turned on at 60 µs, there is only a gradual evolution due to decay. The right-hand column where the initial spin wave is not stable shows a rapid evolution to a stationary spin wave, marked by a horizontal discontinuity in the plot, in both the experimental data and simulated results.

Once the spin wave has reached a steady state in terms of shape, it continues to decay at a rate given by the control field scattering. The spin-wave decay rate is measured as (10 ± 1) kHz in the experiment, which roughly agrees with the value 12 kHz used in the simulations.

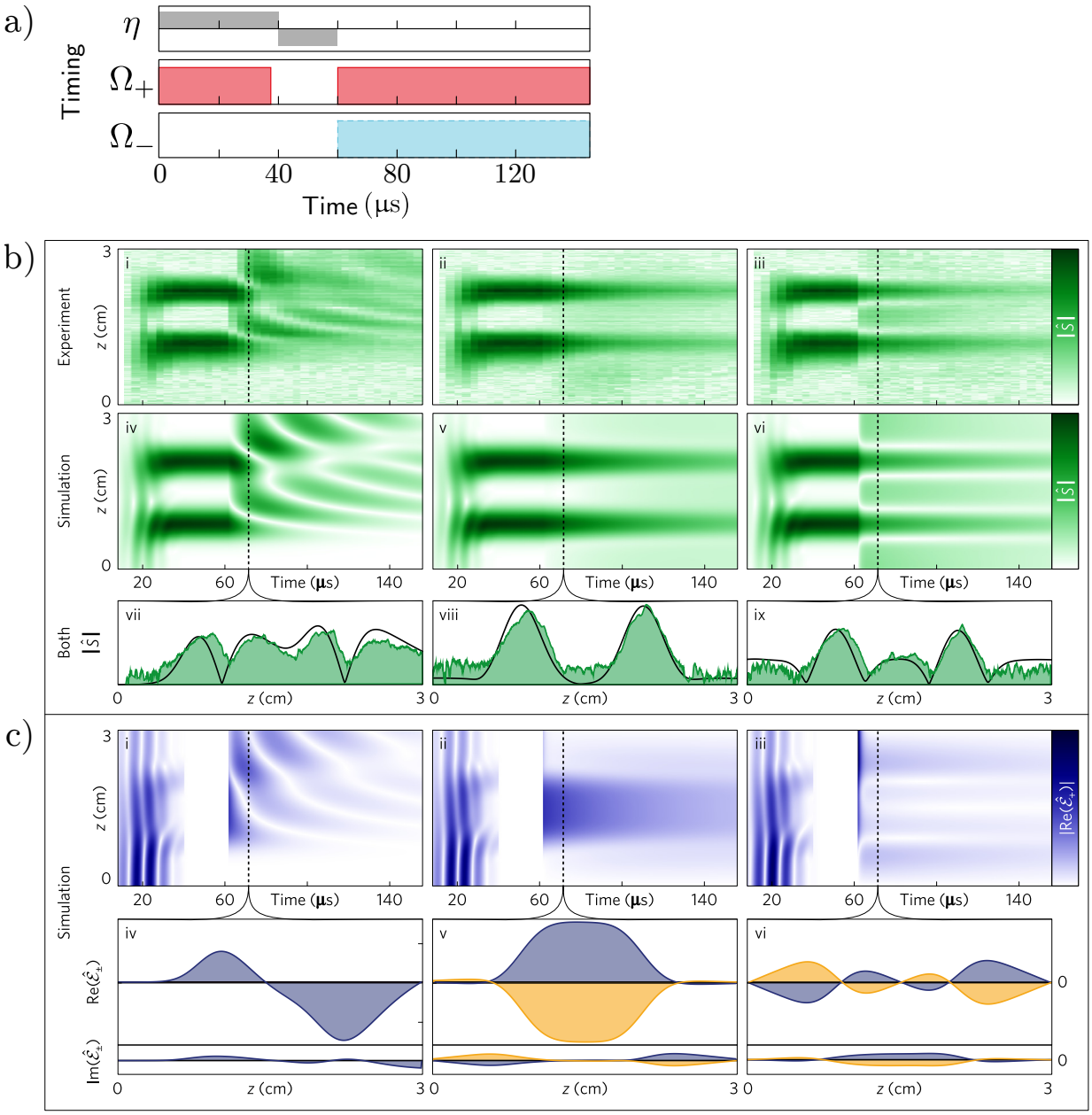

Figure 5.9: a) Timing of the gradient η and control fields $\Omega_{\pm}$ for the stabilisation of stationary light. b) Top row shows the experimentally measured evolution of the spin-wave. Middle row shows simulations of the spin-wave. Bottom row compares experiment (green) and simulation (black line) over the z direction at time 70 µs. In the results of the left column, only the forward control field is on after 60 µs. The other columns have forward and backward control fields on, as shown in the timing of sub-figure (a). The two spin waves have a relative phase of $\varphi = \pi$ in the middle column, and $\varphi = \pi$ in right column. c) Simulations of the probe field intensities for the situations corresponding to the columns of sub-figure (b). Top row shows the magnitude of the forward probe. Bottom row shows cross-sections at 70 µs with both forward (blue) and backward (yellow) probe field components.

5.4 Time-Reversed And Coherently-Enhanced memory

Stationary light has been observed by altering optical memory schemes but it does not *a priori* constitute a memory itself. In the previous sections, however, we have seen what spin-wave profiles give rise to SL. The spatial anti-symmetry of the spin-wave eigenmode resulting in SL suggests some symmetry would be beneficial for a memory scheme relying on the conversion of light into collective atomic excitations. Moreover, from general considerations on Λ-type atoms, it is known that spatial and temporal symmetries favour the efficient interfacing between atoms and light [Gorshkov2007b]. On another hand, the interference between polaritons recalled from storage and to be stored had already been investigated in the group [Campbell2012, Pinel2015]. The synthesis of these two aspects is made with the new scheme we have developed: Time-Reversed and Coherently-Enhanced (TRACE) memory. The symmetries with counter-propagating signals sent simultaneously as well their recall corresponding to their temporal reversal correspond to the *time-reversed* in the name, while *coherently-enhanced* refers to the constructive interference of the two signals.

The theory for this scheme was initiated by Jesse Everett, who also coined its name. Upon my return to ANU in 2016, I pushed for its experimental trial, which led to the first observation of the interference in February 2017. From there, we tamed this new memory scheme, figuring out how to align the many different beams involved and their precise frequency.

5.4.1 Single-mode memory without a cavity

Whereas a multimode memory stores distinguishing information about the different modes in some internal degree-of-freedom of its medium (location within the memory, polarisation or frequency mode), there is little variation in the distribution of the stored information in a single-mode memory. Placing a cavity around an absorbing medium is a widespread technique to create a single-mode optical memory. This configuration enables the signal to traverse the memory many times, which leads to a uniform interaction along the memory medium. The stored information, in that case, is contained in the phase and magnitude of the uniform atomic excitation.

The spatially-distributed reflection of light in an atomic medium can create useful optical interactions, with applications in quantum information processing. The origin of the spatially-distributed reflection can be a Bragg grating effect due to spatially-ordered atoms, or, in a disordered medium, a reflection process with imposed phase-matching. We use this second process to implement a single-mode optical memory, specifically with four-wave mixing between two counter-propagating signals mapped to the same spin-wave mode by a control field.

5.4.2 Phase matching and interference

The configuration for TRACE is closely related to the one for SL, with two counter-propagating signals, each coupled to the atoms by a control beam making an angle so that both pairs address the same spin-wave. The difference in this case is the simultaneous injection of both signals. The pulse shape for optimal storage is the rising exponential profile, shown in the figure inset.

Taking the dimensionless spatial variable $\zeta = z/L$, the coupling of both signals to the same spin wave is described by the following equations:

$$\begin{cases} \partial_t \hat{S}(\zeta,t) = \mathrm{i}\sqrt{d}\,\Gamma \dfrac{\Omega_c^*}{\Delta}\left(\hat{\mathcal{E}}_+(\zeta,t) + \hat{\mathcal{E}}_-(\zeta,t)\right) \\ \partial_\zeta \hat{\mathcal{E}}_\pm(\zeta,t) = \pm\mathrm{i}\sqrt{d}\,\dfrac{\Omega_c}{\Delta}\hat{S}(\zeta,t) \end{cases}$$

A formal integration of the $\hat{\mathcal{E}}_\pm$ equations over space yields:

$$\partial_t \hat{S}(t) \;=\; -d\Gamma\frac{|\Omega_c|^2}{\Delta^2}\int_0^1 \mathrm{d}\zeta'\,\hat{S}(\zeta',t) \;+\; \mathrm{i}\sqrt{d}\,\Gamma\frac{\Omega_c^*}{\Delta}\left(\hat{\mathcal{E}}_+(\zeta=0,t) + \hat{\mathcal{E}}_-(\zeta=1,t)\right) \quad (5.2)$$

As explicitly denoted in the left-hand side of the equation, the time evolution of the spin wave is independent of the position within the memory, only the overall spin wave is involved in the spin-wave dynamics. With no input field and a constant control field, an exponential decay of the spin wave occurs simultaneously with signal fields exiting both sides of the memory.

When input signals sent from both sides are chosen symmetric and equal to $\hat{\mathcal{E}}_{\mathrm{in}}(t)$ we have at each exit the same output $\hat{\mathcal{E}}_{\mathrm{out}}(t)$:

$$\begin{cases} \hat{\mathcal{E}}_{\mathrm{in}}(t) = \hat{\mathcal{E}}_+(\zeta=0,t) = \hat{\mathcal{E}}_-(\zeta=1,t) \\ \hat{\mathcal{E}}_{\mathrm{out}}(t) = \hat{\mathcal{E}}_+(\zeta=1,t) = \hat{\mathcal{E}}_-(\zeta=0,t) \end{cases}$$

In particular when $\hat{\mathcal{E}}_+(\zeta=0,t) + \hat{\mathcal{E}}_-(\zeta=1,t) = 2\hat{\mathcal{E}}_{\mathrm{in}}(t)$ corresponds to the value which compensates the first term of equation 5.2, a condition expressed as:

$$\hat{\mathcal{E}}_{\mathrm{in}}(t) = -\frac{1}{2}\mathrm{i}\sqrt{d}\,\Gamma\frac{|\Omega_c(t)|^2}{\Delta^2}\int_0^1 \mathrm{d}\zeta'\,\hat{S}(\zeta',t),$$

then it cancels the re-emission of light at each exit, $\hat{\mathcal{E}}_{\mathrm{out}}(t) = 0$.

To ensure the result $\hat{\mathcal{E}}_{\mathrm{out}}(t) = 0$ during storage, the time evolution of the input fields must match the evolution of the time-varying term $|\Omega_c(t)|^2 \int_0^1 \mathrm{d}\zeta'\,\hat{S}(\zeta',t)$. In particular, for a constant control field Rabi frequency during storage, the condition is verified with an exponentially-rising pulse with the profile of the form:

$$\hat{\mathcal{E}}_{\mathrm{in}}(t) \propto \exp\left[d\Gamma(\Omega/\Delta)^2 t\right].$$

When the whole signal is absorbed, turning the control fields off prevents re-emission. Turning the controls back on at a later time leads to the retrieval of the time-reversed

counter-propagating signals, providing a single-mode optical memory[1]

5.4.3 Efficiency scaling with optical depth

An approach to determine the limit on the memory efficiency is given in [Gorshkov2007]. In this model, the limit comes from the decay of the excited state coherence, $\hat{P}$. We define forward and backward excited state coherence, $\hat{P}_+$ and $\hat{P}_-$, associated with each probe field. Assuming full absorption of the input probe pair, the equations governing the atomic system are:

$$\begin{cases} \hat{\mathcal{E}}_+(\zeta=1,t) = \mathrm{i}\sqrt{d}\,\hat{P}_+ \\ \hat{\mathcal{E}}_-(\zeta=0,t) = \mathrm{i}\sqrt{d}\,\hat{P}_- \\ \partial_t \hat{P}_+ = -[\Gamma(1+d\zeta)+\mathrm{i}\Delta]\hat{P}_+ + \mathrm{i}\Omega\hat{S} \\ \partial_t \hat{P}_- = -[\Gamma(1+d(1-\zeta)+\mathrm{i}\Delta]\hat{P}_- + \mathrm{i}\Omega\hat{S} \\ \partial_t \hat{S} = \mathrm{i}\Omega^*(\hat{P}_+ + \hat{P}_-) \end{cases}$$

From these equations, we can for the time derivative of the quantity $\left|\hat{S}\right|^2 + \left|\hat{P}_+\right|^2 + \left|\hat{P}_-\right|^2$, which corresponds to the total energy transferred to the atoms. This gives:

$$\partial_t\left(\left|\hat{S}\right|^2 + \left|\hat{P}_+\right|^2 + \left|\hat{P}_-\right|^2\right) = -2\Gamma\left(\left|\hat{P}_+\right|^2 + \left|\hat{P}_-\right|^2\right) + 2d\Gamma\left(\zeta\left|\hat{P}_+\right|^2 + (1-\zeta)\left|\hat{P}_-\right|^2\right)$$

In the adiabatic limit, $P_+ = P_-$ and the integration over time of the output light field $\hat{\mathcal{E}}_{\mathrm{out}}(t) = \hat{\mathcal{E}}_+(\zeta=0,t) = \hat{\mathcal{E}}_-(\zeta=1,t)$ gives:

$$\int_0^\infty \mathrm{d}t' \left|\hat{\mathcal{E}}_{\mathrm{out}}\right|^2 = -\frac{d}{d+2}\left[\left|\hat{S}(t)\right|^2 + \left|\hat{P}_+(t)\right|^2 + \left|\hat{P}_-(t)\right|^2\right]_{t=0}^{t\to\infty}$$

which corresponds to a maximum storage-and-retrieval efficiency equal to $d^2/(d+2)^2$. Asymptotically, this yields an efficiency scaling as $1-4/d$, for $d \gg 1$. Our scheme therefore has a favourable dependence on OD compared to other typical free-space memories, for which ideal storage followed by retrieval goes as $1-5.8/d$ [Gorshkov2007b]. The term *coherently enhanced* refers to the ability to distribute the spin-wave throughout the memory, making the most efficient use of the available OD, as well as enhancing the absorption through the constructive interference of the forward and backward processes.

In comparison, the efficiency of the ideal storage followed by retrieval is $1-1/C$ in a cavity-enhanced memory with cooperativity C. Cooperativity is proportional to the OD, with $C = 2dc/(L\kappa)$, where L is the cavity length and κ is the transmission of the cavity output coupler. The lower efficiency obtainable in our scheme is due to the extra control field and associated decay. However, cavity single-mode memories require back-action on the atomic ensemble from light building up in the cavity to be prevented. This imposes that the decay rate out of the cavity is significantly faster than

[1] A formal demonstration of this argument requires to prove that the Green's function describing storage followed by retrieval is factorable. Here it is instead shown that there is a single signal mode which prevents re-emission of light, which is a weak demonstration of the single-mode operation.

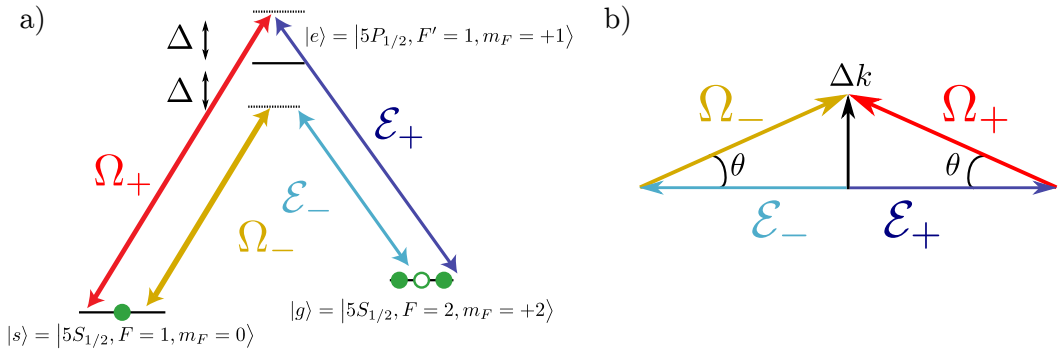

Figure 5.10: Configuration of the signal and control beams: a) A forward-propagating signal, denoted $\mathcal{E}_+$, is blue-detuned by Δ from the $|g\rangle \rightarrow |e\rangle$ transition. A forward control beam of Rabi frequency Ω_+ is equally detuned from the $|s\rangle \rightarrow |e\rangle$ transition. Backward signal $\mathcal{E}_-$ and backward control of Rabi frequency are symmetrically red-detuned from $|e\rangle$ b) Forward signal and control form an angle of θ, the backward signal is counter-propagating with $\mathcal{E}_+$ and backward control also forms the angle θ. In this symmetrical configuration, both pair address the same spin-wave whose wave vector is orthogonal to the signal axis.

the memory decay rate, which is a limitation the bandwidth of such memories. On the other hand, in the TRACE memory scheme, although it acts as a single-mode memory like a cavity-enhanced memory, there is no such back-action as light that reaches the end of the ensemble never returns to the ensemble.

5.4.4 Experimental realisation

The implementation of this novel memory protocol was performed in the ANU cold atomic ensemble, whose preparation is described in 2.3.4. The atoms are prepared in $|g\rangle = \left|5S_{1/2}, F = 2, m_F = +2\right\rangle$ and the storage state is chosen to be $|s\rangle = \left|5S_{1/2}, F = 1, m_F = 0\right\rangle$. The excited state is taken as $|e\rangle = \left|5P_{1/2}, F' = 1, m_F = +1\right\rangle$, on the D_1-line. The configuration in frequency and beam geometry is identical to the Raman memory described in chapter 4: each signal and control pair forms a 6 mrad angle to match the hyperfine splitting of rubidium-87, so they both address the same spin wave, as shown on figure 5.10. The forward and backward pairs are symmetrically detuned from the excited state, blue and red detuned respectively. The detuning was chosen as 160 MHz or 230 MHz in different experimental trials. The OD on the signal transition is measured on the absorption on the Raman lines for $m_F \in \{-1, 0, +1\}$ with varying control power, as described in 2.3.5. OD as high as 500 ± 100 were obtained.

Interference between counter-propagating signals

Counter-propagating probes with a profile shaped as a rising exponential are sent simultaneously in the prepared atomic ensemble. Photodiodes are placed at both ends

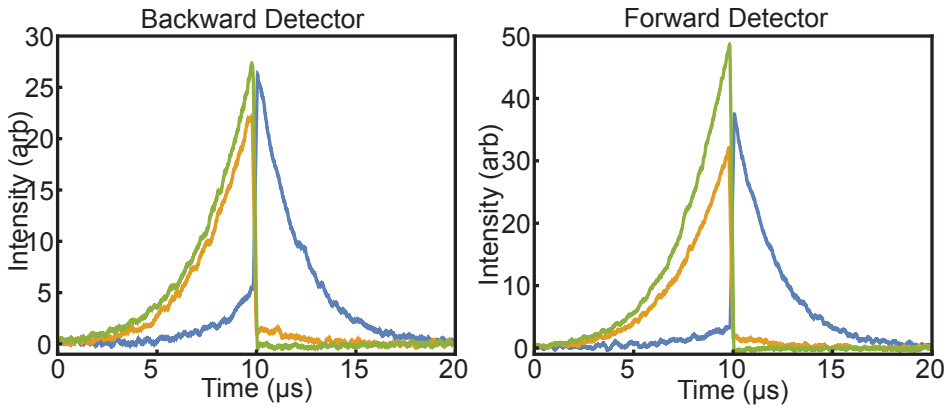

Figure 5.11: Photodiode signals on forward and backward detectors during the realisation of the TRACE protocol. A rising-exponential-shaped probe is sent from both sides of the cold atomic ensemble. Depending on the relative phase of the counter-propagating probes, the absorption process of each one interfere either constructively (in blue) or destructively (orange). Here the forward and backward control beams are sent continuously and the probes are immediately retrieved, with their time-reversed profile. The reference probes without atoms is shown for reference (green).

of the atomic ensemble, in the same configuration as for the backward-retrieval Raman memory experiment presented in chapter 4.

Initially only one probe is sent at a time, the control fields are kept on, so that each probe experiences storage in the atomic ensemble as a spin wave immediately followed by its retrieval. The forward and backward control intensity are tuned to result in the distribution of each probe pulse in four equal parts: leakage to the detector in the same direction, reflection to the detector in the opposite direction and retrieval in both directions.

Both probes are sent simultaneously and their relative phase becomes random from run to run from the interferometric instability between their different paths. Figure 5.11 shows the forward and backward photodiode signals for the cases of minimum and maximum absorption on the probe pair.

The relative phase between control-probe pairs is almost completely random after each loading phase, of the order of a second. However, it varies only by a small amount over each memory sequence, which lasts about 400 µs. Therefore a series of 17 pairs of probe pulses are sent within the same sequence, with constant control field intensity, in order to investigate the phase dependence of the observed interference. The phase of each successive $\mathcal{E}_+$ pulse is incremented by 0.3π while in a second experiment, the phase is not incremented. The spin waves produced by each counter-propagating pair interfere. Constructive interference results in an enhanced mapping to the spin wave while destructive interference corresponds to a dark state which inhibits the absorption. A complete interference fringe is obtained when a total of 2π is incremented to the phase over the length of the train of pulses. The results are shown in figure 5.12. Interference

is also visible when the frequency of the control fields are detuned from the two-photon resonance.

Visibilities were calculated by comparing the most constructive and destructive interference into the spin wave relative to the total optical power of the input pulses. Visibilities of 70% are achieved which testifies to the spatio-temporal matching of the forward and backward pairs. The production of temporal interference fringes indicates that deterministic storage could be achieved by measuring the relative phase of input probes and adjusting a control field phase or a path length accordingly.

Performance as a memory scheme

The interference fringe shows that some pulses are efficiently stored while others destructively interfere into the ensemble. By monitoring the leakage from the atomic ensemble as the phase shifts between and within experimental runs we could herald the efficient writing of constructively-interfering spin waves and recall them on-demand. We have measured the amount of probe light retrieved from the stored spin waves and characterised this heralded probabilistic optical memory and compared it to gradient echo and Raman memory schemes using the same preparation of the atomic ensemble.

At large ODs around 500, we could not conclude favourably on the relative performance of the TRACE memory scheme compared to GEM or Raman memory: the schemes performed equivalently in the $50 - 65\%$ storage-and-retrieval efficiency range. With an OD decreased to a few tens, TRACE performed comparatively better in the only experimental attempt of performing the three memory schemes at high and low OD within a few hours. However, we cannot assert that the GEM and Raman parameters and alignment were optimised to reach the highest efficiency. In particular, the configuration with an angle between the probe and control does not minimise the spin-wave wave vector and is therefore sub-optimal for these memory schemes.

The decay of the TRACE memory with storage time was investigated by varying the duration for which both controls are kept off after absorption of the probe pulses. Figure 5.13 shows the dependence of the retrieval efficiency against storage time, which is fitted to exponential decay of characteristic time $(130 \pm 10)\,\mu s$, which corresponds to a temperature $(270 \pm 40)\,\mu K$, compatible with an independent time-of-flight temperature measurement.

5.4.5 Outlook

We have demonstrated a new type of optical memory based on a distributed reflection within an atomic ensemble. We have shown how the memory has improved efficiency expected of a single-mode memory, while still being accessible to free-space atom-light interaction techniques. The cost of this improvement is the division of the signal in two

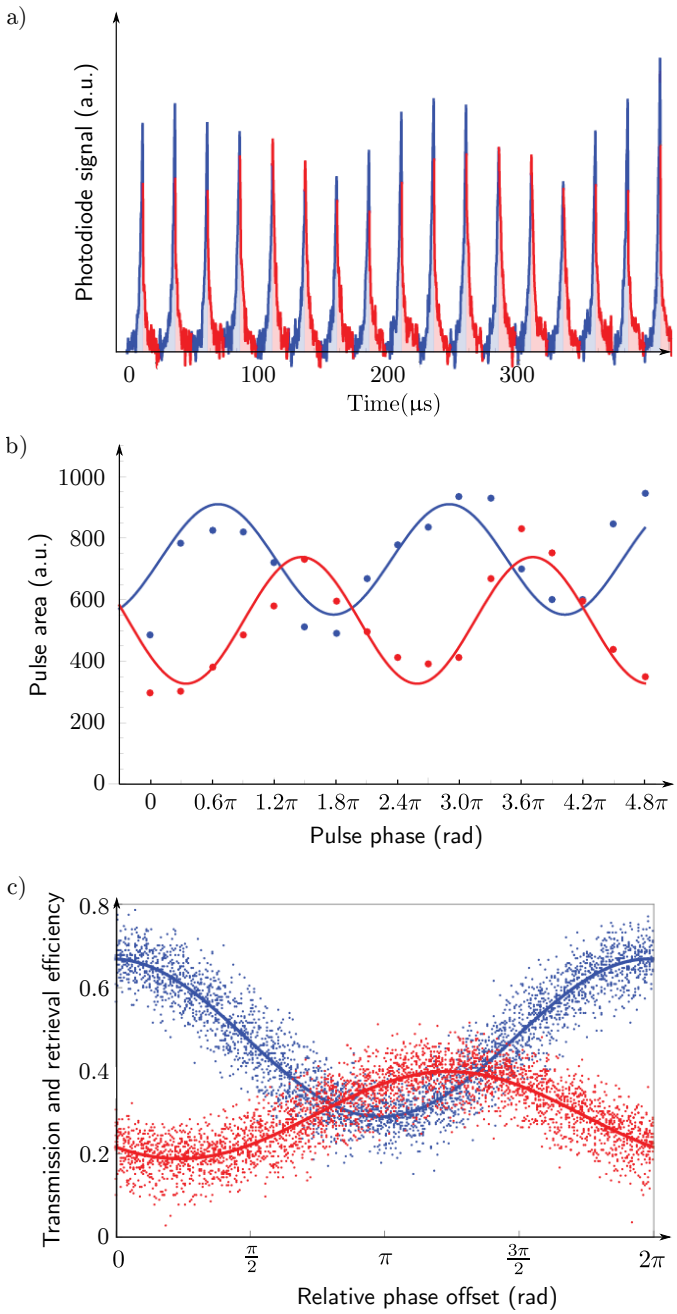

Figure 5.12: a) A series of 17 pairs of probe pulses are sent within the same sequence, with constant control field intensity. Here, the phase of each successive $\mathcal{E}_+$ pulse is incremented by 0.3π. The spin waves produced by each counter-propagating pair interfere constructively or destructively, which enhances or inhibits the absorption, respectively. The retrieval which immediately follows is similarly enhanced or inhibited. b) The area of the pulse being transmitted and reflected during the sending of the probe (blue dots), or retrieved in the following time window (red dots), are represented for each phase increment. Solid lines correspond to sinusoidal fit functions. c) A complete interference fringe compiled over all acquisitions to find the relative phase offset, as well as the visibility of the interference.

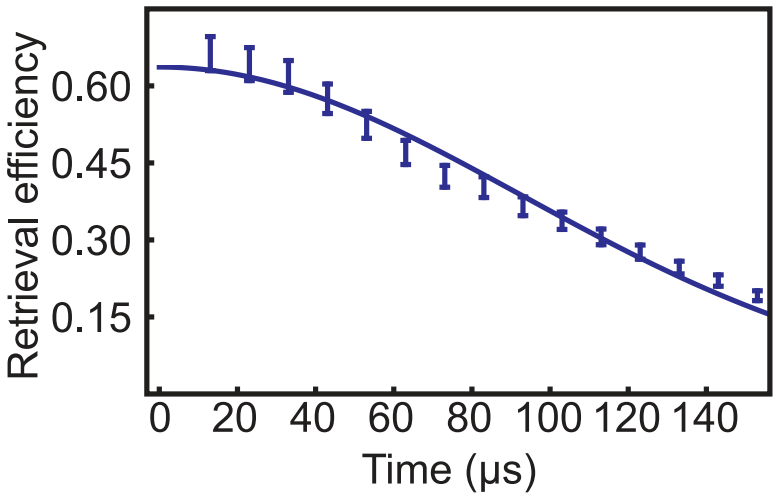

Figure 5.13: Decay of the memory efficiency with storage time. The decay time is fitted to a Gaussian decay of characteristic time $(130 \pm 10)\,\mu s$.

halves, the addition of a second, backward, control and the relative phase control of all four beams.

The TRACE memory scheme can be linked up with SL and specifically the application proposal to generate cross-phase modulation between a target state, stored in the middle of an atomic ensemble, and a signal state producing stationary light [Everett2017]. The ideal signal state can be efficiently generated using the TRACE protocol, while leaving the memory accessible for storing the target state at the centre and in the same mode as the signal state.

5.5 Future investigation of stationary light

The two experiments reported in this chapter demonstrate our increasing understanding of Raman SL systems, whose dynamics was confused with diffraction off Bragg gratings in the earlier investigations from the community. Harnessing this form of light promises applications in non-linear photon-photon interaction between stored signals which keep a non-vanishing optical component, in contrast with stopped-light experiments. Our future endeavour are aimed at this direction, with the experimental realisation of cross-phase modulation between a single photon and coherent light, or even between two single photons. Our single photons would either be provided by a spontaneous-parametric-down-conversion (SPDC) source built in Andrew White's group and brought to the ANU [Rambach2016], or generated by four-wave mixing in a second cold atomic ensemble for which a MOT is being built.

Chapter Conclusion

In this chapter, I have reported on two experiments based on stationary light:

- The first one provided a model for the dynamics of self-stabilisation of stationary light. Several spin-wave spatial distributions were prepared in an atomic ensemble and their evolution was monitored by imaging the spin waves at different times. The model and the measured spin wave structure over time showed excellent agreement. This work enabled the observation of stationary light although this light was not directly observable as it does not escape the atomic ensemble.
- The TRACE memory scheme was proposed and demonstrated. This scheme relies on the interference between the writing process of counter-propagating signals to the same spin wave. This new form of a free-space memory shows a single-mode character, which benefits from a better scaling of the efficiency with OD than regular free-space memories. It also enables the efficient generation of the ideal target state to perform cross-phase-modulation with a stationary-light signal.

Conclusion

The work of this PhD has been focused on the preparation of large atomic ensembles and the enhancement of their interfacing with light. The increase of the optical depth in these ensembles is the universally-known method of accessing the efficient mapping of light to and from collective excitations in atomic ensembles. The implementation of state-of-the-art cold-atom preparation methods both at ANU and LKB has led to a steady increase of this figure of merit over the last years. This has enabled the high-performance memory-scheme implementations described in this thesis. In particular this PhD work has seen the breaking of the no-cloning limit for EIT-based qubit storage, more than doubling the previous figure for any qubit storage, along with a memory fidelity close to unity. A second highlight was the advantageous use of backward retrieval in a Raman memory, which contributed to beating the efficiency record for Raman optical memories. These experimental achievements were nonetheless accompanied by significant theoretical progress on understanding these platforms, especially at high optical depths, with the development of a model describing the contributions of additional excited levels in EIT storage, a model which showed a strong agreement with the experimental data, which could be taken over a large range of optical depths thanks to the efficient preparation method. In Raman configurations, it was the symmetries in the geometry and detunings to the excited level that were central to the study of the self-stabilisation of stationary light in a gradient echo memory and the time-reversed and coherently-enhanced memory scheme envisioned and its concept proved experimentally in the course of this PhD.

The performance of the investigated memory schemes is shown in table 5.1. The implementations aimed at different figures of merit but as the achieved optical depths were relatively similar, we are not surprised to observe comparable memory efficiencies. In all cases, this high atomic ensemble density was a prerequisite for efficient light-matter interfacing, which has been the common theme of all the experiments presented in this thesis.

The developments described in this thesis offer many options for future investigations. The generation of single photons with the DLCZ protocol is still a source of struggle, but now that the atomic ensemble has overcome the optical-depth limitation it was running into as a standard 3D-MOT, there should be a sufficiently-strong atom-light coupling to enable the efficient heralding efficiency of the single-photon while keeping a high non-classical character. Machine-learning applied to the optimisation of an atom-light experiment has been a increasingly-exciting aspect of this PhD over the last months, and a significant help generating and maintaining a high-performance atomic ensemble, with an automatic execution of the parameters tweaks to go from high to very high optical depths, which can otherwise be quite a burden on a daily basis in the lab. However, machine-learning is giving promises to provide much more than a few time-saving adjustments: the solutions it has found to optimise compression-and-cooling sequences,

Memory scheme	Qubit storage with EIT	Backward-retrieval Raman		TRACE
Efficiency η	$(68.5 \pm 2)\%$	$(65 \pm 6)\%$		$(58 \pm 8)\%$
Storage time T_S (Signal duration)	15 µs (1.0 µs)	60 µs (360 ns)	110 µs (5 µs)	110 µs (5 µs)
Other figures of merit	Quantum with 0.02 photons Fidelity up to $97 \pm 1\%$	Delay-bandwidth product= 160		
Corresponding section	Section 3.3	Section 4.2		Section 5.4

Table 5.1: Performance figures for the memory scheme implementations reported in this thesis.$\Delta\omega_{\max}$ stands for maximum memory bandwidth. References to the articles reporting the figures for efficiency and storage time are given in table .

for example, demonstrate that it can find unexpected optimal sequences, which would probably be impossible for a human to converge to. In a not-so-distant future, new applications of such machine-learning algorithms will be to directly optimise an optical memory. From there, we can expect the emergence of machine-learning optimisation of any atom-light interaction protocol, which is definitely a fascinating prospect and is likely to revolutionise our approach to quantum-information implementations in atomic ensembles.

Appendix

Numerical simulations: optimal signal shape (Mathematica)

Computation of storage-and-retrieval integral kernels (Surmacz2008.m)

As hinted by its name, this script adapts the optimisation method presented in Appendix A of [Surmacz2008]. The script uses the same notations as subsection 4.1.2 of this thesis, itself after this research article. The reader is referred to those concerning the formalism and theory behind this computation.

The combined processes of storage and retrieval of an incident signal field by given control fields is associated with a Green's function K. To compare the cases of forward and backward retrieval, we introduce here the integral kernels $\tilde{K}_{\mathrm{FW}}$ and $\tilde{K}_{\mathrm{BW}}$, respectively, defined as:

$$\tilde{K}_{\mathrm{FW}} = \int_0^C \mathrm{d}x\, k(y,x)k(C-x,y) \exp\left[2\mathrm{i}\left(\delta\chi + k_d L\right) x/C\right] \quad \text{and}$$

$$\tilde{K}_{\mathrm{BW}} = \int_0^C \mathrm{d}x\, k(y,x)k(x,y) \exp\left[2\mathrm{i}\left(\delta\chi + k_d L\right) x/C\right].$$

The complex exponential factor $\exp\left[2\mathrm{i}\left(\delta\chi + k_d L\right) x/C\right]$ accounts for the momentum mismatch of the stored spin-wave. The phase-matching is supposed perfect in this script, and so this factor is ignored.

Surmacz2008.m

```
(* ::Package:: *)
d = 100. (* OD *)
Delta = 20. (*in units of gamma*)
ComplexGamma = 1+I*Delta (*in units of gamma*)
BetaParam = Pi/2. - Arg[ComplexGamma]

(*for reference*)
gamma = 5.*^6 (*Hz*)
Tau = 1.*^-5 (*s*)
c = 3.*^8
L = 1.*^-2

PulseDuration = 1./12. (*in units of Tau*)
ControlDuration = 1./6. (*in units of Tau*)
$Assumptions=Element[t,Reals]
```

```
(*Gaussian, squared normalised*)
Gaussian = Function[{x,sigma},
    (2./Pi)^(1./4.)/Sqrt[sigma]*Exp[-x^2/sigma^2]]
(*Control Rabi frequency*)
Omega0 = 5.
OmegaPrime[t_?NumericQ] := OmegaPrime[t] =
    Omega0*Gaussian[t-1,ControlDuration]

W = NIntegrate[OmegaPrime[x]^2, {x, 0.,2.}]
R = Re[Sqrt[W/d]]
Coupling = Re[Sqrt[d*W]/Abs[ComplexGamma]]
omega = Function[t, NIntegrate[OmegaPrime[x]^2, {x,0., t}]]

k = Function[{x, y}, Exp[-Sin[BetaParam]*(x/R + R*y)]
    * BesselJ[0, 2.*Exp[I*BetaParam]*Sqrt[x*y]]]
(*Gorshkov: k[x_,y_] := k[x,y] = d/2. * Exp[-d*(1.-(x+y)/2.)]
    * BesselI[0, d*Sqrt[(1.-x)*(1.-y)]]*)

KtildeFW = Function[{y, yPrime}, NIntegrate[Re[k[y, x]]
    * Re[k[Coupling - x, yPrime]], {x, 0., Coupling}]]
KtildeBW = Function[{y, yPrime}, NIntegrate[Re[k[y, x]]
    * Re[k[x, yPrime]] * Exp[2.*I*0.*x/Coupling], {x, 0., Coupling}]]
```

Optimal signal profile from Singular Value Decomposition (SpinwavesFW_Surmacz2008.nb)

This notebook imports the KtildeFW and KtildeBW functions from **Surmacz2008.m** and finds their Singular Value Decomposition (SVD). The right singular function associated with the largest singular value corresponds to the optimal input mode for the provided control profile.

SpinwavesFW_Surmacz2008.nb

```
Get["Surmacz2008.m"]
SVD[Sampling_] :=
  Module[{Sampl = Sampling},
      KtildeMatrixFW := ParallelTable[KtildeFW[y*Coupling/Sampl,
          yPrime*Coupling/Sampl],{y, 0, Sampl}, {yPrime, 0, Sampl}];
      {u,LambdaFW1,PhiFW1temp} =
    SingularValueDecomposition[KtildeMatrixFW,1];
  ]

Table[ParallelSubmit[{i}, SVD[i]], {i, 50, 150, 50}]
```

```
Output = WaitAll[%]

PhiFW[i_] := Output[[i]][[1]]; LambdaFW[i_] := Output[[i]][[2]];
VectorY[Sampling_] := Range[0, Coupling, Coupling/Sampling];
FPhyFW[Sampling_] := Table[{VectorY[Sampling][[n]],
    PhiFW[Sampling/50][[n]][[1]]}, {n, 1, Sampling}]

Sampling = 150;
InterPhiFW[Sampling_] := Interpolation[FPhyFW[Sampling]]

VarPhiFW1 = Function[t, Exp[I*omega[t]*Delta/Abs[ComplexGamma]^2]
    * OmegaPrime[t]*InterPhiFW[150][Coupling*(1. - omega[t]/W)]]
InterVarPhiFW1 = Interpolation[ParallelTable[{0.5 + n/Sampling,
    VarPhiFW1[0.5 + n/Sampling]}, {n, 1, Sampling}]];

A0 = NIntegrate[Abs[InterVarPhiFW1[y]]^2, {y, 0.5, 1.5}]
InterVarPhiFW1Norm[y_] = InterVarPhiFW1[y]/Sqrt[A0]
{MaxY, ruleX} = FindMaximum[Abs[InterVarPhiFW1Norm[t]]^2,
    {t, 1., 0.5, 1.5}]
MaxX = t /. ruleX

KtildeMatrixBW = ParallelTable[KtildeBW[y*Coupling/Sampling,
    yPrime*Coupling/Sampling], {y, Sampling}, {yPrime, Sampling}];

{uBW, LambdaBW1, PhiBW1} =
    SingularValueDecomposition[KtildeMatrixBW, 1]

FPhyBW[Sampling_] := Table[{VectorY[Sampling][[n]],
    PhiBW1[[n]][[1]]}, {n, 1, Sampling}]
InterPhiBW[Sampling_] := Interpolation[FPhyBW[Sampling]]
VarPhiBW1 = Function[t, Exp[I*omega[t]*Delta/Abs[ComplexGamma]^2]
    * OmegaPrime[t]*InterPhiBW[150][Coupling*(1. - omega[t]/W)]]
MaxVarPhy = FindMaxValue[Abs[VarPhiBW1[y]], {y, 1., 0.6, 1.4}]

Plot[{OmegaPrime[x]/OmegaPrime[1], Abs[VarPhiBW1[x]]/MaxVarPhy},
    {x, 0.5, 1.5}, PlotRange -> All]
```

Bibliography

[Afzelius2010a] Mikael Afzelius & Christoph Simon. *Impedance-matched cavity quantum memory.* Physical Review A, 82(2):022310, 2010. doi:10.1103/physreva.82.022310. 28

[Afzelius2009] Mikael Afzelius, Christoph Simon, Hugues De Riedmatten & Nicolas Gisin. *Multimode quantum memory based on atomic frequency combs.* Physical Review A, 79(5):052329, 2009. doi:10.1103/physreva.79.052329. 28

[Afzelius2010] Mikael Afzelius, Imam Usmani, Atia Amari, Björn Lauritzen, Andreas Walther, Christoph Simon, Nicolas Sangouard, Jiří Minář, Hugues De Riedmatten, Nicolas Gisin et al. *Demonstration of atomic frequency comb memory for light with spin-wave storage.* Physical Review Letters, 104(4):040503, 2010. doi:10.1103/physrevlett.104.040503. 28

[Alexander2006] A. L. Alexander, J. J. Longdell, M. J. Sellars & N. B. Manson. *Photon Echoes Produced by Switching Electric Fields.* Physical Review Letters, 96(4):043602, February 2006. doi:10.1103/PhysRevLett.96.043602. 31, 93

[Alzetta1976] G. Alzetta, A. Gozzini, L. Moi & G. Orriols. *An experimental method for the observation of r.f. transitions and laser beat resonances in oriented Na vapour.* Il Nuovo Cimento B (1971-1996), 36(1):5–20, November 1976. doi:10.1007/BF02749417. 28

[Andre2005] A André, M D Eisaman, R L Walsworth, A S Zibrov & M D Lukin. *Quantum control of light using electromagnetically induced transparency.* Journal of Physics B: Atomic, Molecular and Optical Physics, 38(9):S589–S604, April 2005. doi:10.1088/0953-4075/38/9/010. 28, 115

[Andre2002] A. André & M. D. Lukin. *Manipulating Light Pulses via Dynamically Controlled Photonic Band gap.* Physical Review Letters, 89(14):143602, September 2002. doi:10.1103/PhysRevLett.89.143602. 115, 116

[Anisimov2008] Petr Anisimov & Olga Kocharovskaya. *Decaying-dressed-state analysis of a coherently driven three-level Λ system.* Journal of Modern Optics, 55(19-20):3159–3171, November 2008. doi:10.1080/09500340802302378. 70

[Arimondo1996a] Ennio Arimondo. *Relaxation processes in coherent-population trapping.* Physical Review A, 54(3):2216–2223, September 1996. doi:10.1103/PhysRevA.54.2216. 40

[Aspect1988] A. Aspect, E. Arimondo, R. Kaiser, N. Vansteenkiste & C. Cohen-Tannoudji. *Laser Cooling below the One-Photon Recoil Energy by Velocity-Selective Coherent Population Trapping.* Physical Review Letters, 61(7):826–829, August 1988. doi:10.1103/PhysRevLett.61.826. 28

[Aspelmeyer2003] M. Aspelmeyer, T. Jennewein, M. Pfennigbauer, W. R. Leeb & A. Zeilinger. *Long-distance quantum communication with entangled photons using satellites.* IEEE Journal of Selected Topics in Quantum Electronics, 9(6):1541–1551, 2003. doi:10.1109/JSTQE.2003.820918. 20

[August2017] Moritz August & Xiaotong Ni. *Using recurrent neural networks to optimize dynamical decoupling for quantum memory.* Physical Review A, 95(1):012335, 2017. doi:10.1103/PhysRevA.95.012335. 59

[Autler1955] S. H. Autler & C. H. Townes. *Stark Effect in Rapidly Varying Fields.* Physical Review, 100(2):703–722, October 1955. doi:10.1103/PhysRev.100.703. 67

[Bajcsy2003] M. Bajcsy, A. S. Zibrov & M. D. Lukin. *Stationary pulses of light in an atomic medium.* Nature, 426(6967):638–641, December 2003. doi:10.1038/nature02176. 115, 117

[Balabas2013] M. V. Balabas & O. Yu Tretiak. *Comparative study of alkali-vapour cells with alkane-, alkeneand 1-nonadecylbenzene-based antirelaxation wall coatings.* Quantum Electronics, 43(12):1175, 2013. doi:10.1070/QE2013v043n12ABEH015196. 40

[Bao2012] Xiao-Hui Bao, Andreas Reingruber, Peter Dietrich, Jun Rui, Alexander Duck, Thorsten Strassel, Li Li, Nai-Le Liu, Bo Zhao & Jian-Wei Pan. *Efficient and long-lived quantum memory with cold atoms inside a ring cavity.* Nature Physics, 8(7):517–521, July 2012. doi:10.1038/nphys2324. 110

[Bennett1983] Charles H. Bennett, Gilles Brassard, Seth Breidbart & Stephen Wiesner. *Quantum Cryptography, or Unforgeable Subway Tokens.* In *Advances in Cryptology*, pages 267–275. Springer, Boston, MA, 1983. ISBN 978-1-4757-0604-8 978-1-4757-0602-4. 20

[Blatt2016] Frank Blatt, Lachezar S. Simeonov, Thomas Halfmann & Thorsten Peters. *Stationary light pulses and narrowband*

light storage in a laser-cooled ensemble loaded into a hollow-core fiber. Physical Review A, 94(4):043833, October 2016. doi:10.1103/PhysRevA.94.043833. 29

[Boller1991] K.-J. Boller, A. Imamoglu & S. E. Harris. *Observation of electromagnetically induced transparency*. Physical Review Letters, 66(20):2593–2596, 1991. doi:10.1103/PhysRevLett.66.2593. 28

[Bouchiat1966] M. A. Bouchiat & J. Brossel. *Relaxation of Optically Pumped Rb Atoms on Paraffin-Coated Walls*. Physical Review, 147(1):41–54, July 1966. doi:10.1103/PhysRev.147.41. 40

[Braje2004] Danielle A. Braje, Vlatko Balić, Sunil Goda, G. Y. Yin & S. E. Harris. *Frequency mixing using electromagnetically induced transparency in cold atoms*. Physical Review Letters, 93:183601, October 2004. doi:10.1103/PhysRevLett.93.183601. 102, 112

[Braunstein2005] Samuel L. Braunstein & Peter van Loock. *Quantum information with continuous variables*. Reviews of Modern Physics, 77(2):513–577, June 2005. doi:10.1103/RevModPhys.77.513. 9

[Briegel1998] H.-J. Briegel, W. Dür, J. I. Cirac & P. Zoller. *Quantum repeaters: The role of imperfect local operations in quantum communication*. Physical Review Letters, 81(26):5932–5935, 1998. doi:10.1103/PhysRevLett.81.5932. 20

[Burks2010PhD] Sidney Burks. *Towards A Quantum Memory For Non-Classical Light With Cold Atomic Ensembles*. Ph.D. thesis, Université Pierre et Marie Curie - Paris VI, October 2010. `https://tel.archives-ouvertes.fr/tel-00699270/document`. 65

[Bussieres2013] Félix Bussières, Nicolas Sangouard, Mikael Afzelius, Hugues de Riedmatten, Christoph Simon & Wolfgang Tittel. *Prospective applications of optical quantum memories*. Journal of Modern Optics, 60(18):1519–1537, October 2013. doi:10.1080/09500340.2013.856482. 22, 23, 26

[Bustard2013] Philip J. Bustard, Rune Lausten, Duncan G. England & Benjamin J. Sussman. *Toward quantum processing in molecules: A THz-bandwidth coherent memory for light*. Physical Review Letters, 111(8):083901, 2013. doi:10.1103/PhysRevLett.111.083901. 30

[Campbell2012] G. Campbell, M. Hosseini, B. M. Sparkes, P. K. Lam & B. C. Buchler. *Time- and frequency-domain polariton interference*.

New Journal of Physics, 14(3):033022, 2012. doi:10.1088/1367-2630/14/3/033022. 110, 129

[Campbell2014] GT Campbell, Olivier Pinel, Mahdi Hosseini, Timothy Cameron Ralph, BC Buchler & Ping Koy Lam. *Configurable Unitary Transformations and Linear Logic Gates Using Quantum Memories.* Physical Review Letters, 113(6):063601, August 2014. doi:10.1103/PhysRevLett.113.063601. 26

[Chaneliere2005] T. Chanelière, D. N. Matsukevich, S. D. Jenkins, S.-Y. Lan, T. A. B. Kennedy & A. Kuzmich. *Storage and retrieval of single photons transmitted between remote quantum memories.* Nature, 438(7069):833–836, December 2005. doi:10.1038/nature04315. 21

[Chaneliere2015] Thierry Chanelière & Gabriel Hétet. *Light-shift-modulated photon-echo.* Optics Letters, 40(7):1294–1297, April 2015. doi:10.1364/OL.40.001294. 31

[Chen2013a] Bing Chen, Kai Zhang, Chengling Bian, Cheng Qiu, Chun-Hua Yuan, L. Q. Chen, Z. Y. Ou & Weiping Zhang. *Efficient raman frequency conversion by coherent feedback at low light intensity.* Optics Express, 21(9):10490–10495, May 2013. doi:10.1364/OE.21.010490. 29

[Chen2013] Yi-Hsin Chen, Meng-Jung Lee, I-Chung Wang, Shengwang Du, Yong-Fan Chen, Ying-Cheng Chen & Ite A. Yu. *Coherent optical memory with high storage efficiency and large fractional delay.* Physical Review Letters, 110(8), February 2013. doi:10.1103/physrevlett.110.083601. 34

[Cho2016] Y.-W. Cho, G. T. Campbell, J. L. Everett, J. Bernu, D. B. Higginbottom, M. T. Cao, J. Geng, N. P. Robins, P. K. Lam & B. C. Buchler. *Highly efficient optical quantum memory with long coherence time in cold atoms.* Optica, 3(1):100–107, January 2016. doi:10.1364/OPTICA.3.000100. 27, 31, 34

[Cho2010] Young-Wook Cho & Yoon-Ho Kim. *Atomic vapor quantum memory for a photonic polarization qubit.* Optics Express, 18(25):25786–25793, December 2010. doi:10.1364/OE.18.025786. 28

[Choi2008] K. S. Choi, H. Deng, J. Laurat & H. J. Kimble. *Mapping photonic entanglement into and out of a quantum memory.* Nature, 452(7183):67–71, March 2008. doi:10.1038/nature06670. 28

[Chou2004] C. W. Chou, S. V. Polyakov, A. Kuzmich & H. J. Kimble. *Single-photon generation from stored excitation in an*

atomic ensemble. Physical Review Letters, 92(21):213601, 2004. doi:10.1103/PhysRevLett.92.213601. 21

[Chrapkiewicz2014] Radosław Chrapkiewicz, Wojciech Wasilewski & Czesław Radzewicz. *How to measure diffusional decoherence in multimode rubidium vapor memories?* Optics Communications, 317:1–6, 2014. doi:10.1016/j.optcom.2013.12.020. 40

[Cirac2000] J. I. Cirac & P. Zoller. *A scalable quantum computer with ions in an array of microtraps*. Nature, 404(6778):579–581, April 2000. doi:10.1038/35007021. 21

[Clausen2012] Christoph Clausen, Félix Bussières, Mikael Afzelius & Nicolas Gisin. *Quantum storage of heralded polarization qubits in birefringent and anisotropically absorbing materials*. Physical Review Letters, 108:190503, May 2012. doi:10.1103/PhysRevLett.108.190503. 28

[Clausen2011] Christoph Clausen, Imam Usmani, Felix Bussieres, Nicolas Sangouard, Mikael Afzelius, Hugues de Riedmatten & Nicolas Gisin. *Quantum storage of photonic entanglement in a crystal*. Nature, 469(7331):508–511, January 2011. doi:10.1038/nature09662. 28

[Clauser1969] John F. Clauser, Michael A. Horne, Abner Shimony & Richard A. Holt. *Proposed Experiment to Test Local Hidden-Variable Theories*. Physical Review Letters, 23(15):880–884, October 1969. doi:10.1103/PhysRevLett.23.880. 7

[Cviklinski2008PhD] Jean Cviklinski. *Interface quantique atomes-champ en régime de variables continues*. Ph.D. thesis, Université Pierre et Marie Curie - Paris VI, 2008. `https://tel.archives-ouvertes.fr/tel-00315360`. 40

[Dajczgewand2014] Julián Dajczgewand, Jean-Louis Le Gouët, Anne Louchet-Chauvet & Thierry Chanelière. *Large efficiency at telecom wavelength for optical quantum memories*. Opt. Lett., 39(9):2711–2714, May 2014. doi:10.1364/OL.39.002711. 31

[Damon2011] V. Damon, M. Bonarota, A. Louchet-Chauvet, T. Chanelière & J.-L. Le Gouët. *Revival of silenced echo and quantum memory for light*. New Journal of Physics, 13(9):093031, 2011. doi:10.1088/1367-2630/13/9/093031. 31

[Datta2012] Animesh Datta, Lijian Zhang, Joshua Nunn, Nathan K. Langford, Alvaro Feito, Martin B. Plenio & Ian A. Walmsley. *Compact Continuous-Variable Entanglement Distillation*. Physical Review Letters, 108(6):060502, February 2012. doi:10.1103/PhysRevLett.108.060502. 110

[Riedmatten2008] Hugues de Riedmatten, Mikael Afzelius, Matthias U. Staudt, Christoph Simon & Nicolas Gisin. *A solid-state light-matter interface at the single-photon level.* Nature, 456(7223):773–777, December 2008. doi:10.1038/nature07607. 26

[Du2008] Shengwang Du, Pavel Kolchin, Chinmay Belthangady, G. Y. Yin & S. E. Harris. *Subnatural linewidth biphotons with controllable temporal length.* Physical Review Letters, 100(18):183603, May 2008. doi:10.1103/PhysRevLett.100.183603. 89

[Duan2001] L.-M. Duan, M. D. Lukin, J. I. Cirac & P. Zoller. *Long-distance quantum communication with atomic ensembles and linear optics.* Nature, 414(6862):413–418, November 2001. doi:10.1038/35106500. 21, 23

[Dudin2013] Y. O. Dudin, L. Li & A. Kuzmich. *Light storage on the time scale of a minute.* Physical Review A, 87(3):031801, 2013. doi:10.1103/PhysRevA.87.031801. 24, 110

[Eberly1994] J. H. Eberly, M. L. Pons & H. R. Haq. *Dressed-field pulses in an absorbing medium.* Physical Review Letters, 72(1):56–59, January 1994. doi:10.1103/PhysRevLett.72.56. 66

[England2012] D. G. England, P. S. Michelberger, T. F. M. Champion, K. F. Reim, K. C. Lee, M. R. Sprague, X.-M. Jin, N. K. Langford, W. S. Kolthammer, J. Nunn & I. A. Walmsley. *High-fidelity polarization storage in a gigahertz bandwidth quantum memory.* Journal of Physics B: Atomic, Molecular and Optical Physics, 45(12):124008, 2012. doi:10.1088/0953-4075/45/12/124008. 34

[Erhard2001] Michael Erhard & Hanspeter Helm. *Buffer-gas effects on dark resonances: Theory and experiment.* Physical Review A, 63(4):043813, March 2001. doi:10.1103/PhysRevA.63.043813. 40

[Everett2017] J. L. Everett, G. T. Campbell, Y.-W. Cho, P. Vernaz-Gris, D.B. Higginbottom, O. Pinel, N. P. Robins, P. K. Lam & B. C. Buchler. *Dynamical observations of self-stabilizing stationary light.* Nature Physics, 13(1):68–73, January 2017. doi:10.1038/nphys3901. iv, 29, 115, 121, 122, 136

[Everett2018] J. L. Everett, P. Vernaz-Gris, G. T. Campbell, A. D. Tranter, K. V. Paul, A. C. Leung, P. K. Lam & B. C. Buchler. *Time-reversed and coherently enhanced memory: A single-mode quantum atom-optic memory without a cavity.* Phys. Rev. A, 98:063846, Dec 2018. doi:10.1103/PhysRevA.98.063846. iv, 115

[Fekete2013] Julia Fekete, Daniel Rieländer, Matteo Cristiani & Hugues de Riedmatten. *Ultranarrow-Band Photon-Pair Source Compatible with Solid State Quantum Memories and Telecommunication Networks.* Physical Review Letters, 110(22):220502, May 2013. doi:10.1103/PhysRevLett.110.220502. 89

[Fleischhauer2002] M. Fleischhauer & M. D. Lukin. *Quantum memory for photons: Dark-state polaritons.* Physical Review A, 65(2):022314, January 2002. doi:10.1103/PhysRevA.65.022314. 28, 69, 70

[Fleischhauer2000] M. Fleischhauer, S.F. Yelin & M.D. Lukin. *How to trap photons ? storing single-photon quantum states in collective atomic excitations.* Optics Communications, 179(1-6):395–410, 2000. doi:10.1016/s0030-4018(99)00679-3. 22, 23, 28

[Fleischhauer2005] Michael Fleischhauer, Atac Imamoglu & Jonathan P. Marangos. *Electromagnetically induced transparency: Optics in coherent media.* Reviews of Modern Physics, 77(2):633–673, July 2005. doi:10.1103/RevModPhys.77.633. 67

[Gaubatz1988] U. Gaubatz, P. Rudecki, M. Becker, S. Schiemann, M. Külz & K. Bergmann. *Population switching between vibrational levels in molecular beams.* Chemical Physics Letters, 149(5):463–468, September 1988. doi:10.1016/0009-2614(88)80364-6. 66

[Gea-Banacloche2010] Julio Gea-Banacloche. *Impossibility of large phase shifts via the giant Kerr effect with single-photon wave packets.* Physical Review A, 81(4):043823, April 2010. doi:10.1103/PhysRevA.81.043823. 27

[Geng2014] J. Geng, G. T. Campbell, J. Bernu, D. B. Higginbottom, B. M. Sparkes, S. M. Assad, W. P. Zhang, N. P. Robins, P. K. Lam & B. C. Buchler. *Electromagnetically induced transparency and four-wave mixing in a cold atomic ensemble with large optical depth.* New Journal of Physics, 16(11):113053, 2014. doi:10.1088/1367-2630/16/11/113053. 65

[Giner2013] L. Giner, L. Veissier, B. Sparkes, A. S. Sheremet, A. Nicolas, O. S. Mishina, M. Scherman, S. Burks, I. Shomroni, D. V. Kupriyanov, P. K. Lam, E. Giacobino & J. Laurat. *Experimental investigation of the transition between Autler-Townes splitting and electromagnetically-induced-transparency models.* Physical Review A, 87(1):013823, January 2013. doi:10.1103/PhysRevA.87.013823. 65, 68

[Giner2013PhD] Lambert Giner. *Etude de la transparence électromagnétiquement induite dans un ensemble d'atomes froids et application aux mémoires quantiques.* Ph.D. thesis, Université Pierre

et Marie Curie - Paris VI, 2013. `http://www.theses.fr/2013PA066099`. 38, 46, 65

[Gisin2002] Nicolas Gisin, Grégoire Ribordy, Wolfgang Tittel & Hugo Zbinden. *Quantum cryptography*. Reviews of Modern Physics, 74(1):145–195, March 2002. doi:10.1103/RevModPhys.74.145. 20

[Gorshkov2007] Alexey V. Gorshkov, Axel André, Michael Fleischhauer, Anders S. Sørensen & Mikhail D. Lukin. *Universal approach to optimal photon storage in atomic media*. Physical Review Letters, 98:123601, March 2007. doi:10.1103/PhysRevLett.98.123601. 23, 102, 131

[Gorshkov2007a] Alexey V. Gorshkov, Axel André, Mikhail D. Lukin & Anders S. Sørensen. *Photon storage in Λ-type optically dense atomic media. i. cavity model*. Physical Review A, 76:033804, September 2007. doi:10.1103/PhysRevA.76.033804. 23, 30, 95

[Gorshkov2007b] Alexey V. Gorshkov, Axel André, Mikhail D. Lukin & Anders S. Sørensen. *Photon storage in Λ-type optically dense atomic media. ii. free-space model*. Physical Review A, 76:033805, September 2007. doi:10.1103/PhysRevA.76.033805. 12, 23, 95, 96, 101, 102, 103, 129, 131

[Gorshkov2007c] Alexey V. Gorshkov, Axel André, Mikhail D. Lukin & Anders S. Sørensen. *Photon storage in Λ-type optically dense atomic media. iii. effects of inhomogeneous broadening*. Physical Review A, 76:033806, September 2007. doi:10.1103/PhysRevA.76.033806. 95

[Gorshkov2008] Alexey V. Gorshkov, Tommaso Calarco, Mikhail D. Lukin & Anders S. Sørensen. *Photon storage in Λ-type optically dense atomic media. IV. Optimal control using gradient ascent*. Physical Review A, 77(4):043806, April 2008. doi:10.1103/PhysRevA.77.043806. 102

[Gouraud2016PhD] Baptiste Gouraud. *Optical nanofibers interfacing cold toms. A tool for quantum optics*. Ph.D. thesis, Université Pierre et Marie Curie - Paris VI, 2016. `https://tel.archives-ouvertes.fr/tel-01359867/document`. 46

[Grosshans2001] Frédéric Grosshans & Philippe Grangier. *Quantum cloning and teleportation criteria for continuous quantum variables*. Physical Review A, 64(1):010301, 2001. doi:10.1103/PhysRevA.64.010301. 23

[Gundogan2013] M Gündoğan, M Mazzera, P M Ledingham, M Cristiani & H de Riedmatten. *Coherent storage of temporally multimode light using a spin-wave atomic frequency comb memory.* New Journal of Physics, 15(4):045012, 2013. doi:10.1088/1367-2630/15/4/045012. 28

[Gundogan2012] Mustafa Gündoğan, Patrick M. Ledingham, Attaallah Almasi, Matteo Cristiani & Hugues de Riedmatten. *Quantum storage of a photonic polarization qubit in a solid.* Physical Review Letters, 108:190504, May 2012. doi:10.1103/PhysRevLett.108.190504. 28, 86

[Hammerer2010] Klemens Hammerer, Anders S. Sørensen & Eugene S. Polzik. *Quantum interface between light and atomic ensembles.* Reviews of Modern Physics, 82:1041–1093, April 2010. doi:10.1103/RevModPhys.82.1041. 25, 37

[Harrow2009] Aram W. Harrow, Avinatan Hassidim & Seth Lloyd. *Quantum Algorithm for Linear Systems of Equations.* Physical Review Letters, 103(15):150502, October 2009. doi:10.1103/PhysRevLett.103.150502. 20

[Hedges2010] Morgan P. Hedges, Jevon J. Longdell, Yongmin Li & Matthew J. Sellars. *Efficient quantum memory for light.* Nature, 465(7301):1052–1056, June 2010. doi:10.1038/nature09081. 26, 93

[Heinze2013] Georg Heinze, Christian Hubrich & Thomas Halfmann. *Stopped Light and Image Storage by Electromagnetically Induced Transparency up to the Regime of One Minute.* Physical Review Letters, 111(3):033601, July 2013. doi:10.1103/PhysRevLett.111.033601. 24, 34

[Heshami2016] Khabat Heshami, Duncan G. England, Peter C. Humphreys, Philip J. Bustard, Victor M. Acosta, Joshua Nunn & Benjamin J. Sussman. *Quantum memories: emerging applications and recent advances.* Journal of Modern Optics, 63(20):2005–2028, 2016. doi:10.1080/09500340.2016.1148212. 10, 22, 23

[Higginbottom2015] D. B. Higginbottom, J. Geng, G. T. Campbell, M. Hosseini, M. T. Cao, B. M. Sparkes, J. Bernu, N. P. Robins, P. K. Lam & B. C. Buchler. *Dual-rail optical gradient echo memory.* Optics Express, 23(19):24937–24944, September 2015. doi:10.1364/OE.23.024937. 25, 31, 93

[Higginbottom2012] D. B. Higginbottom, B. M. Sparkes, M. Rancic, O. Pinel, M. Hosseini, P. K. Lam & B. C. Buchler. *Spatial-mode storage in a gradient-echo memory.* Physical Review A, 86:023801, August 2012. doi:10.1103/PhysRevA.86.023801. 25, 31

[Horodecki1996] Michał Horodecki, Paweł Horodecki & Ryszard Horodecki. *Separability of mixed states: necessary and sufficient conditions.* Physics Letters A, 223(1):1–8, November 1996. doi:10.1016/S0375-9601(96)00706-2. 7

[Horsley2013] Andrew Horsley, Guan-Xiang Du, Matthieu Pellaton, Christoph Affolderbach, Gaetano Mileti & Philipp Treutlein. *Imaging of relaxation times and microwave field strength in a microfabricated vapor cell.* Physical Review A, 88(6):063407, December 2013. doi:10.1103/PhysRevA.88.063407. 40, 46

[Hosseini2012] M. Hosseini, B. M. Sparkes, G. T. Campbell, P. K. Lam & B. C. Buchler. *Storage and manipulation of light using a Raman gradient-echo process.* Journal of Physics B: Atomic, Molecular and Optical Physics, 45(12):124004, 2012. doi:10.1088/0953-4075/45/12/124004. 40

[Hosseini2011] M. Hosseini, B.M. Sparkes, G. Campbell, P.K. Lam & B.C. Buchler. *High efficiency coherent optical memory with warm rubidium vapour.* Nature Communications, 2:174, February 2011. doi:10.1038/ncomms1175. 31, 34, 93

[Hosseini2012PhD] Mahdi Hosseini. *Quantum Optical Storage and Processing Using Raman Gradient Echo Memory.* Ph.D. thesis, The Australian National University, 2013. `http://photonics.anu.edu.au/qoptics/theses.php`. 106

[Hosseini2009] Mahdi Hosseini, Ben M. Sparkes, Gabriel Hétet, Jevon J. Longdell, Ping Koy Lam & Ben C. Buchler. *Coherent optical pulse sequencer for quantum applications.* Nature, 461(7261):241–245, September 2009. doi:10.1038/nature08325. 31

[Hsiao2014] Ya-Fen Hsiao, Hung-Shiue Chen, Pin-Ju Tsai & Ying-Cheng Chen. *Cold atomic media with ultrahigh optical depths.* Physical Review A, 90:055401, November 2014. doi:10.1103/PhysRevA.90.055401. 40

[Hsiao2016] Ya-Fen Hsiao, Pin-Ju Tsai, Hung-Shiue Chen, Sheng-Xiang Lin, Chih-Chiao Hung, Chih-Hsi Lee, Yi-Hsin Chen, Yong-Fan Chen, Ite A. Yu & Ying-Cheng Chen. *Highly efficient coherent optical memory based on electromagnetically induced transparency.* Phys. Rev. Lett., 120:183602, May 2018. doi:10.1103/PhysRevLett.120.183602. 75, 89

[Hughes2002] Richard J. Hughes, Jane E. Nordholt, Derek Derkacs & Charles G. Peterson. *Practical free-space quantum key distribution over 10 km in daylight and at night.* New Journal of Physics, 4(1):43, 2002. doi:10.1088/1367-2630/4/1/343. 20

[Hush2016] Michael Hush. *M-loop: Machine-learning online optimization package*, 2016. `https://github.com/michaelhush/M-LOOP`. iv, 59

[Hetet2008b] G. Hétet, M. Hosseini, B. M. Sparkes, D. Oblak, P. K. Lam & B. C. Buchler. *Photon echoes generated by reversing magnetic field gradients in a rubidium vapor.* Optics Letters, 33(20):2323–2325, October 2008. doi:10.1364/OL.33.002323. 31

[Hetet2008] G. Hétet, J. J. Longdell, A. L. Alexander, P. K. Lam & M. J. Sellars. *Electro-Optic Quantum Memory for Light Using Two-Level Atoms.* Physical Review Letters, 100(2):023601, January 2008. doi:10.1103/PhysRevLett.100.023601. 31, 93

[Hetet2008a] G. Hétet, J. J. Longdell, M. J. Sellars, P. K. Lam & B. C. Buchler. *Multimodal Properties and Dynamics of Gradient Echo Quantum Memory.* Physical Review Letters, 101(20):203601, November 2008. doi:10.1103/PhysRevLett.101.203601. 93

[Iakoupov2016PhD] Ivan Iakoupov. *Enhancement of optical nonlinearities with stationary light.* Ph.D. thesis, University of Copenhagen, 2016. `http://theoretical-quantum-optics.nbi.ku.dk/studtheses/`. 115

[Iakoupov2016] Ivan Iakoupov, Johannes Borregaard & Anders S. Sørensen. *Controlled-phase gate for photons based on stationary light.* Phys. Rev. Lett., 120:010502, Jan 2018. doi:10.1103/PhysRevLett.120.010502. 29

[Iakoupov2016a] Ivan Iakoupov, Johan R. Ott, Darrick E. Chang & Anders S. Sørensen. *Dispersion relations for stationary light in one-dimensional atomic ensembles.* Physical Review A, 94(5):053824, 2016. doi:10.1103/PhysRevA.94.053824. 29

[Jamonneau2016] P. Jamonneau, G. Hétet, A. Dréau, J.-F. Roch & V. Jacques. *Coherent Population Trapping of a Single Nuclear Spin Under Ambient Conditions.* Physical Review Letters, 116(4):043603, January 2016. doi:10.1103/PhysRevLett.116.043603. 28

[Jenkins2012] S. D. Jenkins, T. Zhang & T. A. B. Kennedy. *Motional dephasing of atomic clock spin waves in an optical lattice.* Journal of Physics B: Atomic, Molecular and Optical Physics, 45(12):124005, 2012. doi:10.1088/0953-4075/45/12/124005. 108

[Jin2015] Jeongwan Jin, Erhan Saglamyurek, Marcel. lí Grimau Puigibert, Varun Verma, Francesco Marsili, Sae Woo Nam, Daniel Oblak & Wolfgang Tittel. *Telecom-wavelength atomic*

quantum memory in optical fiber for heralded polarization qubits. Physical Review Letters, 115:140501, September 2015. doi:10.1103/PhysRevLett.115.140501. 28

[Jobez2014] P. Jobez, I. Usmani, N. Timoney, C. Laplane, N. Gisin & M. Afzelius. *Cavity-enhanced storage in an optical spin-wave memory*. New Journal of Physics, 16(8):083005, 2014. doi:10.1088/1367-2630/16/8/083005. 28, 34

[Jobez2015] Pierre Jobez, Cyril Laplane, Nuala Timoney, Nicolas Gisin, Alban Ferrier, Philippe Goldner & Mikael Afzelius. *Coherent Spin Control at the Quantum Level in an Ensemble-Based Optical Memory*. Physical Review Letters, 114(23):230502, June 2015. doi:10.1103/PhysRevLett.114.230502. 34

[Jobez2016] Pierre Jobez, Nuala Timoney, Cyril Laplane, Jean Etesse, Alban Ferrier, Philippe Goldner, Nicolas Gisin & Mikael Afzelius. *Towards highly multimode optical quantum memory for quantum repeaters*. Physical Review A, 93(3):032327, March 2016. doi:10.1103/PhysRevA.93.032327. 28

[Julsgaard2001] Brian Julsgaard, Alexander Kozhekin & Eugene S. Polzik. *Experimental long-lived entanglement of two macroscopic objects*. Nature, 413(6854):400–403, September 2001. doi:10.1038/35096524. 40

[Julsgaard2004] Brian Julsgaard, Jacob Sherson, J. Ignacio Cirac, Jaromír Fiurášek & Eugene S. Polzik. *Experimental demonstration of quantum memory for light*. Nature, 432(7016):482–486, November 2004. doi:10.1038/nature03064. 40

[Kalb2015] Norbert Kalb, Andreas Reiserer, Stephan Ritter & Gerhard Rempe. *Heralded storage of a photonic quantum bit in a single atom*. Physical Review Letters, 114:220501, June 2015. doi:10.1103/PhysRevLett.114.220501. 28

[Katz2017] Or Katz & Ofer Firstenberg. *Light storage for one second in room-temperature alkali vapor*. Nature Communications, 9(1):2074, May 2018. doi:10.1038/s41467-018-04458-4. 40

[Kielpinski2002] D. Kielpinski, C. Monroe & D. J. Wineland. *Architecture for a large-scale ion-trap quantum computer*. Nature, 417(6890):709–711, June 2002. doi:10.1038/nature00784. 21

[Kimble2008] H. J. Kimble. *The quantum internet*. Nature, 453(7198):1023–1030, June 2008. doi:10.1038/nature07127. 19

[Knill2001] E. Knill, R. Laflamme & G. J. Milburn. *A scheme for efficient quantum computation with linear optics*. Nature, 409(6816):46–52, January 2001. doi:10.1038/35051009. 20

[Kozhekin2000] A. E. Kozhekin, K. Mølmer & E. Polzik. *Quantum memory for light.* Physical Review A, 62(3):033809, August 2000. doi:10.1103/PhysRevA.62.033809. 95

[Kupchak2015] Connor Kupchak, Thomas Mittiga, Bertus Jordaan, Mehdi Namazi, Christian Nölleke & Eden Figueroa. *Room-temperature single-photon level memory for polarization states.* Scientific Reports, 5:7658, January 2015. doi:10.1038/srep07658. 28

[Kurtsiefer2002] C. Kurtsiefer, P. Zarda, M. Halder, H. Weinfurter, P. M. Gorman, P. R. Tapster & J. G. Rarity. *Quantum cryptography: A step towards global key distribution.* Nature, 419(6906):450–450, 2002. doi:10.1038/419450a. 20

[Kuzmich2003] A. Kuzmich, W. P. Bowen, A. D. Boozer, A. Boca, C. W. Chou, L.-M. Duan & H. J. Kimble. *Generation of nonclassical photon pairs for scalable quantum communication with atomic ensembles.* Nature, 423(6941):731–734, June 2003. doi:10.1038/nature01714. 21

[Lambropoulos] Peter Lambropoulos & David Petrosyan. *Fundamentals of Quantum Optics and Quantum Information / Peter Lambropoulos / Springer.* Springer-Verlag Berlin Heidelberg, 2007. doi:10.1007/978-3-540-34572-5. 5, 54, 66

[Laplane2015] Cyril Laplane, Pierre Jobez, Jean Etesse, Nuala Timoney, Nicolas Gisin & Mikael Afzelius. *Multiplexed on-demand storage of polarization qubits in a crystal.* New Journal of Physics, 18(1):013006, December 2015. doi:10.1088/1367-2630/18/1/013006. 28

[Laurat2006] Julien Laurat, Hugues de Riedmatten, Daniel Felinto, Chin-Wen Chou, Erik W. Schomburg & H. Jeff Kimble. *Efficient retrieval of a single excitation stored in an atomic ensemble.* Opt. Express, 14(15):6912–6918, Jul 2006. doi:10.1364/OE.14.006912. 33

[LeGouet2009] J.-L. Le Gouët & P. R. Berman. *Raman scheme for adjustable-bandwidth quantum memory.* Physical Review A, 80(1):012320, 2009. doi:10.1103/PhysRevA.80.012320. 96

[Lettner2011] M. Lettner, M. Mücke, S. Riedl, C. Vo, C. Hahn, S. Baur, J. Bochmann, S. Ritter, S. Dürr & G. Rempe. *Remote entanglement between a single atom and a bose-einstein condensate.* Physical Review Letters, 106:210503, May 2011. doi:10.1103/PhysRevLett.106.210503. 28

[Lin2008a] Yen-Wei Lin, Hung-Chih Chou, Prashant P. Dwivedi, Ying-Cheng Chen & Ite A. Yu. *Using a pair of rectangular coils in the MOT for the production of cold atom clouds with large optical density.* Optics Express, 16(6):3753–3761, March 2008. doi:10.1364/OE.16.003753. 44

[Lin2009] Yen-Wei Lin, Wen-Te Liao, Thorsten Peters, Hung-Chih Chou, Jian-Siung Wang, Hung-Wen Cho, Pei-Chen Kuan & Ite A. Yu. *Stationary Light Pulses in Cold Atomic Media and without Bragg Gratings.* Physical Review Letters, 102(21):213601, May 2009. doi:10.1103/PhysRevLett.102.213601. 116, 118

[Longdell2008] J. J. Longdell, G. Hétet, P. K. Lam & M. J. Sellars. *Analytic treatment of controlled reversible inhomogeneous broadening quantum memories for light using two-level atoms.* Physical Review A, 78(3):032337, September 2008. doi:10.1103/PhysRevA.78.032337. 108

[Ma2017] Lijun Ma, Oliver Slattery & Xiao Tang. *Optical quantum memory based on electromagnetically induced transparency.* Journal of Optics, 19(4):043001, 2017. doi:10.1088/2040-8986/19/4/043001. 22, 27, 34

[Maring2017] Nicolas Maring, Pau Farrera, Kutlu Kutluer, Margherita Mazzera, Georg Heinze & Hugues de Riedmatten. *Photonic quantum state transfer between a cold atomic gas and a crystal.* Nature, 551(7681):485–488, November 2017. doi:10.1038/nature24468. 22, 25

[Maring2014] Nicolas Maring, Kutlu Kutluer, Joachim Cohen, Matteo Cristiani, Margherita Mazzera, Patrick M. Ledingham & Hugues de Riedmatten. *Storage of up-converted telecom photons in a doped crystal.* New Journal of Physics, 16(11):113021, 2014. doi:10.1088/1367-2630/16/11/113021. 34

[Massar1995] S. Massar & S. Popescu. *Optimal extraction of information from finite quantum ensembles.* Physical Review Letters, 74:1259–1263, February 1995. doi:10.1103/PhysRevLett.74.1259. 24, 86

[Matsukevich2006] D. N. Matsukevich, T. Chanelière, S. D. Jenkins, S.-Y. Lan, T. A. B. Kennedy & A. Kuzmich. *Entanglement of remote atomic qubits.* Physical Review Letters, 96:030405, January 2006. doi:10.1103/PhysRevLett.96.030405. 28

[Matsukevich2004] D. N. Matsukevich & A. Kuzmich. *Quantum State Transfer Between Matter and Light.* Science, 306(5696):663–666, October 2004. doi:10.1126/science.1103346. 22

[Mavadia2017] Sandeep Mavadia, Virginia Frey, Jarrah Sastrawan, Stephen Dona & Michael J. Biercuk. *Prediction and real-time compensation of qubit decoherence via machine learning.* Nature Communications, 8:ncomms14106, 2017. doi:10.1038/ncomms14106. 59

[Michelberger2015] P. S. Michelberger, T. F. M. Champion, M. R. Sprague, K. T. Kaczmarek, M. Barbieri, X. M. Jin, D. G. England, W. S. Kolthammer, D. J. Saunders, J. Nunn & I. A. Walmsley. *Interfacing GHz-bandwidth heralded single photons with a warm vapour Raman memory.* New Journal of Physics, 17(4):043006, April 2015. doi:10.1088/1367-2630/17/4/043006. 29, 30

[Mishina2011] O. S. Mishina, M. Scherman, P. Lombardi, J. Ortalo, D. Felinto, A. S. Sheremet, A. Bramati, D. V. Kupriyanov, J. Laurat & E. Giacobino. *Electromagnetically induced transparency in an inhomogeneously broadened Λ transition with multiple excited levels.* Physical Review A, 83:053809, May 2011. doi:10.1103/PhysRevA.83.053809. 73

[Moiseev2006] S. A. Moiseev & B. S. Ham. *Quantum manipulation of two-color stationary light: Quantum wavelength conversion.* Physical Review A, 73(3):033812, March 2006. doi:10.1103/PhysRevA.73.033812. 29, 115

[Moiseev2001] S. A. Moiseev & S. Kröll. *Complete Reconstruction of the Quantum State of a Single-Photon Wave Packet Absorbed by a Doppler-Broadened Transition.* Physical Review Letters, 87(17):173601, October 2001. doi:10.1103/PhysRevLett.87.173601. 22, 30

[Moiseev2003] S. A. Moiseev, V. F. Tarasov & B. S. Ham. *Quantum memory photon echo-like techniques in solids.* Journal of Optics B: Quantum and Semiclassical Optics, 5(4):S497, 2003. doi:10.1088/1464-4266/5/4/356. 30

[Moiseev2011] S A Moiseev & W Tittel. *Optical quantum memory with generalized time-reversible atom-light interaction.* New Journal of Physics, 13(6):063035, 2011. doi:10.1088/1367-2630/13/6/063035. 95, 97

[Nicolas2014] A. Nicolas, L. Veissier, L. Giner, E. Giacobino, D. Maxein & J. Laurat. *A quantum memory for orbital angular momentum photonic qubits.* Nature Photonics, 8(3):234–238, March 2014. doi:10.1038/nphoton.2013.355. 25, 65, 79

[Nicolas2014PhD] Adrien Nicolas. *Optical quantum memories with cold atomic ensembles : a free space implementation for multimode*

storage, or a nanofiber-based one for high collection efficiency. Ph.D. thesis, Université Pierre et Marie Curie - Paris VI, 2014. `https://tel.archives-ouvertes.fr/tel-01127631/document`. 38

[Nikoghosyan2009] Gor Nikoghosyan & Michael Fleischhauer. *Stationary light in cold-atomic gases.* Physical Review A, 80(1):013818, July 2009. doi:10.1103/PhysRevA.80.013818. 29, 118

[Nilsson2005] Mattias Nilsson & Stefan Kröll. *Solid state quantum memory using complete absorption and re-emission of photons by tailored and externally controlled inhomogeneous absorption profiles.* Optics Communications, 247(4):393–403, March 2005. doi:10.1016/j.optcom.2004.11.077. 30

[Novikova2007] Irina Novikova, Alexey V. Gorshkov, David F. Phillips, Anders S. Sørensen, Mikhail D. Lukin & Ronald L. Walsworth. *Optimal control of light pulse storage and retrieval.* Physical Review Letters, 98(24), June 2007. doi:10.1103/physrevlett.98.243602. 102

[Nunn2013] J. Nunn, N. K. Langford, W. S. Kolthammer, T. F. M. Champion, M. R. Sprague, P. S. Michelberger, X.-M. Jin, D. G. England & I. A. Walmsley. *Enhancing multiphoton rates with quantum memories.* Physical Review Letters, 110(13):133601, 2013. doi:10.1103/PhysRevLett.110.133601. 22

[Nunn2008] J. Nunn, K. Reim, K. C. Lee, V. O. Lorenz, B. J. Sussman, I. A. Walmsley & D. Jaksch. *Multimode memories in atomic ensembles.* Physical Review Letters, 101(26), December 2008. doi:10.1103/physrevlett.101.260502. 25

[Nunn2007] J. Nunn, I. A. Walmsley, M. G. Raymer, K. Surmacz, F. C. Waldermann, Z. Wang & D. Jaksch. *Mapping broadband single-photon wave packets into an atomic memory.* Physical Review A, 75:011401, January 2007. doi:10.1103/PhysRevA.75.011401. 30, 96, 97, 102

[Oreg1984] J. Oreg, F. T. Hioe & J. H. Eberly. *Adiabatic following in multilevel systems.* Physical Review A, 29(2):690–697, February 1984. doi:10.1103/PhysRevA.29.690. 66

[Parigi2015] Valentina Parigi, Vincenzo D'Ambrosio, Christophe Arnold, Lorenzo Marrucci, Fabio Sciarrino & Julien Laurat. *Storage and retrieval of vector beams of light in a multiple-degree-of-freedom quantum memory.* Nature Communications, 6:7706, July 2015. doi:10.1038/ncomms8706. 29, 65

[Peng2005] Cheng-Zhi Peng, Tao Yang, Xiao-Hui Bao, Jun Zhang, Xian-Min Jin, Fa-Yong Feng, Bin Yang, Jian Yang, Juan Yin, Qiang Zhang, Nan Li, Bao-Li Tian & Jian-Wei Pan. *Experimental free-space distribution of entangled photon pairs over 13 km: Towards satellite-based global quantum communication.* Physical Review Letters, 94(15):150501, 2005. doi:10.1103/PhysRevLett.94.150501. 20

[Peres1996] Asher Peres. *Separability Criterion for Density Matrices.* Physical Review Letters, 77(8):1413–1415, August 1996. doi:10.1103/PhysRevLett.77.1413. 7

[Petrich1994] Wolfgang Petrich, Michael H. Anderson, Jason R. Ensher & Eric A. Cornell. *Behavior of atoms in a compressed magneto-optical trap.* JOSA B, 11(8):1332–1335, 1994. doi:10.1364/JOSAB.11.001332. 45

[Pinel2015] Olivier Pinel, Jesse L. Everett, Mahdi Hosseini, Geoff T. Campbell, Ben C. Buchler & Ping Koy Lam. *A mirrorless spinwave resonator.* Scientific Reports, 5:srep17633, December 2015. doi:10.1038/srep17633. 110, 115, 129

[Radnaev2010] A. G. Radnaev, Y. O. Dudin, R. Zhao, H. H. Jen, S. D. Jenkins, A. Kuzmich & T. a. B. Kennedy. *A quantum memory with telecom-wavelength conversion.* Nature Physics, 6(11):894–899, November 2010. doi:10.1038/nphys1773. 21

[Rambach2016] Markus Rambach, Aleksandrina Nikolova, Till J. Weinhold & Andrew G. White. *Sub-megahertz linewidth single photon source.* APL Photonics, 1(9):096101, November 2016. doi:10.1063/1.4966915. 89, 112, 136

[Raymer1981] M. G. Raymer & J. Mostowski. *Stimulated raman scattering: Unified treatment of spontaneous initiation and spatial propagation.* Physical Review A, 24(4):1980–1993, 1981. doi:10.1103/PhysRevA.24.1980. 95

[Raymer1985] M. G. Raymer, I. A. Walmsley, J. Mostowski & B. Sobolewska. *Quantum theory of spatial and temporal coherence properties of stimulated raman scattering.* Physical Review A, 32(1):332–344, 1985. doi:10.1103/PhysRevA.32.332. 95

[Reim2011] K. F. Reim, P. Michelberger, K. C. Lee, J. Nunn, N. K. Langford & I. A. Walmsley. *Single-Photon-Level Quantum Memory at Room Temperature.* Physical Review Letters, 107(5):053603, July 2011. doi:10.1103/PhysRevLett.107.053603. 29, 34, 112

[Reim2012] K. F. Reim, J. Nunn, X.-M. Jin, P. S. Michelberger, T. F. M. Champion, D. G. England, K. C. Lee, W. S. Kolthammer,

N. K. Langford & I. A. Walmsley. *Multipulse Addressing of a Raman Quantum Memory: Configurable Beam Splitting and Efficient Readout.* Physical Review Letters, 108(26):263602, June 2012. doi:10.1103/PhysRevLett.108.263602. 29, 110

[Reim2010] K. F. Reim, J. Nunn, V. O. Lorenz, B. J. Sussman, K. C. Lee, N. K. Langford, D. Jaksch & I. A. Walmsley. *Towards high-speed optical quantum memories.* Nature Photonics, 4(4):218–221, April 2010. doi:10.1038/nphoton.2010.30. 29

[Ringot2001] J. Ringot, P. Szriftgiser & J. C. Garreau. *Sub-recoil Raman spectroscopy of cold cesium atoms.* Physical Review A, 65(1):013403, December 2001. doi:10.1103/PhysRevA.65.013403. 54

[Roy2017] Dibyendu Roy, C. M. Wilson & Ofer Firstenberg. *Colloquium: Strongly interacting photons in one-dimensional continuum.* Reviews of Modern Physics, 89(2):021001, May 2017. doi:10.1103/RevModPhys.89.021001. 10

[Sabooni2013a] Mahmood Sabooni, Qian Li, Stefan Kröll & Lars Rippe. *Efficient Quantum Memory Using a Weakly Absorbing Sample.* Physical Review Letters, 110(13):133604, March 2013. doi:10.1103/PhysRevLett.110.133604. 34

[Saglamyurek2011] Erhan Saglamyurek, Neil Sinclair, Jeongwan Jin, Joshua A. Slater, Daniel Oblak, Felix Bussieres, Mathew George, Raimund Ricken, Wolfgang Sohler & Wolfgang Tittel. *Broadband waveguide quantum memory for entangled photons.* Nature, 469(7331):512–515, January 2011. doi:10.1364/icqi.2011.qtug2. 28

[Sangouard2007] Nicolas Sangouard, Christoph Simon, Mikael Afzelius & Nicolas Gisin. *Analysis of a quantum memory for photons based on controlled reversible inhomogeneous broadening.* Physical Review A, 75(3):032327, March 2007. doi:10.1103/PhysRevA.75.032327. 108

[Sangouard2011] Nicolas Sangouard, Christoph Simon, Hugues de Riedmatten & Nicolas Gisin. *Quantum repeaters based on atomic ensembles and linear optics.* Reviews of Modern Physics, 83:33–80, March 2011. doi:10.1103/RevModPhys.83.33. 23

[Saunders2016] D. J. Saunders, J. H. D. Munns, T. F. M. Champion, C. Qiu, K. T. Kaczmarek, E. Poem, P. M. Ledingham, I. A. Walmsley & J. Nunn. *Cavity-enhanced room-temperature broadband raman memory.* Physical Review Letters, 116(9):090501, March 2016. doi:10.1103/PhysRevLett.116.090501. 29

[Schmidt1996] H. Schmidt & A. Imamoglu. *Giant Kerr nonlinearities obtained by electromagnetically induced transparency.* Optics Letters, 21(23):1936–1938, December 1996. doi:10.1364/OL.21.001936. 27

[Schori2002] C. Schori, B. Julsgaard, J. L. Sørensen & E. S. Polzik. *Recording Quantum Properties of Light in a Long-Lived Atomic Spin State: TowardsQuantum Memory.* Physical Review Letters, 89(5):057903, July 2002. doi:10.1103/PhysRevLett.89.057903. 40

[Scully1992] Marlan O. Scully & Michael Fleischhauer. *High-sensitivity magnetometer based on index-enhanced media.* Physical Review Letters, 69(9):1360–1363, August 1992. doi:10.1103/PhysRevLett.69.1360. 28

[Sheremet2010] A. S. Sheremet, L. V. Gerasimov, I. M. Sokolov, D. V. Kupriyanov, O. S. Mishina, E. Giacobino & J. Laurat. *Quantum memory for light via a stimulated off-resonant raman process: Beyond the three-level Λ-scheme approximation.* Physical Review A, 82:033838, September 2010. doi:10.1103/PhysRevA.82.033838. 73

[Simon2007] Jonathan Simon, Haruka Tanji, James K. Thompson & Vladan Vuletić. *Interfacing collective atomic excitations and single photons.* Physical Review Letters, 98(18):183601, 2007. doi:10.1103/PhysRevLett.98.183601. 33

[Sinclair2014] Neil Sinclair, Erhan Saglamyurek, Hassan Mallahzadeh, Joshua A. Slater, Mathew George, Raimund Ricken, Morgan P. Hedges, Daniel Oblak, Christoph Simon, Wolfgang Sohler & Wolfgang Tittel. *Spectral multiplexing for scalable quantum photonics using an atomic frequency comb quantum memory and feed-forward control.* Physical Review Letters, 113:053603, July 2014. doi:10.1103/PhysRevLett.113.053603. 25

[Sparkes2013] B M Sparkes, J Bernu, M Hosseini, J Geng, Q Glorieux, P A Altin, P K Lam, N P Robins & B C Buchler. *Gradient echo memory in an ultra-high optical depth cold atomic ensemble.* New Journal of Physics, 15(8):085027, 2013. doi:10.1088/1367-2630/15/8/085027. 31, 34, 40, 93

[Sparkes2010] B. M. Sparkes, M. Hosseini, G. Hétet, P. K. Lam & B. C. Buchler. *ac stark gradient echo memory in cold atoms.* Physical Review A, 82(4):043847, October 2010. doi:10.1103/PhysRevA.82.043847. 93

[Sparkes2013PhD] Benjamin M. Sparkes. *Storage and Manipulation of Optical Information Using Gradient Echo Memory in Warm Vapours and Cold Ensembles*. Ph.D. thesis, The Australian National University, 2013. `http://photonics.anu.edu.au/qoptics/theses.php`. 38, 106

[Specht2011] Holger P. Specht, Christian Nolleke, Andreas Reiserer, Manuel Uphoff, Eden Figueroa, Stephan Ritter & Gerhard Rempe. *A single-atom quantum memory*. Nature, 473(7346):190–193, May 2011. doi:10.1364/icqi.2011.qtug3. 23, 28, 86

[SteckCesium] Daniel A Steck. *Cesium D Line Data*. Available online at `http://steck.us/alkalidata` (revision 2.1.4, 23 December 2010). 43, 68, 73

[Surmacz2008] K. Surmacz, J. Nunn, K. Reim, K. C. Lee, V. O. Lorenz, B. Sussman, I. A. Walmsley & D. Jaksch. *Efficient spatially resolved multimode quantum memory*. Physical Review A, 78:033806, September 2008. doi:10.1103/PhysRevA.78.033806. 30, 96, 100, 102, 112, 141

[Tikhonov2015] Kirill Tikhonov, Tania Golubeva & Yuri Golubev. *Atomic thermal motion effect on efficiency of a high-speed quantum memory*. The European Physical Journal D, 69(11):252, 2015. doi:10.1140/epjd/e2015-60370-6. 45, 112

[Tiranov2015] Alexey Tiranov, Jonathan Lavoie, Alban Ferrier, Philippe Goldner, Varun B. Verma, Sae Woo Nam, Richard P. Mirin, Adriana E. Lita, Francesco Marsili, Harald Herrmann, Christine Silberhorn, Nicolas Gisin, Mikael Afzelius & Félix Bussières. *Storage of hyperentanglement in a solid-state quantum memory*. Optica, 2(4):279–287, April 2015. doi:10.1364/OPTICA.2.000279. 29

[Tittel2010] W. Tittel, M. Afzelius, T. Chaneliére, R.l. Cone, S. Kröll, S.a. Moiseev & M. Sellars. *Photon-echo quantum memory in solid state systems*. Laser & Photonics Reviews, 4(2):244–267, February 2010. doi:10.1002/lpor.200810056. 30

[Tranter2018] A. D. Tranter, H. J. Slatyer, M. R. Hush, A. C. Leung, J. L. Everett, K. V. Paul, P. Vernaz-Gris, P. K. Lam, B. C. Buchler & G. T. Campbell. *Multiparameter optimisation of a magneto-optical trap using deep learning*. Nature Communications, 9(1):4360, October 2018. doi:10.1038/s41467-018-06847-1. iv, 59, 62

[Vanier2005] J. Vanier. *Atomic clocks based on coherent population trapping: a review*. Applied Physics B, 81(4):421–442, August 2005. doi:10.1007/s00340-005-1905-3. 28

[Varnava2006] Michael Varnava, Daniel E. Browne & Terry Rudolph. *Loss Tolerance in One-Way Quantum Computation via Counterfactual Error Correction*. Physical Review Letters, 97(12):120501, September 2006. doi:10.1103/PhysRevLett.97.120501. 23

[Veissier2013] L. Veissier, A. Nicolas, L. Giner, D. Maxein, A. S. Sheremet, E. Giacobino & J. Laurat. *Reversible optical memory for twisted photons*. Optics Letters, 38(5):712–714, March 2013. doi:10.1364/OL.38.000712. 65

[Veissier2013PhD] Lucile Veissier. *Quantum memory protocols in large cold atomic ensembles*. Ph.D. thesis, Université Pierre et Marie Curie - Paris VI, 2013. `https://tel.archives-ouvertes.fr/tel-00977307/document`. 38

[Vernaz-Gris2018] Pierre Vernaz-Gris, Kun Huang, Mingtao Cao, Alexandra S. Sheremet & Julien Laurat. *Highly-efficient quantum memory for polarization qubits in a spatially-multiplexed cold atomic ensemble*. Nature Communications, 9(1):363, January 2018. doi:10.1038/s41467-017-02775-8. iv, 65, 66

[Vernaz-Gris2018a] Pierre Vernaz-Gris, Aaron D. Tranter, Jesse L. Everett, Anthony C. Leung, Karun V. Paul, Geoff T. Campbell, Ping Koy Lam & Ben C. Buchler. *High-performance raman memory with spatio-temporal reversal*. Opt. Express, 26(10):12424–12431, May 2018. doi:10.1364/OE.26.012424. iv, 93

[Walther2005] P. Walther, K. J. Resch, T. Rudolph, E. Schenck, H. Weinfurter, V. Vedral, M. Aspelmeyer & A. Zeilinger. *Experimental one-way quantum computing*. Nature, 434(7030):169, March 2005. doi:10.1038/nature03347. 20

[Wasilewski2006] Wojciech Wasilewski & M. G. Raymer. *Pairwise entanglement and readout of atomic-ensemble and optical wave-packet modes in traveling-wave Raman interactions*. Physical Review A, 73(6):063816, June 2006. doi:10.1103/PhysRevA.73.063816. 99

[Wiesner1983] Stephen Wiesner. *Conjugate Coding*. SIGACT News, 15(1):78–88, January 1983. doi:10.1145/1008908.1008920. 20

[Wigley2016] P. B. Wigley, P. J. Everitt, A. van den Hengel, J. W. Bastian, M. A. Sooriyabandara, G. D. McDonald, K. S. Hardman, C. D. Quinlivan, P. Manju, C. C. N. Kuhn, I. R. Petersen, A. N. Luiten, J. J. Hope, N. P. Robins & M. R. Hush. *Fast machine-learning online optimization of ultra-cold-atom experiments*. Scientific Reports, 6:srep25890, 2016. doi:10.1038/srep25890. 59

[Wu2010a] Jin-Hui Wu, M. Artoni & G. C. La Rocca. *Decay of stationary light pulses in ultracold atoms.* Physical Review A, 81(3):033822, March 2010. doi:10.1103/PhysRevA.81.033822. 116, 117, 118

[Wu2010] Jin-Hui Wu, M. Artoni & G. C. La Rocca. *Stationary light pulses in cold thermal atomic clouds.* Physical Review A, 82(1):013807, July 2010. doi:10.1103/PhysRevA.82.013807. 29, 116

[Xu2013] Zhongxiao Xu, Yuelong Wu, Long Tian, Lirong Chen, Zhiying Zhang, Zhihui Yan, Shujing Li, Hai Wang, Changde Xie & Kunchi Peng. *Long lifetime and high-fidelity quantum memory of photonic polarization qubit by lifting zeeman degeneracy.* Physical Review Letters, 111:240503, December 2013. doi:10.1103/PhysRevLett.111.240503. 28

[Yin2017] Juan Yin, Yuan Cao, Yu-Huai Li, Sheng-Kai Liao, Liang Zhang, Ji-Gang Ren, Wen-Qi Cai, Wei-Yue Liu, Bo Li, Hui Dai, Guang-Bing Li, Qi-Ming Lu, Yun-Hong Gong, Yu Xu, Shuang-Lin Li, Feng-Zhi Li, Ya-Yun Yin, Zi-Qing Jiang, Ming Li, Jian-Jun Jia, Ge Ren, Dong He, Yi-Lin Zhou, Xiao-Xiang Zhang, Na Wang, Xiang Chang, Zhen-Cai Zhu, Nai-Le Liu, Yu-Ao Chen, Chao-Yang Lu, Rong Shu, Cheng-Zhi Peng, Jian-Yu Wang & Jian-Wei Pan. *Satellite-based entanglement distribution over 1200 kilometers.* Science, 356(6343):1140–1144, 2017. doi:10.1126/science.aan3211. 20

[Yin2012] Juan Yin, Ji-Gang Ren, He Lu, Yuan Cao, Hai-Lin Yong, Yu-Ping Wu, Chang Liu, Sheng-Kai Liao, Fei Zhou, Yan Jiang, Xin-Dong Cai, Ping Xu, Ge-Sheng Pan, Jian-Jun Jia, Yong-Mei Huang, Hao Yin, Jian-Yu Wang, Yu-Ao Chen, Cheng-Zhi Peng & Jian-Wei Pan. *Quantum teleportation and entanglement distribution over 100-kilometre free-space channels.* Nature, 488(7410):185–188, 2012. doi:10.1038/nature11332. 20

[Zhang2011] Han Zhang, Xian-Min Jin, Jian Yang, Han-Ning Dai, Sheng-Jun Yang, Tian-Ming Zhao, Jun Rui, Yu He, Xiao Jiang, Fan Yang, Ge-Sheng Pan, Zhen-Sheng Yuan, Youjin Deng, Zeng-Bing Chen, Xiao-Hui Bao, Shuai Chen, Bo Zhao & Jian-Wei Pan. *Preparation and storage of frequency-uncorrelated entangled photons from cavity-enhanced spontaneous parametric downconversion.* Nature Photonics, 5(10):628–632, October 2011. doi:10.1038/nphoton.2011.213. 28

[Zhang2016] Wei Zhang, Dong-Sheng Ding, Ming-Xin Dong, Shuai Shi, Kai Wang, Shi-Long Liu, Yan Li, Zhi-Yuan Zhou, Bao-Sen

Shi & Guang-Can Guo. *Experimental realization of entanglement in multiple degrees of freedom between two quantum memories.* Nature Communications, 7:13514, November 2016. doi:10.1038/ncomms13514. 29

[Zhang2012a] Xiao-Jun Zhang, Hai-Hua Wang, Cheng-Zhi Liu, Xing-Wei Han, Cun-Bo Fan, Jin-Hui Wu & Jin-Yue Gao. *Direct conversion of slow light into a stationary light pulse.* Physical Review A, 86(2):023821, August 2012. doi:10.1103/PhysRevA.86.023821. 116

[Zhang2013] Xiao-Jun Zhang, Hai-Hua Wang, Zeng-Bin Wang, Xue Dong, Lei Wang, Li-Li Han, Yan Xu, Cheng-Zhi Liu, Cun-Bo Fan & Jin-Yue Gao. *Tunable reflection based on electromagnetically induced transparency.* JOSA B, 30(7):1905–1910, July 2013. doi:10.1364/JOSAB.30.001905. 116

[Zhou2015] Zong-Quan Zhou, Yi-Lin Hua, Xiao Liu, Geng Chen, Jin-Shi Xu, Yong-Jian Han, Chuan-Feng Li & Guang-Can Guo. *Quantum storage of three-dimensional orbital-angular-momentum entanglement in a crystal.* Physical Review Letters, 115:070502, August 2015. doi:10.1103/PhysRevLett.115.070502. 25

[Zhou2012] Zong-Quan Zhou, Wei-Bin Lin, Ming Yang, Chuan-Feng Li & Guang-Can Guo. *Realization of reliable solid-state quantum memory for photonic polarization qubit.* Physical Review Letters, 108:190505, May 2012. doi:10.1103/PhysRevLett.108.190505. 28

Pierre VERNAZ-GRIS

Sujet : Préparation de grands ensembles atomiques et applications en interface lumière-matière efficace

Résumé : Cette thèse de doctorat en cotutelle a été centrée sur des expériences d'optique quantique faisant intervenir de grands ensembles atomiques. L'étude de l'interaction entre la lumière et la matière et l'augmentation de leur couplage dans ces systèmes sont des étapes fondamentales pour le développement et l'amélioration de protocoles de génération, de stockage et de manipulation d'information quantique. Le travail de thèse exposé ici traite en particulier de l'évolution des techniques de préparation d'ensembles atomiques denses, des protocoles de lumière arrêtée et de lumière stationnaire développés et étudiés expérimentalement. Les ensembles d'atomes froids préparés par refroidissement laser dans les deux réalisations expérimentales ont été portés jusqu'à des épaisseurs optiques de plusieurs centaines, à des températures d'une dizaine de microkelvin. De plus, l'adressage de ces ensembles dans des configurations symétriques ont permis l'étude de protocoles basés sur le renversement temporel de la conversion de lumière en excitations atomiques collectives. Ces améliorations ont mené au stockage de bits quantiques par transparence induite électromagnétiquement, et de lumière cohérente par symétrie temporelle dans une mémoire Raman, tous deux à des record d'efficacité, à de plus de 50%. Ce travail a également conduit à l'étude expérimentale de la lumière stationnaire et de nouveaux protocoles en découlant.

Cette thèse est rédigée en anglais.

Mots clés : Atomes froids, optique quantique, mémoire quantique, communication quantique, transparence induite électromagnétiquement, mémoire Raman

Subject : Preparation of large cold atomic ensembles and applications in efficient light-matter interfacing

Abstract: This cotutelle PhD thesis revolves around quantum optics experiments which involve large atomic ensembles. The study of light-matter interaction and its enhancement are crucial steps in the development and progress of quantum information generation, storage and processing protocols. The work presented here focuses on the evolution of large atomic ensemble preparation techniques, on the development and experimental investigation of stopped and stationary light protocols. Laser-cooled atomic ensembles in both experimental realisations have been brought to optical depths of a few hundreds, at temperatures of tens of microkelvin. Moreover, addressing these ensembles in symmetric configurations has enabled the study of protocols based on the temporal reversal of the mapping of light to collective atomic excitations. These enhancements have led to the storage of qubits based on electromagnetically-induced transparency, and the optical storage in a backward-retrieval Raman scheme, both demonstrating efficiency records, above 50%. This work has also led to the experimental investigation of stationary light and new protocols based on it.

Keywords : Cold atoms, quantum optics, quantum memory, quantum communication, electromagnetically-induced transparency, Raman memory